Rainfall, wind and cities' extreme variability : a multifractal approach from drop scale to catchment scale to improve resilience

Auguste Gires

Mémoire en vue de l'obtention du diplôme
d'Habilitation à Diriger des Recherches

Rainfall, wind and cities' extreme variability : a multifractal approach from drop scale to catchment scale to improve resilience

Auguste Gires

May 2022

Contents

Chapter 1

Introduction

1.1 A journey in research at ENPC and in Europe

Geophysical fields, notably rainfall or atmospheric turbulence, exhibit very specific features : (i) Strongly nonlinear fundamental equations which yield non trivial behaviour; (ii) Extreme variability over wide range of spatial and temporal scales, which is more and more visible with a kind of golden age in data; (iii) Intermittency with fluxes generated by a reduced number of events; (iv) Non-Gaussian statistics commonly leading to underestimation of extremes; (v) Persistence with long range correlation. Understanding and accounting for all these features in various contexts is the backbone of all my research activity which thrived on the 'hydro-meteorology and complexity' axis of the LEESU, which from August 2015 has gradually become the Hydrology, Meteorology and Complexity (HM&Co) laboratory. Its mission is : 'observation, analysis and modelling of the variability of interactions between urban systems and their environment over wide ranges of time and space scales'. In order to achieve this, there is a need to work in parallel on both multi-scale observations and theoretical framework to grasp its complexity and finally extract useful information for practical applications. Multifractal techniques are a powerful, physically based and mathematically robust, tool to handle such extreme variability and are at the core of my scientific work. They rely on the overall idea that underlying fields are generated with the help of a multiplicative cascade process, inherited from the scale invariance properties of Navier-Stokes equations.

My research activities started in 2009 with a PhD thesis in the laboratory LEESU of Ecole des Ponts ParisTech (later denoted ENPC, its administrative name), under the supervision of Pr. Daniel Schertzer. It was entitled 'Improving storm water management in urban and peri-urban areas with the help of multifractal analysis and simulations'. During this work, space-time multifractal analysis were implemented on rainfall events in Paris, the South of France and London using both weather radar data and atmospheric model outputs. It appeared that a scaling behaviour was observed on two distinct ranges of scales separated by a break at roughly 16 km. These data sets were in overall agreement with a simple space-time scaling model relying on a single anisotropy exponent between space and time. I also explored another facet of intermittency, which is particularly important for long time series of precipitation, that of numerous zero rainfall measurements (a pixel or a time step with no recorded rainfall), i.e. long 'dry' periods. I quantified precisely the effect of a threshold on a multifractal analysis and suggested a toy model to introduce some zeros within the cascade process conditioned by the field value. This enabled to explain most of the observed behaviour, and notably the difference between event statistics and overall statistics. Finally the impact of unmeasured small scale rainfall variability (i.e. occurring at scales smaller than 1 km in space and 5 min in time which are available with operational radar networks) was quantified with the help of various types of hydrodynamic models and a stochastic downscaling technique for rainfall. It showed that it should not be neglected and highlighted the need to use fully distributed models to account for it. During this PhD, I stayed two months at the Imperial College London in the Department of Civil and Environmental Engineering. Part of this work was done in the framework of the FP7 European project SMARTesT (2009-2012), which aimed at improving flood resilience of cities. The work developed during my PhD was recognized by Outstanding student poster awards at both the European Geosciences Union and American Geophysical Union.

In the years following my PhD, my research activity was mainly done in the framework of the European project Interreg IV NEW RainGain (2012-2015) whose goal was to test the interest of using dual polarization X-band radar to improve storm water management in urban areas. It involved 13 partners and the academic ones were ENPC, Imperial College London, KU Leuven and Technical University of Delft. I was notably principal investigator for ENPC's contribution to work packages 2 (Fine-scale rainfall data acquisition and prediction) and 3 (Modelling and prediction of urban pluvial flooding). It corresponded to a continuation and deepening of the work initiated during my PhD. These activities were also supported by involvement in the Climate KIC Blue Green Dream project (2013-2015) and regional project RadX@IdF (2013-2018) on the installation of an X-band radar in the Ile-de-France region. During this project, I contributed to the supervision of my first PhD

student in the framework of a partnership with Val-de-Marne county. It is during these years, that I was able to initiate work on disdrometers and impact of drops' location on rainfall retrieval with radars. These activities were later structured within the TARANIS (exTreme and multi-scAle RAiNdrop parIS) platform which aims at putting microphysics at the service of the measurement and modelling of rainfall fields. By microphysics, I mean the size and velocity properties of hydrometeors (drops, flakes, hailstones, etc.). The TARANIS platform of which I have full responsibility is now a pillar of my research work. This is a contribution to HM&Co's broader objective of developing high-resolution urban precipitation measurement products (i.e. with a mesh size typically finer than 100 m and for a time step of the order of the minute), which water practitioners in particular have a crucial need for.

I was also involved as a scientist to the activities of the chair 'Hydrology for resilient cities', a 10 year partnership with Veolia, the world leading company in the field of water. It notably resulted, in collaboration with other projects including RainGain and in the installation and operation of dual polarized X-band radar on ENPC campus. In this framework, the validation of the radar data was mainly done on the upper Bièvre catchment in the South a Paris. It is semi-urbanized 110 km^2 area which suffered severe flooding and is now highly regulated and monitored.

In the years 2015-2016, I coordinated my first project which was a Campus France Hubert Curien partnership in the framework of Germaine de Staël program with Switzerland. It was entitled 'Multi-scale analysis of the spatial and temporal variability of observed and numerically simulated precipitation'. It was in collaboration with Laboratoire Télédétection Environnementale of EPF Lausanne. It supported mobility with a 20 kE grant. During this project, I supervised the work of two PhD students who each published their results in peer-reviewed journals. It enabled to extend some previous findings to snowfall and deepen the analysis of model outputs.

In order to take more responsibility and widen the range of applications investigated at HM&Co, I submitted a project which got granted at the French National Research agency in the program for young researchers (ANR JCJC). It is entitled RW-Turb for 'Rainfall Wind Turbine or Turbulence', and started on 01/10/2019 for a duration of 48 months with a total grant of 295 kE. RW-Turb relies on the expertise of HM&Co in measurement and modelling across wide range of spatio-temporal scales of atmospheric turbulence and rainfall to quantify the impact of the latter on wind power production. This project benefits from an industrial partnership with Boralex, a wind power producer. RW-Turb will open new paths to improve nowcasts of power production, a major challenge in a framework of increasing use of renewable energies in France and Europe. This project was notably designed as an opportunity to integrate wind measurements in the TARANIS platform, which was a required step to enable significant progress, and widen HM&Co activities to wind energy. It notably funds 1.5 PhD projects. Students were recruited on 10/2019 and 10/2020.

My journey in the field of research is presented in a rather linear way with a succession of projects. However, it would be naive to believe this was as smooth as that. Indeed, with success rates at both national and European scales of typically 10-15% to grant proposals, and even assuming that at HM&Co we are better than average ;-), some failures are expected. This obviously happened and I was involved in numerous proposals (sometimes as coordinator) that did not got granted despite excellent scores. Some attempts of industrial partnerships were not successful as well. I have an overall research project, which aims at better understanding, and accounting for in various applications, the extreme variability of geophysical fields such as rainfall and atmospheric turbulence. With colleagues at HM&Co we regularly submit proposals with this overall goal in mind but are also dependent on existing opportunities and fashion trend in research.

1.2 Overall research project

As it can be understood from the previous section, my scientific activity and project is centered on how to better measure, understand, model and simulate the extreme variability observed over wide range of scales of both geophysical and anthropogenic fields and their complex interactions for practical applications. Within both types of fields, there is a focus on rainfall and wind turbulence on one side and cities in the other.

Over the years, I progressively shaped my scientific activity around three interacting pillars :

- Contributions to the theoretical developments of Universal Multifractals
- Dealing with anthropogenic and geophysics' extreme variability to improve urban resilience
- TARANIS (exTreme and multi-scAle RAiNdrop parIS) platform

Each pillar is presented in a dedicated chapter (chapter 2, 3 and 4 respectively) of this document which are all introduced by few paragraphs emphasizing their role in my scientific project. The document only mentions work done after my PhD and its immediate aftermath. Only the elements to which I significantly contributed are discussed, and the remaining can be found in the papers which are listed in annexes.

Finally, research perspectives are discussed in chapter 5 around five main themes which all contribute to this overall project:

- Back to rainfall basics : from individual drops to collective behaviour.
- Improving disdrometers and radar measurements by mimicking device's functioning at drop scale.
- Contributions to the theoretical developments of UM.
- Optimization of storm water management to increase urban resilience.
- Widening the range of applications for UM.

Some of the developments are already initiated with ongoing projects and PhD students while others will require finding additional funding. Leads for potential applications and partnerships that could help shape future investigations are discussed.

1.3 Outreach the general public

Before going on with the scientific core or this document, I would like to mention that I am also involved in science popularization through various activities. I believe that as scientist, we should dedicate some time to explain our work and the underlying complexity of our world to help the general public understand it better before making some decisions.

Activities dedicated to kids include but are not limited to :

- Writing and publishing of two books in the collection 'Minipommes', Ed. 'Le Pommier'. One is on rainfall and the other basically deals with storm water management in cities.
- Design and implementation of participatory workshop entitled 'Fract'Art : hasard et géométrie pour tous' ('Fract'Art : randomness and geometry for all') in the Science Museum Exploradôme of Ivry-sur-Seine.
- Various seminars in classrooms.

Activities dedicated to adults include but are not limited to :

- Contribution to various RainGain stands, notably one at the 'Festival de l'oh' of the Val-de-Marne County.
- Design and implementation of a serious game '1/2 million drops in 114 days' to discover in a pedagogical way disdrometer data and some rainfall features. It was notably used for the celebration of the 20 years of our campus (in 2018) and in few classrooms.
- Design and implementation of a stand with real time measurement of artificial rainfall with a disdrometer. It was used at the Academy of Science during a event of the 'Fondation de l'Ecole des Ponts'.
- Writing a scientific paper describing some of the activities implemented with children.

Chapter 2

Contributions to the theoretical developments of Universal Multifractals

Most of my scientific work relies on the framework of Universal Multifractals (UM), which are a process toward which multiplicative processes converge and are defined with the help of only three physically meaningful exponents. An outline of this framework on geosciences in presented in section 2.1. Throughout my work, I contributed to the development of this framework. During my PhD, I initiated some work on the representation of zeros. In more recent years, I focused mainly on three aspects :

- Blunt extension of discrete UM cascades and applications (section 2.2). It is an update of the discrete cascades to address their non-stationarity issue while preserving their overall simple structure.
- Approximate multifractal correlation and products of universal multifractal fields (section 2.3). It consits in developing a framework and notably simple indicators to quantify the correlation accross scales between two UM fields.
- Stochastically guessing missing data of a binary fractal field (section 2.4). It aims at using the fractal properties of a field and its underlying cascade process to infill missing data.

2.1 Universal Multifractals in geosciences

In this section, the theoretical framework of UM is presented. It should be stressed that only the main ideas are reminded and it is not intended to provide all the details. Interested reader is referred to various review [139, 198, 196, 197, 200] or a dedicated introductory course that can be found in the annexes of my PhD manuscript.

2.1.1 Turbulence and the emergence of scaling laws

Historically, the concept of multiplicative cascades was developed to improve understanding of (atmospheric) turbulence. Hence a small subsection is dedicated to these developments. In such state of the fluid, its irregular velocity randomly fluctuates. The basic concept of energy cascade in turbulence was introduced by Lewis Fry Richardson (1922), in a famous poem :

Big whorls have little whorls,
Which feed on their velocity ;
And little whorls have lesser whorls,
And so on to viscosity

In this approach, turbulence consists in a hierarchy of embedded eddies, in which large scale eddies are unstable and break into smaller eddies while transferring to them all their kinetic energy. Such cascade process is in agreement with the scale symmetry of the Navier-Stokes equations which are governing atmospheric behaviour. This process is then repeating again and again until eddies are small enough so that the energy is dissipated through viscosity. At a given scale l, let us denote Δu_l a characteristic velocity (typically equal to velocity fluctuations $u(x+l) - u(l)$. Through dimensional analysis, the life time of the eddy can be defined as $\tau_l \approx l/u_l$. Over this inertial range of scales, the energy injected at larger scale is simply transferred at smaller

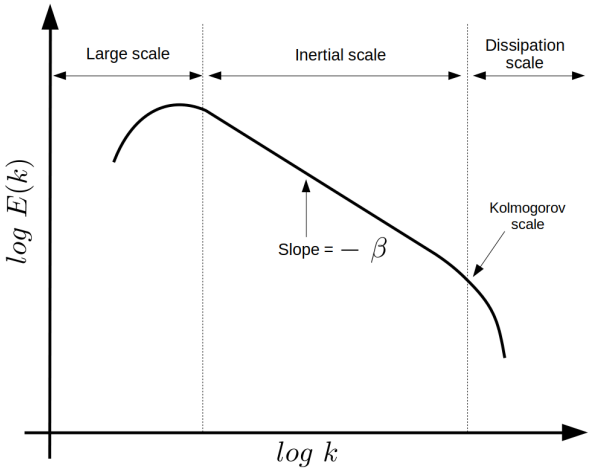

Figure 2.1: Illustration of the energy spectra for wind turbulence (Eq. 2.2)

ones. Hence, the kinetic energy of the eddy, which proportional to Δu_l^2, needs to be transferred during its life time, which means that the dissipation rate, which is also an energy flux across scales, is defined as:

$$\epsilon_l = \frac{(\Delta u_l)^3}{l} \tag{2.1}$$

In Kolmogorov [114], the energy flux ϵ_l is assumed to be homogeneous in space and time. A direct consequence is that the power spectrum of wind turbulence follows a power law over a wide range of wave numbers:

$$E(k) \approx k^{\beta} \tag{2.2}$$

with a spectral slope β equal to 5/3 (as we will see in subsection 2.1.4, it corresponds to $H = 1/3$). This framework is expected to remain valid until the size of eddies reaches the dissipation scale l_ν (also called Kolmogorov scale) for which the Reynolds number becomes equal to 1. $Re = 1 = \frac{\Delta u l}{\nu} = \frac{\epsilon_l^{1/3} l^{4/3}}{\nu}$, which yields $l_\nu = \nu^{3/4}\epsilon^{1/4}$. A schematic summarizing the discussed behaviour is in Fig. 2.1.

In later refinements, which aimed at explaining deviations from expected behaviour, the energy flux was no longer assumed to be homogeneous but to exhibit a variability in space and time generated through a multiplicative cascade process [243]. Various models were suggested, notably a log-normal one [115]; an intermittent one consisting in a so-called β-model [60] (see section ?? example of use in another context); and finally Universal Multifractals [193] which are presented in next seb-section.

Such cascade process concept reproduces the scale symmetries of Navier-Stokes equations. It is assumed that the unknown equations governing other atmospheric fields such as rainfall inherit these properties of scale invariance and can also be modelled with the help of such tools [193, 94]. These features are then also expected to be transferred to hydrological behaviour.

2.1.2 Universal Multifractals basics

For this section let us consider a rainfall field which is assumed to be multifractal here. In order, to grasp an understanding of what is a multifractal field, the first step consists in studying the rainfall support, i.e. the portion of the field where some rain was recorded. This is equivalent to studying a binary field. If the rainfall support is fractal [136, 169], then the number N_λ of rainy time steps in 1D or pixels in 2D at resolution λ ($= L/l$, where l is the observation scale and L the outer scale of the phenomenon), scales as:

$$N_\lambda \approx \lambda^{D_F} \tag{2.3}$$

Where D_F defines the fractal dimension which is a scale invariant notion characterizing how much space a geometrical set occupies (D_F is smaller than the space in which the studied geometrical set is embedded). The fractal co-dimension of a field is defined as:

$$c_F = d - D_F \tag{2.4}$$

where d is the dimension of the embedding space (i.e. 1 in 1D for time series and 2 in 2D for maps). In a mulifractal framework, D_F becomes strongly dependent [142, 95] on the threshold defining the occurrence or

not of rainfall (D_F decreases with increasing thresholds), pointing out that more than one fractal dimension is needed to fully characterize the rainfall field.

If ϵ_λ denotes a multifractal field at resolution λ, then the probability of exceeding a scale dependent threshold (λ^γ) defined with the help a singularity γ, scales with the resolution as

$$Pr(\epsilon_\lambda \geq \lambda^\gamma) \approx \lambda^{-c(\gamma)} \tag{2.5}$$

where $c(\gamma)$ is the codimension function [193] and it can be shown that this is equivalent to the scaling of the statistical moment of order q:

$$\langle \epsilon_\lambda^q \rangle \approx \lambda^{K(q)} \tag{2.6}$$

where $K(q)$ is the moment scaling function. The functions $K(q)$ and $c(\gamma)$ fully characterize the variability through scales of the field ϵ_λ and are linked by a Legendre transform [173]. This notably means that a singularity can be associated uniquely to each moment and vise-versa. As it can be seen on Eq. 2.6, multifractal properties are statistical properties which are valid on average over numerous samples.

In the specific framework of Universal Multifractals, towards which most multiplicative processes converge (this a broad generalization of the central limit theorem, Schertzer and Lovejoy [193, 195]), $K(q)$ is given by:

$$K(q) = \frac{C_1}{\alpha - 1}(q^\alpha - q) \tag{2.7}$$

One can note that for a conservative field, $K(1) = 0$. UM parameters α and C_1 actually characterize the behaviour of the field near the mean moment (i.e. $q = 1$):

- C_1, the mean intermittency co-dimension, which measures the clustering of the (average) intensity at smaller and smaller scales. $C_1 = 0$ for an homogeneous field. $0 \leq C_1 \leq d$, where d is the dimension of the embedding space (a greater C_1 could theoretically exist, but it would correspond to fields almost surely null everywhere). We have $K'(1) = C_1$;
- α, the multifractality index ($0 \leq \alpha \leq 2$), which measures the clustering variability with regards to the intensity level. When $\alpha = 0$, it means that all activity levels exhibit the same intermittency reflecting a fractal field. We have $K''(1) = \alpha C_1$

A Trace Moment analysis basically consists in checking the scaling behaviour of the field and estimating $K(q)$ by plotting Eq. 2.6 in log-log. To achieve this, the field is upscaled from its maximum resolution Λ by averaging over adjacent time steps pixels, then raised to various powers q, and finally the ensemble average (over various samples independently upscaled) is performed to obtain an estimate of the theoretical moments and its scaling behaviour.

UM parameters C_1 and α are usually estimated with the help of the Double Trace Moment (DTM) technique [125]. This technique is based on the fact that if ϵ_λ is a multifractal field, then the field $\epsilon_\lambda^{(\eta)}$ obtained by upscaling the η-th power of the field at maximum resolution, scales like :

$$\langle \left(\epsilon_\lambda^{(\eta)}\right)^q \rangle \approx \lambda^{K(q,\eta)} \tag{2.8}$$

with

$$K(q, \eta) = K(q\eta) - qK(\eta) \tag{2.9}$$

For Universal Multifractals, this yields:

$$K(q, \eta) = \eta^\alpha K(q) \tag{2.10}$$

Therefore the multifractality index α corresponds to the slope of the so-called DTM curve, which is the log-log plot of $K(q, \eta)$ vs. η for fixed q.

2.1.3 Multifractal phase transitions

Singular limit of cascade process and divergence of the fluxes

If ϵ_λ is a multifractal field, then it exhibits a behaviour similar to $\epsilon_\lambda \approx \lambda^\gamma$, where $\approx$ denotes asymptotic convergence and absorbs factors slowly variable with λ and normalization constants. As a consequence for any $\gamma > 0$, $\epsilon_\lambda \to +\infty$, as $\lambda \to +\infty$. It should be mentioned that for $\gamma < 0$ the corresponding point is more a regularity than a singularity, but in practice exponents $\gamma < 0$ are also called singularities.

This singular behaviour means that if a limit exists, it is not in the sense of functions since the singularities will prevent usual convergence of the density. ϵ_λ is actually a mathematical measure, which means that there

is convergence of the fluxes. However moment orders q of the flux will converge only if q is smaller than a critical moment q_d because with higher moments a stronger relative weight is affected to higher singularities which exhibit a singular limit. q_d is defined by :

$$\frac{K(q_d)}{q_d - 1} = D \tag{2.11}$$

where d is the dimension of the embedding space. Such finding has a direct consequence on analysis of geophysical measurements. Indeed, measured field actually corresponds to an integral over a given space - time support. They are often called 'dressed' fields in the literature by opposition to 'bare' ones which correspond to the generation of the direct process. It means that these quantities inherit the singular behaviour of the 'hidden' part of the process. As a consequence, when $q \geq q_d$ dressed quantities exhibit the following three equivalent properties:

- $\langle \epsilon_\lambda^q \rangle = +\infty$; $K(q) = +\infty$
- The probability distribution exhibit a power-law fall off of exponent q_d : $x \gg 1$ $Pr(\epsilon_\lambda \geq x) \approx x^{-q_d}$
- $c(\gamma)$ is linear for singularities greater than the corresponding γ_d : $c(\gamma) = q_d(\gamma - \gamma_d) + c(\gamma_d)$

This transition for dressed quantities $q \geq q_d$ enables retrieving the properties of self-organized criticality [8]. Multifractals exhibiting a divergence of high order statistical moments are called 'hard', by contrast with 'soft' ones for which the d - dimensional integration smooths out rare high order singularities [194]. Such power-law decay of probability of appearance is an ubiquitous feature of geophysical fields well explained by the multifractal framework.

Maximum observable singularity

It is well known that the size of the sample limits the insight one can get of a statistical process by analyzing data. For multifractal processes this will result in a maximum singularity γ_s and corresponding moment order q_s beyond which the values of the statistical estimates of respectively the codimension and scaling moment function are not considered as reliable [138, 140].

More precisely, let's consider N_s independent samples with a resolution λ. In a d-dimensional space, there are λ^d values per sample. The maximum singularity (γ_s) that one can expect to observe is defined by:

$$N_s \lambda^d Pr(\epsilon_\lambda \geq \lambda^{\gamma_s}) \approx 1 \tag{2.12}$$

By introducing the notion of sampling dimension d_s: $N_s = \lambda^{d_s}$ ($d_S = 0$ for a single sample), one obtains a relationship that enables to estimate γ_s :

$$c(\gamma_s) = d + d_s \tag{2.13}$$

For $\gamma > \gamma_s$ one expects that $c(\gamma) = +\infty$, which means that the estimates of $c(\gamma)$ will not be reliable. As a consequence of the Legendre transform, the estimates of $K(q)$ will become linear for $q > q_s = c'(\gamma_s)$: $K(q) = \gamma_S(q - q_s) + K(q_s)$

2.1.4 Non-conservative fields

In this subsection, we mention the standard framework to deal with a non-conservative field, denoted ϕ_λi.e. we have $\langle \phi_\lambda \rangle \neq 1$). In that case, it is usually assumed that it can be written as (with an equality in probability distribution):

$$\phi_\lambda \stackrel{d}{=} \epsilon_\lambda \lambda^{-H} \tag{2.14}$$

where ϵ_λ is a conservative field ($\langle \epsilon_\lambda \rangle = 1$) of moment scaling function $K_c(q)$ (the sub-index "c" refers to the conservativity of ϵ_λ), and H the non-conservation parameter. $K_c(q)$ only depends on UM parameters C_1 and α. H characterizes the scale dependence of the average field, i.e.

$$\langle \phi_\lambda \rangle \approx \lambda^{-H} \tag{2.15}$$

H is equal to zero for a conservative field. The moment scaling function $K(q)$ of ϕ_λ is given by:

$$K(q) = K_c(q) - Hq \tag{2.16}$$

The DTM technique should theoretically be implemented on ϵ_λ, however if $H < 0.5$, it can be implemented directly on ϕ_λ, and will not generate biased estimates. In case of greater H, ϵ_λ should be used. Retrieving ϵ_λ from ϕ_λ theoretically requires a fractional integration of order H (equivalent to a multiplication by kH in the

Fourier space). A common approximation, which provides reliable results [125], consists in taking ϵ_Λ as the absolute value of the fluctuations of ϕ_Λ at the maximum resolution and renormalizing it, i.e. (in 1D) :

$$\epsilon_\lambda = \frac{|\phi_\Lambda(i+1) - \phi_\Lambda(i)|}{\langle |\phi_\Lambda(i+1) - \phi_\Lambda(i)| \rangle} \tag{2.17}$$

Then ϵ_λ is obtained by upscaling ϵ_Λ. H can be estimated with the help of the following formula [218]:

$$\beta = 1 + 2H - K_c(2) \tag{2.18}$$

Where β is the spectral slope that characterizes the power spectrum of a scaling field (Eq. 2.2).

2.1.5 Simulations with the help of discrete cascades

Discrete multiplicative cascades

In this subsection, simulations of UM fields with the help of discrete cascades is presented. In such processes, an average intensity over a large scale structure is iteratively distributed in space and time to smaller scale structures. More precisely a structure is divided into λ_1^d sub-structures where d is the dimension of the embedding space ($d = 1$ in 1D and $d = 2$ in 2D). Usually $\lambda_1 = 2$, i.e. time steps are simply divided in 2, and pixels in 4. The intensity affected to a sub-structure is the intensity of the parent structure multiplied by a random increment. Then the process is iteratively repeated on each of the sub-structure. The process is scale invariant in the sense that the way structures are divided into sub-structures and the probability distribution of the random multiplicative increments are the same at each cascade step.

Such simple and intuitive process enables to parsimoniously reproduce complex patterns exhibiting extreme variability and intermittence over wide range of spatio-temporal scales. This is the reason for their 'success'. However as pointed out by [141] they are essentially a pedagogical model because of their intrinsic limitations, primarily their lack of stationarity. Indeed in such models, the correlation between two points (time step or pixels) strongly depends of their location within the generated field. A suggestion to improve this issue is actually the topic of the next section. A visual consequence of this drawback is the existence of sharp transitions between areas of the generated fields; notably unrealistic square structures in 2D. Although sometimes mentioned, this limitation is basically ignored by the authors previously cited.

More precisely, the process is illustrated with three steps in 1D in Fig. 2.2. We start by a large scale structure with a given intensity B_0. After n steps, the resolution is $\lambda_1^n = \lambda_n$, and the value $B_{n,i}$ of the field is the product of the increments associated to all its successive parent structures:

$$B_{n,i} = B_0 \prod_{i=s}^{n} (b_s) \tag{2.19}$$

β-model simulations

Let us first discuss the simplest possible model, often called β-model. It was initially introduce to model the intermittency of turbulence [60]. In this model, the multiplicative random increment has only two states. It is either dead (equal to 0) or alive (> 0) with the following probabilities :

$$Pr(b = 0) = 1 - \lambda_1^{-c} \tag{2.20}$$

$$Pr(b = \lambda_1^c) = \lambda_1^{-c} \tag{2.21}$$

As a consequence of Eq. 2.19, B_n has only two possible values, either 0 or λ_n^c. c is the characteristic parameter of the model and is equal to the fractal co-dimension of the geometrical field made of the 'alive' portion of the generated field. Fig. 2.3 shows some simulations in 1D and 2D with various c to give the reader an intuitive feeling of the physical meaning of c. One can note the visible square structures, notably in 2D, which were already mmentioned in the previous subsection. This feature is indeed not realistic and a limitation of this model. It is due to the discrete nature of its underlying construction scheme (see Schmitt, 2014, for a continuous version of the β-model). Conservation of the average activity is ensured since $< b >= 1$. It should be noted that this conservation is true only on average, i.e. on numerous realisations, and not for individual ones.

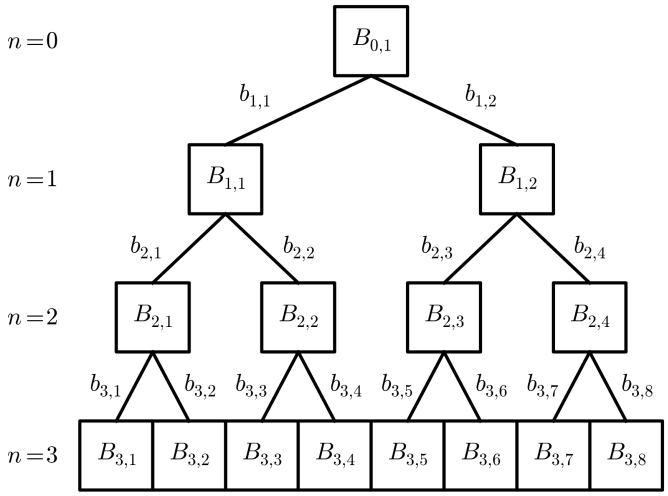

Figure 2.2: Illustration of a standard discrete multiplicative cascade process with 3 steps. $B_{n,i}$ are the values of the field after n steps and $b_{n,i}$ are the increments. (Figure from Gires et al., 2020)

Universal Multifractals simulations

For Universal Multifractals the increment b is given by :

$$b = \frac{exp[(\frac{C_1 ln\lambda_1}{|\alpha-1|})^{1/\alpha} L(\alpha)]}{\lambda_1^{\frac{C_1}{\alpha-1}}} \tag{2.22}$$

where $L(\alpha)$ is an extremal Lévy-stable random variable of index α. It is generated with the help of the procedure given by Chambers et al. [28], and has the following property:

$$\langle exp[qL(\alpha)]\rangle = exp[q^\alpha] \tag{2.23}$$

Combining Eqs. 2.22 and 2.23, we find :

$$\langle b^q\rangle = \frac{\langle exp[q(\frac{C_1 ln\lambda_1}{|\alpha-1|})^{1/\alpha} L(\alpha)]\rangle}{\lambda_1^{q\frac{C_1}{\alpha-1}}} = \lambda_1^{\frac{C_1}{\alpha-1}(q^\alpha-q)} \tag{2.24}$$

Finally, given that the increments b_s in Eq. 2.19 are independent and identically distributed, and keeping in mind $\lambda_1^n = \lambda_n$, we can demonstrate that the field simulated is indeed a UM one :

$$\langle B_{n,i}^q\rangle = B_0^q \langle b^q\rangle^n = \lambda_n^{\frac{C_1}{\alpha-1}(q^\alpha-q)} \tag{2.25}$$

2.2 Blunt extension of discrete UM cascades and applications

This section is mainly based on Gires et al. (2020), in which additional details can be found.

2.2.1 Non-stationary issue of discrete cascades

As pointed out in section 2.1.5, discrete cascade are non-stationnary which is a strong limitation. In order to illustrate this more quantitatively, 10 000 samples of a 8 step discrete cascade with $\alpha = 1.6$ and $C_1 = 0.2$ were generated (hence time series of length 256 are obtained) and the quantities $\langle B_{8,j}^q B_{8,j+t}^q\rangle$ are studied for various j and t. Fig. 2.4 displays, for $q = 0.5$, $\langle B_{8,j}^q B_{8,j+t}^q\rangle$ as a function of t for $j = 1$, $j = 64$ (just before 1/4 of the series, $j = 65$ (just after 1/4 of the series), $j = 128$ (just before the middle of the series), and $j = 129$ (just after the middle of the series). The strongly asymmetric behaviour with a transition for $t = 0$ is visible for $j = 128$ and $j = 129$ with standard discrete cascade simulations (Fig. 2.4.a). It is also the case to a smaller extent for $j = 64$ and $j = 65$, which was expected since these two time steps share one more increment together ($b_{1,1}$).

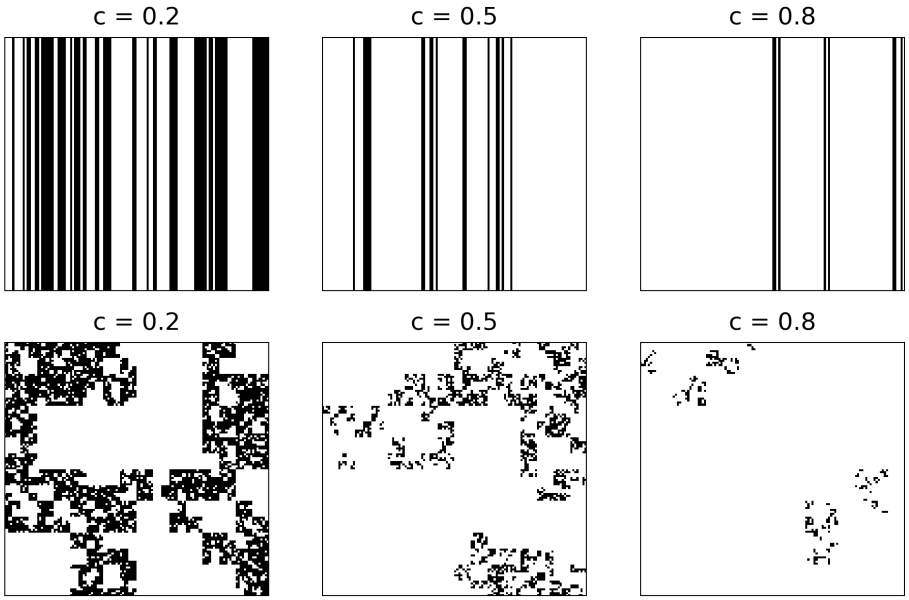

Figure 2.3: Examples in 1D (up) or 2D (bottom) of fields generated through the implementation of a β-model with various c. Figure from Gires et al. (2021).

Despite this strong limitation, discrete random multiplicative cascades have been extensively used to model rainfall [87, 171, 168, 70, 155, 62, 133, 133, 163, 187] because such a seemingly simple and intuitive process enables to parsimoniously (and partly) reproduce complex patterns exhibiting extreme variability and intermittence over wide range of spatio-temporal scales. A novel approach is introduced here to tackle the non stationarity issue while preserving the simple structure of discrete cascades.

2.2.2 Development and analysis of an extension of discrete cascades

The aim of this subsection is to introduce the blunt extension of discrete UM multiplicative cascades, and characterize its mathematical behaviour. It is denoted A in the following. As a consequence it will be introduced starting from the standard well known process, denoted B. The underlying concept is actually rather straightforward and easy. It can be summarized in three successive steps :

- Introducing, the final resolution of the field at all levels of the cascade process. In practice, this is done by simply concatenating successive 'blocks' made of repetitions of the same increments.
- Performing a geometrical average with a moving window to replace the increments at each cascade steps with interpolated ones. The length (or size) of the moving window changes according to cascade level and is characterized with the help of a scale invariant parameter h, which corresponds to the number of adjacent 'true increments' (i.e. in the process B) that will influence the new ones. Hence greater values of h will increase the correlations within the cascade process. As a consequence, this will increase the value of the H parameter for the simulated field. This strong relation is the reason why a lowercase letter h was used. It should be stressed that this geometrical interpolation on the increment is equivalent to the linear interpolation on the corresponding singularities. The weight affected to each time step or pixel of the window are uniformly distributed.
- Adding an additional renormalization to preserve the ensemble average mean

A spectral analysis of the studied field lead to the conclusion that the best option to preserve the scaling behaviour down to small scales consisted in simulating the field with two more cascade steps than needed and then averaging over sequences of the last two cascade steps to recover the wanted resolution. The process is summarized in Fig. 2.5. It is illustrated in 1D and 2D in Fig. 2.6. The final length of the time series in 1D is 256 time steps and the final size of the map in 2D is 64 x 64. Note that in 1D the full increment fields are shown and not only the middle portion as in 2D which is actually the one used in the field generation because of the side effects. The progressive, cascade step by cascade step, addition of variability to the field is visible and highlights the whole interest of cascade processes. The effect of the blunting is also visible, notably in 2D. Indeed, the sharp unrealistic structures of the standard field are replaced by blunted ones. With greater values of h, the smoothing of the increments fields would even be more pronounced.

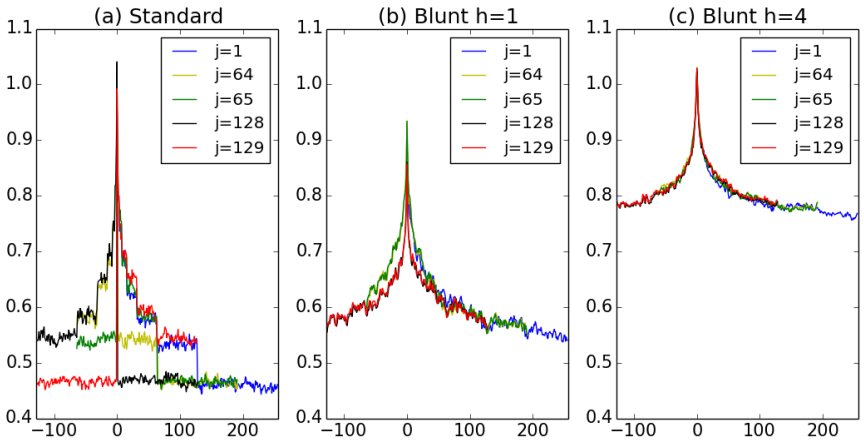

Figure 2.4: $\langle B^q_{8,j} B^q_{8,j+t} \rangle$ as a function of t for $q = 0.5$ and various j on 256 time step series simulated with $\alpha = 1.6$ and $C_1 = 0.2$. (a) Standard cascade, (b) Blunt cascade with $h = 1$, (c) Blunt cascade with $h = 4$. Figure from Gires et al. (2020).

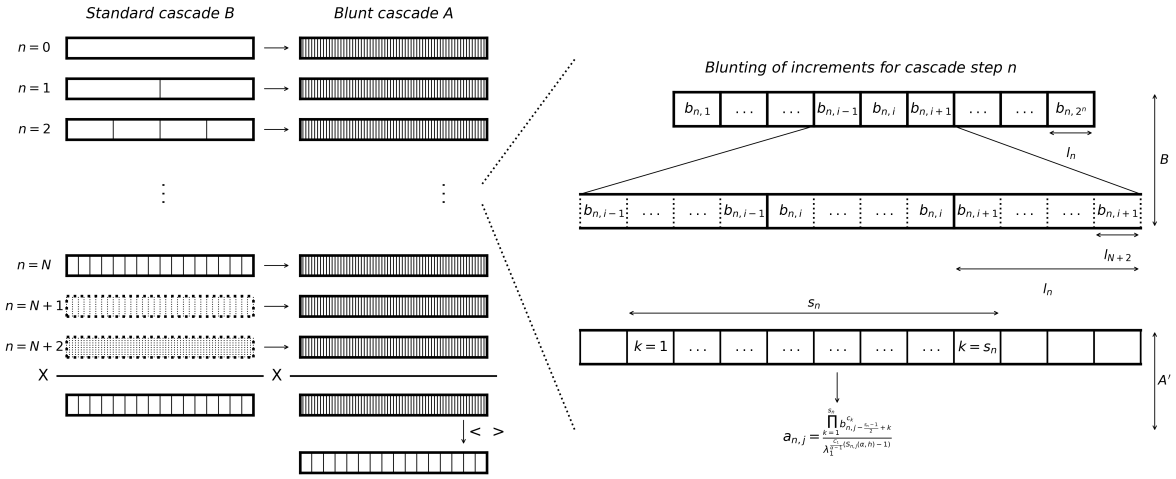

Figure 2.5: Schematic description of the generation of a blunt multiplicative cascade process A from a standard one B. Figure adapted from Gires et al. (2020).

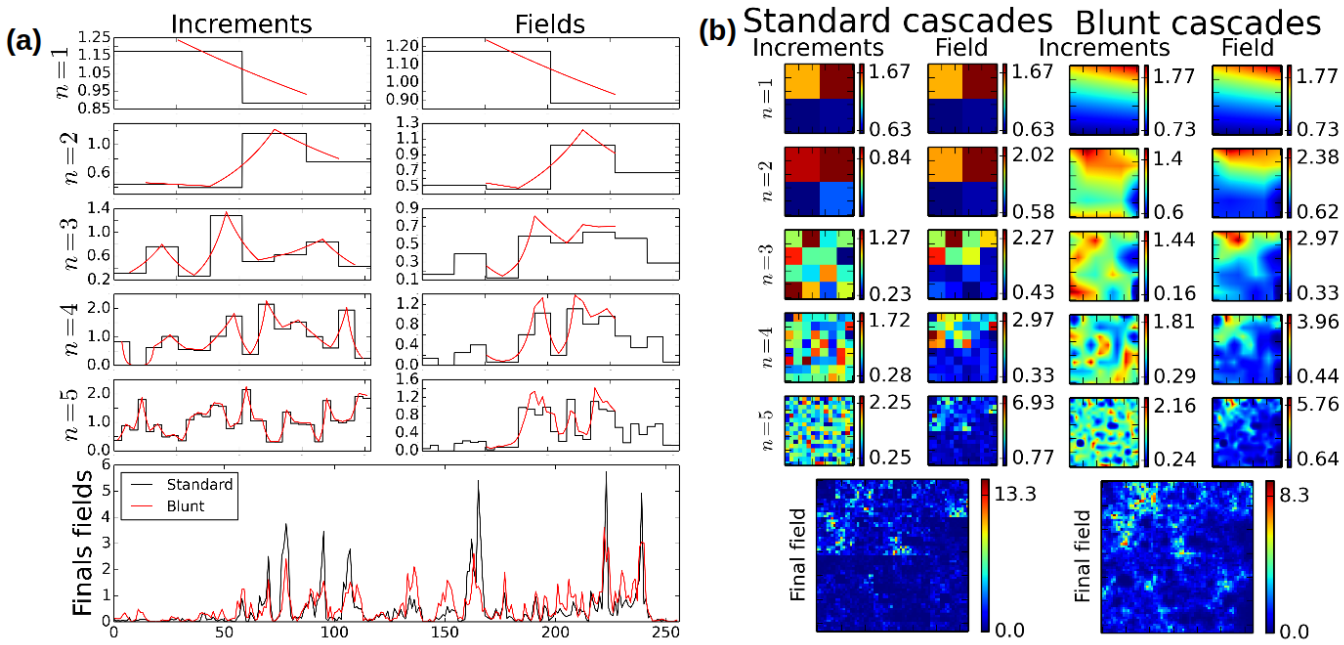

Figure 2.6: (a) Illustration in 1D of the simulation of a field with the help of a standard cascade process B and the corresponding blunt one A. The first 5 cascades steps are shown as well as the final fields of length 256 time steps. $\alpha = 1.6$, $C_1 = 0.2$ and $h = 1$ are used. (b) Illustration in 2D of the simulation of a field with the help of a standard cascade process B and the corresponding blunt one A. The first 5 cascades steps are shown as well as the final fields of size 64 x 64 pixels. $\alpha = 1.6$, $C_1 = 0.2$ and $h = 1$ are used. Figure from Gires et al. (2020).

The detailed calculations are not repeated here, but it can be shown that the generated blunt process is expected to exhibit a multifractal behaviour, with a scaling moment function $K_{blunt}(q)$ of the process A as :

$$K_{blunt}(q) = \frac{C_1}{\alpha - 1} S^1(\alpha, h)(q^\alpha - q) = S^d(\alpha, h) K(q) \tag{2.26}$$

which yields simple relations between the UM parameters of the blunt process and the ones from the standard process :

$$\begin{array}{rcl} \alpha_{blunt} & = & \alpha \\ C_{1,blunt} & = & S^d(\alpha, h) C_1 \end{array} \tag{2.27}$$

where $S^d(\alpha, h)$ can be directly derived from the features of the geometrical interpolation (weight affected to time step or pixel and size of the moving window). It depends on α, the embedding dimension d of the field, and h. It is displayed in Fig. 2.7 for some specific values. This established expected is behaviour is numerically confirmed over a limited range of UM parameters due to strong deviations noted for small α (< 1) and large C_1 ($> 0.3 - 0.4$). This limits the potential applications.

2.2.3 Applications to downscaling

In this subsection, we present how blunt discrete cascades can easily be used to address downscaling which is a very common issue encountered with geophysical fields.

The methodology for downscaling is rather straightforward in the convenient framework of discrete cascades which is intrinsically a downscaling model, and simply consists in generating the additional steps to increase the resolution. Basically, all the missing underlying increments of the standard process (the $b_{n,i}$ with the notations used here) are stochastically generated. From them, the $a_{n,j}$ and ultimately the field are derived. It is summarized in Fig. 2.8 and consists more precisely in four steps:

1. *Estimation of the UM parameters.* It is done by performing a multifractal analysis on the available data. Such estimation is done at coarse resolution, and it is assumed that they remain valid for higher resolutions (or smaller scales), i.e. that there is no scaling break. It should be noted that, following Eq. 2.27, the parameters actually input in the simulation will be α and $C_1/S^d(\alpha, h)$ to retrieve the correct α and C_1 once the blunting has been implemented.

2. *Estimating the starting point of the cascade process.* The only tricky point in the process is to compute the product of the blunt increments $a_{n,j}$ for the 'known' portion of the cascade. This corresponds to the

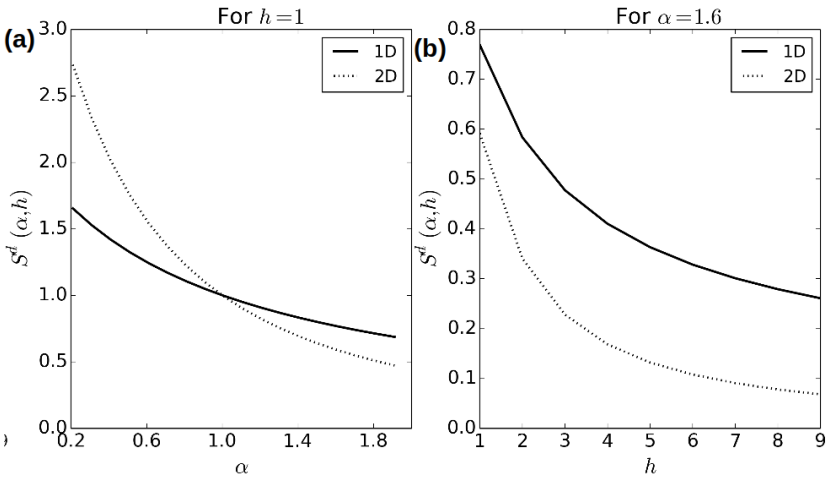

Figure 2.7: (a) $S_n^d(\alpha, h)$ vs. l_n for $\alpha = 1.6$ and $h = 1$ in 1D and 2D. (b) $S^d(\alpha, h)$ vs. α for $h = 1$ in 1D and 2D. (c) $S^d(\alpha, h)$ vs. α for $\alpha = 1.6$ in 1D and 2D. Figure adapted from Gires et al. (2020).

outcome of the cascade process at the initial resolution (the black rectangle in Fig. 2.8). It corresponds to 'inserting' the available data in the cascade process. This is done by performing a linear interpolation of the initial low resolution field at the maximum resolution used in the cascade process. In practice, it is a 'blunting' of the data with $h = 1$. By the way this can be considered as a simplistic way of downscaling a field.

3. *Stochastically simulating the missing increments.* The missing increments at the higher resolutions (in red on Fig. 2.8) are stochastically drawn. It should be reminded that two steps more than needed with regards to the wanted final resolution are implemented.

4. *Generating the fields at the wanted resolution.* The increments at the higher resolutions are then blunt and multiplied to the initial data at low resolution (point (2)). It is the same process as in the simulation of a field except that instead of using the blunt increments for the coarse resolution, the initial data is used.

The fact that the missing unknown increments are stochastically generated in the downscaling process means that not only a single deterministic result will be obtained but an ensemble of realistic realisations. More precisely the outcome of the process is not a deterministic value but an empirical probability distribution. In order to quantify the variability within the simulated ensemble of high resolution fields, quantiles (10, 50 and 90%) can be computed.

In order to validate the downscaling approach, we used disdrometer data (see section 4.2) and X-band radar data from devices operated by HM&Co. The overall concept consisted in averaging the available data at coarser resolution, downscale it and check that downscaled fields exhibit expected UM behaviour and that actual high resolution measurement falls within the expected range of values retrieved form the downscaling process.

It is illustrated in Fig. 2.8 for a radar map. Fig. 2.8.d displays a realisation of downscaled field obtained with the help of a standard B process. The unrealistic sharp squares are visible and too great values are also obtained with regards to the original radar data. Fig. 2.8.e and f display two different realisations for the blunt process A with $h = 6$. As expected the square structures have been removed, and the visual aspect of this simulated downscaled fields are much more satisfactory. In addition, the small scale values within heavy areas which are visible in the standard case are mostly removed in the blunt case. Quantitatively, the expected multifractal behaviour is retrieved. One can note that for the realisation in panel (e) the rainy area in the North-West is well represented while it is not in the realisation of panel (f). Both realisations simulate a 'potential' version of heavy rainfall area in the middle.

Fig. 2.8.g, h and i display respectively the 10, 50 and 90% quantile obtained for each pixel with the help of 100 realisations of downscaled blunt rainfall fields. As expected, the 50% quantile map yields a map very similar to the initial data put at the maximum resolution (Fig. 2.8.c), while the other two maps provide a quantification of the uncertainty associated with the downscaling process. It should be mentioned that in this case, the heavy spot in the South is underestimated with the blunt process. The small square structures visible on the sides (notably on Fig. 2.8.i) are simply due to the fact that the increments that would be needed to implement the blunting of the side increments are not simulated. This could be solved practically very easily by simulating a larger area and only taking the middle portion. This was not done here for computational time reasons.

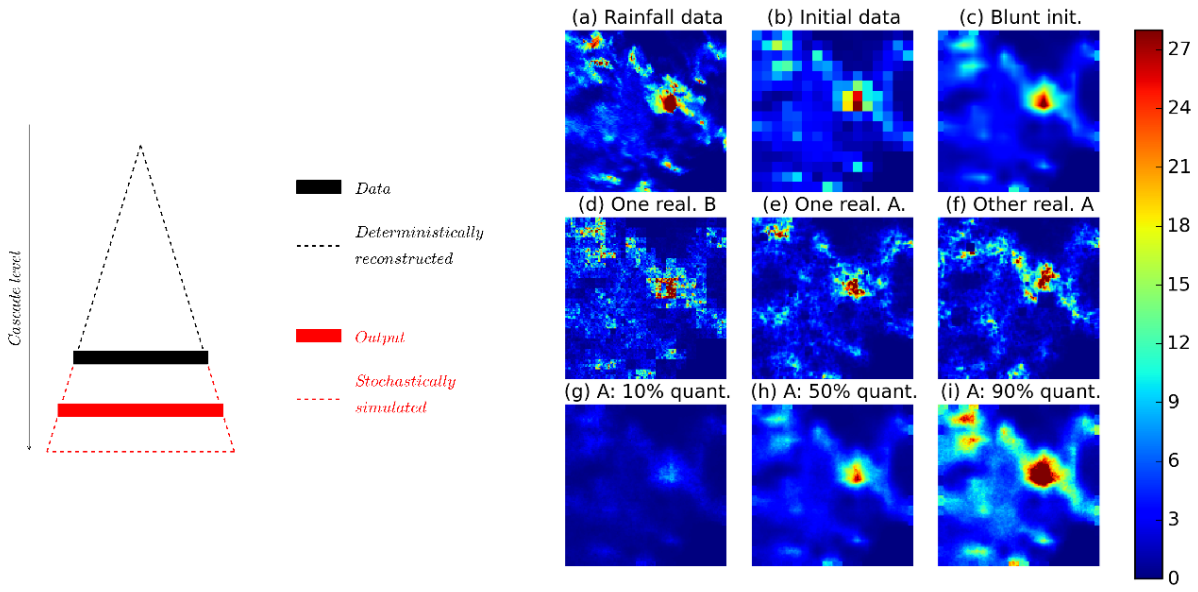

Figure 2.8: Illustration of the downscaling process for the time step 2015-09-16 08:32 (UTC). Unit is mm.h^{-1}. Figure from Gires et al. (2020).

2.3 Approximate multifractal correlation and products of universal multifractal fields

This section is mainly based on Gires et al. (2020), in which additional details can be found.

2.3.1 Overall purpose

As we have seen before, multifractals have been widely used to investigate geophysical fields. Much less work has been devoted to the analysis of the correlations and couplings between two fields exhibiting multifractal properties. A framework was originally presented by Meneveau et al. [156], who suggested studying the properties of joint moments of two multifractal fields (i.e. the product of the two fields raised to two different powers) across scales. The behaviour of the scaling exponent as a function of the two moments provides information on the correlations between the two fields. They tested their framework on velocity and temperature as well as velocity and vorticity. Such a framework has been implemented in many other contexts [12, 207, 239, 107, 242]. Refinement including a renormalization have been suggested [204, 205, 21] and have been implemented for log-normal cascades, for which computations basically boil down to a single parameter and correlation functions are represented by linear ones. Furthermore only two specific cases have been primarily studied, either a proportional or a power law relation between the two studied fields. In this work, we suggest relying on this theoretical framework and extending its use to UMs and to relations between fields consisting of multiplicative power law combinations.

2.3.2 A theoretical framework

Let us consider two fields, ϕ_λ and ϵ_λ, that exhibit multifractal properties. In order to study the correlation across scales Seuront and Schmitt [204] refined the initial framework of Meneveau et al. [156] and suggested performing a joint multifractal analysis as follows:

$$\frac{\langle \epsilon_\lambda^q \phi_\lambda^h \rangle}{\langle \epsilon_\lambda^q \rangle \langle \phi_\lambda^h \rangle} \approx \lambda^{S(q,h)-K_\epsilon(q)-K_\phi(h)} \approx \lambda^{r(q,h)}, \tag{2.28}$$

where $r(q,h)$ is a "generalized correlation exponent". If ϕ_λ and ϵ_λ are lognormal multifractal processes (i.e. $\alpha = 2$), then $r(q,h)$ is linear with regard to both h and q. $r(q,h) = 0$ for independent fields. If they are power law combinations related with $\phi_\lambda = c\epsilon_\lambda^d$, then $r(q,h)$ is symmetric in the dp–q plane.

Now, let us focus on the specific case of Multiplicative combinations of two fields. Hence let us consider two independent UM fields X_λ and Y_λ, with their respective characteristic parameters α_X, $C_{1,X}$, α_Y and $C_{1,Y}$. The goal of this section is to understand the behaviour of a field ϵ_λ consisting of renormalized multiplicative power

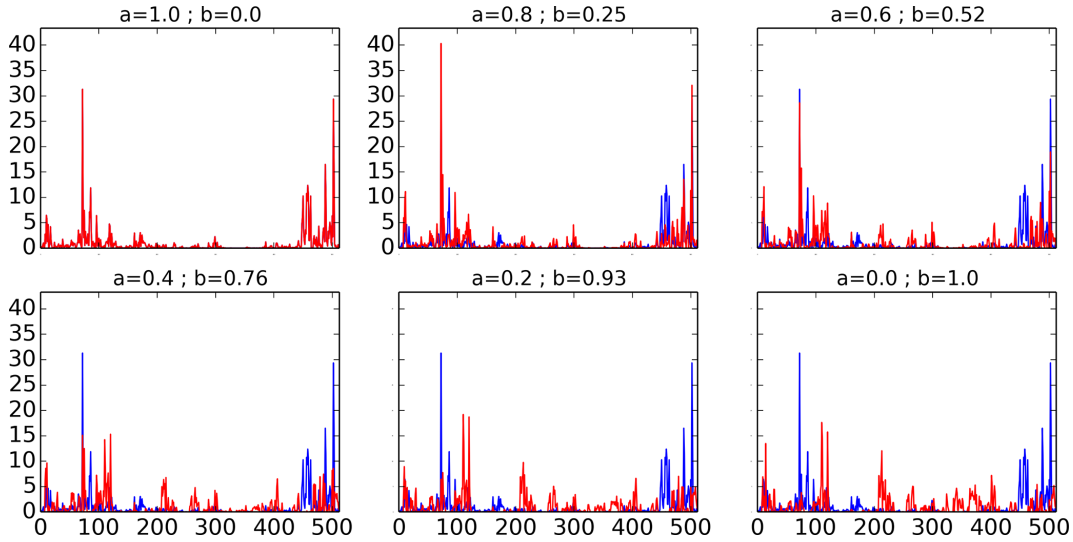

Figure 2.9: ϵ_λ (in red) and X_λ (in blue) for a realisation of X_λ and Y_λ with $\alpha_X = 1.8$, $C_{1,X} = 0.3$, $\alpha_Y = 0.8$ and $C_{1,Y} = 0.3$. Definition of Eq. (2.29) is used. Various values of a are shown; b is tuned to ensure the same C_1 is retrieved on all the fields. Figure from Gires et al. (2020).

law combinations of X_λ and Y_λ. ϵ_λ is then defined by

$$\epsilon_\lambda = \frac{X_\lambda^a \, Y_\lambda^b}{\langle X_\lambda^a \, Y_\lambda^b \rangle}, \tag{2.29}$$

where a and b are exponents characterizing the relative weight of X_λ and Y_λ in the combination.

Let us first discuss intuitively the influence of the parameters a and b. Figure 2.9 displays the fields ϵ_λ (in red) and X_λ (in blue) for a realisation of X_λ and Y_λ with $\alpha_X = 1.8$, $C_{1,X} = 0.3$, $\alpha_Y = 0.8$ and $C_{1,Y} = 0.3$ (Eq. 2.29 is used). Values of a ranging from 1 to 0 are shown. b was tuned to ensure the same C_1 is retrieved on all the fields. For $a = 1$ and $b = 0$ (upper left), the two fields are obviously equal and hence superposed. The opposite case is $a = 0$ and $b = 1$ (lower right), for which ϵ_λ is simply equal to Y_λ, and hence fully independent of X_λ. In the intermediate cases, the progressive decorrelation between the two fields is visible with decreasing values of a. In that sense the parameters a and b characterize the level of correlation between the two fields.

In order to evaluate the expected multifractal behaviour of ϵ_λ, its statistical moments of order q are computed to evaluate $K_\epsilon(q)$. Given that X_λ and Y_λ are independent, it yields

$$\begin{aligned} \langle \epsilon_\lambda^q \rangle = \lambda^{K_\epsilon(q)} &= \frac{\langle X_\lambda^{qa} \rangle \left\langle Y_\lambda^{qb} \right\rangle}{\langle X_\lambda^a \rangle^q \langle Y_\lambda^b \rangle^q} \\ &= \lambda^{K_X(qa) - qK_X(a) + K_Y(qb) - qK_Y(b)}, \end{aligned} \tag{2.30}$$

which means we have

$$\begin{aligned} K_\epsilon(q) &= a^{\alpha_X} K_X(q) + b^{\alpha_Y} K_Y(q) \\ &= a^{\alpha_X} \frac{C_{1,X}}{\alpha_X - 1}(q^{\alpha_X} - q) + b^{\alpha_Y} \frac{C_{1,Y}}{\alpha_Y - 1}(q^{\alpha_Y} - q) \\ &\approx \frac{C_{1,\epsilon}}{\alpha_\epsilon - 1}(q^{\alpha_\epsilon} - q). \end{aligned} \tag{2.31}$$

The exact computation of $K_\epsilon(q)$ is written in the second line of Eq. (2.31). The third line is not exact and corresponds the form $K_\epsilon(q)$ would have if ϵ_λ was actually a UM. This is not true in the general case. In order to assess pseudo-UM parameters $C_{1,\epsilon}$ and α_ϵ, we suggest to use the properties of Eq. 2.7 and equalize the first and second derivatives of the two last lines of Eq. 2.31 for $q = 1$. This yields

$$\begin{aligned} C_{1,\epsilon} &= C_{1,X} a^{\alpha_X} + C_{1,Y} b^{\alpha_Y}, \\ \alpha_\epsilon &= \frac{C_{1,X} a^{\alpha_X} \alpha_X + C_{1,Y} b^{\alpha_Y} \alpha_Y}{C_{1,X} a^{\alpha_X} + C_{1,Y} b^{\alpha_Y}}. \end{aligned} \tag{2.32}$$

It should be noted that in the specific case of $\alpha_X = \alpha_Y$, α_ϵ is also equal to this value and ϵ_λ is actually an exact UM field.

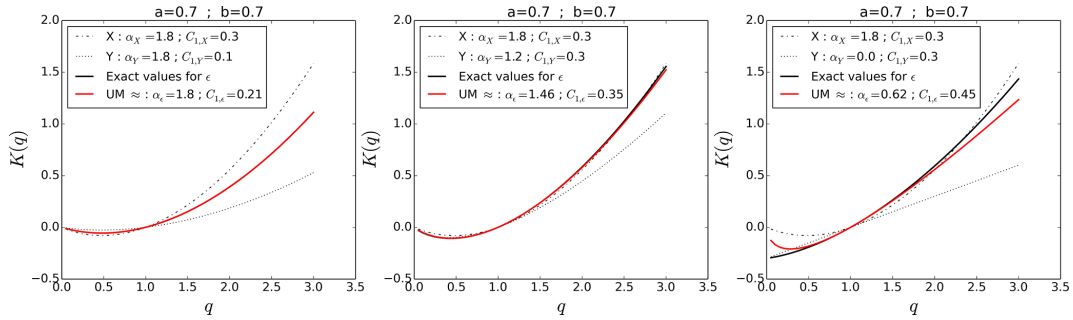

Figure 2.10: Illustration of the scaling moment functions $K(q)$ of X_λ, Y_λ and ϵ_λ, along with the UM approximation for ϵ_λ (fitted around $q = 1$). Three possible sets of parameters are displayed. Figure from Gires et al. (2020).

Figure 2.10 displays the scaling moment functions of the previously discussed fields for various sets of parameters. Similar results are found for other sets of UM parameters and combinations of a and b exponents. In Fig. 2.10a, the same α is used for both X_λ and Y_λ, and the expected exact UM behaviour is correctly retrieved. When $\alpha_X \neq \alpha_Y$, ϵ_λ is not exactly a UM. As it is illustrated in Fig. 2.10b and c, the smaller the differences, the better the UM approximation for ϵ_λ. In the extreme case when $\alpha_Y = 0$ (Fig. 2.10c), the approximation remains valid only for q ranging from ~ 0.6 to 1.6. This range is much wider when the α values are closer. It should be noted that for great moments, some discrepancies are visible, with the exact value of $K_\epsilon(q)$ always being greater than its UM approximation. This could wrongly be interpreted suggesting that a multifractal phase transition associated with the divergence of moments is occurring, whereas it is merely an illustration of the limits of validity of the approximation of ϵ_λ as a UM field. Indeed, the values of q_d are much greater than the moment for which the discrepancies start to be visible. In the cases of Fig. 2.10, we have $q_d = 5.96$ for panel (a), $q_d = 4.58$ for panel (b) and $q_d = 119$ for panel (c), for which the approximation as a UM field is less valid. These values are obtained by looking for the solution > 1 to the Eq. 2.11 using the pseudo-UM parameters of ϵ_λ (d is the dimension of the embedding space). When confronted with such behaviour, keeping in mind this sort of interpretation could be interesting.

An algorithm was developed and numerically validated on synthetic simulations to retrieve the UM parameters of the underlying fields as well as the exponent a and b.

2.3.3 Toward an indicator of correlation

Let us consider two fields ϵ_λ and ϕ_λ. It is assumed that they both exhibit UM properties, with known UM parameters. The purpose of this section is to present a framework to study the correlations across scales between the two fields. This relies on the joint multifractal analysis presented before, with the suggestion of a simplified indicator. It furthermore opens the path to numerical simulations of one field from the other.

More precisely, the consequences of describing each field as a multiplicative power law combination of the other and an independent one will be explored. The notations are

$$\begin{aligned} \epsilon_\lambda &= \frac{\phi_\lambda^a \, Y_\lambda^b}{\langle \phi_\lambda^a \, Y_\lambda^b \rangle}, \\ \phi_\lambda &= \frac{\epsilon_\lambda^{a'} \, Z_\lambda^{b'}}{\langle \epsilon_\lambda^{a'} \, Z_\lambda^{b'} \rangle}, \end{aligned} \tag{2.33}$$

where a, b, a' and b' characterize the level of correlation between the two fields, while Y_λ and Z_λ are independent random UM fields. a, b, a' and b' can be assessed with the help of joint analysis as detailed Gires et al. [78]. Without any loss of generality it can be assumed that $C_{1,Y} = C_{1,\phi}$ and $C_{1,Z} = C_{1,\epsilon}$, which simplifies calculations.

In the general case, this framework is not fully symmetric, which is a strong limitation. Indeed some asymmetry becomes visible when the two αs are different. Smaller deviations are found when estimates are closer to the maximum value of 2.

However, it is possible to suggest a rather intuitive indicator enabling most of the information obtained from the joint multifractal correlation analysis (i.e. the computation of $r(q, h)$) to be extracted. This corresponds to the portion of intermittency C_1 of one field explained by the other:

$$\begin{aligned} \mathrm{IC}_{\epsilon\phi} &= \frac{C_{1,\phi} a^{\alpha_\phi}}{C_{1,\epsilon}}, \\ \mathrm{IC}_{\phi\epsilon} &= \frac{C_{1,\epsilon} a'^{\alpha_\epsilon}}{C_{1,\phi}}. \end{aligned} \tag{2.34}$$

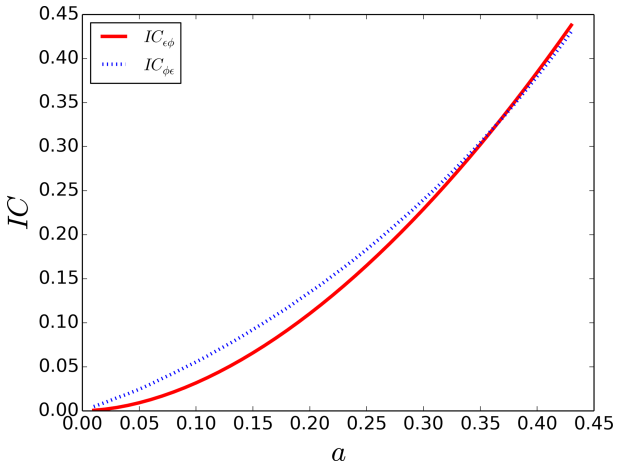

Figure 2.11: Plot of $\mathrm{IC}_{\epsilon\phi}$ and $\mathrm{IC}_{\phi\epsilon}$ as a function of a for numerical simulations of two UM fields in the case $\alpha_\epsilon = 0.8$, $C_{1,\epsilon} = 0.4$, $\alpha_\phi = 0.8$ and $C_{1,\phi} = 0.2$. Figure from Gires et al. (2020).

Both 'indicators of correlation' (ICs) are displayed in Fig. 2.11 for the two UM fields in the case $\alpha_\epsilon = 0.8$, $C_{1,\epsilon} = 0.4$, $\alpha_\phi = 0.8$ and $C_{1,\phi} = 0.2$. Both curves are close, and this symmetric behaviour is what is wanted for such an indicator of correlation. Again, much closer curves are obtained with greater values of α and identical curves are retrieved when the α of ϵ and ϕ are both equal to 2. Forcing $\mathrm{IC}_{\epsilon\phi} = \mathrm{IC}_{\phi\epsilon}$ can actually be a way to find an estimate of a' once a is known without having to implement the whole joint analysis. Hence this IC appears to be a good candidate for characterizing in a simple way the correlations across scales between two fields. One should keep in mind that it is mainly relevant in the case where the studied fields do not exhibit values of α that are too small (typically < 0.8).

2.3.4 Implementation with rainfall data

This innovative joint UM framework was implemented to study the correlation between four quantities :

- R, the rain rate ($\mathrm{mm.h}^{-1}$);
- LWC, the liquid water content ($\mathrm{g.m}^{-3}$);
- N_t, the total drop concentration (m^{-3}); (see Eq. 4.5)
- D_m, the mass weight diameter (mm). (see Eq. 4.6)

TARANIS data (see section 4.1) collected between 15 January 2018 and 9 December 2018 on ENPC campus was used. Ensemble analysis on rainy events are used.

UM analysis on each field independently confirmed very good scaling behaviour for R, LWC and D_m and a good one for N_t. Estimates of α are in the range 1.7-1.8 meaning this is the optimum case for implementing the developed framework.

Joint UM analysis was carried out with good scaling retrieved. Estimates of parameters are reported in Table 2.1. For example, let us consider N_t and R. The scaling is good, with a value of $r^2 = 0.97$ for the linear fit. It enables the exponents a and b to be estimated at 0.33 and 0.75 respectively. The corresponding IC is equal to 0.18. In addition to quantifying the level of correlations between the two fields, it suggests how to simulate one from the other. More precisely, once a time series of fluctuations of R is available, it is possible to simulate a realistic corresponding time series of fluctuations of N_t, by raising to the power $a = 0.33$ the R series and multiplying it with an independent random field Y with $\alpha = 1.76$ and $C_1 = 0.14$ raised to the power $b = 0.75$, and renormalizing the ensemble. Formally it suggests the fluctuations of N_t can be written as

$$\frac{R_{\mathrm{fluctuations}}^{0.33} Y^{0.75}}{\langle R_{\mathrm{fluctuations}}^{0.33} Y^{0.75} \rangle}.$$

Such relations open the path for techniques to simulate fluctuations of N_t knowing only the temporal evolution of the rain rate.

Similar qualitative results are found for the other combinations. As expected given the observed values of α, the ICs computed in one way or the other (i.e. inverting the role of ϵ_λ and ϕ_λ) are very similar. This confirms the relevancy of the developed framework in this case. It appears that the correlation found between R and LWC is much stronger than between R and N_t or D_m. There is no correlation between N_t or D_m which

Table 2.1: Numerical output of the joint multifractal analysis of the four studied fields. For each box, using the notations of Eq. (2.33) ϵ_λ corresponds to the field of the column and ϕ_λ to the row.

	R	LWC	N_t	D_m	
R		0.98	0.97	0.97	r^2
		0.82	0.33	0.45	a
		0.38	0.75	0.80	b
		0.78	0.18	0.26	IC
LWC	0.98		0.95	0.97	r^2
	0.93		0.44	0.36	a
	0.50		0.75	0.92	b
	0.77		0.27	0.15	IC
N_t	0.97	0.95		0.50	r^2
	0.44	0.53		0.00	a
	1.08	0.94		1.11	b
	0.17	0.27		0.00	IC
D_m	0.97	0.97	0.50		r^2
	0.51	0.37	0.00		a
	0.91	0.91	0.89		b
	0.25	0.16	0.00		IC

suggests but is not proof of independence (it would be proof for Gaussian variables). Note that the very bad scaling for the joint analysis of these two quantities is partially due to the very small values found for $r(q,h)$ which are basically equal to zero. R exhibits a slightly greater correlation with D_m ($IC = 0.26$) than with N_t ($IC = 0.18$). It is the inverse for LWC with values of IC equal to 0.15 and 0.27 respectively.

2.4 Stochastically guessing missing data of a binary fractal field

This section is mainly based on Gires et al. (2021), in which additional details can be found.

2.4.1 Overall purpose

Missing data are ubiquitous in hydro-meteorology. As discussed in section 2.1 hydro-meteorology fields exhibit scale invariant feature. The goal of this section is to develop an approach to infill missing data that preserves the key property of scale invariance and is stochastic. The latter feature is much needed in order to obtain not only a single deterministic outcome, but an ensemble of realisations actually yielding to an empirical probability distribution of the outcome for all the time steps or pixels where data is missing.

In this first step, we focus on binary fields and hence work with the β-model (see section 2.1.5). It is assumed that the field which we aim at infilling exhibits fractal feature with are characterized by a fractal dimension. A methodology to condition the β-model, i.e. ensure that the generated field has the correct values at the available locations and expected fractal dimension, is developed and constitutes the core of this work. The main advantages of this conditional model with regards to other approaches are: (i) it is physically based in the sense that it preserves and actually relies on underlying scale-invariant properties of the studied geophysical fields; (ii) it can intrinsically work at any resolution; (iii) it requires only one parameter (the fractal dimension of the studied field), thus it is parsimonious; and (iv) it requires limited computational power.

The general idea of the process presented in this paper is actually rather similar to the one discussed in Tchiguirinskaia et al. [216]. It basically consists in first setting 'manually' the increments needed to ensure that the available values are correctly retrieved (i.e. first level of conditioning of the β-model). In a second steps, the remaining increments are simply stochastically drawn using the laws of Eq. 2.21, with a parameter c yielding to the wanted fractal dimension (i.e. second level of conditioning of the β-model). In Tchiguirinskaia et al. [216], it is done with continuous Universal Multifractals meaning that it is not the increments but the generator that need to be set. It might be seen like adding complexity, while enabling to handle non binary fields. However the process does not ensure that the exact values at the available locations are retrieved, but only approximations.

2.4.2 Description of the conditional β-model and numerical results

The process developed to create this conditional β-model is illustrated in Fig. 2.12, which will be used for pedagogical purposes, while the text description is generic. More precisely, we start with a field at a given

resolution made of zeros (in white), ones (in black), and missing/unknown data (in yellow). The goal is to simulate realistic values for the missing portion of the field, while ensuring that the final field has the desired statistical properties; i.e. that it exhibits a fractal behaviour with the correct fractal dimension.

Since, the field is assumed to be generated through a multiplicative cascade process as described in section (2.1.5), it is actually fully defined by all the multiplicative increments of its underlying cascade process (Fig. 2.12.a). For a series of length 2^n, the increments to be filled can be denoted $b_{k,i}$, where k is the cascade step ranging from 0 to n and i ranges from 1 to 2^k. They are displayed in yellow on Fig. 2.12.a, since at the beginning of the process they are unknown. Hence, the whole concept of the conditional β-model simply consists in affecting a value to each of the cascade's multiplicative increments enabling to both reproduce the available values and the statistical features. This is what is called conditioning a β-model in this paper.

More precisely, the three successive steps of the process are detailed with the illustrations in Fig. 2.12 :

- First, the required alive increments are filled, i.e. for each strictly positive value of the field, the chain of increments (one per cascade step) leading to this value is all set to one (i.e. 'alive'). In the example of Fig. 2.12, there is only one non-null available value and the corresponding increments which then must be set to 'alive' are circled in red in Fig. 2.12.b.

- Second, the increments that are needed to correctly reproduce the zeros of the initial field are set to zero (i.e. 'dead'). Given that it is a multiplicative process and that a single zero in the increments chain leading to a final value is sufficient to have it equal to zero, the process is slightly more elaborated than for the 'alive' values. In practice, each zero of the initial field is treated one after the other. The order is randomly chosen (in practice a random permutation between their positioning indexes is run and they are treated in the obtained order). Then for a given zero, the chain of increments leading to it is considered. If there are no zeros, then a single increment among the available ones (there might already be some 'alive' increments in the chain, and they should not be changed) is set to zero ('dead') and the others are left unknown. Let us remind that given Eq. 2.19, a single zero is sufficient to ensure that the final value (i.e. the product of the multiplicative increments) will be equal to zero. Hence there is no need to set more than one to zero. The increments set to zero is randomly chosen among the available ones (in practice, a random permutation between their defining position indexes is run and the first element is selected). If there is already a zero in the chain of increments, then nothing is done. This is illustrated in Fig. 2.12.c. In this example, the first zero treated is the one circled in red, with its corresponding increment at cascade step 3 set to zero (the ones of cascade step 0, 1 and 2 were already set to one and could not be altered). Then it was the green one (increments at cascade step 1 is set to zero and the ones at cascade step 2 and 3 are left unknown) followed by the dark blue one (increments at cascade step 2 is set to zero while the one at step 3 is left unknown). The last one was the light blue one. For this time step, since a zero was already in its increments' chain, no additional zero was added. This process limits the number of increments set to zero while ensuring that available values are correctly retrieved.

- Third, all the increments which are not yet filled are randomly drawn by using the probabilities distribution of Eq. 2.21 with a parameter c equal to the fractal codimension of the studied field. Once a value has been affected to all the increments, it is straightforward to generate a realisation of the field. See Fig. 2.12.d for an illustration.

Since, it is a stochastic process, numerous realisations are generated. Hence it is possible to compute an average value over all the realisations. This quantity is actually an empirically computed probability for the time step to be equal to one, which corresponds to a probability distribution in this binary framework. Depending on the application, the whole information contained in this probability distribution could be used. In the context of this work, and in order to remain in a binary framework, we suggest to use it to extract a 'most probable' (mp) field by setting a time step to one if this average is greater than 0.5 and zero otherwise. This rather natural threshold of 0.5 is actually not arbitrarily chosen. Indeed a sensitivity analysis showed (not displayed here) that it corresponds to the values leading on average over numerous samples to the maximum percentage of hits (i.e. correct guess for the missing data) for this 'most probable' field. The process was implemented in 1D and 2D on ensembles of numerical simulations. The percentage of hits was used as an indicator or performance. Obviously, it depends on the parameter c as well as the percentage of p of missing data. As it can be expected, the performance decrease with increasing p and decreasing c. Even in the worst case, i.e. removing 90% of the initial field with $c = 0.2$, the % of hits with the 'most probable field' ($\%_{mp}$, the indicator of performance) remains greater than 70%. Such achievement is possible because the developed model relies on the underlying robust structure of a multiplicative cascade. Finally, it should be noted, that the width of the uncertainty interval is rather great (typically 15-20%) meaning that there is a significant variability of the results from one sample of initial field to the other.

When the parameter c of the underlying β-model is unknown, it is possible to implement an iterative process that converges in few steps toward a stable estimate of c.

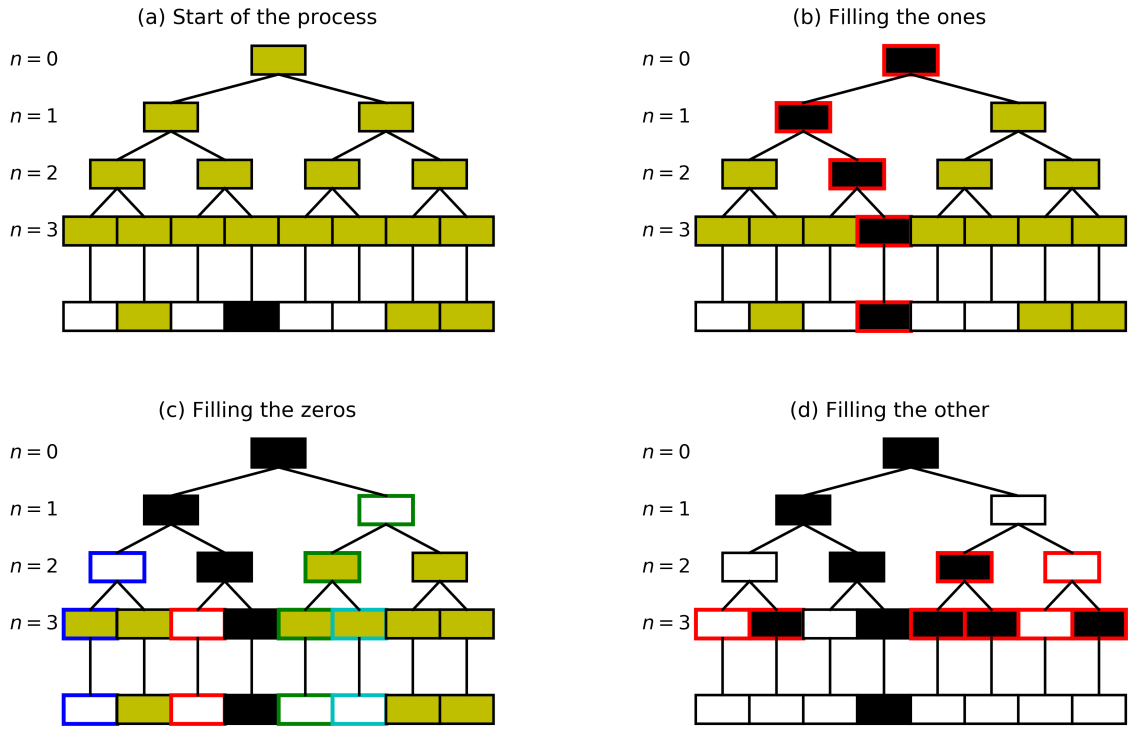

Figure 2.12: Illustration with a simple case of the successive steps of the conditional β-model. Ones are represented in black, zeros in white, and unknown/missing values in yellow. (a) Start of the process : some data is missing and all the underlying increments of the process are unknown. (b) Filling the ones : all the increments needed to retrieve the ones of the original field are set to one. (c) Filling the zeros : a limited number of increments ensuring the zeros of the original field are retrieved are set to zero. (d) The remaining unknown increment are randomly drawn by using the probability distribution of Eq. 2.21. More details (including the edge colour highlights can be found in the text). Figure from Gires et al. (2021).

2.4.3 Implementation on rainfall data

The conditional β-model is implemented here on the occurrence pattern of a 5 min rainfall time series collected with disdrometers on the ENPC campus (see section 4.2). Results are illustrated in Fig. 2.13. The 2048 time steps long occurrence pattern is displayed on top. Below, a partial initial field with approximately half of the time steps set to unknown is shown (obtained with $p = 0.5$). It basically means that 50 % of the recorded data is set aside, and it is tried to reconstruct it with the help of the developed algorithm. Such degraded data was used as input into the algorithm to check its validity. The algorithm was initiated with $c_{algo} = 0.1$, and two iterations were enough to ensure convergence. More precisely, the first iteration yielded a c equal to 0.28, while the second one yielded a value of 0.28 as well, which is also the expected value ($= 1 - D_{F,rainfall}$). Fig. 2.13 displays the outcome after this second iteration of the algorithm : one realisation, average, and 'most probable' field. $\%_{mp} = 94$ is found, which is very good. Since there are numerous zeros in the field, the hit rate (the % of correct hits on missing data) by assuming that all the missing time steps are equal to zero was also computed and found to be equal to 85%. This highlights the benefits of the conditional β-model. In summary, this first implementation of the conditional β-model on actual data enables to confirm its relevancy and efficiency.

It was also tested to threshold the series before implementing the conditional β-model, i.e. to artificially set to zero all the values below a given threshold T. It turns out that as long as $T <\approx 1$, the resulting field still exhibits good fractal behaviour ($r^2 > 0.98$ in the computation of D_F). The conditional β-model also performs well with $\%_{mp}$ scores for $p = 0.5$ equal to 97 and 98% for T equal to respectively .2 and 1 mm.h^{-1} (the hit rate assuming all missing data is equal to zero is equal to 91 and 95 %). For larger thresholds the quality of the scaling becomes dubious meaning that the developed approach is no longer relevant. These findings : (i) are consistent with the intuitive notion of multifractality, i.e. that a multifractal field consists in a hierarchy of embedded fractal fields. (ii) confirm that a simple threshold is not appropriate to address this issue and that the notion of singularity, i.e. a kind of scale invariant threshold would be required. This would result in a qualitative shift which is outside the scope of this work. Some elements in this direction can be found in Tchiguirinskaia et al. [216].

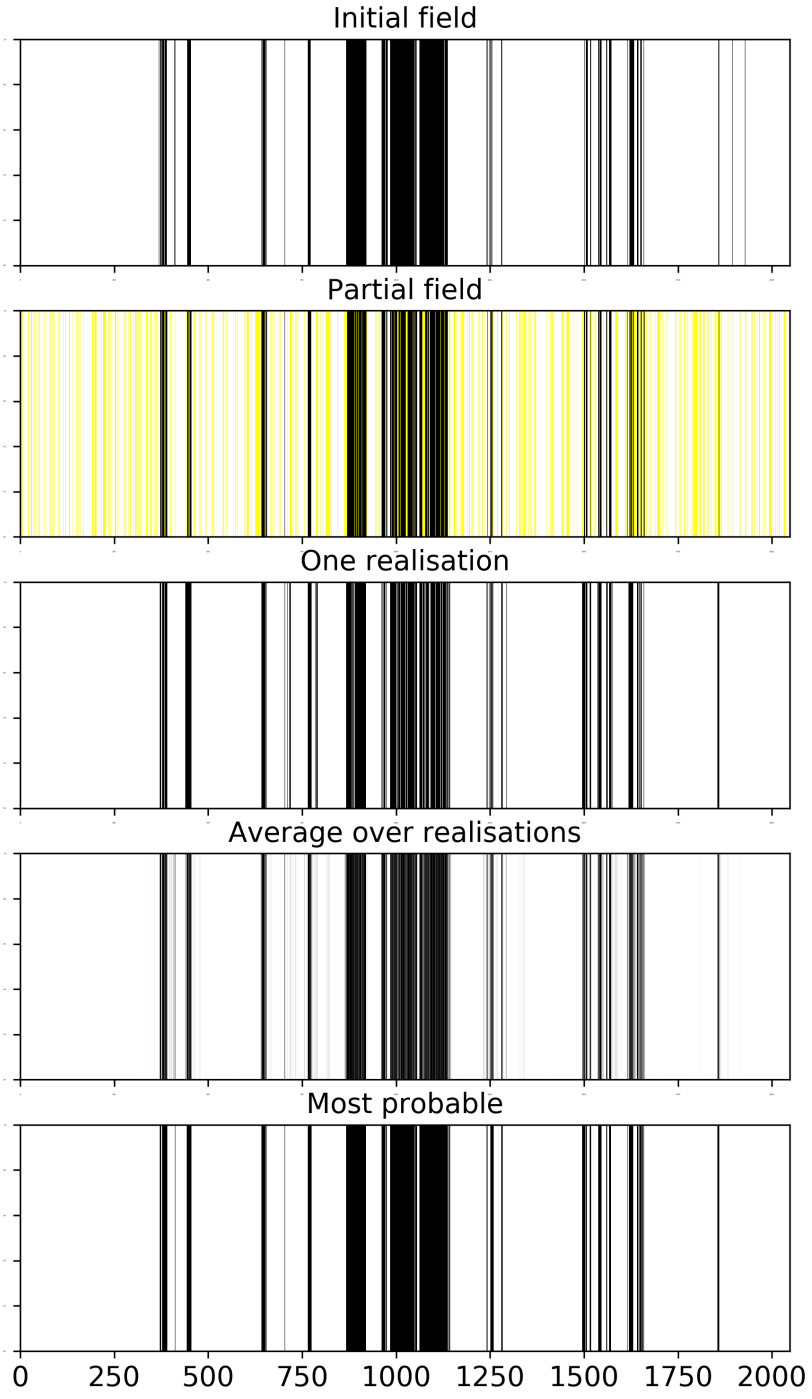

Figure 2.13: Outputs in 1D of the conditional β-model with an 'initial' field consisting of the rainfall time series occurrence pattern (top). The content for each sub-figure is described through the title above them and more details can be found in the text. With regard to the 'partial field' sub-figure, the yellow time steps correspond to the missing data (i.e. the time steps whose content has been artificially removed). With regard to the 'Average over realisations' sub-figure, the colour scale goes for 0 (white) to 1 (black) with various levels of grey. Figure from Gires et al. (2021).

Chapter 3

Dealing with anthropogenic and geophysics' extreme variability to improve urban resilience

During my PhD and in the years right after, my work regarding urban hydrology mainly consisted in quantifying the impact of unmeasured small scale rainfall variability, i.e. the variability that is occurring at scales smaller than 1 km in space and 5 min in time which correspond to the ones measured by operational weather radars. In order to properly address this question, it is necessary to rely on models that are able to handle such high resolution rainfall. This is one of the reasons why, at HM&Co, we initiated the development of Multi-Hydro since 2009 and validated it on numerous case studies. Being among the first users, I contributed to initial corrections and validation through direct work or supervision of students. These elements are not discussed in details in this document but can be found in the list of published papers in detailed CV. This model has a modular structure and is basically an interacting core between various models (most of them already existing), each representing a portion of the water cycle in urban areas (rainfall, runoff, infiltration, sewer flow...). It is physically based (in the sense that it relies on the numeric solving of basic physical equations), fully distributed, and scalable (its resolution can easily be changed). Numerous works showed the importance of accounting for rainfall variability in urban hydrology.

However, rainfall variability is only one aspect of the issue because space-time variability is actually a core feature of all aspects of the functioning of urban areas. Indeed urban settings in terms of land use, pedology, sewer networks exhibit scale invariant properties, which is often mentioned but seldom really accounted for. Urban areas are furthermore embedded in a geophysical context meaning that the well documented scale invariant features of geophysical fields such as rainfall, wind, temperature or humidity obviously affect them. Hence, a strong axis of my scientific work consists in accounting for both anthropogenic and geophysics' extreme variability. This issue is actually required to properly understand the functioning of urban areas and then improve their resilience, which should be understood as their capacity to continue their development despite chronic and punctual shocks (definition taken from 100 Resilient Cities initiative of the Rockefeller Foundation). In my work, there is a focus on issues related to storm water management and notably urban flooding.

In order to properly address this great challenge of the field, an ubiquitous approach is needed, meaning that variability must be studied and accounted for in all aspects from the description of urban settings to the analysis of model outputs. This is what I am doing. More precisely, I started by analysing the variability across scales of the input's fields by continuing to characterize rainfall variability and initiating a fractal characterization of cities (sewer system, imperviousness and green roofs) (section 3.2). Then I made some initial efforts to account for variability in hydrological models by first studying the required input resolution and how to stochastically infill missing data with the example of imperviousness (section 3.3). Finally, I implemented a multifractal characterization of model outputs and notably surface flow (section 3.4). The work was implemented mainly on two cases studies in the Paris area which are presented in details in section 3.1 along with their associated operational purposes.

3.1 Radar rainfall data and case studies

3.1.1 Weather radar measurement and its limitations

There are many reviews on the use of weather radars to estimate rainfall [35, 154, 209], and on its applications in hydrology [44, 117, 18]. For a classical discussion of errors associated with radar rainfall measurements and possible corrections, please refer to Hazenberg et al. [88]. For applications more specifically dedicated to urban

hydrology, interested reader in referred to this review Einfalt et al. [51], or a recent update Thorndahl et al. [223] by the International Group on Urban Rainfall (IGUR) which is a working group of the IWA/IAHR Joint Committee on Urban Drainage. Here I do not aim at all to be all-inclusive on the topic, because my work is not primarily on this, but only to remind the main ideas that a user of such data should keep in mind.

The basic functioning of a weather radar is summarized in Fig. 3.1. The radar basically sends an electromagnetic wave and part of it is backscattered by the hydrometeors that are in the atmosphere. For operational radars, wavelength of the signal usually ranges from ≈ 3 cm (X-band) to ≈ 10 cm (S-band). The most commonly used by national weather service in Europe to generate radar mosaic is C-band radars with wavelength of ≈ 6 cm. The smaller the wavelength, the smaller is the antenna meaning that it is easier to install and operate. The radar range increases with wavelength because longer wavelength are less affected by signal attenuation. The operational resolution also decreases with wavelength from few kilometers for S-band radars to few hundred meters for X-band ones.

The output of a single polarimetric radar consists in successive maps in polar coordinates of radar reflectivity Z ($\mathrm{mm}^6.\mathrm{m}^{-3}$), which basically corresponds to a power received. In the recent decades, polarimetric radar have been widely deployed. They emit and received an electromagnetic wave with both a vertical and an horizontal polarization. Since drops tend to be more and more oblate with increasing size (see section 4.3.1), it means the the signal received on the two polarizations will be different. Hence there is a horizontal Z_{HH} and a vertical Z_{VV} reflectivity which enables to compute a differential reflectivity Z_{dr}. A phase shift Φ_{DP} (in ^{o}) between the two signals is also estimated, and often used as specific phase shift K_{DP} ($^o.\mathrm{km}^{-1}$).

Hydro-meteorologist are actually interested in rain rates, hence there is a need to convert the radar quantities into rain rates. There is an extensive literature on the topic with a wide variety of algorithms which have been developed to account for various bias (see Thorndahl et al. [223] for a recent review). I will only mention few of them which are used in the data analysed in section 3.2.1. The most famous one is the Marshall-Palmer law [149] which relies on strong assumptions on the drop size distribution (DSD):

$$Z = aR^b \tag{3.1}$$

where a and b are two parameters which depend on the DSD and R is the rain rate in $\mathrm{mm.h}^{-1}$. The commonest choice is to have $a = 200$ and $b = 1.6$. Such values are valid for stratiform rain and can also be tuned according to the rain type within a given range of acceptable values ($75 \leq a \leq 1000$, and $1 \leq b \leq 2$).

Another common relation is a power law one between R and K_{DP} :

$$R = cK_{DP}^d \tag{3.2}$$

which is often used for 'great' rain rates. This is for example the case with the dual polarimetric product generated by the HM&Co-ENPC X-band radar in which a $R - K_{DP}$ relation is used for pixels with 'great' rain rates (defined as $Z \geq 35$ dBZ and $K_{DP} \geq 0.3$ $^o.\mathrm{km}^{-1}$) with $c = 19.63$ and $d = 0.823$, and a classical $Z - R$ one for 'low' rain rates.

There are also some non-local algorithms, which compute the rain rate along a full radar beam at once (or a segment of it) and not on a gate by gate basis as in the previous cases. This is the case of the ZPHI algorithm [219] which was implemented on C-band data used in some works presented in this document. It should be mentioned that weather radar suffer from numerous limitations which are due either to meteorological issues (natural vertical profiles of reflectivity, orographic effect) or to the propagation of an electromagnetic wave in the atmosphere (beam blockage, attenuation, ground echo, anomalous propagation...)..., which can be detected and/or partially solved with the help of tailored algorithms. A detailed description of them is outside the scope of this document. A severe issue is that weather radars measure rainfall in volume in altitude while researchers and practitioners are mainly interested by maps of rainfall at ground level. Between the measurement height of typically 1 - 1.5 km, and ground, some physical transformation can affect rainfall. It can also simply be advected by wind which can generate shifts of several radar pixels. This issue is more and more visible at higher resolution. Some operational products also rely on an adjustment, more or less in real time, of radar maps to ground measurement provided by a network of rain gauges.

3.1.2 Multi-Hydro among the models in urban hydrology

A wide variety of models have been developed and used over the years to simulate the portion of the water cycle in urban environments. Given that developing them is not at the core of my scientific work I will not provide an in-depth presentation of their history but only a summary of the main ideas to position the HM&Co platform Multi-Hydro in this overall framework. The next paragraphs are based on a paper by Ichiba et al. (2018), a PhD student I co-supervised.

Models in urban hydrology can be classified according to either the nature of the employed algorithms (empirical, conceptual or physically based; [189]), or their spatial resolution and how they represent the complexity of urban hydrology processes (lumped, semi-distributed and fully-distributed models).

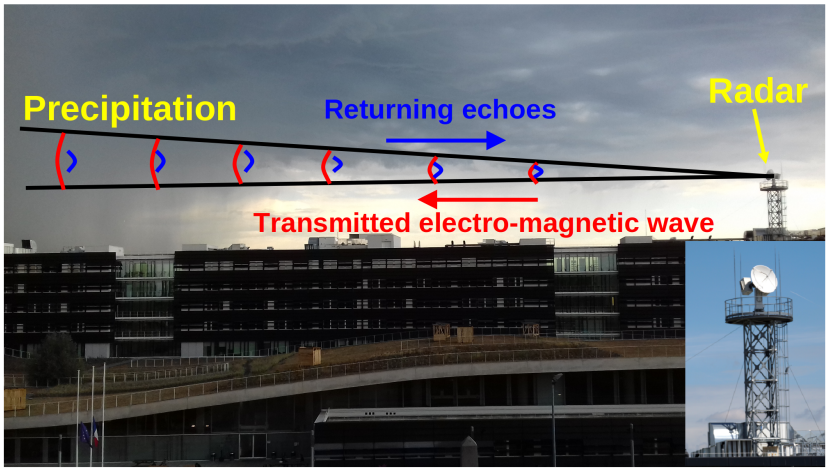

Figure 3.1: Illustration of the overall functioning of a weather radar, with the HM&Co-ENPC X-band radar in the background

Lumped [112] and semi-distributed (see [208, 99] for two examples of models among many other) models are conceptual ones and rely on a simplified representation of urban catchment's heterogeneity. Indeed the whole catchment is considered as a single unit with homogeneous features for the lumped ones, while a catchment is divided into a limited number of homogeneous sub-catchments for the semi-distributed models. These two approaches were widely developed and used for modelling applications because they require limited amount of data for their implementation, and exhibit fast computation time. They often rely on a calibration step that 'forces' the model to represent the observed data. However, these models give output information at the sub-catchment scale, which is too coarse for meeting several urban water managers' requirements in their need to understand some very local flooding problems or to evaluate management strategies at very small scales. Hence, the need has arisen to change the spatial resolution of hydrological models, and several works in the literature have investigated this approach for semi-distributed models (for examples among others, see [175, 210]). It appears that the aggregation and disaggregation of sub-catchments changes the model output, which reflects a 'scale effect issue', and that the complex calibration step must be performed again to obtain performance similar to the previous configuration.

An alternative to these semi-distributed models is to use fully distributed models with a more or less refined direct representation of the various physical processes at stake and their interactions. The ones usually integrated are (1) precipitation, (2) interception and storage, (3) infiltration, (4) overland flow, (5) sewer flow, (6) infiltration into the subsurface zone and (7) sewer overflow. One of the goal is notably to better represent the 2D dynamical behaviour of the water on the ground. A common approach consists in making different modules interact, each of them echoing a portion of the water cycle in urban areas [47, 58, 91, 106, 185]. At HM&Co, we relied on such approach to develop an in-house modelling platform called Multi-Hydro. The model was initially developed in 2009 [52], and later refined [64, 63, 97, 98].

The overall structure of the model is shown in Fig. 3.2. Each of the modules integrated in Multi-Hydro relies on open-source software packages that have already been widely used and validated by the scientific community. The surface module is based on TREX (Two dimensional Runoff, Erosion and eXport model, [230]) which solves fluid mechanics equations for surface flow (diffusive wave approximation of 2D Saint-Venant, see p. 6-7 of the TREX user manual) and infiltration (simplification of Green and Ampt equation). The sewer or drainage module, which is based on SWMM developed by the US Environmental Agency (Storm Water Management Model, [186]), is a 1D-model dealing with sewer flows through numerical solutions of Saint-Venant 1D equations in pipes. The interactions between the surface and sewer flow, i.e. input or output of water, are handled through the gully pixels at a 3 min time step. When there is no overflow, gully pixels are considered to have an infinite infiltration rate, and the water passing through them is directly inputted into the corresponding node of the sewer model. This way of modelling implies that a large transport capacity is assumed for gully, especially with 10 m pixel size which are commonly used. Future developments of Multi-Hydro will enable to improve the model with regards to this coarse assumption. They could notably rely on the experimental and computational studies of gully inflow capacity, including 3D CFD studies, which analyse phases in the flow, inlet capacity, reverse flow when the piezometric level in the sewer is above the ground level [48, 45]. In case of sewer overflow through a node, the corresponding gully pixel is converted into a road pixel and the water exiting the node is inputted on this pixel (considered as a source in TREX). The infiltration module relies on the VS2DT model developed by the US Geological Survey. It is used to simulate the infiltration into the unsaturated subsurface zone [123, 89]. This module uses the infiltration depth calculated by the surface module as input, and simulates

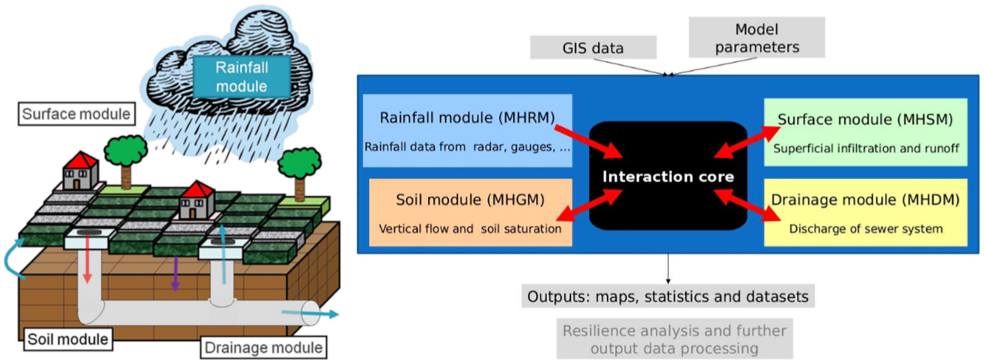

Figure 3.2: The Multi-Hydro model is an interacting core between four modules, each of them representing a portion of the water cycle in urban environments. Figure from Giangola-Murzyn (2013).

a 2D infiltration (vertical and 1D horizontal) into the subsurface. This module was not used in the examples presented in this document because the analysis of the subsurface infiltration was not among the objectives pursued.

In order to run Multi-Hydro, data needs to be shaped in a standard format. Commonly available Geographical Information System (GIS) data, such as land use and topography provided in France by IGN (the French agency producing geographical information) are inputted to MH-AssimTool [184]. This software formats the inputs with the desired resolution and makes Multi-Hydro a transportable model, rather easy to implement on a new catchment. Once a resolution is chosen, one has to affect an elevation and a land use class to each pixel. The elevation is obtained by an interpolation of the raw available data. With regards to the land use, a priority order has been determined to assign a unique land use class for a given pixel according to the hydrological importance of the given class. If a gully is located on a pixel, the entire pixel will be considered as a gully. This process is repeated in the following order for this case study: roads, houses, forest, grass, and water surface. See Ichiba et al. [98] for a comparison with other possible strategies, notably relying on the surface represented by this each class within a given pixel.

Multi-Hydro has already been implemented and validated in several locations for different purposes: in the cities of Villecresnes (France) and Manchester (UK) for flood mitigation by using barriers and retention basins [63], in Sucy (France) for retention basin management [97], in Sevran (France) to study the impact of small-scale rainfall variability in urban areas [79], in Jouy-en-Josas to analyse the output (see section 3.4, [82], and in Villepinte and Champs-sur-Marne (France) for quantifying the impact of large-scale implementation of blue and green infrastructures on storm water management [235].

3.1.3 Case studies and associated purposes

As previously stated, I will not present all the case studies I was involved in, but only the main ones used in the coming subsections, i.e. Sucy-en-Brie and Jouy-en-Josas.

Sucy-en-Brie case study is a 2.45 km^2 urban catchment located southeast of Paris, in Val-de-Marne County. Known historically as an agriculture area, the city is now highly urbanized with an imperviousness coefficient around 35 % (see Fig. 3.3). The city is bounded at the north by the Marne river (one of the two main rivers in the Paris region). The area has suffered in the past from several flooding events as a consequence of (1) the very steep slope (34 $\mathrm{m\,km}^{-1}$) that increases water speed and causes overflows in the downstream portion of the storm water network and (2) the increase of impervious areas combined with a soil structure that limits infiltration to the subsurface. The drainage system in this area is a separated one (i.e. there are separate networks for waste water and storm water). The storm water system is routed to the Marne River. This area was studied in the framework of a CIFRE PhD with DSEA 94, the service of Val-de-Marne County managing the sewer system, to optimize according to expected nowcasts of rainfall the management of a retention basin designed to both prevent flooding in case of extreme rainfall and de-pollute storm water when there is no risk of flooding. Indeed both aims yield different strategies at the beginning of a rainfall : not storing water to keep some space during expected peak flow in the first case, or storing all the water in the second case.

The Jouy-en-Josas catchment (Yvelines County, South-west of Paris) occupies a 3.017 km^2 area, mainly on the left bank of the Bièvre River. A small portion of the right bank near the river bed is also included. The remaining portion of the right bank is drained to a small river that flows into the Bièvre River downstream the outlet of the studied catchment. The Bièvre River is a tributary of the Seine River which it meets in Paris. It flows through increasingly urbanised areas along its 33 km path. This has led to strongly modify its natural bed, both in underground pipes which are integrated in the storm water sewer system, or in a highly artificial open air bed. An effort is currently undertaken to restore its "natural" aspect. A striking feature of this catchment is

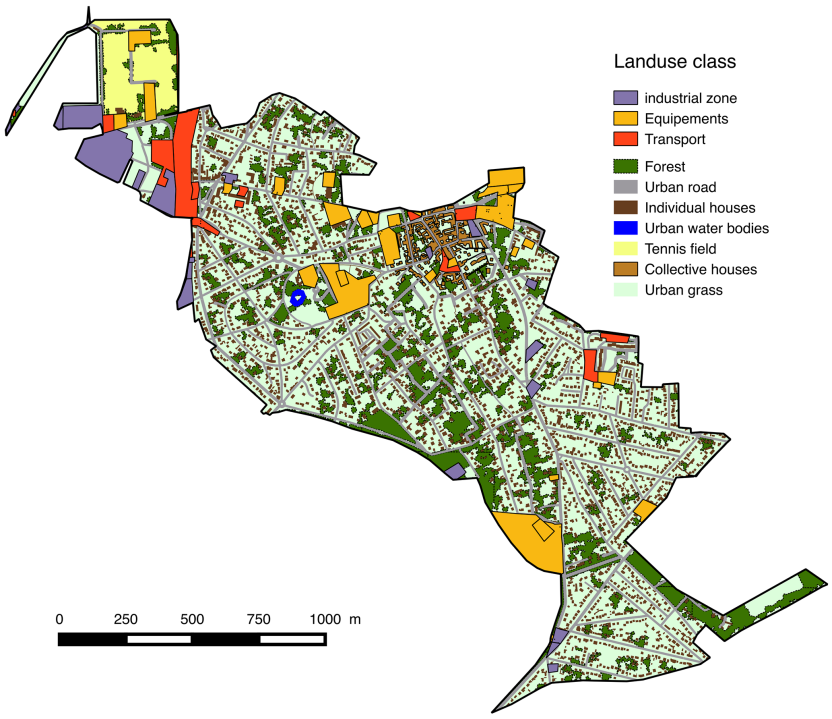

Figure 3.3: The land cover data available for Sucy-en-Brie catchment and used to implement the Multi-Hydro model. Figure from Ichiba et al. (2018).

that, it exhibits steep slopes. There is a difference of approximately 100 m between the plateau in the north of the catchment, and the outlet of the catchment (Fig. 3.4.a). The downhill portion strengthens overland runoff, and the combination of pluvial and fluvial processes on the river bank has led to severe flooding in 1973 and 1982. Some details are available on the SIAVB (Syndicat Intercommunal d'Assainissement de la Vallée de la Bièvre, the local authority in charge of urban drainage of the area) website (http://www.siavb.fr/). Following the severe flooding, the SIAVB has created 15 storage basins (integrated in the landscape) along the up-stream part of the Bièvre River to mitigate flooding risks, through a integrated real time optimized management. One, the Bassin des Bas Près, is located just upstream the Jouy-en-Josas catchment. In this catchment, urbanisation and imperviousness are concentrated along the river bank, and on a housing estate along one major North-South road. The remaining of this semi-urban catchment is mainly made of forests. The sewer system is a separate one, and the storm water is routed into the Bièvre River which is considered as a pipe in Multi-Hydro drainage module (the long and West – East oriented pipe located in the South of the Basin in Fig. 3.4.a, left). The representation of the catchment in Multi-Hydro with pixels of size 10 m and 2 m is displayed in Fig. 3.4.b. Thanks to water depth measurement at "Pont de Pierre" (Fig. 3.4.a), the implementation of Multi-Hydro was validated using four rainfall event of various intensity and duration that occurred between 2009 and 2011 (see Gires et al. [82] for all the details).

3.2 Multifractal quantification of input fields' variability

It appears that variability across scales is basically visible on all the input fields used in the modelling of the water cycle in urban areas. A good example of this can be found in a study focusing on green roof (Versini, Pierre-Antoine et al., 2018). Using data collected on the Blue-Green wave pilot site of ENPC campus, it showed that precipitation, humidity, integrated water vapor, wind velocity, air temperature, CO_2 concentration, and soil water content all exhibited good scaling behaviour. Furthermore the distributions of the fluctuations of the fields were found to be non Gaussian and heavy tailed. These features represent the wild part of the randomness of the field; the much more frequent occurrence of extremes characteristic of a multiplicative cascade process.

As previously mentioned, accounting for the complexity and heterogeneity typical of urban water systems is crucial to obtain insights in the urban catchment response behaviour at the various spatial scales that control the relation between rainfall and sewer flows; to develop convenient methods that allow for evaluation of the urban catchment characteristics implemented in urban drainage models (the ones that are of importance for obtaining reliable spatially variable urban catchment responses; e.g. spatial imperviousness structure); to develop methods that support the urban hydrological modeller in the decision making process with regard to spatial details required to obtain reliable model (impact) results.

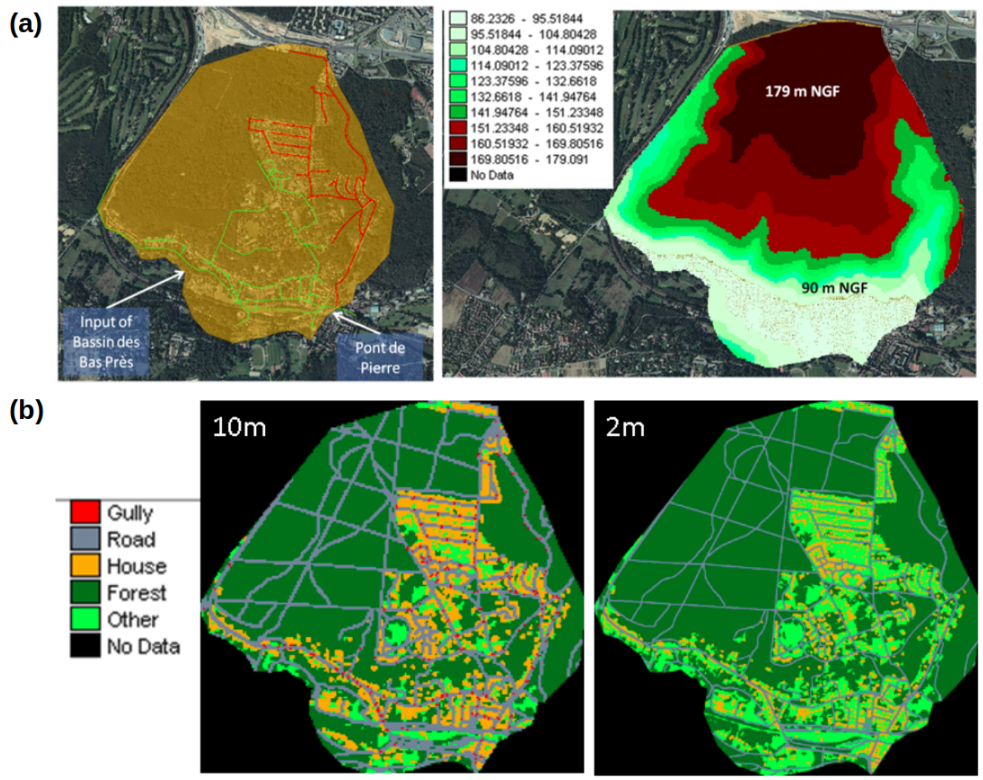

Figure 3.4: (a) Maps of the Jouy-en-Josas catchment: (left) aerial photography and sewer system (The green portion of the sewer network corresponds to the portion over which validation is possible), (right) elevation in m. (b) Map of the land use obtained with the help of MH-AssimTool over the Jouy-en-Josas catchment for two different resolutions. Figure adapted from Gires et al. (2018)

In this section, I will focus on two aspects on which I worked more : rainfall variability and imperviousness distribution in urban areas.

3.2.1 Multifractal space-time characterization of rainfall fields

Numerous UM analysis have been carried out on rainfall fields for various events measured with various QPE products based on both X-band and C-band radars. 2D analysis on successive maps yielding to both ensemble analysis results or temporal evolution of UM parameters have been implemented. 1D analysis on the time series for each pixels yielding to both ensemble analysis results or maps of UM parameters have also been implemented. Detailed results can be found in A. Ichiba PhD manuscript [97], annual reports for the chair Hydrology for resilient cities, or Paz et al. [176]. Given the amount of results obtained, I will not mention all of them but only overall conclusions and few examples selected to illustrate benefits of UM techniques in the comparison of radar products.

In general, collected rainfall data exhibited a good to excellent scaling behaviour, regardless of the radar product. For some events, a scaling break is observed at roughly 5-10 km in space and 10-15 min in time. Hence a change in scaling behaviour may occur at smaller scales. Not accounting for it may affect the overall scaling behaviour. It was tested on the range of scales 0.25 - 1 Km and gave spurious estimates of α, suggesting that a wider range of scales would be needed to fully explore the high resolution scaling behaviour. The break could be associated to either the process itself or to measurement artifacts as we will show later. Anyway, if the break is indeed real, it would mean that rainfall structures and extremes could not be extrapolated from measurements at larger scales. With regards to the UM parameters, they are within the following range : $\alpha \approx 1.3 - 1.7$, $C_1 \approx 0.05 - 0.3$ and $H \approx 0.3 - 0.7$. This is rather in agreement with previous findings obtained on radar reflectivity on the range of scales 75 m - 19 km [218], on African mousson data [232], intense rainfall on rocky montains in the US [166, 165], Mediterranean events , or results that I obtained on rainfall events studying events in the South of France [66], in the Paris area [65, 71] and in the London area [68]. This hints to some kind of universality for rainfall parameters that would need to be studied further with more data and also accounting for potential bias introduced by both QPE radar algorithms and the analysis techniques, with for example a known effect of the zeros that I studied during my PhD [69]. Finally, it should be mentioned that the differences in UM parameters' estimates retrieved between radar products for a given event are in

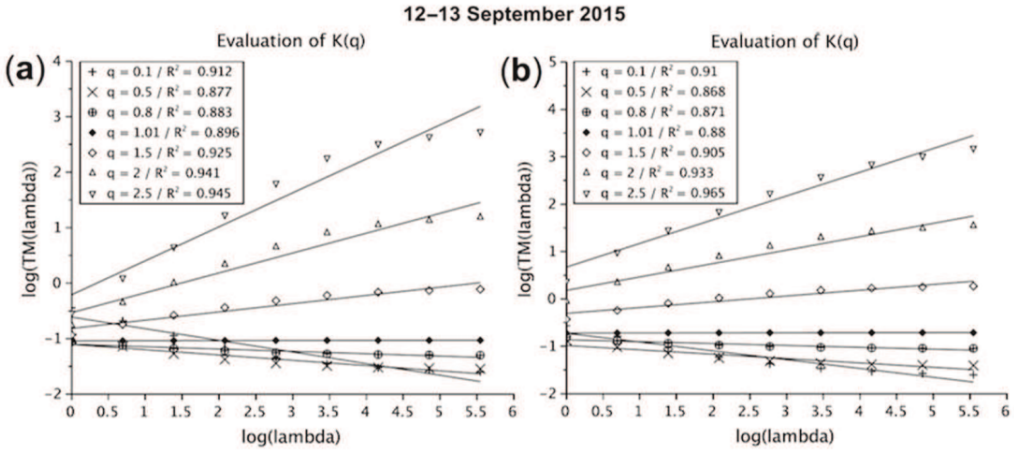

Figure 3.5: TM (Eq. 2.6 in log–log plot) analysis for the 12–13 September 2015 event: X-band DPSRI rainfall products at 1.5 km obtained with (a) FIR filter and Z-R parameters $a = 200$ and $b = 1.6$ for low intensities; (b) FIR filter and $Z - R$ parameters $a = 150$ and $b = 1.3$ for low intensities. Figure from Paz et al. (2018).

general significantly smaller than the difference found between events. These findings shows that despite some differences, the various radar products basically grasp the same multiscale structure.

This observed scaling behaviour is a further confirmation of extreme variability of rainfall down to very small scales. Rainfall is known to be among the greatest source of uncertainty in hydrological modelling, and accounting for such variability remains a great challenge for the community.

Although it is intrinsically hard to distinguish between physical effects and artifacts from measurement techniques; implementing UM technique to carry out morphological comparison of radar products enabled to hint at possible explanations to the retrieved discrepancies. As stated in A. Ichiba's PhD [97] "This new methodology overcomes some limitations of the classical radar - rain gauge comparison technique widely used for QPE validation and radar data comparison but involves a very limited number of radar pixels and does not provide any information about the rainfall structure." This subsection is ended with two illustrations of the use of UM tools to compare radar product features.

A first illustration of the interest of using UM tools to analyse various rainfall products is displayed in Fig. 3.5. The left panel shows TM analysis for the FIR filtered DPSRI product with Z–R parameters $a = 200$ and $b = 1.6$ (a product of he HM&Co-ENPC X-band radar). This standard Marshall-Palmer law is used for low rain rate while $R - K_{DP}$ is used for greater rain rate. A slight curvature is visible on the curves and a scaling break could be considered at roughly 1 km. It turns out that changing the parameters of the $Z - R$ relation to $a = 150$ and $b = 1.3$ (which remains in the bounds commonly reported in the literature), enables to significantly improve the scaling behaviour (see Fig. 3.5.b) and make it more consistent with the expected behaviour widely reported in the literature. It also increases rainfall estimates for low rain rates. This example illustrates well how UM tools can be used to help tune QPE radar algorithms. A more in-depth discussion on the changes of the parameters of the $Z - R$ relations to account for variability of the rainfall drop size distribution can be found in section 4.3.2.

A second illustration corresponds to an analysis made by A. Ichiba in his PhD. He performed a UM analysis of the successive radar maps for three products (HM&Co X-band radar, CALAMAR which is a processing of C-band data with either a adjustment to rain gauge data or not) and obtained temporal evolution of the estimated UM parameters. Fig. 3.6 summarizes the obtained results for a rainfall event that occurred on 12/09/2015. It can be seen that the data from X-band polarimatric exhibits greater values of α and smaller values of C_1. Such difference in terms of UM parameters reflects a profound difference on their spatial structure. At first guess, such differences could be associated to the differences in percentage of zeros of the field. However, since the shift in UM parameters remains during the second half of the event while the portion of zeros become similar, this explanation is not valid. It turns out that the difference is actually well explained by the evolution of the fractal dimension D_F. Indeed the latter remains smaller for CALAMAR data during the whole event despite the percentage of zeros becoming comparable. This emphasizes the benefits of considering a parameter characterizing the structure of the field across scales, and not only a simple percentage at a given scale. This suggests to investigate more closely how ground clutter are treated in the CALAMAR process, which may create artificial zero rainfall pixels.

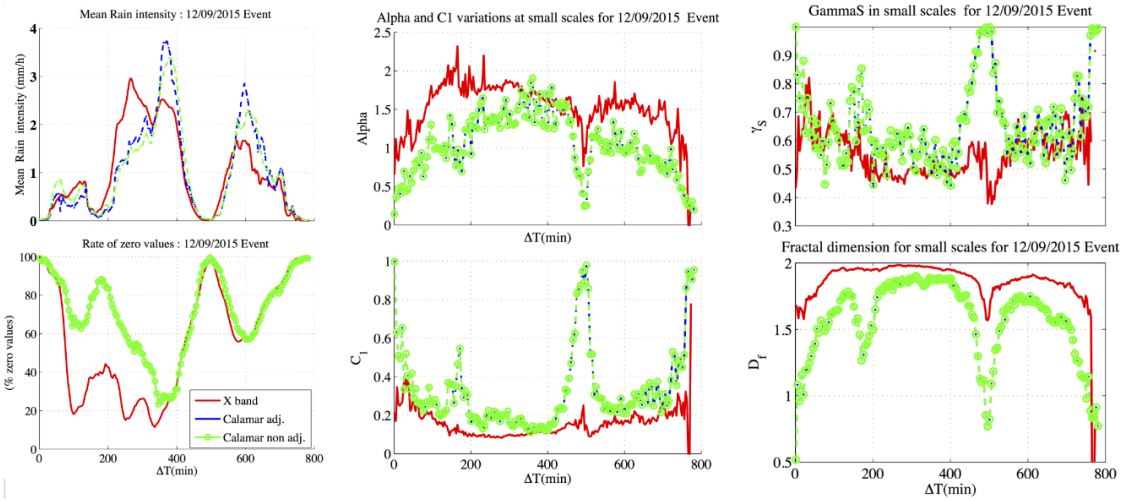

Figure 3.6: Temporal evolution of parameters computed for each radar map of C-band and X-band radar products for the rainfall event of 12/09/2015 in the Paris area : rainfall intensity mean calculated, percentage of zero values, UM parameters α and C_1, maximum observable singularity γ_s and fractal dimension D_f. Figure adapted from Ichiba (2016).

3.2.2 Fractal characterization of cities : sewer system, imperviousness and green roofs

This section is based on Gires et al. (2017) and Versini et al. (2020), in which additional details can be found.

Sewer network and distributed land use imperviousness

In this subsection, I summarize the main findings of a multi-catchments study that is focused on two main properties of urban catchments, namely the geometry of the sewer system and the distribution of impervious surfaces. It allows for obtaining robust results that are representative of a wide range of hydrological characteristics. It was carried out in the framework of the RainGain project, and notably through a workshop that that I organized during which all participants were trained to fractal techniques and implemented them on their own case study.

In total, 10 urban catchments, with areas in the range of 2–8 km^2 and located in five European countries (UK - Cranbrook North, Cranbrook South Torquay North, Torquay South- , France - Sucy-en-Brie, Jouy-en-Josas, Morée-Sausset-, the Netherlands -Rotterdam Centrum, Rotterdam Kralingen-, Belgium - Ghent North, Ghent South, Herent West, Herent West-, and Portugal - Coimbra East-) were adopted as pilot sites in this study. They covered various levels of urbanization ranging from highly urbanized areas to more peri-urban areas. For each catchment, the following data was used :

- The sewer system. It is considered as a network of linear pipes. For all catchments except two, all pipes down to street level (not the connections from building or houses to the network) are available.
- An imperviousness map at a resolution of 2 m × 2 m. It was generated with the help of QGIS (www.qgis.org) to rasterize data vector land use derived mainly from Open Street Map (www.openstreetmap.org). This yielded to a binary map tailored for fractal analysis.

Examples of sewer system and imperviousness maps can be found in Fig. 3.7.

For each catchment, a fractal analysis was implemented on both the sewer network and imperviousness maps. An illustration of the upscaling of the sewer network (i.e. observing it with pixels of various sizes) for the specific catchment of Herent (Belgium) is displayed in Fig. 3.8. The computation of the fractal dimensions for the Torquay north study area are shown in Fig. 3.7.

For the sewer system (Fig. 3.7.a), a single scaling behaviour over the whole range of available scales is not retrieved. Indeed, the plot exhibits a scale break at roughly 64 m pixel scale, separating two distinct scaling regimes. Over each regime, the scaling is robust with r^2 all above 0.99, and visible straight lines. Similar qualitative features, i.e. two distinct well-defined scaling regimes separated by a break, are retrieved for the other studied areas and not displayed. Numerical values of the computed fractal dimensions along with the values of scale break for all studied areas.

For the scaling regime associated with small scales (i.e. right portion of the graph), a fractal dimension basically equal to 1 is found for all the study areas. This does not contain any information on the network's

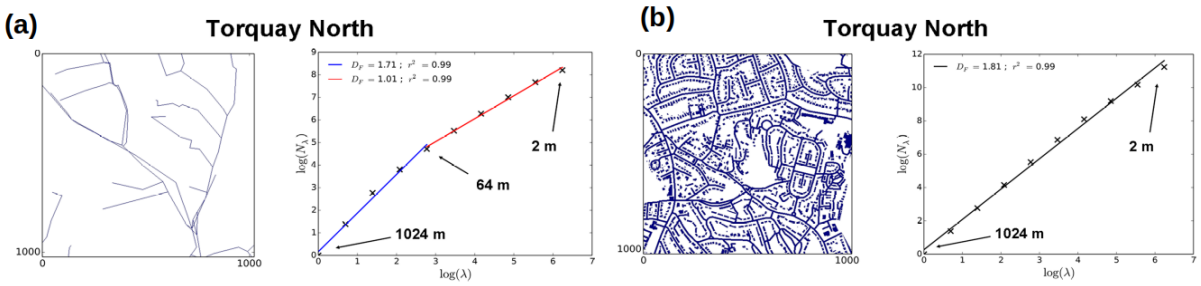

Figure 3.7: Illustration of the computation of the fractal dimension (Eq. 2.3 in log-log plot) for the Torquay North study area. (a) Sewer system (b) Imperviousness. For the maps, the axes correspond to metres (m). Figure adapted from Gires et al. (2017).

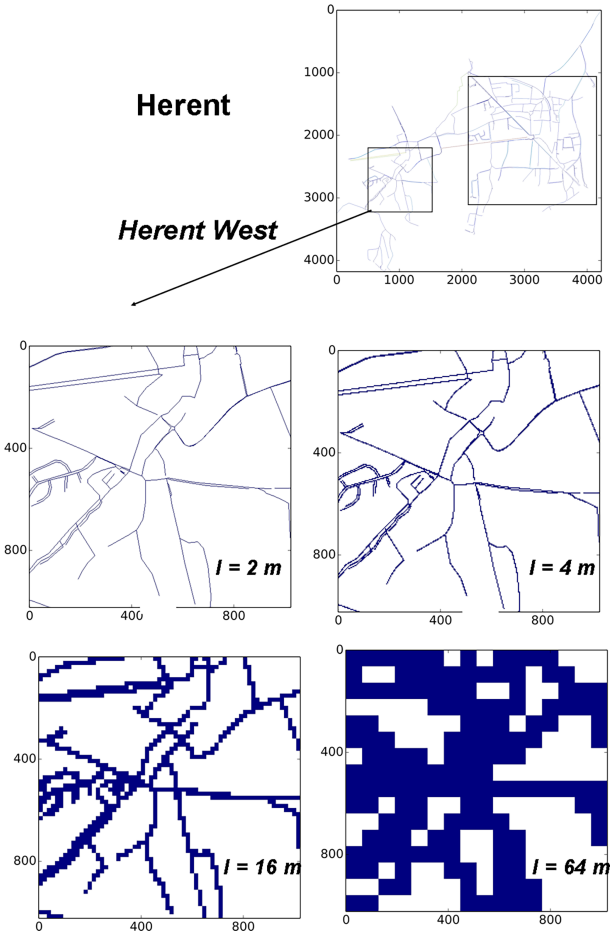

Figure 3.8: Illustration of the upscaling of the sewer network map for the Herent west study area. The axes correspond to metres (m). Figure from Gires et al. (2017)

features but simply reflects the linear structure of the pipes at these scales. It also means that the maximum resolution of the available data (2 m pixels here) is not critical to the analysis and does not introduce a potential bias. Indeed, increasing or decreasing it would simply yield to extending or shrinking the widths of the scale range of this regime but will not affect the values at larger scales discussed below. The break is located at roughly 64 m for most of the areas, which is consistent with the distance between two streets. It is at 32 m for two catchments which correspond to densely urbanized city centres. It appears that for all the catchments the break is observed at roughly the approximate inter-pipe distance of the portion of network taken into account. For the large-scales regime ($\sim$64 to 2048 m), an actual fractal dimension between 1 and 2 characterizing the space filled by the network is retrieved. According to the catchment, we find D_F ranging from 1.69 to 1.94. With smaller scales, this regime is expected to continue until the physical scales of structures is reached below which a fractal dimension of 2 would obviously be found. It, is in any case, smaller than 2 meaning that the network does not completely fill the 2-D space. An interpretation of these values is that these are representative of the level of urbanization of the areas. For instance, we find the greater fractal dimensions in the Rotterdam districts and smaller ones in less-urbanized Jouy-en-Josas and Torquay. This will need to be confirmed with the analysis of imperviousness maps.

These results are consistent with values found in similar studies for drainage networks. Sarkis [192] found a fractal dimension equal to 1.67 for the pluvial drainage network of the Val-de-Marne County (south-east of Paris), based on an analysis at scales of 290 m to 18 km, only considering the main pipe network. Typical values for natural river network fractal dimensions (computed with the box-counting technique) are usually smaller than those found here for urban catchments. For instance Takayasu [212] found D_F for the Amazon and Nile rivers equal to 1.85 and 1.4 respectively.

Figure 3.7.b displays the impervious pixels (in blue), along with the computation of the fractal dimension of the corresponding geometrical set for the Torquay North area. It appears that a unique scaling regime on the whole range of available scales is identified (single straight line), resulting in a fractal dimension of 1.81. Unique scale regimes are also found for impervious surface distributions in all the other studied areas. The scaling regime is robust with visible straight lines as for the sewer system and r^2 is always greater than 0.995. The uniqueness of the regime also means that results are not sensitive to the initial pixel size of 2 m as for the sewer system analysis (but for a different reason). Increasing this size would simply reduce the width of the range of scales available to compute the fractal dimension but not change its value. Similar scaling features are found for the other catchments. Despite the fact that the impervious pixels do not represent the majority of the pixels at a 2 m resolution, their fractal dimension is rather elevated meaning that the impervious areas fill the space in urban areas. As expected less-urbanized areas exhibit lower fractal dimension.

For a given catchment, numerical values of fractal dimension for distributed imperviousness are similar to the ones found at large scales in the sewer system analysis. Discrepancies are usually smaller than 0.1; smaller than the differences between the various catchments. Areas of similar urban density have similar fractal dimensions and lower density urban areas are consistently characterized by lower fractal dimensions. These numerical similarities are worth noting and actually one of the main finding of this analysis, confirmed on a wide set of study areas. Indeed it suggests that the scaling behaviours observed on sewer networks and distributed land use have the same physical basis and reflect a unique underlying level of urbanization. The only difference being that it stops at the inter-pipe distance for the sewer network, whereas it expands down to 2 m scale for the imperviousness. Contrary to other formalism, such as the use of a single percentage of imperviousness defined with data at an arbitrary scale, this fractal dimension is a quantity valid across scales and furthermore based on the characterization of two aspects related to urbanization (namely the sewer network and the distributed imperviousness), which makes it robust.

Representation of imperviousness of buildings

Using the opportunity of this multi-catchment study, a comparison of fractal dimensions computed on two different geometrical sets was implemented: the total imperviousness areas as roads and buildings ($D_{F,all}$) and the buildings only ($D_{\mathrm{F,build}}$). This analysis was made as a first step to investigate the relationships between the fractality of building distributions, as a source for potential green roofs implementation for water flow management, within fractality of the whole imperviousness areas. Indeed green roofs are one of the available tools that can be used to optimize (if needed) water flows in urban and peri-urban areas, hence the need to better understand their potential distribution. More precisely, to increase the functionality of green roofs over the full range of catchment scales [235], an optimization of green roof locations could be made to increase their fractal dimension up to the fractal dimension of the total imperviousness area. The fractal tools could also be used to evaluate the potential impact of green roofs.

Obtained results show that for each catchment the geometrical set of buildings alone behaves as a fractal set. Indeed as for the analysis carried out in previously (total imperviousness) straight lines are found in the linear regression yielding to the fractal dimension with r^2 remaining greater than 0.99, meaning that numerical values of fractal dimensions are robust. Obviously $D_{F,build}$ could not be greater than $D_{F,all}$, since the building

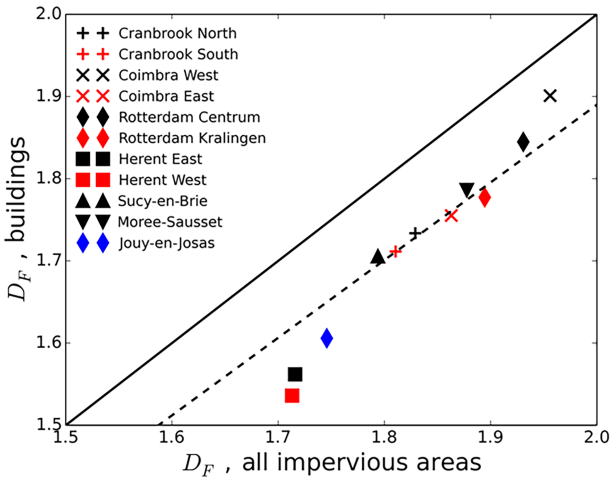

Figure 3.9: Empirical relation between the fractal dimensions of the total impervious area and of buildings only. The continuous line indicates the first bisector, while dotted line is given by $D_{F,build} = 0.945 D_{F,all}$. Figure from Gires et al. (2017).

areas are embedded within a larger fractal set of all impervious areas, and we have $N_{build} = \lambda^{D_{F,build}} = \lambda^{aD_{F,all}}$. The empirical results displayed in Fig. 3.9 suggest that a common value $a = 0.945$ remains suitable for the majority of the catchments. Such a small coefficient may influence the scaling at the smallest scales only. The changes seem to increase with smaller values either meaning that the network of road has a greater importance in these cases, or is simply due to a slight decline of scaling.

Zoom on the green roofs distribution

In order to go a step further in understanding potential role green roofs in storm water management, the fractal dimension of both buildings (so called 'undifferentiated' roofs) and those with green roofs was studied for 9 European cities using. This was achieve in the framework of the "Hydrology for Resilient Cities", and the ANR-17-CE22-0002-01 EVNATURB project.

The scaling features of all buildings was basically found to exhibit same features as those found in the previously discussed study, which enabled to further confirm them with new case studies. With regards to the green roofs, in general three scaling regimes were identified. A large scale regime ($>$ 256-512 m) similar to the one found for all roofs. A small scale regime ($<$ 16-32 m) with values of fractal dimension close to 2 which simply reflects the 2D nature of green roofs and the fact that they tend to be installed only on roofs with typical size greater than $\sim$16 m ($\sim$256 m^2). This explains why such regime is not observed when studying all the roofs. The most interesting regime is actually the intermediary regime (between 32 or 64 m and 256 m or 512 m). It characterizes not only single roofs but their distribution in space which is what we are interested. Fractal dimension characterizing this regime is highly variable from one city to another, ranging from 0.49 for Paris to 1.35 for Frankfort. They are displayed in Fig. 3.10 vs. the fractal dimension for all roofs. These fluctuations illustrate a real difference between roof vegetalization in European urban centres. This suggests that for now and given the current stage of green roofs deployment there is no intrinsic relation between green and undifferentiated roofs, and that the distribution of green roofs is hence strongly influenced not by universal underlying city features but by political will and the architectural history. Such interpretation is well documented in Versini et al. [234]. The scale boundaries of this regime seems also to be an indicator of green roof distribution. It seems to characterize their size (area). The upper boundary is usually equal to 32 m except for Berlin, Lyon and Paris for which it is equal to 64 m (corresponding to a pixel area of 4096 m^2). This approach highlights the benefits of using a scale invariant notion of fractal dimension rather than a single % defined at the maximum resolution.

3.3 Accounting for variability in hydrological models

3.3.1 Required input resolution

As we have seen in previous sections, urban areas exhibit a strong variability notably in terms of land use. Such variability must be appropriately accounted for in order to properly simulate sewer flows. In this overall context, a significant aspect of A. Ichiba work consisted in investigating at which resolution should an urban hydrologic model be implemented ? The main results are reported in this subsection and the interested reader

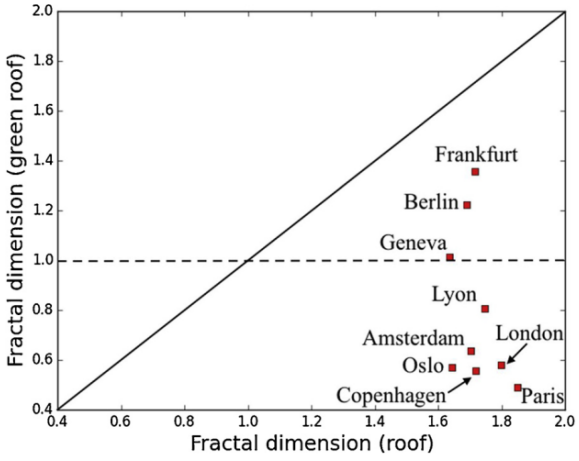

Figure 3.10: Comparison between fractal dimensions computed for undifferentiated and green roofs for 9 European cities. Figure from Versini et al. (2020).

is referred to Ichiba et al. [98] for more information. Figures and part of the text are are based on this paper. To address this issue, he carried out Multi-Hydro simulations on the Sucy-en-Brie catchment at 17 resolutions ranging from 100 m to 5 m using 8 rainfall events.

For this study, a majority rule was used to affect a land use type to a pixel, i.e. for a given pixel the the land use type having the greater proportion is used. However, gully class has priority, to ensure the connection between the surface and the drainage modules. Such rule was found to be more suitable to take into account urban catchment heterogeneity at coarser resolutions. Fig.3.11.a displays the representation of a square portion of the catchment with pixels of size 50, 10, 5 and 2 m. It can be seen that the grid size strongly affects the way land cover heterogeneity is represented in the model, which was expected given the scaling behaviour identified in the previous section. It is this raterization process to prepare Multi-Hydro inputs that generated the scale dependence discussed in this section.

Fig. 3.11.a shows the distribution of the four main land cover classes (forest, road, grass and house) considered in the Multi-Hydro model, as well as the imperviousness coefficient C_{imp} – defined as the ratio between impervious surface (gully, roads, houses) and the total surface – as a function of the model spatial scale. The imperviousness coefficient is actually not a parameter of the modelling formulation. Corresponding to the areas directly participating in the rapid runoff, it should simply be seen as a quantity used to gain some insight into the inputs of the model and how its overall features change with resolution. Its variations (red line) provide an insight into the model behaviour across scales. In this case, three ranges of scales can be identified: (i) large scales (100–30 m) at which the imperviousness coefficient decreases significantly from 55 % observed at 100 m to its minimum value of 27 % at 30 m – this is due to a great redistribution of land cover classes; (ii) medium scales (30–10 m), at which the imperviousness coefficient increases from 27 to 37 % estimated at 10 m; (iii) small scales (10–5 m), at which we observe what can be considered as the final configuration of the catchment, i.e. the most accurate, and closer to the reality on the ground. Across small scales the imperviousness coefficient remains stable around 38 %, which suggests that the model response will be stable across this range of scales.

The flow simulated at the outlet of the catchment for all the studied resolution and rainfall events is in Fig. 3.12, along with the measured one (bold black curve). It can see that regardless of the spatial scale, this physically based model is able to reproduce the observed flow dynamics. This visual impression is confirmed by the the computation of the correlation coefficient between simulations and observations with ranges between 0.84 and 0.98 with an average between 0.94 and 0.98. Such findings, obtained using simply somewhat representative range of parameters value for each land use class and without any calibration was quite interesting. First it was reassuring with regards to its potential. Indeed as pointed out by Pr. Witek Krajewski at the end of a talk during a webinar series dedicated to "Scaling and multifractals : from historical perspectives to recent developments" (hmco.enpc.fr/scaling-and-multifractals-campfire/), "Rainfall-runoff models are essential but only if they have skill without calibration". Furthermore, as pointed out by Pr. Ioulia Tchiguirinskaia such finding enable to go further than simply investigating the required spatial resolution of hydrological models as initially planned, and actually suggested an innovative alternative approach to the classical model calibration. Indeed, instead of tuning the parameters to force the model to reproduce the simulated flow, one can simply change the implementation scale to one enabling a proper representation of the catchment's land cover variability. As an illustration, the overestimation of the volume visible with coarse pixels is in fact mainly due to an overestimation of impervious areas observed with such pixel size.

In order to provide hints on how to select the appropriate modelling scale, the simulation outputs are

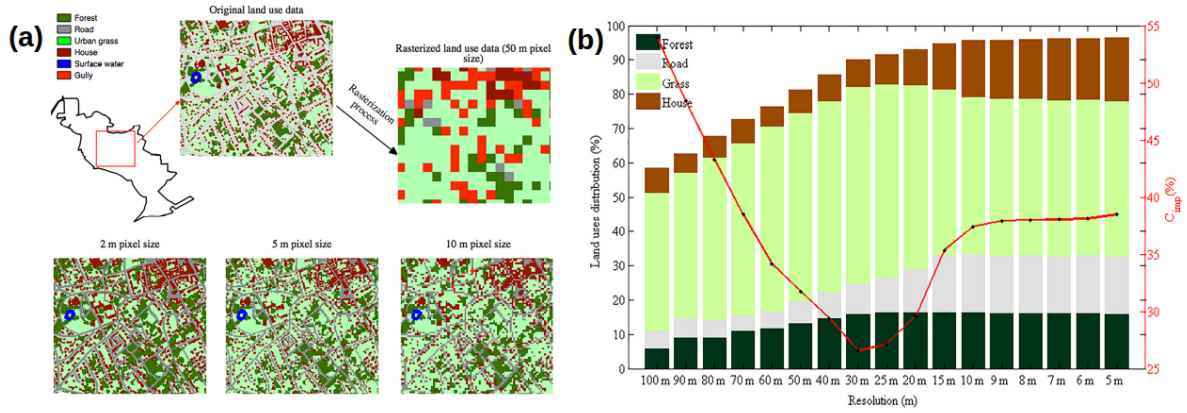

Figure 3.11: (a) Scale effect observed on the catchment land cover. The grid size strongly affects the way land cover heterogeneity is represented in the model. (b) Scale dependence observed in the overall distribution of land cover classes and the imperviousness coefficient C_{imp} with majority rule. Figure adapted from Ichiba et al. (2018).

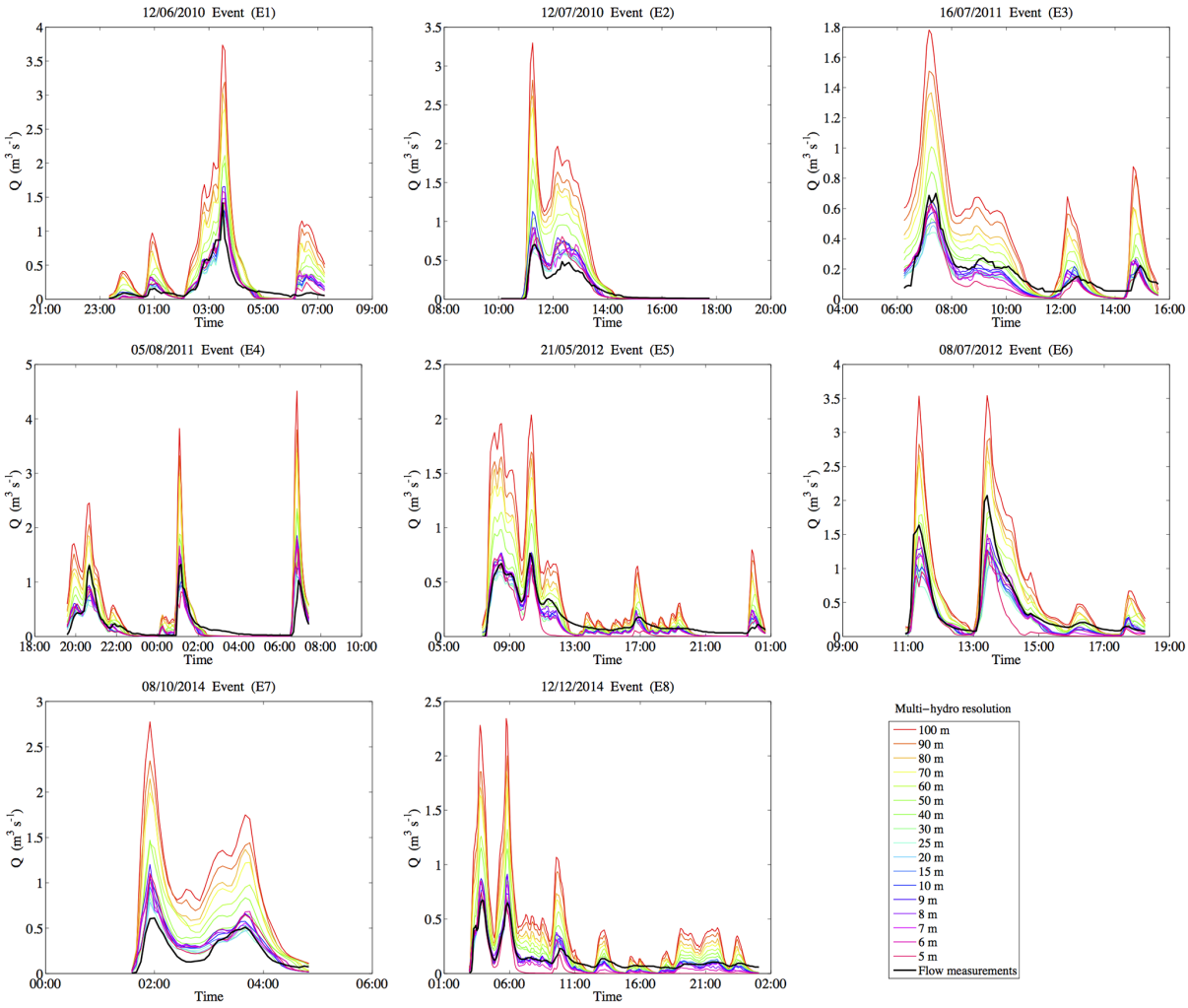

Figure 3.12: Multi-scale modelling outputs compared with observed flow for the 8 studied rainfall events, showing the high sensitivity of Multi-Hydro response to the spatial resolution of the model. Figure from Ichiba et al. (2018).

discussed with the help of three standard and very commonly used indicators : (i) Nash-Sutcliffe efficiency (NSE), which measures how well the model outputs reproduce the observation outputs in comparison with a model that only uses the mean of the observed data. NSE ranges from $-\infty$ to $+1$. A value of 1 indicates a perfect model, while a value of zero indicates performance no better than simply using the mean. A negative value corresponds to performance worse than using just the mean. (ii)The coefficient of regression CR. The CR is used here to distinguish spatial scales for which the model overestimates and those for which the model underestimates the observed flow. The CR values range between $-\infty$ and $+\infty$ and a value of $CR = 1$ indicates an ideal match between the observed and simulated flows. If $CR < 1$, then the model is underestimating the observed flow, otherwise it is overestimating the observed flow.(iii) Peak flow relative error δr. It is used to address effects of scale changes on the modelled peak flow.

These indicators were computed for each of the 17 input resolutions and 8 rainfall events. They are displayed in Fig. 3.13 for each event, along with boxes corresponding to the 20 and 80 % quantiles which were added for indicative purpose. Contrary to the dynamic evaluation, a trend is visible for all indicators, with higher performance at higher resolution. A more detailed analysis can be done using the three scale regimes identified in the interpretation of the land use according to the resolution (Fig. 3.11).

- At large scales (100–40 m), i.e. for which the imperviousness coefficient C_{imp} is very high, all performance indicators are bad. NSE values range from -13.92 at 100 m scale to observed at 40 m scale. With an average value of 2, the CR indicator suggests that the model is highly overestimating observed flow. Same trend as C_{imp} is found. The relative error indicator of the peak flow (δr) confirms clear overestimation of the peak flow of up to 369 %. In fact, the catchment behaviour at this range of scales is consistent with the high imperviousness coefficient observed, which means that infiltration is limited and water is in the majority of cases rapidly routed to the sewer system.

- At medium scales (30–15 m): the model shows its best performance. NSE values range from 0.63 to 0.91, with an average around 0.79. The CR indicator takes values between 0.54 and 1.25, and its mean is around 0.89, suggesting a good fit between modelled and observed data. The relative error indicator (δr) ranges from -0.31 to 0.51 with a mean value around 0.17, meaning that the model still overestimates the peak flow by 17 % on average.

- At small scales (10–5 m): at this range of scales, the overall model performance remain good but potential trends with regards to scale are unclear. Indeed, some fluctuations are visible in the trend observed in statistics as a function of pixel size and there is no longer a clear improvement as for the medium scales. Such findings highlight some specific issues related to high resolution modelling : (i) Quality of the data. Accurate topography data, which is the main driving force for surface water movements, is required; and here it was simply interpolated from the 25 m available resolution. As pointed out in Ichiba et al. [98], there is a great portion of missing land use data at high resolution. Even if the data was available at 25 cm scale, approx. 20 % of the area was missing. Given that the physical properties defined for each pixel depend exclusively on its land cover, this obviously generate issues at high resolution. At large scales, the problem associated with "no data" pixels has a much more limited influence, because large pixels usually include a large portion of well-identified land cover classes, like roads and houses. (ii) Mismatch between rainfall input space-time resolution and model resolution. Indeed, model performance strongly depends on rainfall input resolution [182, 167, 67, 79]. Here uniform 5-min data coming from a rain gauge was applied, in order to focus on the sensitivity model performance to model input resolution. Rainfall data space-time resolution should be tailored to model resolution for best performance (iii) Numerical instabilities. Indeed numerical schemes can be sensitive to small scale fluctuations and they should be better quantified in future investigation.

3.3.2 Stochastic infilling of missing data : the binary case of imperviousness

This section is mainly based on Gires et al. (2021), in which additional details can be found.

Overall purpose

Missing data, which can arise due to measurement devices malfunctioning, errors in measurements and natural hazards as well as budget reductions, are ubiquitous in hydrology. The topic is likely to remain crucial in the coming years given the overall tendency, on the one hand, to rely more and more on data-driven approaches, and on the other hand to physically model catchments at higher and higher resolution. Both approaches require large amounts of high-quality data. Indeed, this is a topic with relevance beyond the field of hydrology [61]. This explains the motivation of the general, mathematical approach developed by [190] to define a multifractal objective analysis, based on multifractal conditioning and interpolation.

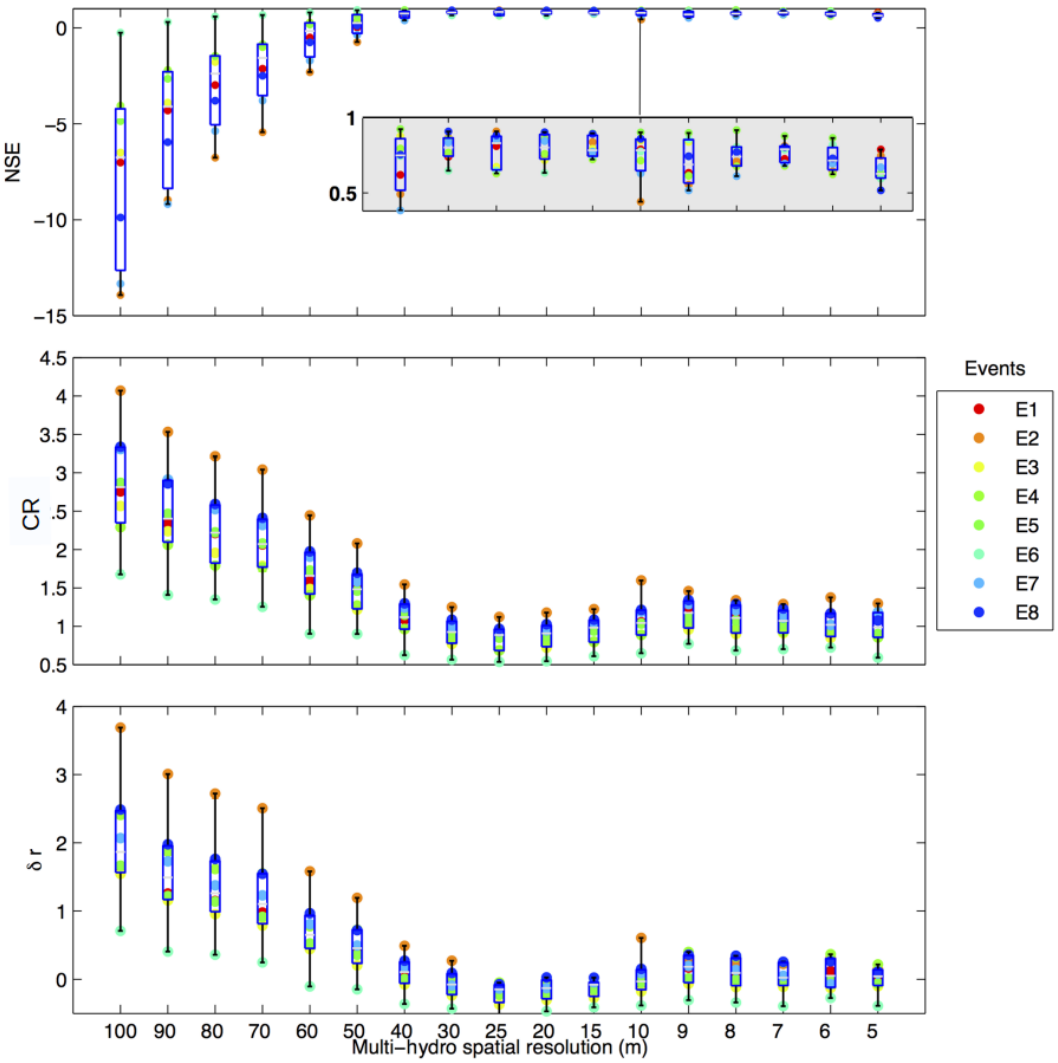

Figure 3.13: Performance indicators NSE, CR and δr estimated from Multi-Hydro modelling output obtained at the 17 spatial scales with respect to observed data. Figure from Ichiba et al. (2018).

Given the increasing need for data without gaps, significant efforts to develop infilling techniques have been made. It should be noted that the action of filling missing data is also called imputation, completion, reconstruction or patching, depending on the authors and/or fields of application. The interested reader is referred to a recent review on the topic of missing data in hydrology by Aissia et al. [1].

As reminded in the introduction, an comprehensive approach to deal with missing/incomplete data in model inputs is to rely on ensemble simulations. It consists in generating not only a single deterministic time series / fields without missing data; but an ensemble of realistic ones and simulate a corresponding ensemble of model outputs. This paradigm shift was initiated in the meteorology community with the increase of computer power and is now spreading to hydrology. This enables a proper quantification of the uncertainty associated with a given missing data which is seldom done although much needed Bárdossy and Pegram [19], Aissia et al. [1]. I widely used this approach during my PhD and few years after in order to quantify the uncertainty associated with unmeasured small scale rainfall variability.

In this subsection, it is implemented using the conditional β-model described in section 2.4 in order to fill the missing impervious data on the case study of Jouy-en-Josas (section 3.1.2), and quantify the associated hydrological uncertainty. The conditional β-model preserves the key property of scale invariance and enables generation of numerous stochastic realisations. This field was chosen for both technical and practical reasons. Indeed, there is a growing demand for high-resolution (typically a few metres to tens of metres) hydro-dynamic modelling by researchers and stakeholders to improve the understanding and management of storm water in urban areas, and notably for accurate prediction of local pluvial flooding. However a current limitation is the fact that when dealing with high resolution on the order of a few metres, there is often a lot of missing data with regard to land cover, topography or soil properties Ichiba et al. [98]. In the meantime, imperviousness is of paramount importance in cities because impervious areas are responsible for rapid runoff that can generate surface flooding. In order to retrieve the binary framework needed to implement the developed conditional β-model two classes of pixels are distinguished : impervious pixels (i.e. here the pixels corresponding to gully, road and building), and pervious ones (i.e. here forest and grass).

Filling the imperviousness gaps with the conditional $\beta-$model

As said before, we implement the conditional β-model on the land use representation of the Jouy-en-Josas catchment. Fig. 3.14 (left column) displays a representation of the studied catchment with pixels of size 2 and 10 m respectively. The pixels in yellow correspond to data not available (which were simply filled with 'grass' in Gires et al. [82]). They represent 16.2 % of the pixels with 2 m pixels and 5.6 % with 10 m pixels. As it can be seen, they are primarily located within the urbanized portion of the catchment around the buildings, meaning that they could typically correspond to small gardens attending the individual house or private drive ways / parking lots. Such areas were not identified on the available GIS data (BD ORTHO, professionnels.ign.fr). This suggests that the automatic treatment performed to obtain the data from the available areal photographs does not enable to distinguish such type of area at the required resolution. Improving the treatment of such pictures to refine the data could be a relevant approach, but it is another field of expertise. Here, the implementation of the conditional β-model will enable to distinguish in a simplified binary way whether these pixels are pervious or impervious, and hence behave in a very different manner hydrologically speaking.

The geometrical set consisting of the impervious area of this catchment was found to exhibit an excellent scaling behaviour, with a fractal dimension equal to ≈ 1.7 (Gires et al. [74, 82], section 3.2.2. Such fractal behaviour suggests that it is possible to use the developed conditional β-model to fill the missing data. This was achieved after overcoming few technical details associated with the required dyadic size of studied area [84].

Fig. 3.14 (right column) displays a representation of the studied catchment with pixels of size 2 and 10 m respectively, with missing data filled using the 'most probable' approach. The missing data found to be impervious ('alive' in the β-model) is in blue, while the one found to be pervious ('dead' in the β-model) is in green (considered to be grass). As it could be expected, given the lower initial amount of impervious pixels at 2 m and the priority rule set, a greater portion of pervious areas was generated at 2 m. The quality of the scaling behaviour is slightly improved with this most probable field (r^2 goes from 0.998 to 0.999), and the fractal dimension estimate is slightly increased as well from 1.72 to 1.76.

The current version of the hydro-dynamic model only enables to have a limited number of land use classes. Hence, it was chosen to use the binary output of the conditional β-model in the form of the 'most probable' field. However, in terms of perspectives, with models having a different approach to represent land use distribution, the actual probability distribution of the output for a given pixel could be used. Here, for example, it could mean using the average output over numerous realisations to define a given level of imperviousness for each pixel; rather than the binary approach presented here. The purpose of this is simply to illustrate the other possibilities of the developed conditional β-model. Their actual implementation should be carried out in further investigations.

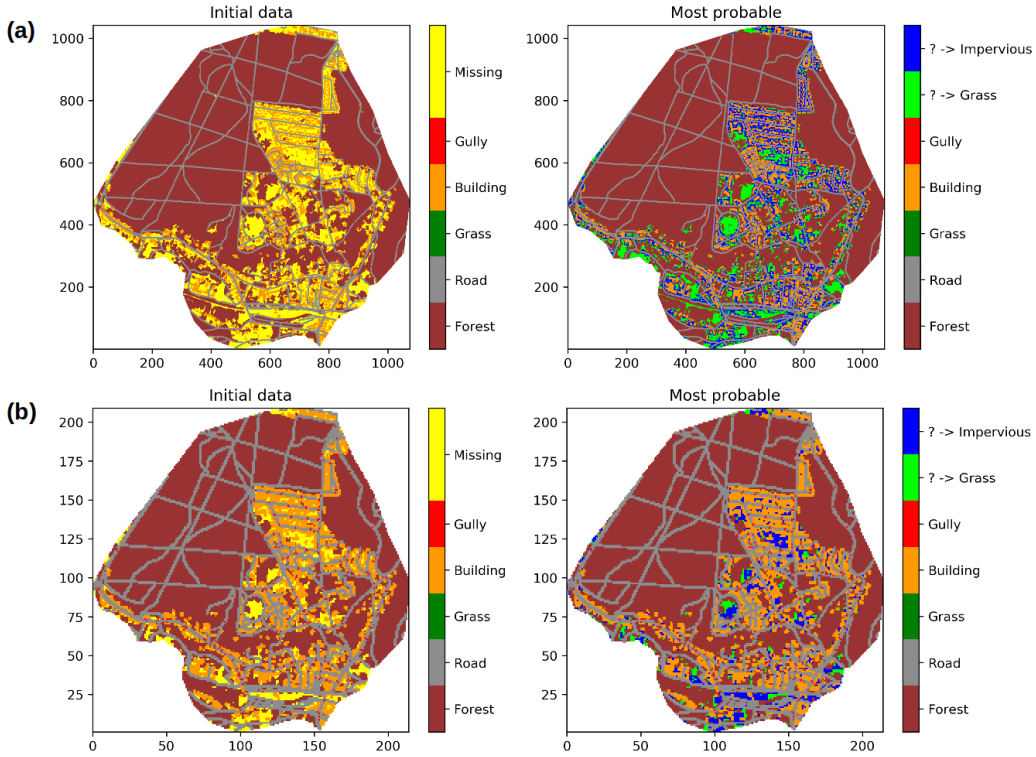

Figure 3.14: (a) Representation of the Jouy-en-Josas catchment in Multi-Hydro with 2 m pixels. Left : 'Initial' data, hence with missing data. Right : 'Most probable' field where missing data has been replaced by either grass or an impervious area using the developed conditional β-model. (b) Same as in (a), but with pixels of size 10 m. Figure adapted from Gires et al. (2021).

Exploring hydrological consequences

Hydrodynamic simulations were then carried out with the help of the Multi-hydro model with pixels of size 10 m. The initial land use field with missing data taken as grass, along with the 100 realisations of realistic ways of filling the 5.6% of missing data, and the most probable field were used as input. All the other inputs are kept the same. A moderate rainfall event that occurred over roughly 10 hours on 9 February 2009 and resulting in an average cumulative depth of 9.4 mm over the catchment is used. Distributed C-band radar rainfall provided by Meteo-France is used. This event was already studied in Gires et al. [82] and presented in more details there.

As in Gires et al. [82], a pseudo coefficient of variation CV'_{95} is used to quantify the variability within the 100 realisations of the generated ensemble (here of land use distribution). For a given quantity, it consists in taking half of the difference between the 5 and 95 % quantile divided by the 50 % quantile (median) over the 100 realisations:

$$CV'_{95} = \frac{1}{2}\frac{Q_{0.95\%} - Q_{0.05\%}}{Q_{0.5\%}} \tag{3.3}$$

where Q is the studied quantity, here peak flow or maximum water depth for a given pixel.

The outcomes of the simulations are shown in Fig. 3.15. In panel (a) the flow at link #507 is visible. It drains the water from the North of the catchment. A zoom during the peak flow is in Fig. 3.15.b. The relative difference at the time of peak flow between the 'initial' field and the 'most probable' one is of 2%. The uncertainty range is limited and the CV'_{95} between the various realisations is of only 0.5%. These variations are limited, but given that there was only 5.6% of missing data, it was expected. Implementing it with the 2 m representation for which there are 16.2% of pixels which data is missing would yield stronger variability.

In term of maximum depth for each pixel, the difference between the 'most probable' case and the 'initial' one is displayed in Fig. 3.15.c. It reaches 2 cm and is obviously mainly located on the pixel corresponding to missing data. The CV'_{95} for this maximum depth is displayed in Fig. 3.15.d. It can reach more than 5% for some pixels, in the area that concentrated the more missing data.

3.4 Multifractal quantification of output fields' variability

This section is mainly based on Gires et al. (2018), in which additional details can be found. It corresponds to a work primarily done by Jean-Baptiste Abbes during an internship.

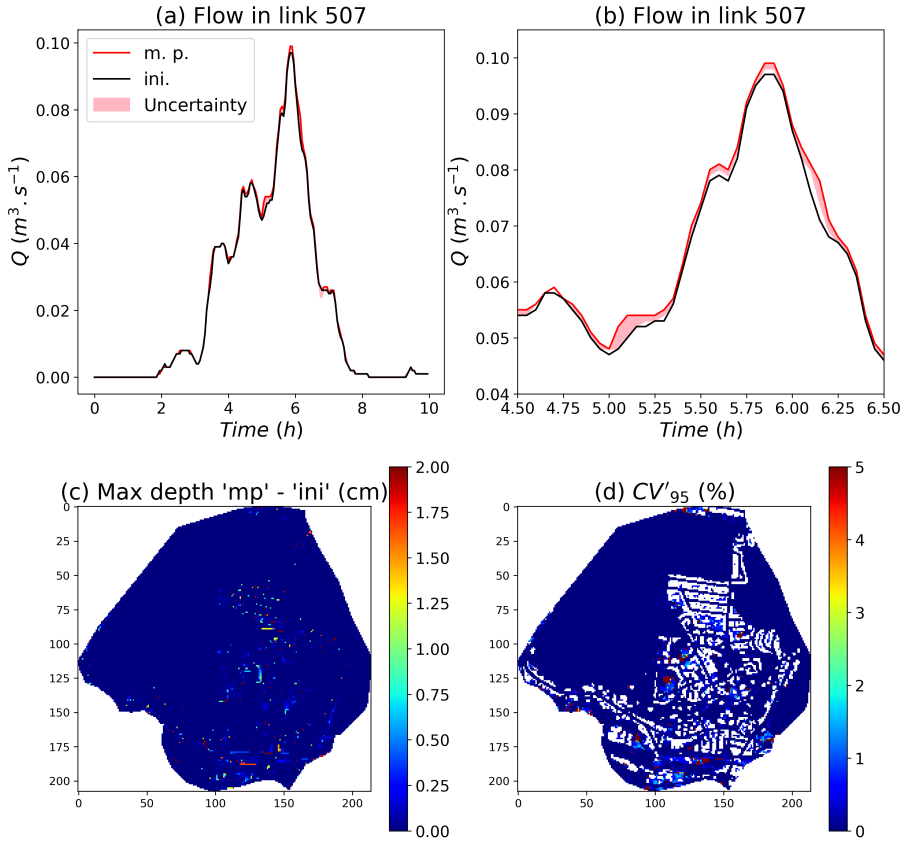

Figure 3.15: Outcome of the hydrodynamic simulations carried out with the Multi-Hydro model. 'Initial' land use data with the missing data taken as 'grass' is used as input along with the 100 realisations of realistic ways of filling the 5.6% of missing data, and the 'most probable' field. (a) Simulated flows at link #507. Time is indicated since the beginning of the simulation. (b) Zoom of (a) near the peak flow. (c) Map of the difference of simulated maximum water depth between simulations carried out with the 'most probable' field and the 'initial' one. (d) Map of the CV'_{95} coefficient for the maximum water depth.. Figure from Gires et al. (2021).

3.4.1 Overall purpose

In previous work [71], I used UM tools to analyse the flow simulated with the help of a semi-distributed model. Here it is suggested to go a step further and to study surface flow which are often not studied in details. For example, in case of overflow most models simply consider a volume output from the sewer system and deduce a local water depth, but the dynamical behaviour of the water added on the ground is not addressed. Basically, urban surface flow is not commonly perceived as a geophysical process and is therefore not addressed with geophysical tools capable of grasping its intrinsic complexity visible across all scales. Indeed, it results from the non-linear interactions between the highly spatially and temporally variable rainfall field, the topography and the strongly inhomogeneous land use cover.

To the knowledge of the authors it has never been used to study either surface runoff flow (urban drainage) or surface flow in general including stream rivers. Investigating the potential multifractal features of surface flow and notably whether it inherits rainfall features is the main purpose of the paper used as basis for this section and constitutes its main novelty. It is a contribution to the better understanding of urban flood processes which are to become a more and more severe issue. Indeed, the combined effects of a growing urbanisation - approximately 80% of Europe's population will live in cities by 2020 (https://www.eea.europa.eu/articles/analysing-and-managing-urban-growth) - and potential increase of extreme events as a consequence of climate change [100, 150] expose more and more people to surface pluvial flooding. Pitt [181] carried out a review on flood events in the United Kingdom and showed that two thirds of the flood related damages were caused by surface water flooding.

The study in carried out on the Jouy-en-Josas case study (see section 3.1.2).

3.4.2 UM analysis of surface flow with actual rainfall

Multifractal analyses of overland water depth during rainfall events are presented in this section for two heavy rainfall events that occurred on 14-07-2010 and 15-12-2011. The total depth, duration and maximum catchment average intensity over 5 min is of 43.2 mm, 17 h and 52 mm/h for the 14-07-2010 event, and of 26.2 mm, 13 h and 24 mm/h for the 15-12-2010 event. C-band radar data provided by Meteo-France with a 1 km and 5 min resolution is used.

Figure 3.16.a displays the spectral analysis of the water depth for the 14-07-2011 event. Maps of water depth for each time steps during the event are used to carry out 2D ensemble analyses. The quality of the scaling is low, with a coefficient of determination for the linear regression equal to 0.42. The fact that the spectral slope is close to zero (β is found roughly equal to 0.2) indicates that the field is conservative, i.e. its mean is conserved across scales. It is therefore possible to implement directly on the field a TM analysis. Figure 3.16.b shows the TM ensemble analysis performed over all the time steps of the same 14-07-2011 event. Two scaling regimes can be identified: a small scales regime from 10 m to 80 m (right part of Fig. 10.b) and a large scales regime from 80 m to 1280 m (left part of Fig. 3.16.b). The coefficient of determination r^2 of the linear regression for $q = 1.5$ in Fig. 3.16.b is taken as an indication of the quality of the scaling. The scaling from small scales (10 m - 80 m) is much more robust than for large scales (80 m to 1280 m), as illustrated by the r^2 equal to respectively 0.99 and 0.91. Given the low quality of the scaling for large scales, UM parameters estimates will not be reported and discussed for this regime because they are not reliable. Furthermore, small scales are crucial for surface runoff because it is at these scales that it is generated into the drainage system.

The location of this break at approximately 80 m indicates a possible physical interpretation. Indeed, it is the same location as the break in the fractal analysis of the sewer network (section 3.2.2) and corresponds roughly to the inter-distance between roads. This would mean that this break is driven by the influence of the collection of water by sewer network. The more robust scaling behaviour for surface flow is found for the scales for which the sewer network does not behave yet as network but as isolated linear pipes. Before going on, it should be mentioned that numerous pixels have very small depth, for which the model uncertainties might be great. These zeros values or spurious ones close to zero will affect the scaling analysis for small moments (typically $q \leq 0.5$) through a multifractal phase transition (see Gires et al. [69], for a detailed analysis of this issue). Here the influence of this bias does not extend to moments close to 1 around which the estimates of UM parameters are carried out, meaning that they are not affected by this issue.

Although intrinsically less robust since scaling properties are statistical ones requiring numerous data to be properly observed, TM analyses were also carried out independently on each sampling time step of Multi-Hydro (3 min in this paper). The purpose is to see whether there is an impact of the current rainfall rate on it. Figure 3.17.a and b display for the 14-07-2010 event the temporal evolution of both the rainfall rate and the r^2 for $q = 1.5$ in the TM analysis for the two regimes identified in the ensemble analysis, i.e. small (10 m – 80 m) and large scales (80 m – 1280 m). For this event, two rainfall peaks are observed, and they both result in a sudden loss of the scaling quality, more pronounced for large scales than small ones. For the first peak (yellow bars on Fig. 3.17) the decrease of r^2 lasts approximately 20 min, while it lasts only few minutes for the second peak (red bars on Fig 3.17). In both cases the quality of the scaling behaviour improves again over few tens

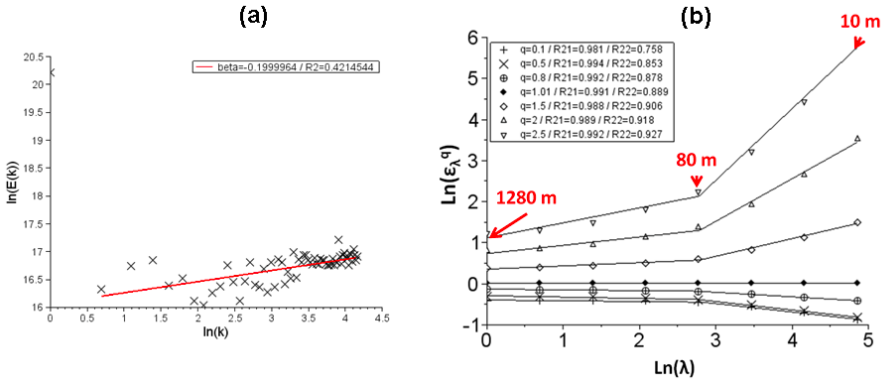

Figure 3.16: For the 14-07-2010 event and 2D ensemble analysis over all the time steps: (a) Spectral analysis, i.e. Eq. 2.2 (5) in log-log plot; (b) TM analysis, i.e. Eq. 2.6 in log-log plot. Figure from Gires et al. (2018).

of minutes. The physical meaning of such loss is not clear, but could be due to a bad representation of the surface flow process during intense rainfall (it might take some time to retrieve a realistic surface flow simulation following a sudden change in rainfall input), a bias in the geometrical distribution, or an intrinsic feature of the process. For the latter, a possibility is that during intense rainfall period, the surface flow exhibits more directly the rainfall features than its intrinsic ones which are retrieved once the flow process has "adapted" to the new conditions. This would explain both the loss of scaling quality and why scaling properties closer to rainfall ones are observed during these short periods. Analysis with a higher resolution model would be needed to further investigate this issue, which would also enable to have access to a wider range of small scales.

Similar features are retrieved for the other studied event (15-12-2011). Finally, it should also be mentioned that similar results are also found when performing the analysis on the North-South or West-East 1D-samples, which means that the preferential slope of the catchment (North-South) does not seem to have an influence on the scaling features of the simulated water depth. Both raw radar data and downscaled rainfall fields to 12 m in space and 20 s in time were used. In terms of scaling quality, very similar results are also found with both rainfall inputs suggesting a limited impact of small scale rainfall variability on these features.

UM parameters retrieved on the maximum water depth were computed for small scales, and are displayed in Table 3.1 for the two events (14-07-2011 and 15-12-2012) and for simulations with raw radar data and also a realisation of downscaled rainfall field with $\alpha = 1.8$ and $C_1 = 0.1$ (other realisations yield very similar results). The temporal evolutions of α and C_1 for the 14-07-2011 event are shown in Fig. 3.17.c and d. It appears that the UM parameters are also affected by the "jumps" that were noticed on r^2 in Fig. 3.17.b. Indeed after an intense period, sharp increase of α and decrease of C_1 are noticed. These pronounced variations mean that the values obtained with ensemble analyses should not be over-interpreted. Nevertheless few comments can be made. First the values of C_1 are much greater than the ones reported for rainfall (typically 0.1-0.3 at small scale) meaning that significant levels of water depth are much more concentrated than the rainfall field, which reflects the influence of the physical processes associated with surface flow on the transferred field, notably the flow concentration. The most relevant one is the topography that routes water through specific paths and tends to concentrate it. Second the values of UM parameters are quite different between the two events. These differences are much greater than the ones observed on the rainfall fields (see Ichiba [97], for a detailed analysis of these storms) at small scales. This suggests that the large scales rainfall pattern has a strong influence on the retrieved parameters. Indeed, the topography and small scale rainfall features are the same between the two simulations; the only difference is the large scale rainfall features. Thirdly the values of γ_s are rather similar for both events (the differences between α and C_1 tend to compensate themselves).

The temporal evolutions of the UM parameters obtained by inputting raw and downscaled rainfall data are very similar. The differences are slightly more pronounced on the values computed on ensemble analysis but as previously said this should not be over-interpreted given the strong variations visible in the temporal analysis. This similarity highlights the low influence of small scale rainfall variability on the retrieved parameters which seems to be more dependent on features associated with surface flow process itself or large scale rainfall.

3.4.3 Sensitivity to small scale rainfall features

In order to test the sensitivity of the results to small scales rainfall features, synthetic rainfall fields with various sets of known parameters are used as input to Multi-Hydro simulations. More precisely the pseudo-events tested last 30 min with an average intensity of 10 mm/h. Three pairs (α; C_1) of parameters are tested: (1.8; 0.1), (1.8; 0.05), (1.4; 0.1). Figure 3.18 displays the temporal evolutions of the rain rates, r^2, α and C_1 for water depth

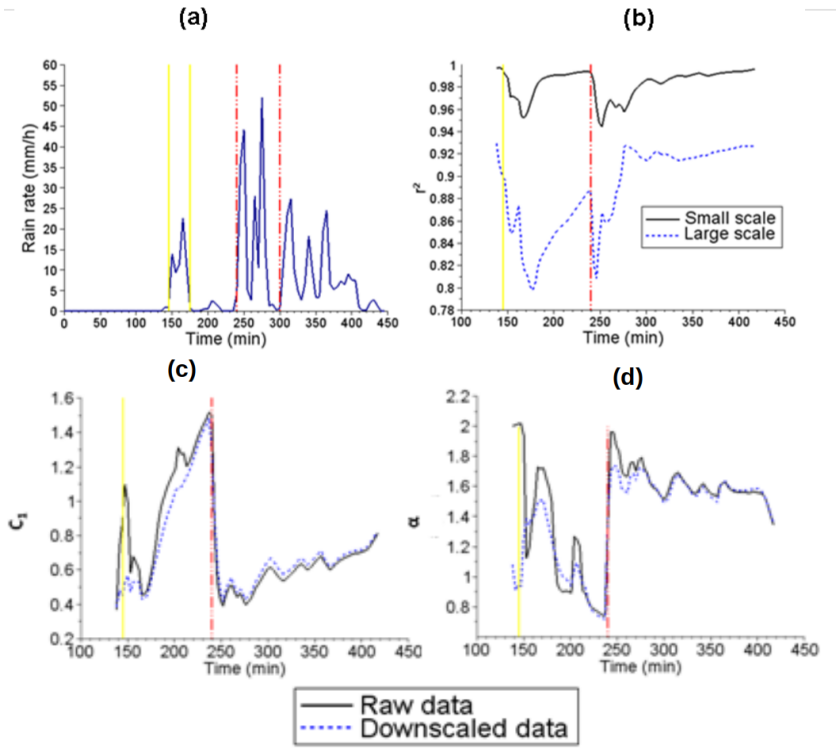

Figure 3.17: For the 14-07-2010 event. (a) Temporal evolution of the rain rate; (b) Temporal evolution of the r^2 for $q = 1.5$ in the TM analysis for the two regimes identified in Fig. 3.16. (c,d) Temporal evolution of the UM parameters α and C_1 of the maximum water depth field over 3 min for small scales (10–80 m). Figure from Gires et al. (2018).

Table 3.1: UM parameters for small scales (10 m–80 m) computed with the help of a 2D analysis with either raw radar data or a realisation of downscaled rainfall field (with $\alpha = 1.8$ and $C_1 = 0.1$) as rainfall input for the 14-07-2010 and 15-12-2011 events. Table from Gires et al. (2018).

Event	Rainfall input	α	C_1	γ_s
14-07-2010	Raw radar data	1.55	0.62	1.52
	Downscaled rainfall	1.25	0.90	1.68
15-12-2011	Raw radar data	0.95	1.42	1.74
	Downscaled rainfall	0.99	1.22	1.65

for the three synthetic rainfall events.

The temporal evolution shows the same general tendency as the one observed with the real events. A loss of scaling quality is observed during the event itself, and it improves afterwards. α and C_1 have a constant behaviour during the rainfall, while they decrease and increase respectively after the rainfall has stopped. The comparison of the UM parameters for the overland maximum water depth shows that they do not seem to depend on the small scale rainfall variability in this case. α is constant around 1.4 while C_1 is constant around 0.6 during the rainfall. γ_s is again constant around 1.7 on average. The rainfall UM parameters do not seem to modify the structure of the overland flow, and its geometrical distribution. Successive simulations with the same parameters for synthetic rainfall yielded same results. A physical explanation of the C_1 parameter could be that during the rainfall, the surface flow is more homogenous due to a ubiquitous input of water. UM parameters on water depth are thus closer to the rainfall ones (small C_1). However after the rain has stopped, the disparities of simulated water depth are increased due to predominant pathways (roads) or topographic depressions where the water can accumulate. The greater C1 after the event could reflect this fact. The smaller values of α mean that the disparities among the areas where water remains tend to decrease after the rainfall event. This study seems to highlight the fact that UM parameters α and C_1 for water depth are rather relying on the large scale structure of the rainfall and on the catchment features, while the maximum observable singularity γ_s is conserved for all events. Further studies could infirm or confirm the fact that γ_s depends on the studied catchment. The temporal evolutions of the UM parameters also deeply rely on the rainfall rate. Synthetic events with block structures enabled to stand out rather simple general tendencies. They become more complex

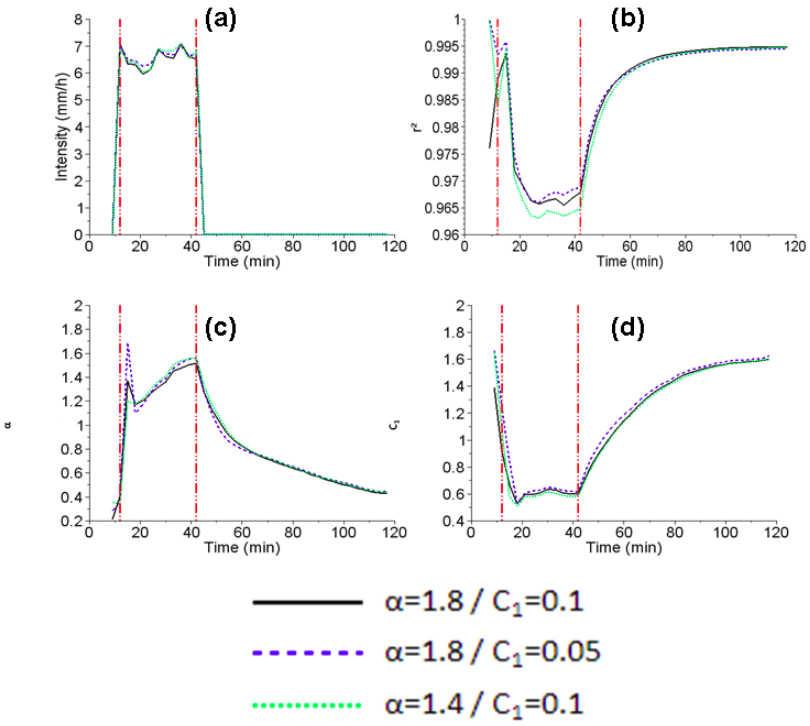

Figure 3.18: For three synthetic rainfall events with different sets of UM parameters; temporal evolution of the average rain rate over the catchment (a), and for the simulated overland maximum water depth, r^2 (b), α (c) and C_1 (d) for small scales (10 m–80 m). Figure from Gires et al. (2018).

with real rainfall, when the intensity has a higher temporal variability. The temporal evolutions of the UM parameters also enable to quantify a catchment response time. Due to the sampling time step of the simulations, the uncertainty associated with the response is of 3 min. Still, it can be noted that in urban catchments (or semi-urban here), the response time of water depth UM parameters to the beginning of a rainfall or to an important peak of intensity is almost non-existent. This is due to the presence of impervious area over which rainfall directly transfer into surface runoff.

Chapter 4

TARANIS platform

4.1 Overall concept and purpose

The purpose of the TARANIS platform is to put microphysics at the service of the measurement and modelling of precipitation. By microphysics, I mean the size and speed properties of hydrometeors (drops, snow flakes, hailstones, etc.). Indeed rainfall is a "collective" phenomenon emerging from numerous drops. Hence, understanding the relation between the physics of individual drops and that of a population of drops remains an open challenge, both scientifically and at the level of practical implications.

The major 5-year objective of the activities around the TARANIS platform is to develop a 3D+1 (i.e. spatio-temporal) model of drop fields including a coupling with atmospheric turbulence and to exploit it in the corresponding applications. In order to be relevant, this model must be able to take into account the variability of the drop size distribution and to cover a volume at least comparable to a radar gate (typically at least a cube of a few tens of meters on a side) . This model will in particular make it possible to pursue and amplify a central approach of this platform, which is to strive to best mimic the instrumental measurement at the drop scale. This is the overall approach underlying TARANIS, i.e. to improve not only the measurement itself, but also the quantification of the corresponding uncertainty.

This platform is based on a triptych to be advanced in parallel (see Fig. 4.1 for a summary scheme): (i) An observatory. This involves collecting precipitation data over long periods and in different places with disdrometers. These are instruments that give access to the size and speed of the drops passing through their measurement surface of a few tens of cm^2. By collection, we naturally mean the collection itself, but also the preparation of a database that can be easily exploited by different people. Acquisition of instruments began in 2013 with RainGain, Blue Green Dream and RadX@IdF projects as well as the Chair "Hydrology for resilient cities". More recently they were continued thanks to RW-Turb project which I am coordinating. It notably enabled an extension to wind measurements. (ii) Instrumental developments. The purpose is to improve the existing instruments, i.e. having a critical and constructive look at the measures provided. Particular attention should be paid to the uncertainties of the various measurements. This concerns both disdrometers and the improvement of measurement algorithms with radars which do not measure rainfall directly (see section 3.1.1). (iii) Methodological developments. The purpose to suggest innovations making it possible to exceed the current limits and thus to improve the precision of the instruments and the exploitation of the data. A focal point is the previously mentioned 3D+1 drop field model. There is also the idea of shifting to probabilistic measurements; i.e. providing the user not with a single deterministic measure, but rather with a probability distribution. This is a paradigm shift that has already taken place in weather forecasting since the 2000s, and which should be extended to measurement itself. This will require working with sets of possible values in the corresponding processing chains.

4.2 An observatory

The TARANIS platform now operates 6 disdrometers (5 Parsivel^2 and 1 PWS100), 3 3D sonic anemometers, and 3 mini-meteorological stations. Their overall functioning as well as the 9 measurements campaigns in which they ave been involved are described in the following subsections. Some of them are based on three data papers presenting measurement campaigns and corresponding data base (Gires et al. [75], Gires et al. [77] and one on RW-Turb wind farm campaign which has been submitted.

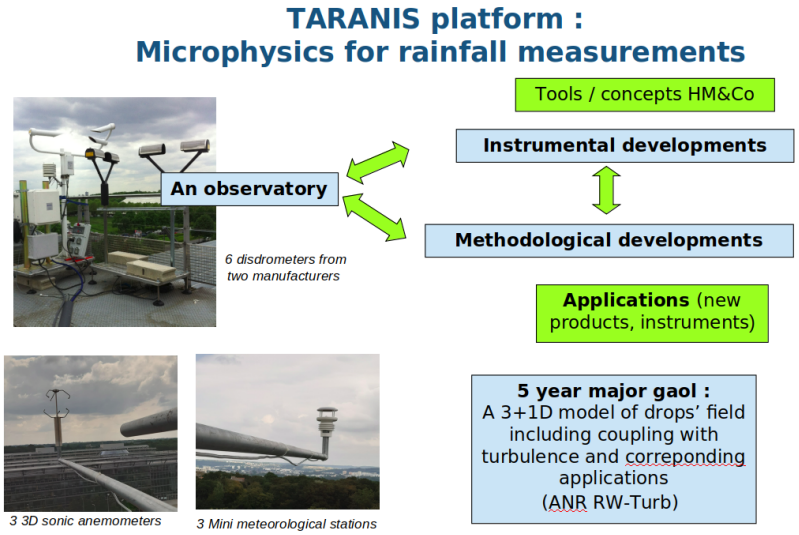

Figure 4.1: Illustration of the overall stucture of the TARANIS platform

4.2.1 Disdrometers and associated outputs

The two devices are optical disdrometers operating with different principles. The goal of this section is only to briefly explain how the two devices work and highlight the main differences. The interested reader is then referred to papers and manufacturer documentation for more information. Fig. 4.2 illustrates the functioning for both devices.

The OTT Parsivel^2 is made of a transmitter generating a laser sheet and a receiver aligned with the transmitter. When a drop falls through the sampling area of roughly 50 cm^2, the laser beam is partially occluded and the intensity of the received signal decreases. Then the size (more precisely the equivolumic diameter) and fall velocity of the drop is assessed from the amplitude and duration of the decrease in received intensity. An ellipsoidal shape model for the drops with a standard relation between the axis ratio and the equivolumic diameter is assumed in the process. More details can be found in Battaglia et al. (2010) or in the device documentation (OTT, 2014).

The PWS100 configuration is different. It is made of a transmitter that generates four horizontal parallel light sheets, and two receptors which are not aligned with the transmitter. One is set on a vertical plane with an angle $\theta_D (= 20^o)$ and the other is set on a horizontal plane with the same angle θ_D. When a drop falls through the sampling area of size $S = 40\,\text{cm}^2$ a portion of the light is refracted and reaches the receptors. The signal received by each receptor contains four consecutive peaks associated with each laser sheet. From the delay between these peaks, the fall velocity of the hydrometeor is assessed. Then due to the refraction inside the drop, the signal will reach the vertical receiver slightly before the horizontal one. From this time shift the diameter of the drop can be estimated. Computations are carried out assuming a spherical shape, and a correction accounting for oblateness is then implemented. More details can be found in Ellis et al. (2006) or in the device documentation (Campbell-Scientific-Ltd, 2012). Actually the authors could improve the oblateness correction of the PWS100 rationale (see section 4.3.1).

The main output provided by the disdrometers is a matrix containing the number of drops recorded during the time step Δt (30 s here) according to classes of equivolumic diameter (index i and defined by a centre D_i and a width ΔD_i expressed in mm) and fall velocity (index j and defined by a centre v_j and a width Δv_j expressed in $m.s^{-1}$). The classes' tables are slightly different for the two devices but both are more refined for smaller drops and velocities than larger ones.

From this matrix, it is possible to compute the rain rate (in mm.h^{-1}) for each time step as :

$$R = \frac{\pi}{6\Delta t} \sum_{i,j} \frac{n_{i,j} D_i^3}{S_{eff}(D_i)} \tag{4.1}$$

where $S_{eff}(D_i)$ is the sampling area of the device (expressed in mm^2) and Δt is in h. In the data presented in the paper, it is slightly modified according to the drop size to account for edge effects for large drops. For the Parsivel^2, we used $S_{eff}(D_i) = L(W - \frac{D_i}{2})$ where $L = 180$ mm and $W = 30$ mm are respectively the length and width of the sampling area ($LW = 54$ cm^2) (OTT, 2014). The user has access to the raw data (i.e. the matrix), so he/she can decide on whether to use this correction.

Finally, the Drop Size Distribution (DSD), denoted $N(D)$, can be computed from disdrometer data. It is

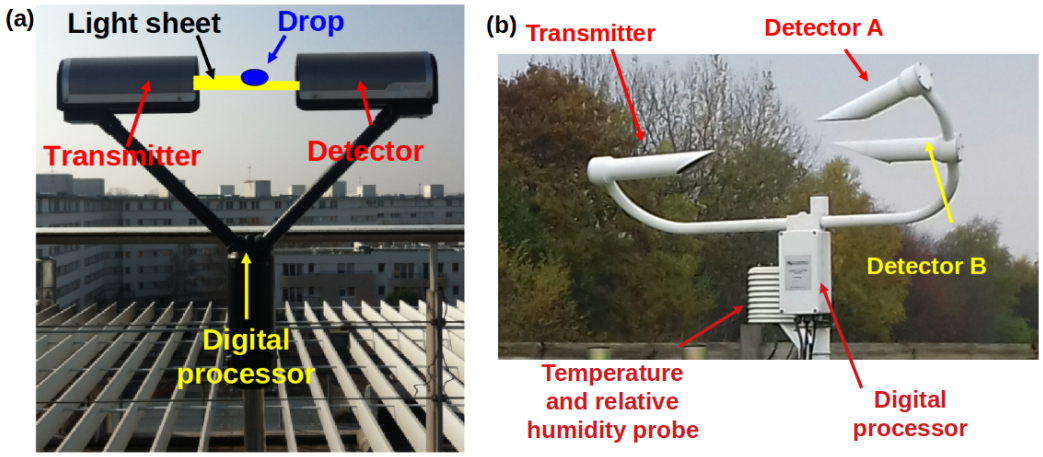

Figure 4.2: Illustration of the overall functioning of disdrometers. (a) OTT arsivel[2] (b) Campbell Scientific PWS100.

expressed in $m^{-3}.mm^{-1}$ and $N(D)dD$ is the number of drops per unit volume (in m^{-3}) with an equivolumic diameter between D and $D + dD$ (in mm). It is actually possible to reconstruct many quantities relevant to researchers and practitioners from this DSD, since they are simply moments of the DSD, i.e. they can be written as weighed integrals of the DSD ($\int_0^{D_{max}} f(D)N(D)dD$, where $f(D)$ is a function of the diameter D, typically a coefficient multiplied by a power of D). Actually, it is a discrete DSD $N(D_i)$ that can be derived for a given time step from the raw matrix as :

$$N(D_i) = \frac{1}{S_{eff}(D_i)\Delta D_i \Delta t} \sum_j \frac{n_{i,j}}{v_j} \tag{4.2}$$

$N(D_i)\Delta D_i$ gives the number of drops with a diameter in the class i per unit volume (in m^{-3}).

For the data presented here, we also included a filter suggested by various author [120, 226, 103] to remove drops that, according to their size and velocity, are considered as non-meteorological measurements. Practically hydrometeors whose velocity differs of more than 60% from the terminal fall velocity expected from its diameter and Beard's formula [10] are removed. Again, this filter is not implemented in the available raw matrices, so users are obviously free to use it or not.

4.2.2 3D-sonic anemometers and associated outputs

Two 3D sonic anemometers manufactured by ThiesCLIMA [220] are used in this measurement campaign. A 3D sonic anemometer is made of three pairs of transducers. Let us denote L the distance between two transducers and u_L the wind velocity along the corresponding axis. The transducers can be either transmitters or receivers of a sound pulse, and they constantly swap roles. It means that the device actually measures the travel time of a pulse of sound between the two transducers in one way or the other. If these times are denoted t_1 and t_2, with c being the local speed of sound in the air, then we have $t_1 = L/(c + u_L)$ and $t_2 = L/(c - u_L)$, which yields :

$$u_L = \frac{L}{2}\left(\frac{1}{t_1} - \frac{1}{t_2}\right) \tag{4.3}$$

Which does not depend on c. The wind velocity is assessed along the axis between each three pairs is assessed enabling to reconstruct 3D wind.

It is also possible to estimate c from :

$$c = \frac{L}{2}\left(\frac{1}{t_1} + \frac{1}{t_2}\right) \tag{4.4}$$

Since c mainly depends on the local temperature T, the latter can be derived using standard relationships assuming a dry air. This yield a virtual sonic temperature. Additional correction can be implemented to derive a corrected temperature accounting for relative humidity and pressure (see [220] for more details). Hence the 3D anemometers provide 3D wind measurement along with an estimate of temperature. The sampling rate used in this campaign is of 100 Hz for these devices.

4.2.3 Mini meteorological stations and associated outputs

Two mini meteorological stations manufactured by ThiesCLIMA [221] are used in this measurement campaign. They give access to the most relevant meteorologial parameters : wind speed and direction, air temperature, relative humidity, precipitation and brightness. The sampling rate used in this campaign is of 1 Hz for these devices.

The wind information is obtained thanks to a 2D sonic anemometer made of two pairs of transducers positioned at right angles in relation to each other. See section 2.2 for more details on the functioning of such device. Build-in sensor are dedicated to measurement of air temperature and relative humidity. The pressure sensor if based on a micro-electro-mechanical system. The latter three are protected within a shelter. Precipitation intensity is estimated using the signal reflected back from a mini Doppler radar. Brightness is measured with the help of four photo sensors, whose spectral sensitivity curve is tuned to the human eye's sensitivity. In addition, there is a GPS sensor.

4.2.4 Measurement campaigns

With TARANIS devices HM&Co took part to 9 measurement campaigns. They are summarized in Table 4.1 and pictures can be found in Fig. 4.3. They can can be gathered in four groups :

- Carnot / Radar tower : these are measurement campaign on the ENPC campus (East of Paris), either on the roof the Carnot building (thanks to the help of colleagues from the 'Departement Positionnement Terrestre et Spatial' of the ENSG) and the radar tower with disdrometers and more recently anemometers and meteorological stations. Meteorological data from the radar tower is now incorporated in the RadX@HM&Co platform as well (radx.enpc.fr/)

- IdF-Precip : it corresponds to a national measurement campaign organized by the precipitation working group of SIRTA (https://sirta.ipsl.fr/). It involved participation of HM&Co-ENPC, SIRTA/IPSL, LATMOS/IPSL (https://sirta.ipsl.fr/), LAMP - Univ. Clermont-Auverge (UMR 6061) LTHE (now IGE) - Univ. Grenoble Alpes (UMR 5564) and Meteo-France. Various in-situ and remote rainfall measurement devices were installed at SIRTA on the Ecole Polytechnique campus (South of Paris). C-band radar of Trappes (Meteo-France) as well as our X-band radar were also used.

- RW-Turb Pays d'Othe wind farm : It corresponds to a campaign carried out on a meteorological mast located on the Pays d'Othe wind farm which is operated by Boralex on the city of Les Sièges (Yonne, approx 110 km from ENPC campus). It is done in the framework of the RW-Turb project (supported by the French National Research Agency – ANR-19-CE05-0022). Six devices are used : two 3D sonic anemometers, two mini meteorological stations (manufactured by Thies), and two disdrometers (Parsivel 2 , manufactured by OTT). They are installed at two heights (approx. 45 m and 80 m), which enables to monitor potential effects of altitude will be used.

- Sense-City rainfall generator. This is a rather non-conventional indoor campaign to test the rainfall generator of the Sense-City climate chamber which is located on the ENPC campus. I will not go into the details of the results in this document. Full description of the campaign can be found in Gires et al. [77]. I can simply mention that a close look at the DSD revealed that the drops generated by the rainfall simulators are smaller than actual ones. More precisely the DSD is much thicker and centred on smaller drops. Furthermore, drops tend to reach the disdrometers with lower velocities than expected from standard relations according to their size.

4.2.5 Good practices for data collection

I designed and implemented the collection process of the data. It relies on the use of raspberry pi which are cheap mini-computers (www.raspberrypi.com). The use of such device is convenient because they are mini-computuer running an linux enabling basically to achieve any task. In addition, in case of failure, they are rather easy to change. Once, the operating system is installed, one simply has to copy to needed scripts on it and it is ready to use. I should mention, that despite there limited price (few tens of euros) they turned out to be robust. Some have been running for 6 years without any issue. The only failure to report was caused by a lightning strike. The collection process is organized as follow :

- The actual collection of the data is ensured by rasberry pi via USB ports mimicking serial port communication with measurement devices. Exchanges with devices are handled via dedicated scripts written in Python and running 24/7. The outputs, which corresponds to the raw data, are text files which are generated every 30 s or min depending in the devices.

Table 4.1: Involvement of TARANIS devices in measurement campaigns : summary table

Name	Location	Date	Devices
Carnot #1	ENPC Campus, Carnot building roof	09/2013 - 11/2016	2 Parsivel^2, 1 PWS100
IdF-Precip	Ecole Polytechnique Campus, SIRTA	11/2016 - 09/2017	2 Parsivel^2, 1 PWS100
Radar tower #1	ENPC Campus, Bienvenüe building	05/2017 - 06/2018	1 Parsivel^2
Sense-City rainfall generator	ENPC Campus, Sense-City climate chamber	09/2017 - 09/2017	2 Parsivel^2
Radar tower #2	ENPC Campus, Bienvenüe building	01/2019 - 09/2021	1 Parsivel^2
Carnot #2	ENPC Campus, Carnot building roof	12/2017 - 07/2020	2 Parsivel^2, 1 PWS100
RW-Turb wind farm	Pays d'Othe wind farm (Les Sièges, Yonne)	12/2020 - ...	2 Parsivel^2, 2 3D sonic anemometers, 2 mini meteo-stations
Radar tower #3	ENPC Campus, Bienvenüe building	09/2021 - ...	1 Parsivel^2, 1 3D sonic anemometer, 1 mini meteo-stations
Carnot #3	ENPC Campus, Carnot building roof	10/2021 - ...	2 Parsivel^2, 1 PWS100

- Once a day, in the middle of the night, the raw data of the previous day is converted into daily (or hourly) Python files or formatted .csv files which are easy to read for a user of the data. The raw data as well as the formatted one are then transferred into the servers of ENPC for robust and replicated storage.
- The same scripts generated a daily quicklook which summarizes the data collected the previous day. This daily quicklooks is sent via-email to me which enables to easily check in few seconds via that everything is running as expected. With such process, a failure is rapidly detected and actions to solve it can be initiated to avoid loosing to much data.
- Time of rasberry pi is checked and updated every night via a connection to a NTP (Network Time Protocol) server either on the campus or outside.

Data bases for all the measurement campaigns are structured in a similar way with the following main elements :

- Zipped raw data : the direct .txt files collected from the devices. Standard users are not expected to have to use these files, they are stored in case of a special need
- Daily (or hourly) Python files or .csv formatted. They contain the all the data that a standard user needs
- Python scripts to easily extract information from the previously mentioned files.
- A calendar and the associated daily quicklooks, which are described in details in the next section.

The purpose of this calendar and daily quicklooks is to provide the user with a rapid access to a visual overview of the available data and enable him/her to easily identify relevant periods / days according notably to the rainfall conditions. This is done through the an .html file providing an overview of the measurement campaign with a rapid access to the daily quicklooks. Fig. 4.4 displays a snapshot of it for three months of the RW-Turb wind farm campaign. The links (which are relative) direct daily quicklooks, which are the same as the ones sent to me via email. Fig. 4.5 shows an example of daily quicklook for this measurement campaign. It provides a summary of the recorded weather conditions for the day with (explained from top to bottom and left to right in a given row):

- The temporal evolution of the rain rate.
- The temporal evolution of the cumulative rainfall depth
- Indication of the missing data if any. Each line corresponds to a device. One minute time steps are used.
- The temporal evolution of the DSD $N(D)$ (middle left)

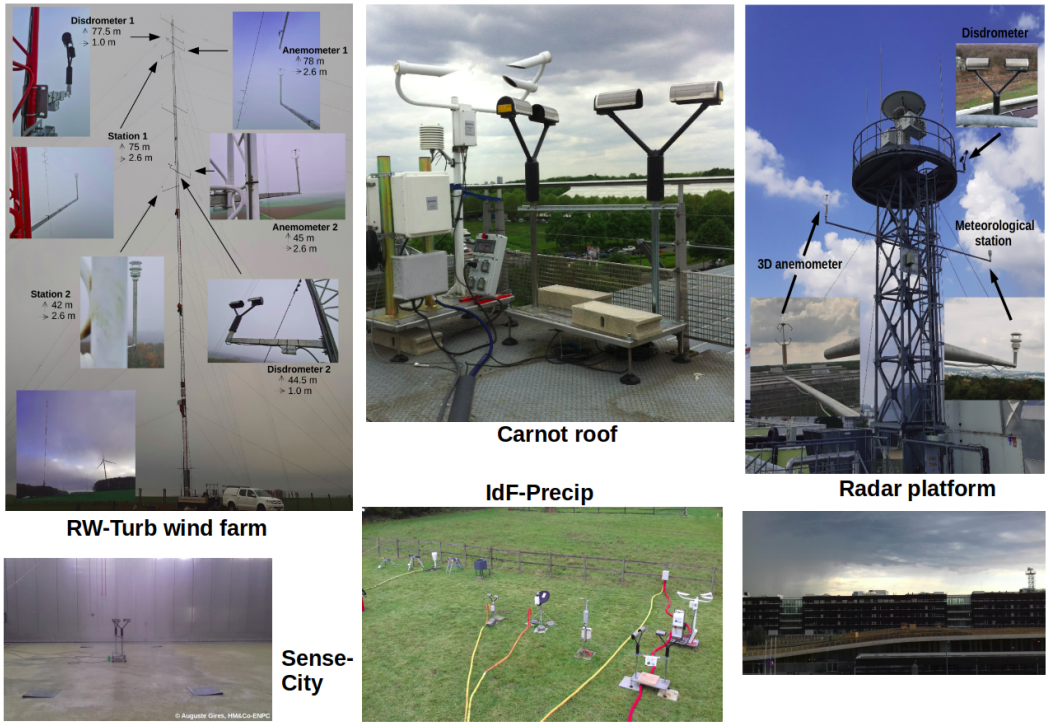

Figure 4.3: Pictures from the measurement campaigns in which TARANIS devices were involved.

- The temporal evolution of the total horizontal wind ($\sqrt{u_x^2 + u_z^2}$ for the various available devices. One minute time steps are used.

- The temporal evolution of the temperature (^oC) with the various available data. One minutes time steps are used.

- A map of the number of drops according the velocity and size classes (middle right; the solid black line is the curve corresponding to the relation between the terminal fall velocity of drops as a function of their equivolumic diameter obtained by Lhermitte, 1988)

- A wind rose using the horizontal wind measurements (u_x and u_y) of the two 3D sonic anemometers.

- The temporal evolution of the pressure (hPa) from the two meteorological stations. One minutes time steps are used.

- $N(D)D^3$ as a function of D (lower left, it was chosen to plot $N(D)D^3$ and not simply $N(D)$ because it is proportional to the volume of rain obtained according to the drop diameter hence providing the reader a greater immediate insight of the influence of the various drops size on the observed rainfall event)

- The temporal evolution of the vertical wind (u_z) from the two 3D sonic anemometers. One minutes time steps are used.

- The temporal evolution of the relative humidity (%) from the two meteorological stations. One minutes time steps are used.

Similar quicklooks are generated for the other campaigns with slight adaptation depending on the data available. For an easier use in the data base, the date and the name of the device or measurement campaign is directly included in the name of the files. Finally, measurement campaigns as well as data base and associated tools are described in details in data papers with samples provided to the community as an effort toward open-access in data. A first one was published in 2018 (Gires et al. [75]) on the Carnot building campaigns. A specific one dedicated to the Sense-City experiment was published in 2019 (Gires et al. [77]). One has recently been submitted on the RW-Turb campaign. This enables use of the data at HM&Co by various PhD student in their work. In addition, calendar and daily quicklook are available from our website with an automatic daily update.

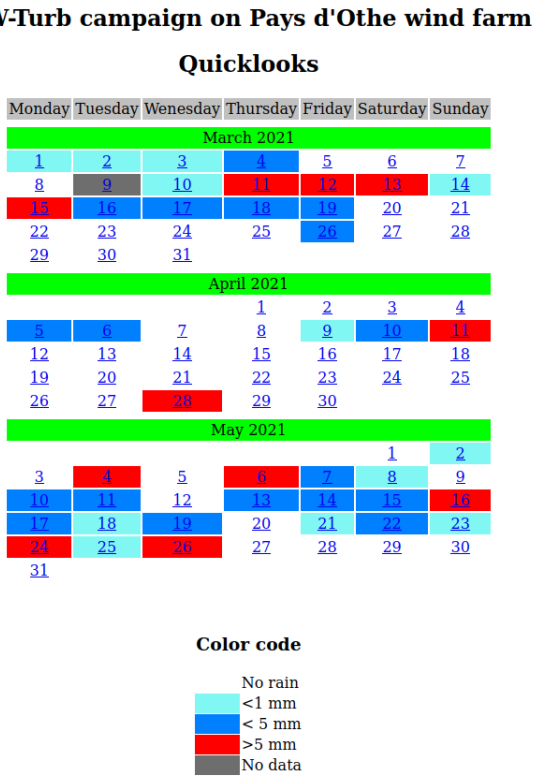

Figure 4.4: Snapshot of the calendar summarizing the March-May 2020 measurement campaign on the meteorological mast of the Pays d'Othe wind farm.

4.3 Instrumental developments

4.3.1 Patent to improve a device

After few months of measurements with TARANIS, we noticed that the average rainfall depth estimated by the PWS100 was basically almost 40% greater than the one obtained with the two Parsivel[2] which were consistent between themselves. Since, having a rainfall amount roughly proportional to the price of the devices did not appear to be a scientifically acceptable explanation, a deeper look at the two rationales was carried out. The functioning of the PWS100 basically relies on the deviation of light by the drops in their fall. It is illustrated in Fig. 4.6.a. An accurate estimation of the drops equivolumic diameter requires a knowledge on the relation between the angle of deviation of the ray (θ) and the offset of the incident ray from the middle of the drop (h). It turns out that the correction implemented to account for the oblateness of drops in their fall, i.e. a simple power law correction at the end of the process, was not correct.

Hence, a new correction was suggested. It relied on simple ray trace analysis through a drop modelled as an ellipsoid with axis ratio changing according to the equivolumic diameter (Fig. 4.6.a). It enables to obtained more robust estimation of the deviation according to offset (Fig. 4.6.b). It significantly improved measurements (4.6.c). A European patent was submitted in 2016 and ultimately granted in 2021.

4.3.2 Toward improvement of radar algorithms with use of DSD

This section is mainly based on Gires et al. (2018), in which additional details can be found.

Overall purpose

As we have seen in section 3.1.1, rainfall retrieval with radars rely on the use of radar relations to convert radar measurements to rain rate. The most famous ones are the $Z-R$ (Eq. 3.1) and the $R-K_{DP}$ one (3.2). An other one is the $R-Z_h-Z_{dr}$ which is also a power law. In this subsection, we suggest to use disdrometer data to reconstruct radar quantities and study (i) the variability of the parameters of the radar relations at various scales ("climatic", "event", and "local") (ii) the consequence on rainfall retrievals with radars. In this subsection, I will focus on $Z-R$ relation, but similar results were obtained on the other two studied relations.

In order to achieve this, we used data collected on Carnot roof in May and June 2016. This period was extremely rainy over this area, and resulted in severe floods of the Seine River in Paris and its tributaries. The

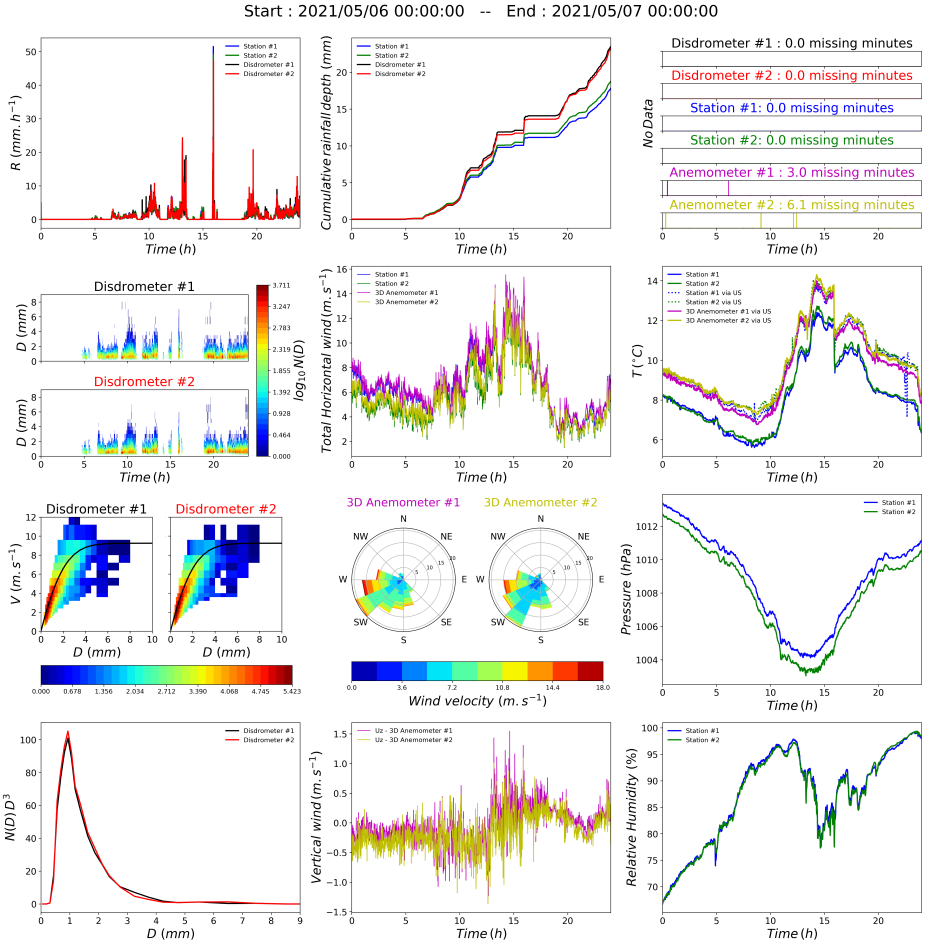

Figure 4.5: Quicklook of the meteorological data available on 6 May 2021 from the RW-Turb wind farm high resolution measurement campaign

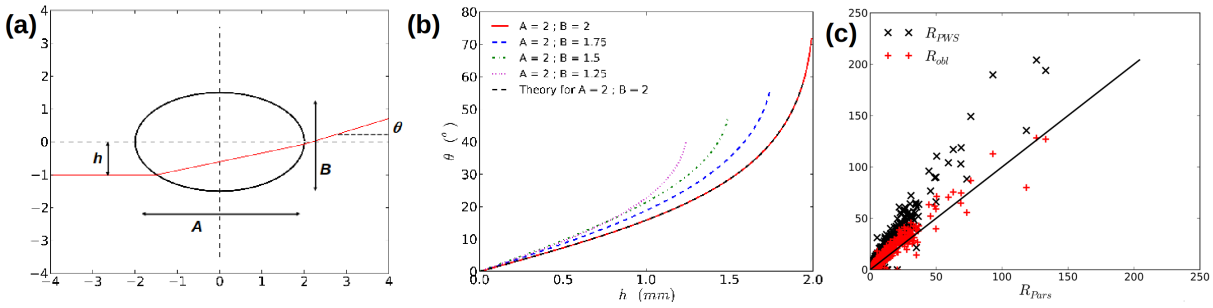

Figure 4.6: (a) Illustration of the deviation (characterized by an angle θ) of a light ray passing through an oblate drop with an offset h (b) θ vs. h for various ellipsoid shapes. (c) Scatter plot of the R_{PWS} (initially given by the PWS100) and R_{obl} (obtained with the PWS100 with the new correction suggested here) vs. the rain rate measured by the Parsivel^2 (R_{Pars}). The time step is 30 s. Adapted from Patent EP3246692.

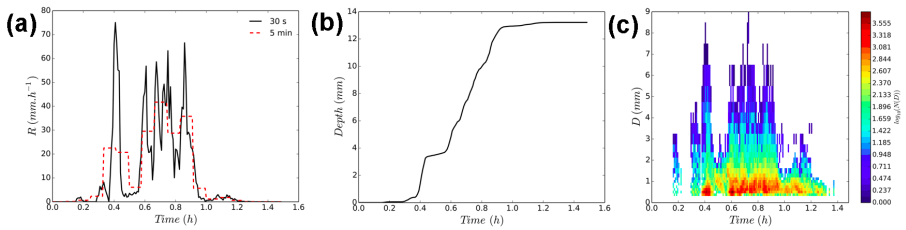

Figure 4.7: For the 17 June 2016 event with device Pars #2. (a) Temporal evolution of the rain rate in mm.h^{-1} with 30 s time steps (solid black, the observation time step) and 5 min time steps (dashed red). (b) Cumulative rainfall depth in mm. (c) Temporal evolution of the DSD $N(D)$. Figure from Gires et al. (2018).

peak flow in Paris was reached on 7 June 2016 with levels not observed since 1982 on the Seine River. Some upstream tributaries of the Paris area, especially the Loing, reached levels greater than the ones of the famous 1910 flood (http://www.developpement-durable.gouv.fr/Point-sur-les-inondations-6-juin.html). Various rainfall events were isolated in this period and we will focus on the 17 June 2016 event. It was due to the presence of a cold and instable air mass over France that resulted in numerous storms all over the country. It started on 17-6-2016 at 17:36:00 (local times are provided) and lasted until 17-6-2016 at 19:05:00. It is a short event during which great rain rates (Fig. 4.7.a) were recorded (more than 70 mm.h^{-1} at 30 second time steps and more than 40 mm.$^{-1}$ at 5 min time steps). No significant damage was reported on this area. The DSD exhibits a heavier tail (Fig. 4.7.c) with $D_m = 2.08$ mm. The number of large drops, i.e. with diameters greater than 3-4 mm, might be overestimated with the Parsivels, as this issue was reported by Park et al. [174] for intense rainfall. The interpretation that it could be due to the orientation of the Parsivel sampling area with regards to the wind direction is discarded in this case because both perpendicular devices exhibit similar DSD. This possible overestimation could be due to nearly coincident drops intersecting the Parsivel laser causing multiple smaller drops to appear as a larger drop.

More precisely, with the strong simplifying hypothesis that the drop size distribution (DSD) is homogeneous in the radar scanned volume and corresponds to the one measured with the help of disdrometer, it is possible to define pseudo radar quantities based on the pointwise disdrometer measurement. This furthermore assumes incoherent scattering, i.e. there is no clustering of the drops inside radar pulse volumes, whose radial scale is usually in the range of 100 m to 1 km. In other words that drop centres are homogenously distributed. It has been shown that this hypothesis may lead to strong statistical biases [143, 199]. Details of the computation of $Z_{h,v}$ and K_{DP} via an integral on the DSD can be found on the paper. It can only be mention that it was achieved with with the help of the Python PyTMatrix library [128], which relies on the T-Matrix code [159]. A radar wave length of 33.3 mm (X-band) is used and an oblate spheroids model for drop shape is taken with an axis ratio - equivolumic diameter relation corresponding to the one implemented in the Parsivel^2 rationale [9].

Radar relations at various scales

First we consider all the available data to compute average values of the radar relations' parameters. In this study they will be denoted 'climatic' values keeping in mind that they were obtained only with two months of data which is limited for such a statement. The plots yielding to the parameters' estimates of the $Z - R$ and $R - K_{DP}$ relations for the Pars #2 data are shown in Fig. 4.8. The quality of the regression is good with coefficient of determination greater than 0.8. For the $Z - R$ relation, it appears that the values found here for a and b are located respectively in the lower range and upper range of reported values in the literature. This apparent slight discrepancy is actually not surprising. Indeed Verrier et al. [233] showed that a and b are dependent on the scale at which they are computed. Given that they are computed here at 30s which is much smaller than the minute or few minutes commonly used, the differences are expected. Values are in agreement with those found by Verrier et al. at this temporal scale. It should also be reminded that one should be careful when comparing values because they are also dependent on the regression method (mainly the choice to express quantity in log or not, and the regression type) used to extract them [23, 103, 233]. With regards to the parameters of the $R - K_{DP}$ power law, are in agreement with the ones found in the literature.

Then the parameters of the power law relations were computed at the event scale for the 17 rainfall events of the period. See Fig. 4.9.a for an illustration with Pars #2 and 17 June event. The linear regression illustrating the radar relations are good meaning the underlying radar relations are reliable. Similar feature is found for the other events and devices. In general, a great variability is visible from one event to the other. For example, for the Pars #2 device, a is ranges from 100 to 450 (coefficient of variation equal to 14%) and b from 1.3 to 2.1 (coefficient of variation equal to 33%). Such variability is consistent or slightly greater than the one reported in the literature [103, 152]. No tendency was found between the event general features (duration, total rainfall amount...) and the parameters of the radar relations.

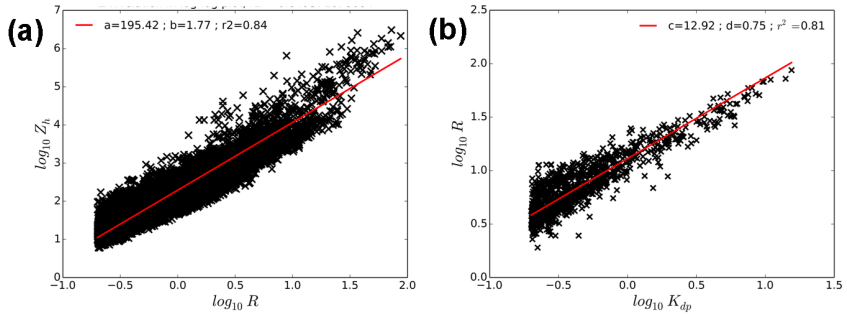

Figure 4.8: For the Pars #2 device, estimation of the exponents of the power-law relations $Z_h - R$ (a) and $R - K_{DP}$ (b) by regression in a log-log plot, considering all the available events. Figure from Gires et al. (2018).

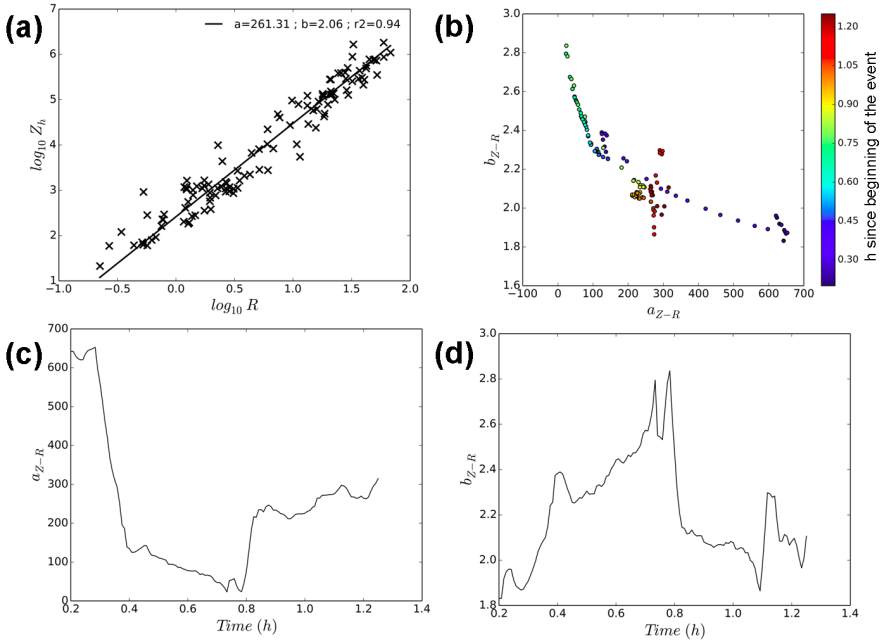

Figure 4.9: $Z_h - R$ relation for the 17 June 2016 event with Pars #2. (a) Computation of the parameters a and b at the event scale (Eq. 3.1 in a log-log plot). (b) Scatter plot of b vs. a estimated for each time step (20 min moving window). The colour of the points corresponds to the time within the event at which the parameters are estimated (c) temporal evolution of a. (d) Temporal evolution of b. Figure from Gires et al. (2018).

Finally, we went a step further to investigate this variability in radar relations parameters at the highest available temporal resolution. In order to achieve this, they are computed for each time step considering a moving window of 40 time steps (i.e. 10 minutes before and 10 minutes after). This is illustrated for the 17 June event in Fig. 4.9 with Pars #2 data. Figure 4.9.c and d shows the temporal evolution of the 'local' (i.e. with the moving window) of respectively a and b; while a scatter plot of b vs. a is in Fig. 4.9.b. Note that the colour of the points in Fig. 4.9.b corresponds to the time within the event at which a and b are estimated. It means that two points with similar colours correspond to the same moment of the storm. It appears that the variability observed between events is also present within an event. Indeed the temporal evolutions of radar parameters exhibit some quick variability, even with the use of the moving window technique. It highlights that parameters a and b exhibit a very local variability, which if taken into account could improve rainfall retrieval with radars. Furthermore although with some differences (local variability, sampling variability, device functioning), it appears that similar patterns are found for the three devices during a given rainfall event. It suggests that the temporal variability of a and b is associated with a variability of the underlying physical processes and not instrumental or sampling uncertainties. An attempt was made to study the correlation between the mass weighted diameter D_m and the radar parameters. Contrasted results were obtained and they did not enable to obtain strong conclusions.

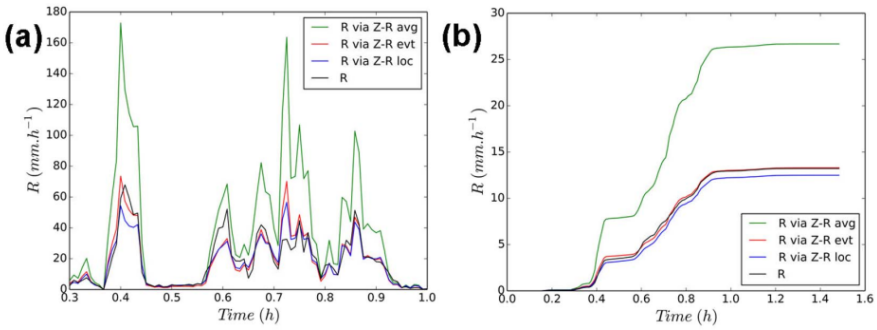

Figure 4.10: For the 17 June 2016 event and Pars #2 data. (a) Temporal evolution of the rain rates obtained via reconstructed pseudo-radar data and the three algorithms ('climatic', 'event', and 'local') along with the direct estimation of R. (b) Corresponding cumulative depth. Figure adapted from Gires et al. (2018).

Consequences on rainfall retrievals with radars

Here, the portion of radar algorithms converting filtered radar quantities to rainfall rates are mimicked with the help of disdrometer measurements. All computations are carried out at 30 s time steps. More precisely:

- Pseudo-radar quantities ($Z_{h,v}$, Z_{dr}, K_{DP}) are estimated with the help of the instantaneous DSD. The rain rate is computed from the raindrops collected
- The parameters of the radar relations are estimated at various temporal scales ("climatic", event, and local) with the help of log-regressions, as described in previous section
- Rain rates that would have been obtained with radars are simulated by implementing the radar relations. $Z-R$, $R-K_{DP}$ and $R-Z_h-Z_{dr}$ relations are tested; along with an additional hybrid one consisting in a Z_h-R one for low rain rates ($K_{DP}<0.2^o.km^{-1}$) and $R-K_{DP}$ otherwise.

Common scores as well as UM analysis were used to compare generated series against actual rain rate to sort the various algorithms in terms of performance. Both types of metrics yielded similar results. Considering a fixed temporal scale for the computation of the radar relations' parameters (i.e. 'climatic', 'event' or 'local') it appears that the hybrid algorithm is the one performing best. Then follow respectively the $R-Z_h-Z_{dr}$ and Z_h-R algorithm. The behaviour of the relation is trickier to analyse. Indeed contrasted results are found depending on the metric. This is related to the behaviour for 'small' intensity for which there is a strong negative bias. For each algorithm it appears that the performance improves when going from using 'climatic' to 'event' to 'local' estimates of the radar relations' parameters. This effect was expected and is now quantified. It is illustrated in Fig. 4.10 for the Z_h-R relation during the 17 June event with Pars#2 data.

4.4 Methodological developments

4.4.1 Accounting for scale differences in comparison radar vs. rain gauges

This section is mainly based on Gires et al. (2014), in which additional details can be found.

Overall purpose

In this work we focus on the observation scale gap between the rain gauges or disdrometers devices which are considered here as point measurements and weather radars. A rain gauge typically collects rainfall at ground level over a circular area with a diameter of 20 cm and the sample area of operational disdrometers is roughly 50 cm^2 whereas a radar scans the atmosphere over a volume whose projected area is roughly 1 km^2 (for standard C-band radar operated by most of the western Europe meteorological national services). Hence observation scales differ with a ratio of approximately 107 between the two devices. A basic consequence, (e.g. Wilson and Brandes [240], is that direct comparison of the outputs of the two sensors is at least problematic.

Standard comparison between rain gauge and radar rainfall measurements are based on scatter plots, rain rate curves, cumulative rainfall depth curves, and the computation of various scores such as normalized bias, correlation coefficient, root mean square errors, Nash-Sutcliffe coefficient etc. [46, 54, 56, 118, 162]. Despite usually being mentioned the issue of the representativeness of point measurement (i.e. disdrometer or rain gauge) with regards to average measurements (i.e. radar) is basically not taken into account and its influence on the standard scores is not assessed. Furthermore the authors who addressed it either to separate instrumental

errors from representativeness errors [30, 244, 162], or to introduce an additional score taking into account an estimation of the representativeness error [54, 103] all rely on a geostatistical framework which may tend to underestimate rainfall variability and especially the extremes. Indeed this framework assumes that the rainfall field or a transform of it is Gaussian, which does not enable to fully take into account the fact that the extremes of rainfalls exhibit a power law behaviour as it has been shown by various authors [198, 93, 122, 41, 194].

Here we suggest to revisit how the representativeness issue is taken into account in standard comparison tools between point measurement devices (disdrometers or rain gauges) and radar rainfall measurements by explicitly modelling the small scale rainfall variability with the help of Universal Multifractals. The issue of instrumental errors is not addressed in this paper.

Validation of a downscaling process

In order to validate a downscaling process, we relied on two sets of dense network of point measurements located within a 1km^2 area which corresponds to a radar pixel:

- A network of 16 autonomous optical disdrometers (first-generation Parsivel, OTT) which was deployed over EPFL campus from March 2009 to July 2010 (see Jaffrain et al. [101], for more detailed information). The minimum distance between 2 disdrometers was about 8 m, the maximum one about 800 m. Six heavy rainfall events were selected.

- A network of 16 tipping bucket rain gauges installed over the campus of Bradford University (United Kingdom). Eight measuring locations with 2 co-located rain gauges are installed on the roofs of the campus. The maximum distance between two rain gauges is 404 m and the time resolution 1 min. Three rainfall events were analysed.

The following methodology is used to test a simple spatio-temporal downscaling process :

- The average rain rate over the surrounding 1 km^2 area with a 5 min resolution is estimated by simply taking the arithmetic mean of the rain rates computed by the available devices over 5 min.

- The obtained field is downscaled with the help of discrete cascade (see section 2.1.5). It simply consists in continuing the cascade process down to smaller scales. Space-time cascades are used and an anisotropy between space and time is accounted for. Hence, to be consistent with the scaling of life-time vs. the structure size in the framework of the Kolmogorov [115] picture of turbulence the scale of the structure is divided by 3 in space and 2 in time at each step of the cascade process [148, 13, 66] which leads to 18 child structures. More precisely, seven steps of discrete cascade process are implemented leading to a spatial resolution of 46 cm and a temporal one of 2.3 s. The field is then re-aggregated in time to obtain a final temporal resolution of 1 min equal to the one of the two measuring devices. The output of the process consists in a realistic (if the downscaling process is correct!) rainfall estimate for 2187x2187 virtual disdrometers (or rain gauges) located within the 1 km^2 area.

- The observed and simulated data are compared with the help of the temporal evolution of rain rates simulated for the various virtual disdrometer and quantile plots. More precisely the temporal evolution of the rain rate and the cumulative rainfall depth are computed for each of the virtual disdrometer (or rain gauge). Then, instead of plotting the 2187 x 2187 curves which leads to unclear graph, for each time step the 5, 25, 75 and 95 % quantiles among the virtual disdrometers are evaluated. The corresponding envelop curves ($R_5(t)$, $R_{25}(t)$, $R_{75}(t)$, $R_{95}(t)$ for rain rate, and $C_5(t)$, $C_{25}(t)$, $C_{75}(t)$, $C_{95}(t)$ for cumulative depth) are then plotted with the recorded measurements on the same graph.

The corresponding curves for the EPFL data set are displayed in Fig. 4.11. Concerning the 6 June 2009 event of the EPFL data set, it appears that the disparities among the temporal evolution of the rain rate of the various disdrometers are within the uncertainty interval predicted by the theoretical model. Indeed the empirical curves are all between $R_5(t)$ and $R_{95}(t)$ and some are greater than $R_{75}(t)$ or lower than $R_{25}(t)$ for some time steps. It should be noted that for a given disdrometer the position of the measured rain rate varies within the uncertainty interval according to the time step (i.e. not always greater than $R_{75}(t)$ for instance), which is expected if the theoretical framework is correct. Concerning the temporal evolution of the cumulative rainfall depth, the measured curves are all within the $[C_5(t);C_{95}(t)]$ uncertainty interval except for two disdrometers. There is furthermore a significant proportion (8 out of 15) of disdrometers within the $[C_{25}(t);C_{75}(t)]$ interval which is expected. Hence for this specific event the downscaling model can be validated overall. Similar comments can be made for the other rainfall events with may be a tendency to slightly overestimate of the uncertainty interval for the rain rate. The quantile plots (not shown here) for a random selection of virtual disdrometer confirm the overall validity of the downscaling model for rain rates lower than 60 – 70 mm/h. For the extreme values (rain rates greater than 60 – 70 mm/h which corresponds to probability of occurrence roughly lower than 10-3) some discrepancies are visible and the simulated quantiles tend to be significantly greater than the observed

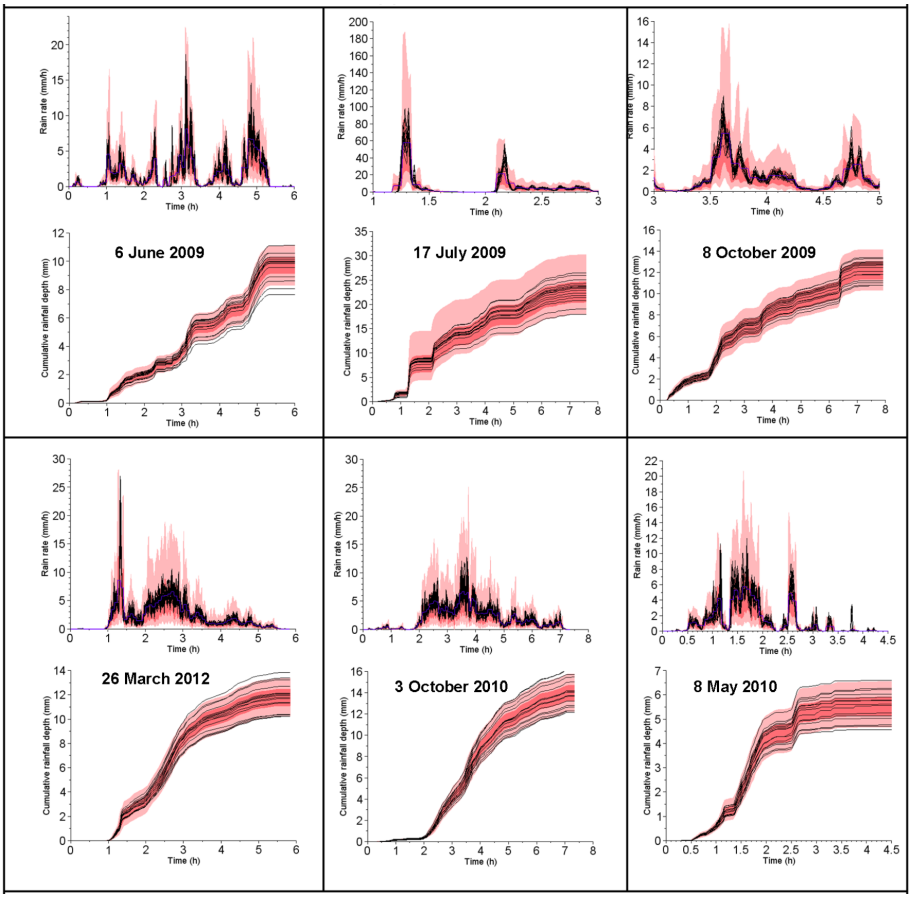

Figure 4.11: Temporal evolution of the rain rate and cumulative rainfall depth for point measurements for the EPFL data set. For each event the uncertainty range of the average measurement at the disdrometers or rain gauge observation scale is displayed ($R_{25}(t) - R_{75}(t)$ or $R_5(t) - R_{95}(t)$ and $C_{25}(t) - C_{75}(t)$ or $C_5(t) - C_{95}(t)$ are the limit of respectively the dark and the light area). Average measurement with 5 min resolution in blue. Figure from Gires et al. (2014).

ones. Given the validity of the UM model for rest of the curve, an interpretation of this feature could be that the measurement devices have troubles in the estimation of extreme time steps and tend to underestimate them. More extreme events should be analysed to properly confirm this. This nevertheless hints at a possible practical application of this downscaling process; generating realistic rainfall quantiles at "point" scale. Indeed they do not seem accessible to direct observation because of both limitations in the accurate measurement of extreme rainfall and sparseness of point measurement network. Results on the Bradford Univ. network are less straightforward to interpret, notability because the discrete nature of the measurement with tipping bucket rain gauges makes is hard to analyse the results for the rain rates at a 1 min resolution.

Impact of small scale rainfall variability on the standard indicators

Here we aim at estimating the expected values of the scores if neither radar nor rain gauges were affected by instrumental error, and the deviations from the optimum values were only due to the small scale rainfall variability. We will also investigate the related issue of the variations of the scores depending on where the rain gauges are located within their respective radar pixel. To achieve this, data coming from a network of 26 tipping bucket rain gauges distributed over the 236 km^2 Seine-Saint-Denis County (North-East of Paris) is used. The rain gauges are operated by the Direction Eau et Assainissement (the local authority in charge of urban drainage). Also C-band radar data from Meteo-France is used. For each rain gauge, the corresponding radar pixel is considered. Four rainfall events are studied. We implemented the following methodology :

- Downscaling the radar data for each radar pixels to a resolution of 46 cm in space and 5 min in time which is similar to the rain gauge resolution. This is done by implementing 7 steps of the spatio-temporal downscaling process validated in the previous section and re-aggregating it in time. This yields the outputs of "virtual rain gauges" for each of the 26 radar pixels.

- Randomly selecting a "virtual rain gauge" for each radar pixel and computing the corresponding scores.

In order to generate a distribution of possible values for each score, 1000 sets of 26 virtual rain gauges locations (one per radar pixel) are tested

The distributions of the scores obtained for the 1000 samples of virtual rain gauges set are displayed on Fig. 4.12 for time steps of 5, 15 and 60 min, with the numerical value of the 5, 50 and 95% quantile. The scores obtained with rain gauge and radar data are in red (vertical bars). The 50% quantile for each score provides an estimation of the expected value if neither radar nor rain gauges are affected by instrumental errors. The differences with regards to the optimal values of scores are simply due to the fact that rainfall exhibits variability at small scales (i.e. below the observation scale of C-band radar in this paper) and that radar and rain gauge do not capture this field at the same scale. Practically it means that when a score is computed with real data (i.e. affected by instrumental errors), its value should not be compared with the theoretical optimal values but to the ones displayed on Fig. 4.12, which is never done. The extent of the distributions, which can be characterized with the help of the difference between the 5 and 95%, reflects the uncertainty on the scores associated with the position of the rain gauges in their corresponding radar pixel. Practically it means that when comparisons of scores are carried out with real data, as it is commonly done to compare the accuracy of the outputs of various radar quantitative precipitation estimation algorithm for example, the observed differences in the scores should be compared with this uncertainty to check whether they are significant or not. This is never done and could lead to qualifying the conclusions of some comparisons. The values that should be used as reference (i.e. 50% quantile found considering only consequences of small scale rainfall variability) are displayed Fig. 4.12. Some of them are significantly different from the optimal values and as expected the difference is greater for small time steps which are more sensitive to small scale rainfall variability. For instance for 15 min the 50% quantile is equal 0.91, 0.81 and 79 for respectively the corr, Nash and %1.5 scores. The values for the slope are also smaller than one (0.82, 0.90 and 0.96 for respectively 5, 15 and 60 min time steps), which was not necessarily expected.

With regards to the scores computed for the 4 studied events over the Seine-Saint-Denis County, it appears that independently of the event and time step the scores found for Nash, $\%_{1.5}$ and *corr* are not consistent with the idea that they are only due to small scale rainfall variability, meaning that instrumental errors affected the measurement. For RMSE the scores found are explained by small scale rainfall variability for 15 Aug. 2010 and 15 Dec. 2011 and almost for 14 Jul. 2010. For the event of 9 Feb. 2009 the observed RMSE is even lower than the values of the distribution of the "virtual gauges". This is quite surprising since this distribution is a lower limit (for instance instrumental errors are not taken into account), which suggest some error compensation for this specific case. For NB and slope we find that the computed scores reflect instrumental errors for 9 Feb. 2009 and 14 Jul. 2010. It is also the case for the other two events with a time step of 5 min, but not with a 1 h time step. Discussion on the sensitivity of the results to location of rain gauge within the radar pixel and to the choice of UM parameters used for downscaling can be found in the paper [80].

Besides redefining the optimum of standard scores and setting values to which score variations should be compared, this work also suggests changing common practice when temporal evolution of rain rate or cumulative rainfall depth observed by rain gauge or disdrometer and the corresponding radar pixel are plotted on the same graph. This is the last standard way of comparing the output of the two measurement devices to be addressed in this paper. The observation scale gap between the two devices should be visible directly on the plot. A way of achieving this is to explicitly display the range of "realistic" values at the rain gauge scale for a given radar pixel measurement, in order to give an immediate insight into this issue to the reader and suggest whether to look for other explanations than small scale rainfall variability. This is currently not done in usual comparison. We propose to proceed as in the section 3 and to plot the 5, 25, 50 and 95 % quantiles for both rain rate and cumulative depth along with the radar curves. This is done in Fig. 4.13 for the 9 Feb. 2009 and 14 Jul. 2010 rainfall event for one rain gauge. For the 9 Feb. 2009, the cumulative depth (Fig. 4.13.b) is clearly outside the uncertainty range of the radar measurement at rain gauge scale meaning the instrumental error are likely to have affected at least one of the devices. Concerning the 14 Jul. 2010, the rain gauge cumulative depth is in agreement with the radar measurement (Fig. 4.13.d). With regards to the rain rate (Fig. 4.13.c), the rain gauge measurements are in the lower portion of the realistic values for the first peak, outside of it for the second peak (suggesting the effect of instrumental errors), and in the upper one for the third peak. More generally these results suggest that to compare the measurements of two devices that observe the same physical phenomenon at two different scales, it should become a common practice to first simulate an ensemble of realistic outputs at the smallest available scale of observations among two devices, and to compare the latter's output to the generated ensemble. The example of radar and rain gauge was discussed in this paper, but similar techniques could also be implemented on the comparison between satellite and radar data that also do not correspond to the same scale, while with a smaller scale gap compare to the case discussed in this paper.

4.4.2 Multifractal comparison of time series

This section is mainly based on Gires et al. (2016), in which additional details can be found.

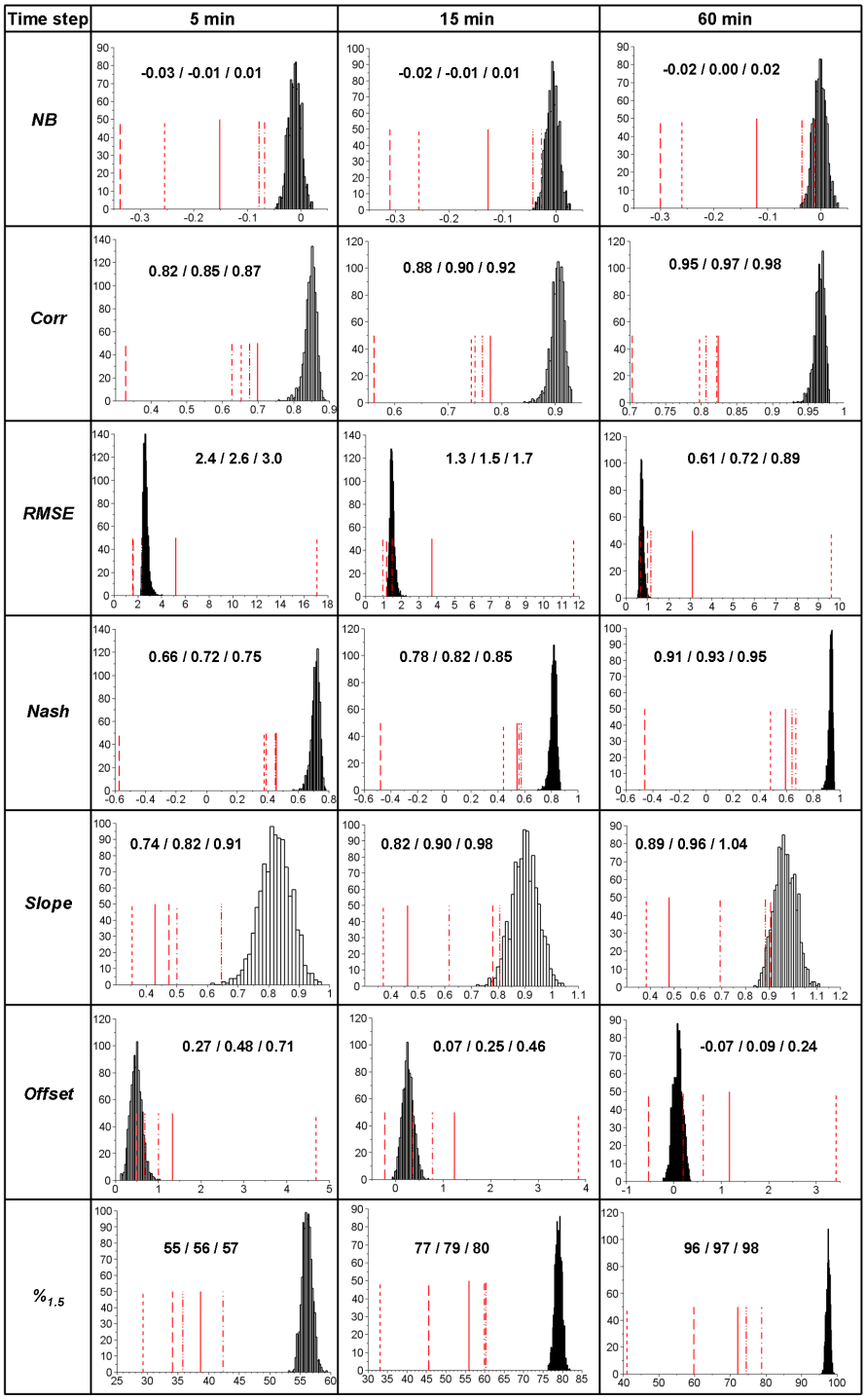

Figure 4.12: Histograms of the scores computed for the 1000 samples of possible combinations of virtual rain gauges. The values of the scores for all the events (solid) and the event of 9 Feb. 2009 (long dash), 14 Jul. 2010 (dash), 15 Aug. 2010 (dash dot) and 15 Dec. 2011 (dash bi-dot) are also displayed in red. The three figures associated with each distribution are the 5, 50 and 95% quantile. Figure from Gires et al. (2014).

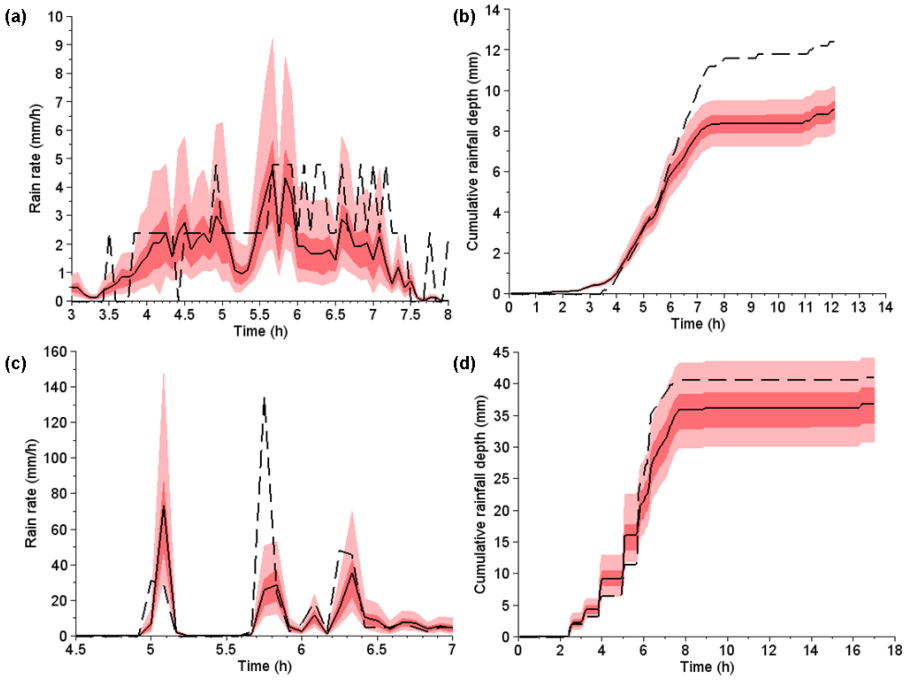

Figure 4.13: Rain gauge (dash), radar (solid), and uncertainty range of the radar measurement at the rain gauge scale for 9 Feb. 2009 and 14 Jul. 2010 (bottom) with the Seine-Saint-Denis data set. Figure from Gires et al. (2014).

Comparison of disdrometer output is usually done on the rain rate at a single resolution, most commonly the maximum one available (i.e. using the time series at the recording time step). In this work, we suggest new ways of comparing the outputs of disdrometers by using other fields. Furthermore, we suggest carrying out the comparison not only at a single scale but across scales. Indeed, considering various scales at once enables robust results valid over a wide range of scales. In order to achieve this UM analysis was implemented on various fields derived from disdrometer measurements, namely the rain rate (R) or the liquid water content (LWC), or even quantities measured directly by polarimetric weather radars such as Z_h and K_{DP}. Parameters characterizing the DSD such as total drop concentration (N_t) and mass-weighted diameter (D_m) is also analysed. In this framework the DSD is written as ; where it appears that D_m characterizes the shape of the DSD and N_t its total intensity. These two parameters are defined as [102, 129]:

$$N_t = \int_{D_{min}}^{D_{max}} N(D)dD \tag{4.5}$$

$$D_m = \frac{\int_{D_{min}}^{D_{max}} N(D)D^4 dD}{\int_{D_{min}}^{D_{max}} N(D)D^3 dD} \tag{4.6}$$

For the practical computation of these quantities (and the other ones), the integral is replaced by a summation over all the classes of diameter. For this study, disdrometer data from the Carnot roof #1 campaign is used (27 September 2013 and 18 January 2014). Fifty rainfall events were isolated during this period and ensemble UM analysis on scales ranging from 30 s to approximately 2 hours were carried out.

Figure 4.14.a displays the spectral analysis of the rain rate for the PWS100. A very good scaling (i.e. a straight line) is observed on the whole range of available scales (30s – 2h). Since the spectral slope is greater than the embedding dimension of the field (1 for time series), R is non-conservative (this will be confirmed with the estimate of H), and hence TM analysis was not implemented on the field itself but on its underlying conservative part, which can the approximated by the absolute value of its fluctuations. The results are displayed on Fig. 4.14.b, where the good scaling with a unique regime is confirmed. The r^2 for $q = 1.5$ is greater than 0.99. The same analysis carried out directly on the field yields non aligned points with a flattening for small scales ($r^2 = 0.94$ for $q = 1.5$). Same curves for spectral and TM analyses for the both Parsivel^2 are found. In general similar scaling behaviour are retrieved for the three devices despite a roughly 10% difference in terms of rain rate. With regards to UM parameters estimates, we find in general $H = 0.7$, $C_1 = 0.2$ and $\alpha = 1.5$ which confirms findings of previous studies.

Very similar results are found for LWC and K_{DP} with a very good scaling on the whole range of available scales on both the spectra and the TM analysis, which also has to be conducted on the fluctuations of the

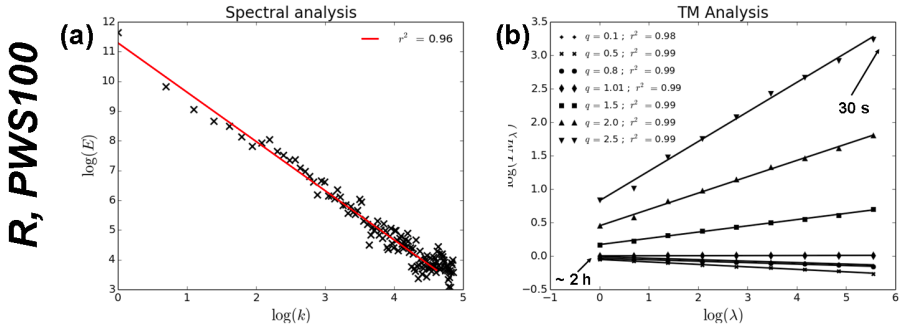

Figure 4.14: Scaling analysis for R measured by the PWS100: (a) spectral analysis, i.e. Eq. 2.2 in log-log plot; (b) trace moment (TM) analysis, i.e. Eq. 2.6 in log-log plot. Figure adapted from Gires et al. (2016).

field. The good scaling behaviour retrieved for K_{DP} is not surprising and was actually expected if relation 3.2 is correct. Indeed a power (K_{DP} here) of a multifractal field (R here) should also behave as a multifractal field (this is the basic concept behind the DTM technique). Furthermore, UM parameters estimates are in rather good agreement with what would be expected if the standard relation is implemented with "climatic" parameters computed for this data set. To the knowledge of the authors, the multifractal behaviour of K_{DP} has not yet been studied in time with disdrometer data this way, and it opens new promising perspectives. A potential one would be to compare these outputs with similar analysis performed in space with data provided by weather radars. This would enable to study scaling relations in a spatio-temporal framework with a quantity directly measured by the radar (so far the only device providing "rather" high resolution space-time data of rain related fields) without having to rely on tailored relations that may introduce biases in the scaling behaviour as it is the case for the rain rate. This would help to improve knowledge about rainfall as a space-time process.

The situation for Z_h is more complex. Indeed the energy spectrum (Fig. 4.15.a) is not linear and could be interpreted as exhibiting two breaks, one at roughly 6 min^{-1} and the other one (the minimum on the curve) at roughly 2 min^{-1}. Authors do not have explanation for this behaviour which is not retrieved on R and K_{DP}. It was not expected and suggests that the 'climatic' relation (Eq. 3.1 does not hold very well. Indeed if it was true, a good scaling behaviour would be observed on the spectra. To confirm this, the same analysis were carried out on the quantity aR^b, where R is the rain rate studied before and a and b are the 'climatic' values estimated on average over all the events. As expected for this analysis a good scaling behaviour is indeed retrieved on both the spectra (Fig. 4.15.c) and the TM analysis (Fig. 4.15.d). It should be mentioned that the greater scattering of the points for the $Z_h - R$ than the $R - K_{DP}$ which is observed on the available data is consistent with the fact that we found a good scaling behaviour on R and K_{DP} and not Z_h. Quite surprisingly the scaling breaks observed on the spectra are not visible on the TM analysis (Fig. 4.15.b) where a unique regime is observed. It was implemented on the fluctuations of the field for which there are a slightly better scaling than for the field itself. However given the lack of scaling observed in the spectral analysis, the TM analysis might be not very reliable and should not be over-interpreted.

Finally we analysed the scaling features of N_t and D_m which are used to characterize the shape of the DSD. For N_t we find a good spectral behaviour but limited to the range 2 min – 2 h, as a flattening of the spectra is observed for small scales. TM is implemented on the fluctuations and yields a good scaling behaviour on a range of scales (4 min – 2 h) similar to the one observed on the spectra. Similar scaling regimes are observed on D_m's spectra (Fig. 4.16.a), but the slope is much lower meaning that the TM analysis should be conducted directly on the field. It yields a good scaling behaviour with a r^2 for $q = 1.5$ equal to 0.99. The flattening of the spectra (almost a horizontal slope) for small scales corresponds to what would be observed for a white noise. This would suggest that N_t and D_m exhibit a scaling structure down to few minutes and behave as a random homogeneous variable for smaller scales. It is not possible to confirm this interpretation with the help of this data. More data at higher resolution, which would extend the range of available small scales, would be needed to achieve this. A possible interpretation of this could simply be that the sampling uncertainty is more visible at smaller scales and for these quantities than the other ones.

4.4.3 Initial steps toward a 3+1 D model for drops and consequences on radar measurements

This section is mainly based on Gires et al. (2015) and Gires et al. (2016), in which additional details can be found.

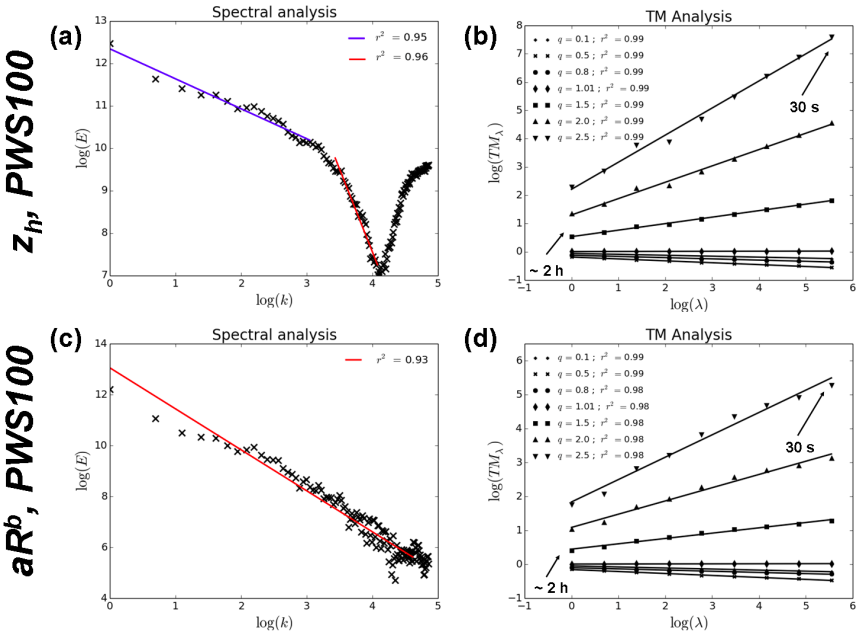

Figure 4.15: (a) and (b) Same as in Fig. 4.14 but for Z_h measured by the PWS100; in (a) a break is considered for $k = 20-30$ (~ 6 min^{-1}) and $k = 60$ ($\sim$2 min^{-1}). (c) and (d) Same as in Fig. 4.14 but for aR^b measured by the PWS100 and 'climatic' parameters a and b found using all data available. Figure from Gires et al. (2016).

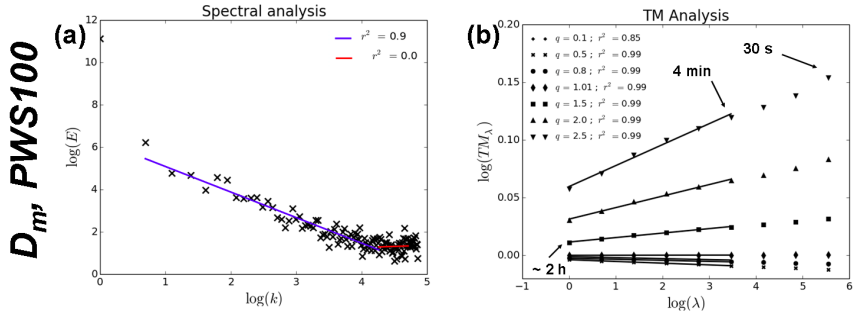

Figure 4.16: Same as in Fig. 4.14 but for D_m measured by the PWS100; in (a) a break is considered for $k = 70$ ($\sim$ 2 min^{-1}), in (b) a break is considered for $\lambda = 32$ (4 min). Figure from Gires et al. (2016).

Overall purpose

Most commonly acknowledged weather radars limitations are discussed in section 3.1.1. In this subsection, the specific issue of how the micro-configuration of drops in position and size affects the large scale scattering properties is addressed. Indeed the electric field measured by radars is the sum of the ones backscattered by individual drops and can therefore be affected by constructive or destructive interferences leading to biased rain rate estimates. The study in this paper is focused on the backscattering by hydrometeors that is a first step toward improved radar measurement. This issue as seldom been addressed [105, 104, 55, 113, 143, 199] and is usually neglected by authors who simply assume a homogenous distribution of drops within the scanned volume.

Here we set up a purely numerical experiment to mimic backscattering by hydrometeors located within a volume of $50 \times 50 \times 50$ m^3. In order to actually mimic radar measurements, other effects, such as antenna direction and range patterns, attenuation, propagation effect, or the presence of nonclear air along the path of the radar wave, would have to be modelled which is not the case in this initial experiment. Numerous radar simulator have been developed [25, 26, 29, 3, 119, 27, 108, 158] but they usually do not go down to drop scale or do so for a very limited number of drops due to computation limitations. The first set consists in developing an initial model of 3+1D drops' field and then explore its radar consequences.

A simplistic 3D+1 drops' field

In order to develop an initial version of the model, we first relied on an innovative use of data collected by a 2D Video Disdrometer (2DVD) [120]. The 2DVD provides detailed information about the geometry and the fall velocity of the particles falling through its sampling area of about 11x11 cm^2, by means of two perpendicular high-speed line cameras (with a pixel size of about 0.2 mm and a time resolution of about 1 ms). The device was installed in Le Pradel, Ardèche, France during the fall 2012 and 2013 in the framework of the HyMeX project [50]. A number of rainfall events were collected, and the two heaviest ones (in terms of 5-min rain rate) for each fall have been selected for the present study.

As already explained, the 2DVD provides for each drop a direct measurement of the fall velocity and of the horizontal position within the 11x11 cm^2 sampling area of the device. Assuming the validity of the hypothesis of vertical ballistic trajectories, i.e. that both remain constant during the last seconds of fall and equal to the ones measured near ground surface, it is possible to reconstruct the trajectory of each drop. Achieving this for all the drops enables to reconstruct the whole rainfall field drop by drop on a column above the device (Fig 4.17.a). The height of the column studied in this paper is 36 m. Despite the numerous limitations associated with the extremely coarse ballistic assumption, this reconstruction can yield some preliminary insight before considering more complex reconstruction, e.g. with randomized trajectories taking into account turbulence effects as well as coalescence and breakup. Then, the column is divided into 8192 boxes of 4.3 mm height, the two horizontal dimensions being the horizontal sampling area ones' i.e. 11 cm (Fig. 4.17.b). Although the minimum inter-drop distance (defined as the drop concentration to the power -1/3) observed for the studied events is roughly 4 cm (and usually much larger), the height of the boxes is chosen much smaller so that results can be compared in the vertical and in the horizontal dimension. For each box we consider the sum of the p-th power of the volumes V_i of the drops (computed with help of the equivolume diameter D_i estimated by the 2DVD device) contained in this box:

$$\chi_p = \sum V_i^p \tag{4.7}$$

As suggested by Lilley et al. [134] by varying p various physical quantities are represented; for instance χ_p for p equal to 0, 1, 7/6 and 2 is respectively proportional to the drop concentration, Liquid Water Content (LWC), rain rate (assuming a fall velocity proportional to the square root of the drop diameter), and radar reflectivity (which is nearly proportional to the 6-th power of the diameter; in the Rayleigh scattering regime). This yields a spatial 1D (vertical) field. An example of vertical evolution of the LWC (basically χ_p for $p = 1$) within the column during the heaviest portion of the 09-24-2012 event is displayed in Fig 4.17.c. Such reconstructed snapshot of the vertical column above the 2DVD is done every second and UM ensemble analysis is performed. Results are compared with those obtained by considering the same drops but with an random homogeneous distribution over the column. Results are displayed in Fig. 4.18 for $p = 1$. Both spectra and TM analysis show that the reconstructed fields exhibit scaling features from 36 m down to roughly 0.5 m. For smaller scales, no scaling is retrieved and a behaviour similar to the homogeneously distributed case is found, with notably a flat spectra. This confirms on an extended range of scales and using more data previous results [134, 144].

These findings were used to develop a simplistic 3D+1 drops' field over a volume of 50 x 50 x 50 m3. The process is summarized in Fig. 4.19.a. It basically consists in :(i) Simulating with the help of a 3D discrete a spatially varying field of LWC. The size of each patch is 0.5 m (ii) Distributing within each patch the total water volume into drops following empirical DSD measured with our disdrometers. (iii) Randomly positioning the drops's center within each patch. (iv) Affecting a simplistic velocity made a vertical component equal

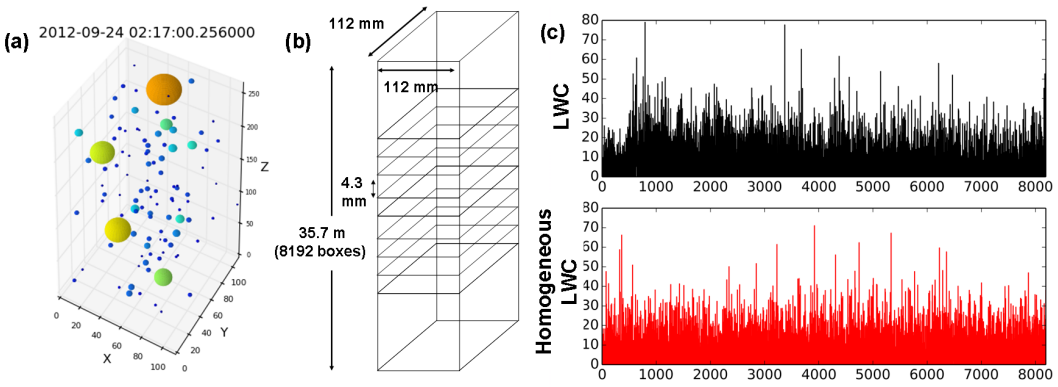

Figure 4.17: (a) Example of a reconstruction for a 26 cm vertical column; dimensions are in mm, drops have been coloured according to size and their diameter has been multiplied by 4 to improve visibility (b) Illustration of the 36 m x 11 cm x 11 cm reconstructed column divided into smaller boxes. (c) Vertical evolution of the LWC (in g.m^{-3}) within the vertical column for the reconstructed field (top in black) and simulated assuming homogenous distribution of drop positions (bottom in red) for an instant of the 09-24-2012 event. The horizontal axis corresponds to the box number (0: ground level, 8192: top of the reconstructed column). Figure from Gires et al. (2015).

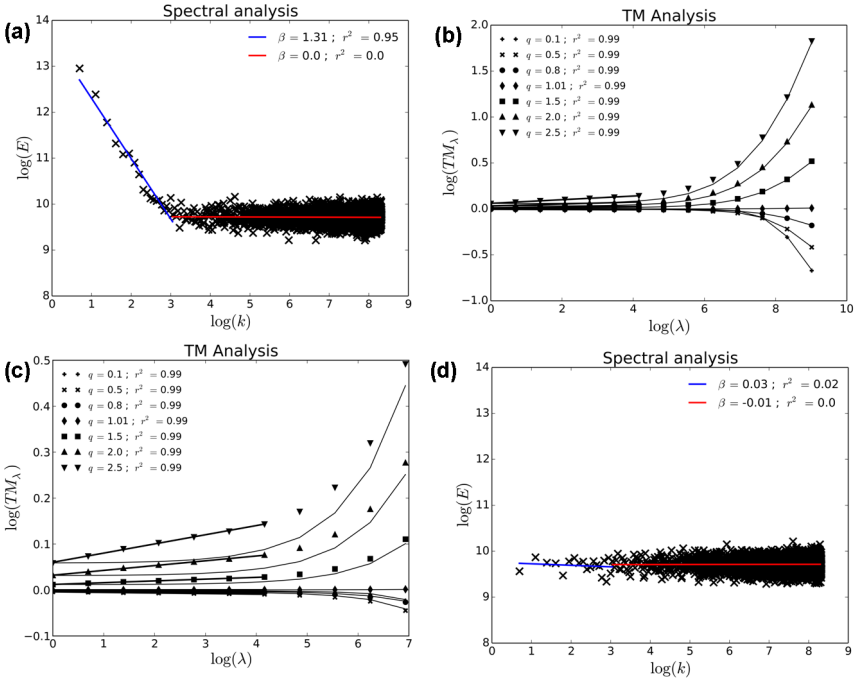

Figure 4.18: a) Spectral analysis of the vertical column snapshots for 60 seconds starting on 24 September 2012 02:17 UTC. (b) TM analysis of the same data (points) and the corresponding synthetic field-same drops (size and velocity) but their position is randomly (uniformly) assigned (solid, curved lines). The linear regressions (straight lines on the right side of the figure) are performed only for large scales, i.e. 0.5 – 36 m (c) Same as in (b) zoomed on the large scales (d) Spectral analysis of the corresponding synthetic field. Figure from Gires et al. (2015).

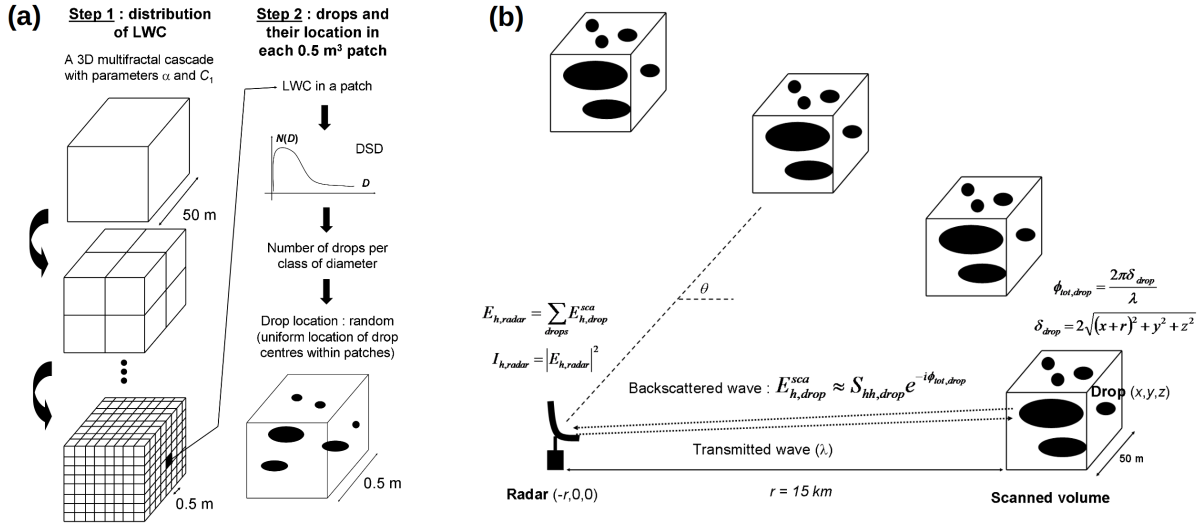

Figure 4.19: (a) Illustration of the process designed to generate synthetic 3D rain drop fields. (b) Illustration of the configuration tested for simulating radar observations of a 50 × 50 × 50 m^3 scanned volume. Figure adapted from Gires et al. (2016).

to terminal fall velocity with Lhermitte [131] formula and horizontal equal to $v_{turb,max}$ multiplied a uniform random field.

Effect of drops' locations on radar measurements

In order to account for potential constructive or destructive interferences between the signal backscattered by each drop, the electric field measured by the radar is computed as the sum of the ones backscattered by each drop (typically few hundred millions in our simulations) by accounting for phase shift. This yields an observed intensity denoted $I_{h,radar}$. It is compared with the case not accounting for phase shift (I_{simple}). This illustrated in Fig. 4.19.b.

The first step of the study was to investigate the influence of drops' positions. As theoretically expected, we retrieved an exponential distribution for potential measured horizontal reflectivity by single radar pulse. Given that 0.5 m is much greater than the radar wavelength, we found that the clustering of drops has no influence on the results. However, a single pulse is not enough to achieve a robust measure. Indeed as shown before a single measure basically yields any measured intensity over a wide range; and it is impossible to relate it to a given average LWC or rain rate. This is precisely why in practice; an average over typically 100 – 200 pulses over approximately 0.1 s is used. The underlying assumption is that the successive pulses correspond to independent realisations of the drop positions (drops are moving during this time interval), meaning that the average value over the pulses yields the desired quantity , which is free of possible interferences influence. Results during 1 s (with time steps of 0.002 s) using the model developed and various levels of turbulence are shown in Fig. 4.20.a along with 0.1 s moving window average. The 'ballistic' approach (blue curve) does not enable to retrieve I_{simple}. With increasing level of turbulence, the situation is improved but some 'slow' fluctuations remain visible. To investigate further this point, the decorrelation time of the signal was computed for the various values of $v_{turb,max}$, similarly to what Capsoni et al. [26] did. Results are plotted Fig. 4.20, and enable to quantify more precisely this effect. If a level of autocorrelation equal to 0.5 is taken as a threshold to define the decorrelation time, we find values equal to 200, 16, 9 and 5 ms for equal to respectively 0, 1, 2 and 4 m.s-1. These values are compatible with Capsoni et al. [26] findings. It means that to properly reproduce backscattering properties of the hydrometeors within the fixed volume, one has to take into account turbulent velocity of drops.

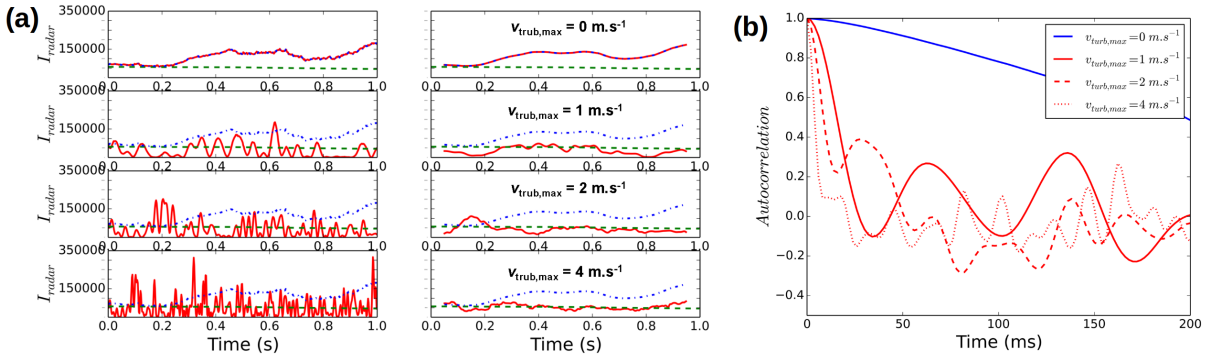

Figure 4.20: (a) (Left columns) Temporal evolution of the intensity measured by a radar on the horizontal polarization ($I_{h,radar}$) during 1 s, by modelling drops either with a 'ballistic' (blue dash) or 'turbulent' (solid red) velocity, along I_{simple} (long green dash). Each line correspond to a value of $v_{turb,max}$ (right column). Same as in left, with a 0.1 s moving window average. (b) Autocorrelation of the simulated backscattered signal for various values of $v_{turb,max}$. Figure adapted from Gires et al. (2016).

Chapter 5

Conclusion and perspectives

In order to insert the following developments in an overall context, it is important to remind few basic elements :

- The latest IPCC AR 6 Report released in 2021 [150] is much more straightforward with regards to rainfall than the previous ones. It reports with 'high confidence' that climate change is already affecting heavy rainfall : 'The frequency and intensity of heavy precipitation events have increased since the 1950s over most land area for which observational data are sufficient for trend analysis (high confidence), and human-induced climate change is likely the main driver (A.3.2)'. It also suggests that in general 'with every additional increment of global warming, changes in extremes continue to become larger. For example, every additional 0.5°C of global warming causes clearly and discernible increases in the intensity and frequency of [...] and heavy precipitation (high confidence)[...] (B.2.2)'

- A recent study [116], made popular after if was used for the cover of Nature in January 2022, with the title 'Rain stops gain', highlighted the negative impact of rainfall on economic development. More precisely, authors analysed 40 years of local economic data covering more the 1 500 regions worldwide and showed that the increase of the number of wet days and extreme daily rainfall results in decrease in economic growth rates.

- The portion of population living in cities is constantly growing (already more than 50% and 80% by 2050 according to UN forecasts). As a consequence, there are numerous international agreements and initiatives calling for improving urban systems, notably by replacing them in their geophysical environment (UN 2030 Agenda for Sustainable Development, COP21 "Paris Agreement", IPCC City conference, network 100 Resilient Cities...). Similar trends are observed in parallel within the scientific community with the emergence of the 'Urban Geosciences' theme in international conferences.

To summarize this boldly, people are living in cities and rainfall extremes, which negatively impact economic developments, are increasing because of climate change. As a consequence, progress on the understanding, measuring and modelling of rainfall in urban areas as well as storm water management will have a strong impact. The latter should be seen as one aspect of the more generic requirement to increase urban resilience. It is a contribution to the UN sustainable development goals 'Sustainable cities and communities' (#11) and 'Climate action' (#13).

In order to significantly contribute to this field, I believe that there are two main challenges which I aim to address through the various sections of this chapter. The first one is to better understand, measure and model rainfall which is known to be the greatest source of uncertainty in hydro-dynamic modelling. In order to achieve this, I suggest to forget the quite common strategy of considering rainfall merely as a statistical process, and to go back to more basic physical processes. Indeed hydro-meteorologists are primarily interested in aggregated quantities, but rainfall is intrinsically made of individual drops of various sizes and shapes. Going back at the roots of the emergence of this collective behaviour from individual drops is required. Then, the consequences of the findings notably in terms of very high space-time variability need to be fully explored. This is very challenging and given that drops are obviously affected by wind during their fall, achieving this requires the introduction of wind and coupling with it. The second challenge to the field is to actually account for the extreme variability over wide range of space-time scales of all the fields, both anthropogenic and geophysical. This has consequence on how urban areas should be monitored, modelled and managed in real time.

Hence I suggest perspectives that can be gathered in 5 axis :

- Back to rainfall basics : from individual drops to collective behaviour. It deals with some basic elements that are needed to develop the 3+1D model of drops' field.

- Improving disdrometers and radar measurements by mimicking devices's functioning at drop scale. Its aims at using the previous findings to significantly improve space-time high resolution (few tens of meters and few seconds) rainfall measurements.
- Contributions to the theoretical developments of UM. Indeed, some theoretical tools are needed to properly handle the observed extreme variability of studied fields.
- Optimization of storm water management to increase urban resilience. The two main challenges are obtaining reliable high resolution measurements and nowcasts of rainfall fields and properly accounting for variability across the modelling chain.
- Widening the range of applications for UM. This axis is based on the fact that similar methodology can be used in various contexts / applications. Given that one should keep in mind that achieving the envisaged goals will require some funding, it is important to highlight potential applications to other fields which could constitute basis for relevant new project developments. This is exactly in this state of mind that the RW-Turb project was initially submitted.

These axis for further investigations are presented in details in the following sections where the reader will notice that, as it could be expected, they are intertwined. The overall backbone being to properly deal with the actual extreme variability across scales of the underlying fields. Some suggestions are rather mature and are therefore described with more details while others are more tentative. In that case, only the main ideas highlighting their interest and feasibility are discussed. Finally, it should be stressed that current scientific life is not a lonely endeavor, meaning that some of these hints for further research emerged during fruitful and stimulating discussion with HM&Co scientists. Hopefully, this collaboration will continue in the future to fulfill these goals.

5.1 Back to rainfall basics : from individual drops to collective behaviour

In section 4.4.3, initial steps toward a 3+1 D model for drops' distribution were presented. The model is based on a UM discrete cascade that distributes LWC down to 0.5 m. Then, within each voxel, a homogeneous DSD is used to convert the total liquid water into drops. The initial position of the drops within their voxel is determined stochastically with a uniform distribution. Radar measurements were mimicked with this model. The analysis of the temporal evolution over 1 s showed that a simple ballistic velocity for drops did not enable to reproduce radar measurements. Hence, initial tests with a simplistic stochastic turbulent portion were carried out and confirmed that a 'turbulent' velocity should be introduced to properly mimic radar measurements.

This is just one example of application of the much needed 3+1 D model for drops' distribution field. Actually, this model will enable to fully deploy TARANIS overall underlying approach which consists in considering that rainfall is a collective behaviour emerging from the fall of individual drops. Indeed, going from drop scale to measurement scale is much needed to significantly improve measurements.

In order to achieve this, there is a need to

- Development of a device / experiment to measure in details rainfall at 100 m x 100 m scale.
- Measure or simulate space-time 3D wind fields within the volume to be considered.
- Introduce a physical equation to model drop movement in the atmosphere.
- Explore possible influence of rainfall on the turbulent properties of wind fields to notably determine if UM properties are affected by rainfall conditions.

Second and fourth items require the deployment of high resolution coupled measurements of wind and rainfall. Enabling such campaign was one of the purpose of the development of the RW-Turb project (see section 5.5.1 for more details). Thanks to it, we (at HM&Co) were able to acquire three 3D sonic anemometers and two additional disdrometers and therefore initiate the much needed coupled high resolution measurement campaign on a wind farm meteorological mast as well as a replication in an urban environment (see section 4.2.4). Developing such model is among the goals of RW-Turb.

5.1.1 Development of an experimental set up to measure rainfall at 100 m x 100 m scale

In order to achieve this wanted model there is a need to better understand rainfall variability at scales smaller than typically 100 m. Indeed, as we have seen before, there is a body of evidence that a transition occurs over this

range of unmeasured scales between a monofractal, individual drop regime to a multifractal, collective behavior at larger scales [134, 199, 81]. However, there is currently a gap at these scales in terms of measurements. Indeed operational X-band radars smaller gates is of few tens or few hundreds meters [130, 176], although there are some measurements down to 3 m as in [127, 220]. On the other end, there are numerous 'point' measurement devices (rain gauges, disdrometers,...) which provide temporal evolution over a sampling area whose typical size is ten cm.

Hence, an obvious suggestion is to design, implement and test an innovative rainfall measurement device to bridge the scale gap between existing instruments. More precisely, a new device of typical surface 10×10 m^2,

An option could be to rely on optical fiber technology [49, 109]. Indeed, it enables to measure the low fluctuations of the mechanical stress and the temperature variations over a specific optical fiber sensing cable, with high spatial resolution ($\approx$ cm). Rainfall could then be inferred from these measurements. Since measurements in optical fiber can be obtained over length greater than km scale, deploying it in a tortuous way over a large area could lead to the wanted measurements. Approaches using network of micro-wave radars could also be envisaged. The relevancy of patenting this new device will need to be explored. Implementing space-time UM analysis on such high resolution rainfall data will enable to explore and better quantify the transition from individual to collective behaviour occurring at these scales.

5.1.2 Simulation of space-time 3D wind fields

In order to better interpret radar measurements, a crucial step is to derive drops' trajectories over large volumes, typically from a radar location measurement at 1 500 m to the ground. To achieve this, there is a need to have 3D wind data at high resolution in both space and time over large areas of typical size few km. Unfortunately such data is not available. Hence a solution could be to reconstruct a somehow realistic 3D wind field from few punctual measurements relying on previous findings on turbulence.

Indeed, Lazarev et al. [126] obtained standard scaling relations between wind fluctuations and distances. In such framework, horizontal wind shifts behave as :

$$\Delta u(\Delta x) \stackrel{d}{=} \epsilon(\Delta x)^{a_h} \Delta x^{H_h} \tag{5.1}$$

where $\epsilon(\Delta x)$ is a UM field, $a_h = 1/3$ and $H_h = 1/3$. $\stackrel{d}{=}$ corresponds to an equality in distribution. An anisotropy between horizontal and vertical shifts is accounted for by considering a different scaling relation in the vertical :

$$\Delta u(\Delta z) \stackrel{d}{=} \epsilon(\Delta z)^{a_v} \Delta z^{H_v} \tag{5.2}$$

with $\epsilon(\Delta z)$ being again a UM field, $a_v = 1/5$ and $H_v = 3/5$.

Using this framework and wind measurements from the RW-Turb wind farm campaign (section 4.2.4), it is possible to envisage the following methodology to simulate a realistic wind field over large area :

- Perform a UM analysis on the field consisting in the difference between wind measurements from the anemometers located at 45 and 78 m. This will enable to tune according to the wind event UM parameters of the UM fields in Eq. 5.1 and 5.2.
- Set an anemometer data as reference, simulate UM fields with parameters found in previous point and use Eq. 5.1 and 5.2 to derive a wind field over large areas.

Vector fields simulations will need to be used. Another tricky point is that Eq. 5.1 and 5.2 correspond to equality in distributions. A first approach which is not fully satisfactory could be to generate ensembles of simulations from this stochastic process, and use this ensemble in applications before further analysis.

Partial space-time low resolution wind measurement can actually be derived from Doppler radar measurements (requiring at least two radars to obtain more than the radial component), or scanning LIDARs. It will be relevant to access or generate such kind of data to (at least partially) validate the previously mentioned methodology.

5.1.3 A deterministic equation for oblate drops in a wind field

In order to model drop trajectories within a 3D wind field assumed to be known, it is possible to rely on a deterministic equation, basically the second law of Newtons which equals the mass times the acceleration to the net forces.

Here a drop is subjected to three forces :

- The gravity
- The buoyancy

- The drag, which is commonly written as a function of the relative velocity between the wind and the falling particle and a drag coefficient c_D depends in general of the Reynolds number and the equivolomic diameter of the drop.

The tricky point to fully establish the motion equation is to compute the drag coefficient c_D as a function of the Reynolds number accounting for the oblateness of drops, i.e. for a non spherical shape. In a common approach available in the literature [96, 6], three dimensionless parameters are used to characterize the non spherical shapes of the falling particle : the sphericity, the crosswise sphericity and the lengthwise sphericity. In the general case, these parameters may be complex to assess but with the drops' shapes derived by Thurai et al. [224] using 2D-video disdrometer data [120], theoretical formula can be obtained enabling to compute the wanted relationship.

Then, thanks to the turbulent wind simulations, the tortuous trajectories of individual drops will be simulated. This will enable to deepen our understanding of drops' actual trajectories, and notably to investigate their scaling features compared to the wind input ones. The required wind space-time resolution to be inputted will need to be determined

5.1.4 Rainfall influence on turbulent wind field properties

The envisaged work presented before rely on the fact that turbulent properties and notably the intermittency of wind field are assumed to be known and understood in a UM framework.

To the knowledge of the author, it has seldom been investigated how these findings are modified under rainy conditions. Using high resolution wind and rainfall measurements from the RW-Turb wind farm campaign it will be possible to explore potential influence of rainfall on the turbulent properties of wind field to notably determine if UM properties are affected by rainfall conditions. This will be done by carrying out UM analysis for various samples corresponding to different rainfall conditions. A classification of rainfall conditions will be developed accounting for both rain rate and drop size distribution, and the corresponding set of parameters characterizing wind turbulence estimated. Larger scale indicator characterizing the meteorological conditions will also be used to shape the classification.

Thanks to this detailed analysis which is actually one of the tasks of the RW-Turb project, it be possible to tune the UM parameters of wind fields according to rainfall conditions which corresponds to a first step of the coupling between rainfall and wind fields.

5.2 Improving disdrometers and radar measurements by mimicking device's functioning at drop scale

5.2.1 Accounting for DSD variability in radar relations

In section 4.3.2, the variability of various radar relations, computed from DSD time series, was highlighted. It appeared to be significant between events and even within events, and to have a strong impact on radar relations. UM analysis of DSD features such as total drop concentration (N_t) and mass-weighted diameter (D_m) confirmed the extreme variability of DSD in time.

The DSD variability in space has been less studied. Some authors used dense networks of disdrometers and also report that DSD variability within an event can be greater than between events and tend to increase with the size the studied area [213, 103, 183]. Such variability at scales smaller than radar gate has an impact on rainfall retrieval with radars. For example, Raupach and Berne [183] used simulations of DSD maps based on few punctual measurements to study this effect on areas of size 5 km (typical ground resolution of the Global Precipitation Measurement -GPM- space-borne weather radar) or 2.8 km (operational pixel size of the Consortium for Small-Scale Modelling (COSMO) numerical weather model). They found contrasted results depending on the rainfall intensity with an underestimation of punctual measurement for light rainfall and an overestimation for heavier rainfall. In general, they report that the error distribution is mostly positively skewed. A related issue to this DSD spatial variability is the 'speckle' effect or how drops' positions within the radar gate affect radar measurement. It is partially addressed at the end of section 4.4.3. which highlighted the need to account of turbulent velocities in 3+1 D drops' positions model. Schertzer et al. [199] addressed it in a UM framework by assuming a multifractal distribution of raindrop volumes and showed that it could generate bias of up to 33% for statistical moment of order $q = 1.5$ and 60% for $q = 2$.

These radar applications highlight a need to study much more precisely the spatial variability of DSD to be understood in wide meaning, i.e. including drops' positions. Polarimetric radars are a powerful tool to achieve this. Indeed polarimetric variables such as Z_{dr} or K_{DP} can be used to derive DSD features. This has been a challenge for a long time (see Brandes et al. [16] for a 2004 review on the available techniques) and is still an active research area (see [183] for a more recent example). By the way, remote estimation of DSD features could

also have applications in numerical weather predictions (through improved sub-grid parametrization), rainfall microphysics studies or agriculture.

The infrastructure available at HM&Co through the Fresnel platform and UM tools are a convenient set up to make a valuable contribution to the field. The initial steps to be implemented are :

- Implementation of the existing techniques on the HM&Co-ENPC X-band radar data to generate maps of DSD parameters.
- Validation of the algorithms with the help of disdrometer data collected by devices of the TARANIS observatory.
- Implementation of spatial UM analysis on the computed fields to characterize their scaling variability (quality of the scaling, scaling regimes, UM exponents).
- Comparison with the UM analysis already performed on time series to be extended with larger data sets.

UM tools have seldom been used in this context and their large scale implementation could lead to significant progress on the topic. Achieving these initial steps will enable to create an innovative space-time model for DSD which relies on the observed multifractal properties of rainfall. Once space-time DSD characterization is available, which is a major challenge to be addressed through a combination of data analysis and theoretical development, implications on radar relations and potential algorithms improvements will need to be carried out.

Up to now, I limited the discussion to DSD maps. However rainfall being intrinsically a process in 3D space, investigating DSD variability in the vertical is an issue that should also be addressed. The advent of Micro Rain Radars (MRR) since early 2000's [179] has renewed the interest in this topic. Despite some limitations related to vertical wind and turbulence, it is basically the only way to get insights into the vertical DSD variability, and has sampling volumes more comparable to radar ones [228]. MRR have been used to infer a DSD to tune radar relations (see [110] for a recent illustration where MRR data is used to separate stratiform from convective rainfall events), to perform absolute radar calibration [158], or more generally study rainfall microphysics (see [245] for an example). Deploying MRRs and adding a vertical component to the developed approach could be fruitful in the future.

Finally, once DSD space-time variability is quantified more precisely, it will be possible to use the 3+1D model of drops' positions to implement updated versions of the work presented in section 4.4.3 which mimicked radar functioning at drop scale and pointed to the need to better account for both turbulence and DSD variability. Better accounting for DSD variability will also open new paths for real time merging of various rainfall products measured at various scales such as disdrometers and radars. Indeed the scale gap between the two devices is often mentioned but seldom truly accounted for in currently used merging algorithms.

5.2.2 Wind drift of drops and impact on radar measurements

During their fall, drops are advected by wind. Quantitative rainfall estimation with the help of weather radars are affected by this issue since drops can be displaced horizontally between their measurement location in altitude and their ground impact location which is of interest for hydro-meteorologists. This effect is usually called wind drift in the literature and sometimes wind advection. The potential bias and uncertainty introduced in radar measurement is stronger at higher resolution, i.e. typically with pixel size smaller than 1-2 km^2 which are needed for urban applications for example. Collier [36] suggests that correction schemes should be implemented for this kind or higher radar resolution. Lauri et al. [124] reported that far from radar (i.e. typically more than 150 km), even with low elevation (0.3°), displacements of few tens of km are found, which actually even distort the measured area.

Most correction schemes rely on the use of 4D wind profiles derived from numerical predictions models [160, 121, 124, 191] or combination of such with reanalysis [38, 39]. The latter also accounts for drop size distribution (DSD). With such, they report an improvement by $\approx 3\%$ of the correlation between radar and rain gauge measurement and a reduction of discrepancy of $\approx 18\%$ over eight selected events. Lack and Fox [121] used directly Doppler radar wind measurement at 2.5 km scale to adjust for wind drift effect. In general, correction schemes use wind data at rather coarse resolution (typically km(s)) and assume a constant wind shear. Nevertheless, some variability at smaller space-time scales is usually acknowledged, especially during convective events, i.e. the ones for which wind drift causes the greatest uncertainty [121].

Wind effects on rainfall drops is also reported to generate discrepancies between measured vertical velocities and expected terminal fall ones. For example, Montero-Martinez and Garcia-Garcia [161] studied events with calm, light and moderate wind with various rainfall levels, and found a widening of the fall velocity distribution under windy conditions. For example, they found super-terminal drops only for diameters < 0.7 mm and more often under windy conditions. Sub-terminal fall velocities for drops of size up to 2 mm are reported. Bringi et al. [17] found that under low wind speed and turbulence, no discrepancies are found with expectations while under high wind speed and turbulence, there is a clear widening of the distribution. A linear decrease of mean fall

velocity with increasing turbulent intensity is reported. Maximum decreases of 25–30 % are observed. Thurai et al. [225] also found such decrease for drops greater than 2 mm in high turbulence intensity conditions. It is associated to an asymmetry also appearing in the drop shape. They also found that drop horizontal velocities in both direction and magnitude show "remarkable agreement" with the wind sensor at 10 m. Stout et al. [211] explored the effect of non linear drag coefficient on fall velocity through numerical simulations. They showed that even heavy drops exhibited a reduced settling velocity in isotropic turbulence.

Turbulence is found to have contradictory effects on the distribution of fall velocity. Indeed increasing turbulence level in windy and rainfall condition will yield to more collisions and breakups, resulting in smaller drops inheriting the speed of larger parent ones, hence observations of super-terminal velocities. On the other hand, turbulence is said to yield to a decrease in fall velocities because drops (especially ones < 1 mm) are more affected by eddies. Such findings on the discrepancies between observed and expected fall velocities has effects on the relation between rainfall and kinetic energy, i.e. the erositivity 'power' of rainfall [177] and also building performance to outdoor conditions [227, 14].

The studies previously mentioned basically do not account for small scales wind fluctuations in both space and time. Hence, it would be relevant to use the model developed in section 5.1 to quantify more precisely the effect of wind drift of drops during their fall and the impact on radar measurements. In a first step, the trajectories of drops initially all located within a radar gate could be simulated and their ground distribution computed. Shift of more than few kilometers are expected for small drops (typically 0.5 mm). Furthermore, for a given diameter, the spread between various drops is expected to be larger for smaller drops and can cover various radar pixels.

A deeper investigation of the wind drift effect on radar measurement should include :

- Quantification of the uncertainty associated with the stochastic nature of the wind used as input.
- Use of actual DSD series measurement.
- Use of longer series to study the spread of drops at event scale.

This will enable to create probabilistic maps of ground rainfall from radar products accounting for wind drift. It should be stressed that the data collected during the RW-Turb project will enable to carry out such investigation, which is a way of adding value to data initially collected for another purpose.

5.2.3 Quantifying uncertainties with disdromerters

Uncertainties associated with drop shapes

In section 4.2.1, the functioning of both types of optical disdrometer is described. As we have seen both occlusion (Parsivel^2) and transmission (PWS100) rationales rely on strong assumptions on the drop shape. By the way, this is the observation of an improper account of drops' oblateness by the PWS100 process that lead to the developments now patented (section 4.3.1). Currently, drop shapes are assumed to be ellipsoids characterized by an axis ratio which depends on the equivolumic diameter of the drop.

More complex models have been developed as for example the one by Thurai et al. [224] (already mentioned in section 5.1). In order to improve rainfall measurements with the help of disdrometers, it would be highly relevant to :

- Mimic precisely the disdrometer functioning accounting for drop shapes other than a simple ellipsoid.
- Quantify of the uncertainty associated with unknown drop shape.

Again, the long disdrometer series available at HM&Co will enable to properly investigate the consequences of these findings on rainfall measurements.

Uncertainties associated with wind

Wind obviously affects in-situ rainfall measurements. It is a well known effect that standard rain gauges tend to underestimate rainfall during windy periods simply because rain does not fall vertically anymore while the gauge's funnel remains horizontal. Correction factors have been developed. In addition, a rain gauge deforms the airflow pattern around itself. This is why it is recommended to mount the rain gauge below ground level, which is often not possible in practice. This results in an increase of wind velocity above the orifice of the gauge. As a consequences, falling hydrometeors will tend to be deflected away from the gauge which induces an overall undercatch. Several authors suggested a numerical approached based on computational fluid dynamics (CFD) simulations relying on a time-averaged Reynolds-Averaged Navier-Stokes model to investigate this issue. An illustration can be found with the work by Colli et al. [32, 33], later used in [34] to assess how modifications of rain gauges' shape can improve the aerodynamic behaviour around it and hence limit this effect. The shape of three commercial rain gauges were used in this study.

Due to the more recent advent of disdrometers, less work has been done with regards to the impact of wind on measurements. Using data collected by an occlusion optical disdrometer (manufactured by Thies [59]), a rain gauge and a cup anemometer, during a measurement campaign on Montevergine Observatory terrace in Italy, Capozzi et al. [24] recently highlighted a wind induced bias on disdrometer measurements. They also suggested a tailored filtering procedure that improves by 8% rainfall estimates with respect standard approaches.

Studying more precisely the effect of wind on disdrometer measurements is a relevant issue for the community. Relying on existing knowledge, a combination of various steps should be implemented to properly address the topic :

- Analysis of high resolution measurement data combining wind and rainfall, which are already available at HM&Co.
- Mimic precisely the disdrometer functioning to quantify the impact of actual drop's trajectory on diameter and velocity estimates with regards to currently assumed vertical fall. The model developed in section 5.1 will be used.
- In a similar way to the work described before, use CFD simulations to account for potential impacts of the device itself on the wind features around it.

5.2.4 Toward a probabilistic measurement

With the increase of computer capabilities, meteorologists changed paradigm and usually no longer rely on a single deterministic simulation output but on ensembles of outputs to account for uncertainties in the input data and parametrization of models. From these ensembles, users can derive a probability distribution.

Such paradigm shift is slowly expanding to measurement directly. A striking example is the work by Kirstetter et al. [111] who focused on radar data from the United States of America. They developed a process that accounts for the uncertainty arising from the radar measurement itself, the correction algorithms and the conversion to rain rate algorithms. It is tailored to account for rainfall rate and type. The output of the process is a probability distribution for the rain rate over each pixel. Another example, with a different purpose was recently developed by Wolff et al. [241] to improve an algorithm estimating rainfall from commercial micro-wave links. More precisely acknowledging the uncertainties in algorithm's structure, input data, and parameters; they developed a stochastic process to optimize the parameters of the algorithm to improve rainfall estimates. It could be seen as an initial step toward a probabilistic measurement.

It would be highly relevant to fully acknowledge uncertainties associated with disdrometer measurements such as unknown drop shape or wind effect which were discussed in previous subsection and expand this paradigm shift to disdrometer measurements. The goal would be to obtain a probability distribution for measured rain rate and DSD features.

5.3 Contributions to the theoretical developments of UM

5.3.1 Improving UM discrete cascades

In section 2.2, the blunt extension of the discrete UM cascades is introduced along with an example of application related to downscaling of rainfall times series or maps. Before going on, it should be reminded that Schertzer and Lovejoy [193] argued on the necessity to go beyond discrete (in scale) cascades to respect the nonlinearity, continuous translation and scale invariances of the generating equations. Therefore, they introduced continuous (in scale) cascades. Although nonphysical, notably because of the stationarity issue (see section 2.2.1), discrete cascades are simply used for pedagogical purpose. A kind of intermediate solution, the blunt extension, was actually introduced to tackle the non stationarity issue while preserving the simple structure of discrete cascades. The developed process basically consists in performing a geometrical interpolation of the singularities at each cascade step. Theoretically expected multifractal behaviour is retrieved for the range of UM parameters corresponding to atmospheric fields; making this process relevant for simulations of atmospheric fields. Furthermore, such simple structure enables to address various common issues encountered with geophysical fields such as downscaling, guessing the missing half of a field (which can be considered as a first step toward nowcasting) and interpolation as we will see.

To widen the range of applications of blunt extension of discrete UM cascades, there is a need to carry out several improvements which are discussed below. For one of them, some preliminary results are displayed as illustration and will require further tests / developments for practical implementation.

Simulation of zero rainfall

The issues of the representation and simulation of zeros in rainfall field is commonly reported in the literature. In previous work [69], I showed that the presence of zeros can strongly affect the UM analysis of rainfall fields. Indeed, the zeros which are basically not accounted for in UM framework introduce a multifractal phase transition for small moments resulting notably in a linear behaviour of the scaling moment function for small moments. This in turns yields biases in UM parameter estimates with underestimation of α and overestimation of C_1.

In order to improve the simulation of zeros with discrete cascades, I introduced later [70] a simple model in which the real zeros are explicitly distinguished from the artificial ones. As stated in the conclusion of this paper, these zeros are generated within the cascade process, in a scale invariant way, and not independently from the rainfall values. It basically consists in setting to zero with a given probability the rainfall field if it is smaller than a given singularity, at the previous step of the cascade process. The underlying assumptions are that the conserved quantity is the total flux of water in all its phases in the atmosphere and not the rain rate, and that if there is not enough water, then the rainfall process is not certain to occur. In that way the model can be physically justified. Finally, the field is thresholded at its maximum resolution to mimic the limit of detection of any rainfall measurement device. This rather simple scale-invariant model enables to retrieve many of the properties observed on actual rainfall fields: a scaling break, non-conservation (only a portion of it is explained), differences between UM parameters for small and large scales and discrepancies between event-based analysis and long time series analysis. Nevertheless, some of the properties of the generated fields are not in agreement with those of actual rainfall fields: the spectral behaviour is not modified, the exponent of non-conservation is greater for large scales than for small scales and its dressed values are too small, and the fractal dimension is greater for small scales than for large ones. This means that this model model should be considered as nothing more than an interesting and encouraging simple toy model.

Future work should be carried out to refine and improve this simple model and implement it in the framework of blunt extension of discrete UM cascades. It will notably require analysis of total water flux in all its phases in the atmosphere, and not only rain rate. Such developments would constitute valuable contribution to the challenging task of properly modelling the zeros of rainfall fields.

Anisotropy

Geophysical fields, and in particular rainfall fields exhibit anisotropy, i.e. the statistical properties are not the same according to the direction. This is a well-know feature and it has been addressed in continuous UM simulations since its early developments [137, 193] with the so called 'Generalized Scale Invariance'. It basically relies on the fact that the contraction operator used to generate the field is no longer isotropic but anisotropic with the possibility to tune the wanted level of anisotropy. A new method to quantify spatial anisotropy has rather recently been suggested [164].

This anisotropy feature is not yet addressed with blunt extensions of discrete Universal Multifractal cascades. Future work should aim at extending this framework to account for anisotropy. As previously said, the blunt process basically consists in geometrically interpolating over moving windows the multiplicative increments at each cascade step. Hence an initial rather simple and straightforward approach to introduce some anisotropy is to use different sizes according to the direction for the moving window over which the interpolation is carried out. A more refined approach will consist in using ellipses as 'moving windows' rather than rectangles. The level of anisotropy will then be tuned by the ratio between the minor and major axis. This will notably remove the remaining square structures (already strongly attenuated by the 'blunting') and enable to introduce more easily a preferred direction other than the main axis.

In both cases, the first step is to establish the theoretically expected multifractal behaviour. Then it will be needed to numerically confirmed it with the help of ensembles of stochastic simulations. Finally, the features of simulated fields should be compared with actual rainfall data ones. The data available with the X-Band radar operated in the framework of the Fresnel Platform by HM&Co-ENPC will be used in this context. Obviously, when needed, UM analysis tools will need to be tailored to fully estimate anisotropy in all directions.

Space-time extension of blunt discrete UM cascades

Geophysical processes are intrinsically spatio-temporal, hence blunt discrete cascades should be extended to 3D, i.e. space-time. This extension is theoretically not complicated, except for the fact that a scaling anisotropy coefficient (H_t) between space and time should be accounted for [43, 66]. More precisely, it means that when the spatial scale is changed by a ratio of λ_{xy}, the temporal scale should be changed by a ratio of $\lambda_t = \lambda_{xy}^{H_t}$. By combining Kolmogorov's formulation [115] and the scale invariance of Navier-Stokes equations, one can show that $H_t = 1/3$ is expected [148]. Biaou et al. [13] initially suggested to use $\lambda_{xy} = 3$ and $\lambda_t = 2$, which are integer ratios enabling to remain close to the theoretical expectations given that $3^{1-1/3} \approx 2.08$. Such combination of ratios already reused in Gires et al. [79] and Gires et al. [80] is implemented here to generate the

sharp increments and the standard cascade process. Hence, at each step of a discrete cascade process, a parent structure is divided into 18 ($= 3 \times 3 \times 2$) sub-structures.

Once the sharp increments are simulated, the same process of geometric interpolation as the one described in section 2.2 for 1D and 2D fields is implemented successively in the two spatial directions (taking $\lambda_1 = \lambda_{xy} = 3$) and then in the temporal direction (taking $\lambda_1 = \lambda_t = 2$). Similarly, this will yield a correction coefficient $S^{3D}(\alpha, h)$ for the simulated C_1. As in 1D and 2D, numerical simulations should confirm this theoretical expectations. An issue that will require technical attention is computational effectiveness. Indeed the blunt process requires to simulate two additional cascade steps before re-averaging. This turns out to be quite demanding especially in space-time simulations. Hence, in order to be able to simulate large successive maps over long duration, code optimization will be required.

Widening the range of applications of blunt extension of discrete UM cascades

Application of blunt extension of discrete UM cascades to downscaling is already discussed in section 2.2.3. Here some hints for future applications are given. The issue of guessing the missing half of a field and interpolation will be addressed and constitutes the next steps.

The basic assumption underlying the presented applications is that the studied fields are generated with the help of blunt discrete cascade of known UM parameters α and C_1. This assumption can actually be checked on the available data through a multifractal analysis also enabling the estimation of characteristic parameters. Assuming this, in order to fully determine a final field, one simply has to retrieve (deterministically or stochastically) all the underlying increments of the standard process (the $b_{n,i}$ with the notations of section 2.2) from which the $a_{n,j}$ and ultimately the field are derived.

The overall methodologies envisaged to obtain these increments follow the same steps for the various addressed issues and are similar to the ones implemented for downscaling :

- Estimation of the UM parameters (note that following Eq. 2.27, the parameters inputted in the simulation will be α and $C_1/S^d(\alpha, h)$ to retrieve the correct α and C_1 on the generated fields);
- Filling as much increments as possible from the available data, which is the tricky part for which a process needs to be designed for each application;
- Stochastically drawing the remaining ones.

For all the applications, the presence of stochastic generation of the remaining increments means that not a single deterministic result will be obtained but an ensemble of realistic realisations. More precisely the outcome of the process is not a deterministic value but an empirical probability distribution. When relevant quantiles (10, 50 and 90%) could be computed. It should mentioned that with this process, simulated fields are to exhibit the wanted UM properties and that it will be needed to systematically check this.

Guessing the missing half of a multifractal field

Here I describe a suggestion of new algorithm to guess the missing half of a multifractal field assuming that it is generated through a 'blunt discrete cascade process'. The studied field is assumed to be normalized to one. The envisaged methodology is explained in 1D with the corresponding illustration but the same process can actually be implemented in 2D and 3D.

A scheme of the situation is displayed in Fig. 5.1. The available data which corresponds to the input of the algorithm consists in a series which is shown in blue on the left. The data to be guessed which corresponds to the output of the algorithm (in green) is the follow up of the initial series. The field is assumed to be generated through a blunt discrete cascade, meaning that it is fully determined by its underlying sharp increments. Hence the whole purpose of this algorithm consists in determining these increments while ensuring that the field has the required multifractal properties and has values as close as possible to the actual ones on the available portion. To summarize, a portion of the increments are stochastically simulated (red rectangles) and the rest is deterministically reconstructed through an iterative process (purple rectangles). Before going on, it should be mentioned that the overall concept of deterministically reconstructing a portion of the field and stochastically simulating the other was already implemented in previous work using continuous UM cascades. Interested reader can refer to initial implementation in [147, 146] or further developments in [**?**]. Here we aim to tailor such concept to blunt extension of discrete cascades.

Let us now describe in detail a potential algorithm to achieve this goal. It is made of two successive steps. In the first step, an initial guess of the increments is computed. The ones corresponding more to the portion to be guessed (i.e. in red in Fig. 5.1) are stochastically simulated with given α and C_1 (computed from the available data) and set to a definitive value. The others (in purple in Fig. 5.1) are simply set to one divided by the average renormalization factor at each cascade step. The purpose is to ensure that the blunt field will have values close to its average value of one for this portion.

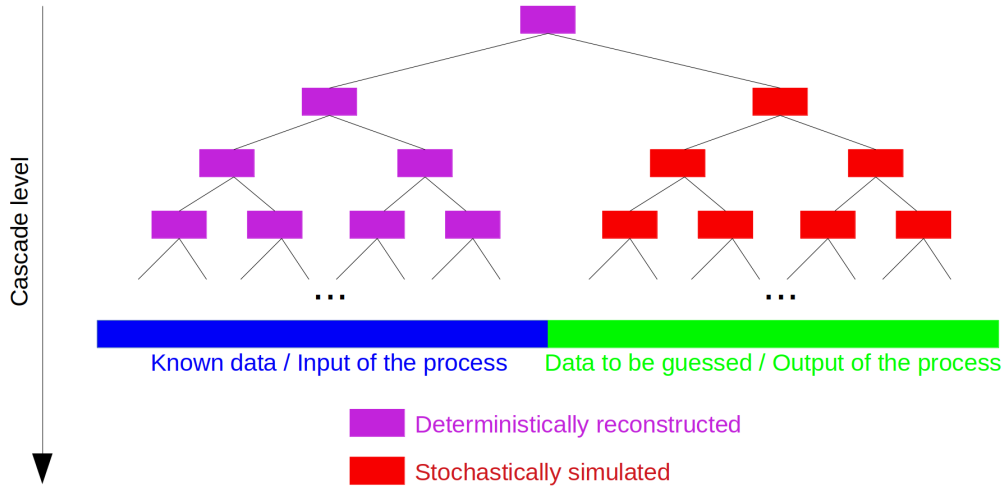

Figure 5.1: Scheme illustrating the newly developed process to guess a missing half of a multifractal field

The second step consists in an iterative process to tune the 'purple' increments so that the blunting of these sharp increments yields the wanted value on the known portion of the series (in blue in Fig. 5.1). This step of the algorithm is actually the trickiest and an heuristic approach yielding to expected good results could be :

- A first estimate of the blunt simulation (denoted Sim_{blunt}) is computed from this first guess of sharp increments. At this first iteration, it will obviously be quite far from from the known data.
- The ratio of the data to Sim_{blunt} ($Ratio = data/Sim_{blunt}$ is computed. For the second half of the series, this $Ratio$ is simply set to one. Since the data is normalized to one and the sharp increments were initially chosen to ensure that Sim_{blunt} is close to one, the average of $Ratio$ will be close to one which is what we want for the next step.
- The sharp increments yielding to this field ($Ratio$) then are assessed. This is done by using at each scale (or cascade step) the same matrices as in the blunting process to obtain a 'smoothed' field. Taking the ratio between two successive cascade steps then yields to the dressed blunt increments. The sharp ones are then assessed by taking the average at the corresponding scale. This approach assumes that the field is normalized to one. Given the choice of initial increments, this is approximately the case. However a small correction is implemented with the total average of the field, by taking it and distributing it uniformly over all the scales (to ensure that the initial average is retrieved).
- The purple sharp increments are then updated by multiplying the current ones with the 'dressed ones from $Ratio$'.
- Finally the process is repeated, i.e. a new blunt simulation is computed from these updated sharp increments, leading to a new ratio enabling a new update of sharp increments.

Such algorithm should in a first step be tested in 1D, 2D and 3D, while potential improvements should be studied, notably to ensure a transition as smooth as possible between the known part of the data and the portion to be guessed.

Multifractal interpolation

Given the sparse nature of most measurement networks, interpolation, i.e. reconstructing a field (in 1D, 2D or 3D) from a limited number of punctual values is a major challenge in geosciences. There is an extensive literature on the topic. The first famous example, which dates back to the beginning of the previous century (1911) is the Thiessen polygons [222] and it is still used in hydrology. Refined methods which rely on polynomial least square fit were later developed Panofsky [172]. They both correspond to deterministic interpolation to which weighed interpolations also belongs (the most famous being inverse distance weighting). Another category of interpolation methods are the geostastical ones which consists in performing statistical linear interpolation, assuming a Gaussian underlying field. It was initiated by Matheron [151] in 1971 and they are called Kriging techniques. They now have many derivatives. Interested reader can refer to reviews on the topic for more information [145, 92, 135]. In general these techniques rely on strong assumptions with regards to the regularity of the underlying field. Hence they are not directly suited for multifractal fields since singularities will not be properly represented. An example of use of UM approach to interpolation can be found in the work of Salvadori et al. [190].

Developing an algorithm to perform multifractal interpolation based on blunt extension of discrete cascades is a goal for future work. As for the previously discussed applications of blunt cascades, the tricky point will be to determine the sharp increments of the underlying cascade process which are needed to obtain expected or close to expected values at the available locations. Exactly as for the conditional β-model (section 2.4), the idea will be to identify within the cascade process the increments which are involved in the generation of the available values, and fill them with possible increments. Various approaches should be tested. A rather natural one would consists in working 'point by point'. More precisely, the available point with the maximum value is considered first. Then, the increments are filled with random ones generated with the expected values of α and C_1 (which by the way might be tricky to estimate with limited number of points in practical cases). The value obtained at the point is then computed. If it is close enough to the known values of the initial data, then the increments are considered as filled and left unchanged after. Otherwise a new set of increments is drawn. After a predefined number of trials, the process is stopped and the increments set yielding the closer value is selected. The process is then repeated for the second available point and so on. The various parameters, and notably the meaning of 'close enough' should be tuned according to the need and patience of the user. Sensitivity tests will obviously be needed.

Going beyond scalar fields

Until now, only scalar fields have been addressed, whereas vector fields are required in some applications. The most obvious one being wind velocity which is intrinsically a vector. Vector simulations with the help of continuous UM are presented in Schertzer and Tchiguirinskaia [197, 200] which discuss recent developments in this area. They correspond to the emergence of multifractal operators which rely on robust algebraic properties.

It would be interesting in the future to expand blunt extensions of discrete UM fields to vector fields. As an illustration of possible leads, vector cascades in a sharp discrete cascade could basically be written as :

$$\begin{bmatrix} X_n \\ Y_n \end{bmatrix} = \begin{bmatrix} a_{11} & a_{12} \\ a_{21} & a_{22} \end{bmatrix} \begin{bmatrix} X_{n-1} \\ Y_{n-1} \end{bmatrix} \tag{5.3}$$

where X_n and Y_n are the two components of a vector and a_{ij} the equivalent of the random multiplicative increments. Taking $a_{12} = a_{21} = 0$ would simply lead to two independent components. Non zero term would enable to introduce some correlations between the components which is what is wanted. Such basic approach could be used to initiate vector discrete UM cascades.

5.3.2 Multifractal correlations and quantification of space-time extremes

In section 2.3, I presented a work on approximate multifractal correlation in the framework of products of UM fields. It lead to the development of an innovative framework to investigate the correlations between two UM fields. It basically consists in looking at the best parameters, enabling one field to be written as a power law multiplicative combination of the other field and a random one. In this context, a good candidate for a simple indicator of the strength of the correlation (called IC) is the proportion of intermittency of a field explained by the other one. In the general case, this framework is not symmetric, which is a limitation. However when the α values are typically greater than ~ 0.8, it is approximately symmetric, meaning that it is relevant to extract some information on the correlations between two fields in most cases. Initial implementation was carried with rainfall and DSD features.

In a first step, further investigations on other fields in various contexts should be carried out to confirm the ability of this framework to both characterize and simulate correlations across scales between two multifractal fields. One can think of few examples which could have strong impacts :

- Temperature & Humidity. Humidity, i.e. the amount of water vapour contained in the air, affects the heat capacity of air. Joint multifractal analysis could for example enable to better understand their correlation and its expected impact on thermal balance of buildings which depends on it.

- Rain rate & kinetic energy. Due to a variable distribution of the size and velocity of drops, the relation between kinetic energy of rainfall and rainfall rate is not trivial. Assuming a gamma distribution for the DSD, a power law relation is expected. It should be studied in depth using this framework, notably to overcome the limitation that the temporal resolution at which the analysis is carried out was shown to have a strong influence on retrieved standard relations. Scale invariant features of the multifractal framework will be used to develop a relation valid not only at a single scale but across scales. Available DSD data will enable to achieve this. Such relations are critical to the understanding and modelling of soil erosion and pollutant detachment of soil through drop impact, or leading edge erosion of wind turbines.

- Rainfall & wind. The need for a combined analysis of these two fields was already highlighted in section 5.1 for the development of the 3+1 D model for drop's locations. Another application more focused on

extremes is that building surfaces suffer damages from a combination of rainfall and wind conditions. However, they are seldom studied together while both are known to exhibit scale invariant features. Such joint UM analysis will enable to overcome these limitations.

By the way, an ongoing PhD project notably aims at addressing this issue. In a second step, once multifractal correlations are well established, there will be the possibility to quantify joint extremes as well.

In addition to these practical implementations, there is a need to generalize the presented framework of joint analysis to more than simply two fields, and develop a framework suitable for any number of fields.

It should reminded that all fields which are previously discussed are actually space-time processes while extremes are in most cases handled via time series. The concept of Intensity-Duration-Frequency curve is widely used for rainfall, and there are plans to extend it to wind (see section 5.5.2), but it lack the notion of area. This is especially unfortunate given the potential impact on urban hydrology for example. Hence adding the notion of area, with tools others than a simple areal reduction factor would also be required. UM tools which are intrinsically spatio-temporal ones are an excellent candidate to achieve this without relying on had-hoc assumptions.

With regards to the quantification of extremes, it should be stressed that at HM&Co, given that we operate the disdrometers since 2013 and the radar since 2015, we are starting to have measurement periods sufficiently long to initiate research on extremes, beginning with return periods of the order of one or few years. Hence it appears timely to focus part of our activity on this aspect which is furthermore highly relevant in the context of increase of extremes with climate change.

5.3.3 Effect of measurement devices' thresholds

Rainfall device are not very good at capturing small rain rate. For example rain gauges do not measure rainfall below 0.2 $mm.h^{-1}$ which is the order of magnitude of the annual average rainfall over France. Such 'high' threshold of detection artificially increases the number of zeros in measured rainfall time series or maps. As we have seen while discussing the issue of modelling the zeros for rainfall fields, this may have a strong influence on the retrieval of multifractal features and notably the ranges of scales over which scaling behaviour is observed and UM parameters' estimates.

More generally, limitations of devices functioning result in the presence of lower and / or upper thresholds on measured fields. Rainfall was already discussed. Visibility or meteorological observable range is another one. Indeed there is usually an upper threshold. For the PWS100 which is operated by HM&Co (see section 4.2) it is of 20 km. More precisely all the values above this threshold are set to 20 km. This results in a lower threshold for scattering coefficient which is basically the inverse of the visibility. All the values below a lower threshold are set to this lower threshold and not to zero. The effect of these lower or upper thresholds on UM analysis should be studied carefully because they are likely to introduce some artificial biases in observed multifractal behaviour leading to wrong physical interpretation of the underlying phenomenon.

Hence, for each type of device, one should systematically :

- Identify the threshold limitation of the device.
- Theoretically convert this limitation into a mathematical properties on the codimension function.
- Derive consequences on the scaling moment function with the help of the Legendre transform (see section 2.1.2).
- Quantify the impact on standard UM analysis tools such as TM and DTM (section 2.1.2).
- Numerically confirm theoretical expectations with the help of synthetic simulations.

Such approach was implemented for lower threshold and rainfall fields. It will be implemented in the framework of an ongoing PhD project to assess the influence of a lower threshold on scattering coefficient, and to assess the influence of an upper threshold on power produced by rated wind turbines.

5.4 Optimization of storm water management to increase urban resilience

5.4.1 High resolution rainfall measurements and nowcasts

As pointed out in previous sections, rainfall is the greatest source of uncertainty in (real-time) urban hydrodynamic modelling and small scale variability has been shown to have a significant impact on simulated surface and sewer flow. As a consequence, it turns out that practitioners are in need for high resolution (i.e. few tens of meters in space and few tens of seconds in time) rainfall data.

The tools developed in previous sections to improve radar rainfall retrieval with regards to data measured directly in altitude as well as at ground level will help in this direction. In addition the interpolation techniques to be developed that actually account for extreme variability of the underlying field will constitute a basic step toward improved merging techniques to generate upgraded rainfall products based on both radar and in-situ point measurements. The use of scaling analysis to confirm that merged fields exhibit expected appropriate scaling behaviour will be helpful (see section 3.2.1 for some initial implementation of such approach).

Once high resolution measurements are available, it will be important not to stop, but to look for solutions to provide improved nowcasts, i.e. short term (up to few tens of minutes) forecasts. The guessing of a missing half of a multifractal field is actually a basic step of the process since it enables to account for growth and decay of rainfall cells in a UM framework. However, nowcasting also requires to account for rainfall advection by wind which should therefore be incorporated. Numerous schemes are available in the literature and an example in this direction could be found in Seed [203] or Bowler et al. [15] who mainly remained in a scale invariant framework. Being able to nowcast vector wind fields will also enable to improve rainfall nowcasts. This is another illustration of the need to study both rainfall and wind in common UM framework. Theoretical limits of predictability will need to be determined depending on the studied space-time scale.

Nowcasts, which basically consist in extrapolating available data can only provide forecasts of up to few tens of minutes. Longer forecasts which are needed for some application require the use of numerical weather models. However the latter do not run at the required resolution for urban applications. Hence, before applying some blending techniques between nowcasts and model outputs, there is a need to statistically downscale both rainfall and wind data. The tools discussed in previous section will enable to achieve such task while remaining in the UM framework which enables to account for the extreme variability across scales of the two fields.

5.4.2 Toolbox for rainfall management for urban applications

In previous sections, additional measurements and theoretical developments to improve rainfall estimation were discussed. Once they are available and validated, it will be required to prepare a corresponding toolbox for practical implementation. Indeed, if UM framework has been widely used in the academic world since its initial developments in the 80's, there is a need to foster its use by practitioners.

The systematic development of a toolbox for various applications should be implemented. The main applications to be incorporated are :

- Multifractal interpolation
- Comparison of measurements between various devices accounting for scale gap between their sampling areas
- Merging of various rainfall products
- Multifractal downscaling
- Joint multifractal nowcasting of wind and rainfall fields

The RadX@HM&Co platform (radx.enpc.fr) which is in place since 2017 (and regularly updated since then) primarily for display of HM&Co X-band radar data and related hydrological applications, will naturally be a tailored platform for initial applications of these tools. It should also be stressed that such toolbox will also constitute a good basis for fruitful partnership enabling further investigations and new developments.

5.4.3 Missing data and ensemble simulations

Missing data has been identified as a major issue for urban hydrology modelling especially at the high resolutions which are more and more required [98]. In section 3.3.2 a methodology based on a newly developed conditional β-model is presented to stochastically infill imperviousness missing data. The hydrological consequences were quantified on the Jouy-en-Josas case study and are rather limited in this specific example which was used as a proof of concept. The overall idea was to use the fractal nature of the underlying field to fill missing data in a way that this main feature is preserved.

In this initial implementation, the approach was developed to handle simply binary fields. This is clearly an oversimplification of the representation of the catchments which exhibit much wider ranges of potential behaviour. Indeed, with regards to the example of imperviousness discussed before, a pervious pixel can actually have a wide range of potential hydraulic conductivity. It turns out that this field is known to exhibit multifratal properties [215], which means that a generalization of the approach developed with the conditional β-model and the innovations discussed in section 5.3.1 could be envisaged. More generally, there is a need to develop infilling techniques that have the following features :

- They should be compatible and actually rely on the (multi)fractal features of the studied fields or area, i.e. the simulated fields should exhibit the expected multifractal features.

- They should enable to generate ensemble of realistic realisations. This will ensure that the corresponding uncertainty can be identified and further propagated within the hydrodynamic modelling chain.

Such approach, which I already developed with rainfall downscaling to quantify the impact of unmeasured small scale rainfall variability, should be deployed for all the input fields. For the case studies modelled with the help of the Multi-Hydro model, this will require to adapt the model to account for this wider variety of possible values for the input parameters apart from rain. Indeed for rainfall fields, a dedicated grid with a value per pixel is used as input while for the other inputs, only a limited number of classes (currently typically 6 to 10) with predefined values is used. Possibility to introduce maps for the various input parameters (hydraulic conductivity (m/s), capillary suction (m), moisture deficit (no unit, ranging from 0 to 1), Manning coefficient ($s.m^{-1/3}$) and depth of interception (mm)) should be developed.

As already pointed out in section 5.2.4 a paradigm shift occurred in the field of numerical weather prediction with the advent of ensemble of simulations (enabling the computation of probability distribution) rather than deterministic ones. This approach is (slowly) spreading into hydrology and it should furthermore expand to urban hydrology. The systematic use of ensemble of input fields and generation of the corresponding hydrodynamic simulations will contribute to this paradigm shift which is much needed to better account for the unavoidable uncertainties.

5.4.4 (Multi)fractal characterization and optimization of land cover

In section 3.2.2, fractal tools were used to characterize urban areas with a focus on impervious areas and sewer system. This approach turned out to be fruitful and enabled to quantify in a scale invariant way some features known to have strong effect on the hydrodynamic behaviour of the corresponding areas. It was then expanded to characterize the space occupied by building or green roofs.

Further steps in this direction should be carried out :

- Switch from binary fields to standard fields and hence from fractal to multifractal tools. This will enable to handle the actual variability of involved fields such as hydraulic conductivity already discussed in previous section.

- Expand the use of these scale invariant tools to optimization and not only characterization. For now, they have been used only to characterize static urban areas, but they could actually be used to optimize implementation of hydro-dynamic devices such green roofs, rain gardens, swales. Indeed such example of nature based solutions to improve resilience of urban areas are implemented locally but should be optimized at much larger scale. Multifractal tools which are intrinsically scale invariant are powerful ones in this context. An example mentioned here for illustrative purposes could be the evaluation of various greening scenarios to ensure that the fractal dimension of the covered areas is as great as possible, which would mean that its distribution enables them to fill as much space as possible.

5.4.5 Robust scale invariant metrics for model comparison

In section 3.1.2, the wide variety of models used to represent the urban portion of the water cycle is summarized. It highlighted the fact that they are based on very different underlying founding principles. Some are simply conceptual ones with basically a series of nested linear reservoirs; while others are much more physically based, in the sense that they aim at solving basic physical equations. Some rely on a mixture of both approaches. Furthermore these models are operated at very different spatial and temporal resolutions from few meters and few tens of seconds to few kilometres and few tens of minutes. Such variety raises a series of basic issues that should be addressed :

- What kind of data is required according the model ? Some elements of answers are provided in section 3.3.1 which showed that land use at 5-10 m provided an optimum. However it should be reminded that it is strongly related to the quality of the available data and the presence of numerous missing data at higher resolution. It is likely that if there was much less missing data, different outcome of the analysis would be obtained from the same analysis.

- Are these models able to properly represent and account for the extreme heterogeneity of both anthropogenic and geophysical fields ? Indeed for example in semi-distributed models, sub-catchments (which can indeed be of various sizes depending on the choice of the modeller) are areas considered as homogeneous which is actually not the case.

- How to compare them ? Indeed given the wide range of resolutions and numerous sources of uncertainty, with regards to both the representation of the areas and the unknown high resolution space-time features of the rainfall field; this seemingly simple question of comparing them is actually not trivial.

Ultimately all these issues boil down to the need to develop an appropriate metric for model comparison. Indeed the most commonly used metrics, which are scores (see section 3.3.1) computed at a given resolution, do not enable proper comparison accounting for the underlying complexity of the process. They are notably usually statistics of order two, meaning that the assumed underlying distribution is a Gaussian one. See for example Gupta et al. [86] for a discussion on the limitations of the famous Nash-Sutcliffe efficiency coefficient and hints for improvement. It turns out that the multifractal formalism, which is intrinsically scale invariant and designed to handle extreme variability across scales is a good candidate.

Some initial steps in this direction can be found in :

- The work of Hoang et al. [90] who developed a process to access the effective quality of rainfall time series based on a combination of three criteria : the percentage of missing data, the effective time resolution (quantified as the 'episode duration having the highest probability'), and the quality of the scaling (quantified with the help of coefficient of regression in scaling curves).

- The paper on fractal characterization of urban environment [74] from which some results are discussed in section 3.2.2. Indeed in addition to imperviousness maps, the representation of imperviousness in operational semi-distributed models was also analysed. It appeared that, by analysing the geometrical set made of sub-catchments with imperviousness greater than a given threshold, it is possible to retrieve urbanization patterns. It was also shown that comparing fractal dimension values related to modelled imperviousness to imperviousness represented in high-resolution GIS datasets allows one to quantify how well imperviousness is represented in urban hydrological models. These results opened perspectives for the development of tools to verify whether a hydrological model properly represents the degree of imperviousness in a catchment and also to study urbanization patterns emerging at different degrees of imperviousness.

Efforts to design a UM based appropriate metric for model comparison in urban areas able to account for variety of models, resolutions and heterogeneity of the underlying field should be implemented. It is a required step to significantly improve our understanding of the functioning of urban area and ultimately our ability to smartly manage them.

5.5 Widening the range of applications for UM

5.5.1 Wind energy

Multifractal tools have initially been designed to address the intermittent nature of wind turbulence. Hence using such tools in the framework of wind energy production is a rather natural step. This is exactly the purpose of the RW-Turb project whose main objectives are reported below.

According to the literature the rainfall effects on wind turbine efficiency seems to be significant, but have surprisingly received little attention. This was confirmed by data analysis [37, 238], lab experiment ([2], or multiphase CFD simulations [20, 31]. The main goal of RW-Turb is to overcome the current lack of knowledge on this topic through a genuine collaboration between an academic institution (HM&Co-ENPC) and a wind power production firm (Boralex).

More precisely two distinct aspects should be studied to properly address the topic; first the rainfall effect on the energy resources and second the rainfall effect on the conversion process of wind power to electric power by the wind turbine. In the following, rainfall should not be understood as commonly done as a simple rain rate expressed in $mm.h^{-1}$, but also considering its full complexity through the spatial and temporal variability of the drop size distribution (DSD).

- Rainfall effects on the wind power available. Both the wind energy and torque available to wind turbines are basically proportional to powers of the instantaneous wind speed. Obviously as wind is neither constant nor uniform, taking into account its small scale spatio-temporal fluctuations is crucial to properly quantify the integrals of these quantities especially given that wind turbines are located in the atmospheric boundary layer. Improving turbulence understanding has been listed among the scientific challenges of this field in a recent joint paper of leading academics of this field (van Kuik et al. [229], for the European Academy of Wind Energy, EAWE). The intrinsic intermittent nature of wind, i.e. the fact that its activity becomes located on smaller and smaller support as observation scale decreases, makes it complex to analyse, notably requiring appropriate theoretical framework and high resolution measuring devices. Rainfall was not up to now considered in such analysis.

- Rainfall effects on the energy conversion by wind turbine. Rainfall affects the functioning of the wind turbine through multiple effects: loss of momentum due to droplets, additional weight (rather balanced with several blades), and changes of the blades' surface features (notably rain induced roughness, and formation of a water layer), deteriorating the aerodynamic performance, which is the most significant effect according to the few studies available. Furthermore, variations in the generated vibrations could lead to adjustment by the wind turbine control system of the working conditions for avoiding accelerated degradation, yielding additional production loss. The effect of rain rate, DSD and drop velocity on this is usually mentioned in the few studies, either experimental or not, but seldom quantified.

RW-Turb aims at quantifying the influence of rainfall conditions on wind turbulence and how it is transferred to power production. In order to achieve this ambitious goal, a detailed scientific program and project organization was set up and is summarized in Fig. 5.2. It is designed to be implemented by two PhD projects which are currently ongoing (one is co-funded by ENPC). It will require some methodological developments which have already been discussed in the previous sections. The main elements are :

- WP 1: Experimental set-up and data collection. An observatory for combined high resolution measurements of wind (speed, direction, shear and turbulence), rainfall (DSD, and fall velocities) and power production will be installed for 2 years on a wind farm operated by Boralex and having a 86 m meteo mast. A user friendly data base will be created and data carefully validated.

- WP 2: Analysis and simulation of rainfall effects on the wind power available. It aims at analysing mainly with UM tools the collected data to quantify the influence of rainfall conditions on wind turbulence and air density. A classification of rainfall events will be designed for this purpose. Interpretation will require the development of innovative models. A new 3+1D model of drop fields in a 3D turbulent wind at wind turbine scale will be also developed. Scalar and vector spatio-temporal wind fields for scales ranging from few cm and to wind turbine size over few tens of seconds will be simulated by improving existing tools based on continuous UM cascades

- WP 3: Analysis and simulation of rainfall effects on energy conversion by wind turbine. The transfer of wind intermittency to power production will be analysed from the collected data (WP1). Then, two numerical modelling chains with increasing complexity will be developed to simulate and quantify the effect of wind turbulence on power production. The wind fields simulated in WP2 will be used (i) to compute available torque fluctuations, and (2) as input in a multi-disciplinary model for numerical simulation of wind turbine behaviour (existing to be customized). Ensembles of possible inputs will be used to quantify the sensitivity of the modelling chains to various input parameters corresponding to the different rainfall conditions.

The share of renewable energy is rapidly growing in France and Europe. Hence it is highly relevant to understand the uncertainty affecting the electricity production by such resources, notably because its intermittent nature raises complex challenges in terms of grid management. RW-Turb will have a strong impact on this field by providing a quantification of rainfall effects of wind power production and opening perspectives for improving nowcasts. Results will be up-scalable to other site because they will mainly be event-based.

5.5.2 Construction sites with cranes

The fulfilment of RW-Turb goals will provide new opportunities with regards to wind and its applications. This by the way is exactly the purpose of the ANR JCJC project, i.e. for young researchers. An example is the management of wind on construction sites involving numerous cranes. Indeed such work heavily relies on the proper functioning of the cranes which cannot operate and should be stopped when the wind is too strong. In order to help practitioners, there is a need to improve the quantification of wind extremes for long term planning, as well as wind nowcast (few minutes) and short term forecast (up to few hours) for real time management.

The data collected during RW-Turb, as well as the skills and tools available at HM&Co enable to envisage more precisely the required investigations :

- In section 2.1.3, the notion of divergence of moment is discussed. It explains theoretically why power law tail for probability distribution of values coming from an underlying UM field are expected. Furthermore the numerical value of the exponent of this power law can be derived from UM parameter estimates. In the case of wind fluctuations, this enables to account for the observed sporadic bursts, which are not treated in a standard Gaussian framework that strongly underestimates the extremes [57]. Similarly, it enables to retrieve power-law fall off for rainfall observations [42, 93]. It also provides a theoretical basis for the commonly used power law relations for Intensity-Duration-Frequency (IDF) curves that are the basic engineering tools used to quantify rainfall extremes [11, 231]. Extending the IDF formalism to wind fluctuations while deepening our understanding of its link with the underlying UM framework; will enable to better quantify wind extremes for practitioners.

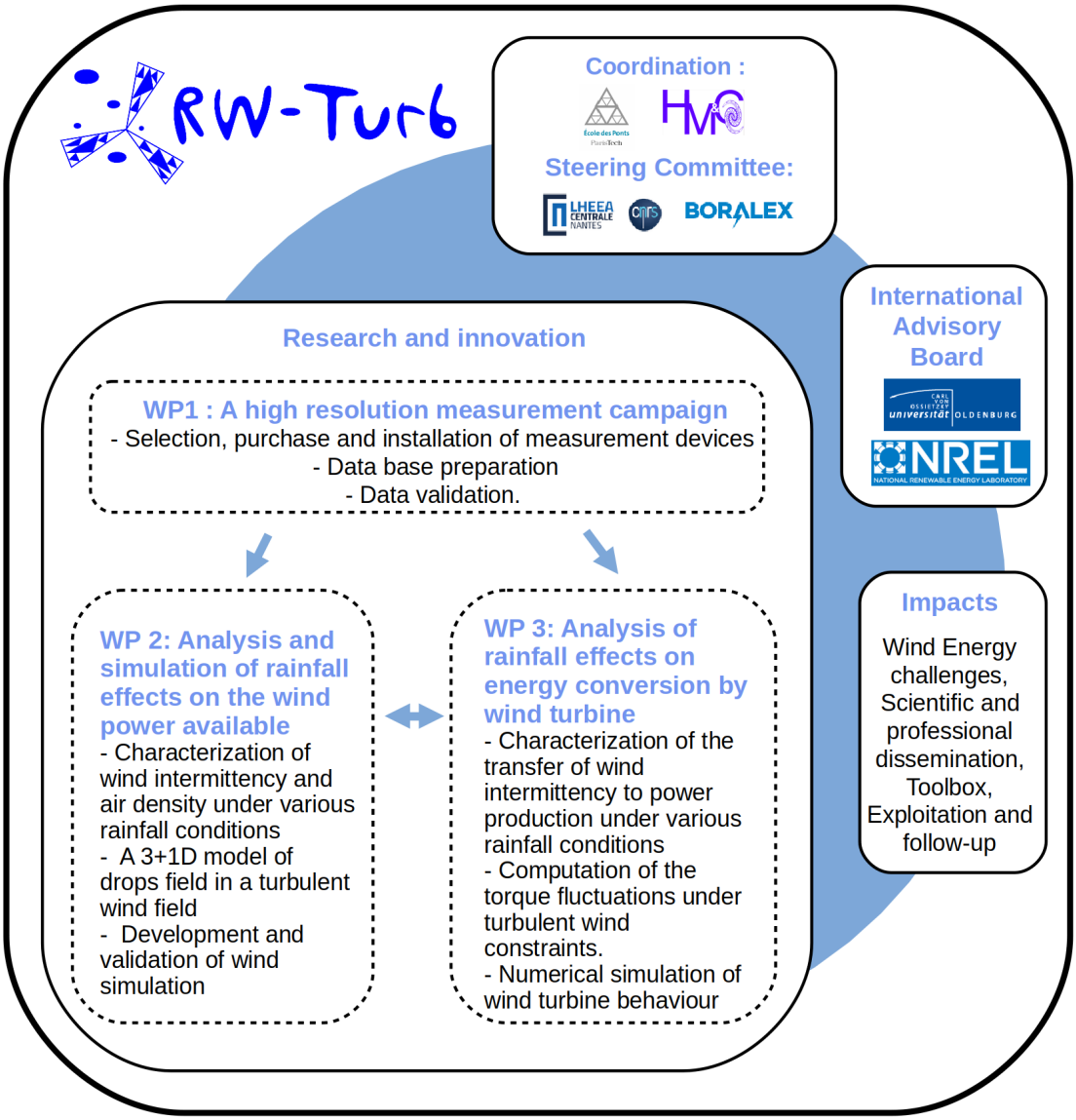

Figure 5.2: Outline of the RW-Turb project

- The tools developed by Schertzer and Tchiguirinskaia [200] to simulate vector fields could also be used to suggest nowcasting techniques for vector wind fields relying on the UM framework. For longer duration, developments of downscaling tools for wind fields to downscale outputs of numerical weather predictions models at construction site scale would also be required for forecasts with lead time of few hours. It should be stressed that such tools could also be implemented to improve power production nowcasts.

The combination of practical issues with underlying relevant and complex scientific challenges suggests that it is a relevant perspective for HM&Co laboratory.

5.5.3 Multifractal characterization of the meteorological condition in an environment chamber

In 2017, a rainfall measurement campaign was set up to test the rainfall generator a climate chamber located on the ENPC campus (see Sense-City campaign in section 4.2.2). It turns out that UM tools could help interpret experiments in this chamber. More precisely, the Sense-City urban innovation lab has built a 400 m^2 environment chamber that can host scale-1 mini districts. The chamber enables to reproduce given conditions of temperature, humidity, sunshine, and it also has a rainfall simulator covering a small portion of the area. Their are some fans whose purpose is to homogenised the atmosphere within the chamber and not to generate specific wind conditions. It is also possible to introduce pollutants to monitor their fate through the mini-district. The chamber is equipped with more than 200 sensors. Hence, Sense-city is an pioneering experimental equipment to study urban phenomena such as pollution, thermal exchange between urban object component or the impact of NBS in cities under different weather, including heat waves.

We live in current weather conditions and future ones are uncertain in the context of climate change. The environment chamber enables to test various scenarios on scale-1 mini-districts. Nevertheless, it is obviously not possible to reproduce exactly a given weather condition in the chamber which is designed to simulate average (potentially extreme) climatic conditions. The reproducible environment enables to quantify precisely the uncertainty associated with given parameters in controlled experiments. However, it also means that the outputs of the experiments carried out in the chamber should be re-interpreted to account for actual weather and notably the extreme variability of the geophysical fields that is actually not reproduced.

Hence there is a need to quantify the gap between some aspects of real weather conditions and simulated ones in the climatic chamber. Once this is achieved, when possible solutions to reduce this gap in both the design and the interpretation of the results of the experiments carried out will be developed and tested. First tests, which were initiated in the framework of Jerry Jose PhD program are focused on : (i) Rainfall and particles. (ii) Temperature & Humidity. (iii) Rain rate and kinetic energy and (iv) Rainfall and wind. They rely on methodologies similar to the ones used and developed in the framework of RW-Turb.

In the framework of growing cities embedded in their geophysical environment, addressing the pending challenge of understanding better the joint extreme variability of various urban geophysical fields and their impact on buildings and infrastructures is crucial. Developments will strengthen stochastic analysis techniques for individual fields and extends existing approaches for joint analysis of vector or multi-scalar fields. In addition, the expected results should contribute to improve parametrization of regional climate models.

5.5.4 Envisaged opportunities

In this section, I will present few examples of potential widening of applications for some of the products, methodologies and tools previously mentioned, notably multifractal ones. They do not correspond to an arbitrary and uncontrolled scattering of activities, but simply to new opportunities for applications of same methods. Hence they should simply be seen as potential fields for fruitful partnerships to help develop these methods.

Road traffic

The primary objective of the operator of a road network is to ensure traffic safety. When traffic is dense, especially on saturated suburban networks during peak hours, the rapid detection of any incident is an absolute priority to avoid additional accidents. Rainfall is one of the meteorological events likely to seriously disrupt road traffic, either by its very localized and intense character (e.g. thunderstorm), or because it is coupled with other meteorological conditions (e.g. freezing rain), or that, after a long episode of dry weather, the change in driving conditions is not immediately perceived by users and leads to a large number of simultaneous incidents at several points on the network.

The detailed study of these questions in particular, and more generally of the impact of rain on traffic, requires measurements of rainfall at a level of spatial and temporal resolution that has up to now been difficult to access. With the HM&Co-ENPC X-band radar which provides data at a resolution high enough for a detailed study of rain on traffic, the Ile-de-France region has become a relevant case study around these questions. The motorway network has had sensors quantifying traffic for many years. Hence the following objectives could be

pursued : (i) It will first be necessary to analyze, and then model, the impact of rain on road traffic in Ile-de-France. (ii) Once this effect has been properly integrated, it will be possible to design real-time operational assistance tools integrating high-resolution rainfall data. Particular attention should be paid to extreme rain events.

The quantification of the effects of rain on traffic has already been the subject of previous research, and some macroscopic effects are already documented (in particular the effects on capacity). However, the level of resolution of the available X-band radar, combined with the density of traffic sensors and other sources of information accessible in the Ile-de-France region, opens the way to an interesting potential for new knowledge and operational applications.

The main scientific obstacles to overcome will be the development of data processing methodologies adapted to the quantification and modelling of the impact of rain on traffic, at different spatial and temporal scales. In particular, it will be needed to adapt to the case of road traffic multifractal techniques of correlation analysis between time series used for example in hydrology or geophysics. There are already some applications of multifractal techniques to road traffic [178, 132, 237] but not integrating the precipitation dimension. The intrinsic space-time framework of these tools will make it possible to maintain a space-time and dynamic vision of the studied flows. Once this step is carried out, it will be possible to improve how rainfall is accounted for in road traffic models.

High resolution precision agriculture and soil erosion

Another example of applications of HM&Co X-band radar could be agriculture. Before going on, some elements should be reminded :

- Precision agriculture is booming, with the development of dedicated offers for spatial meteorological information at a scale of the order of one kilometre.
- There is continuous development of decision support tools for farmers through agronomic modelling (disease spread, plant growth) to optimize irrigation and use of fertilizers/treatments against weeds diseases.

Hence, in this context, it seems relevant to study the potential contribution of even higher resolution (100 m) and more diverse rainfall information on these decision support tools. By more diverse, I mean not only on accumulations of rain, but also information on the distribution of the sizes and velocities of drops which can have an influence on the spread of diseases and erosion of soils. Such dual polarization radar enables to access these distributions and their variability in space. Such kind of applications could help in the developments envisaged in section 5.2.1 on computation of DSD maps and quantification of the variability.

A somehow related issue is soil erosion. The previously mentioned work to be done on relating kinetic energy of rainfall and rate rate, as well as the development of DSD maps could serve as basis of generating maps of rainfall erosion power (erosivity). This kind of information can be helpful for long term management of fields.

Trees and turbulence with a focus on urban areas

Interactions between trees and wind are known to be complex. On the one hand, wind flow in the wake of a tree exhibits complex turbulent features. This has been investigated in numerous studies, numerically with CFD simulations, experimentally (see [7] for a work in a liquid tunnel with fractal tree-like structures) or directly outdoor (see for example [4] for a recent study with LIDAR measurements). On the other hand, wind also impacts trees and can even induce damage in case of strong wind. The behaviour of these partly flexible structures under turbulent wind stress is still a topic of research. In general, several key challenges have been identified on this topic [201]. The ones related to this document are : (i) a need to improve knowledge on the behaviour of wind at spatial and temporal scales of severe storms; (ii) a need to improve understanding of the interactions between wind and trees at local (tree) and landscape (forest) scale accounting for all their complexity.

More recently, there is a growing interest for trees in urban areas, notably in the framework of the advent of nature based solutions as a basic tool for climate change adaptation (see [153, 85] for illustrations). Empirical and numerical studies usually report that trees help mitigate urban heat island effects through evapotranspiration and shade provision. However, trees are also found to affect wind flow in cities with strong aerodynamic effects. In some areas, this can limit heat dissipation and also pollutant dissipation.

Hence, it appears that precisely quantifying the effects of trees in cities remains an open challenge because of the complex nonlinear interactions between the trees, the urban surfaces and turbulent atmosphere. Given the multifractal features of wind turbulence, and the (multi-)fractal properties of urban settings and even trees' shape, the UM framework appears to be an appropriate candidate for enabling significant progress in this area. Comprehensive theoretical, experimental and numerical projects with various partners would be needed to properly address this complex issue which has direct impact on the well being of citizens in cities.

Noise in cities

Another example of new field of application for UM techniques could be the study of noise in cities. Indeed some authors analysed 2D maps of noise and local morphological indicator (street width / building height) and showed that both exhibited multifractal features with a correlation more marked for neighborhood with a more regular map [5]. Other authors relied on simulations to show that the noise exposure level decreased with a higher fractality of the building distribution [206]; a fractal indicator can be used to help chose the resolution of a noise model [157], fractal noise barrier in which the developed surface is increased for the same apparent surface increases sound attenuation by the wall [188]. Fractal features of noise have also been used in 1D series analysis to study voice recognition in noisy environments [180], the noise emitted by crispy food [217] or boiling water [214], or the difference between urban and rural noise [40]. To summarize :

- Noise is found to inherently exhibit (multi)fractal under certain circumstances.
- The environment in which it propagates (city, countryside, wall) can also present fractal properties.
- There are non-trivial interactions between these different properties.

UM tools could relevantly be used in this field to :

- Develop an indicator that takes into account temporal variability. Indeed the current indicators commonly used and on which regulation are based do not take into account the variability of noise, and simply consider hourly aggregation of sound wave energy. UM tools which are designed to address extreme variability seem to be well suited to better account for this observed variability and notably the spikes.
- Improve space-time characterization of noise in an urban environment. Such developments could then be used to improve merging techniques between model outputs and existing measurements for the production of noise maps, or assessment of emission source management scenarios.
- Better understand the role of rain and humidity in reducing noise pollution. Indeed rain and humidity play a very important role in the genesis (tyre/road interaction, wet or not wet roads) and the propagation of sound and therefore the assessment of the nuisance.

Bibliography

[1] Mohamed-Aymen Ben Aissia, Fateh Chebana, and Taha B.M.J. Ouarda. Multivariate missing data in hydrology – review and applications. *Advances in Water Resources*, 110:299 – 309, 2017. ISSN 0309-1708. doi: https://doi.org/10.1016/j.advwatres.2017.10.002. URL http://www.sciencedirect.com/science/article/pii/S0309170816306236.

[2] B.C. Al, C. Klumpner C., and D.B. Hann. Effect of rain on vertical axis wind turbines, proceedings of the international conference on renewable energies and power quality, las palmas de gran canaria (spain), 13th to 15th april 2011. 1986.

[3] Emmanouil N. Anagnostou and W. F. Krajewski. Simulation of radar reflectivity fields: Algorithm formulation and evaluation. *Water Resour. Res.*, 33(6):1419–1428, 1997. doi: doi:10.1029/97WR00233.

[4] N. Angelou, J. Mann, and E. Dellwik. Wind lidars reveal turbulence transport mechanism in the wake of a tree. *Atmospheric Chemistry and Physics*, 22(4):2255–2268, 2022. doi: 10.5194/acp-22-2255-2022. URL https://acp.copernicus.org/articles/22/2255/2022/.

[5] Ana B. Ariza-Villaverde, Francisco J. Jiménez-Hornero, and Eduardo Gutiérrez De Ravé. Influence of urban morphology on total noise pollution: Multifractal description. *Science of The Total Environment*, 472:1 – 8, 2014. ISSN 0048-9697. doi: https://doi.org/10.1016/j.scitotenv.2013.10.091. URL http://www.sciencedirect.com/science/article/pii/S0048969713012357.

[6] Gholamhossein Baheri. *Numerical and experimental investigation of particle terminal velocity and aggregation in volcanic plumes. Thèse de doctorat no. Sc. 4844*. PhD thesis, Univ. Genève, 2015.

[7] Kunlun Bai, Charles Meneveau, and Joseph Katz. Experimental study of spectral energy fluxes in turbulence generated by a fractal, tree-like object. *Physics of Fluids*, 25(11):110810, 2013. doi: 10.1063/1.4819351. URL https://doi.org/10.1063/1.4819351.

[8] P. Bak, C. Tang, and K. Weissenfeld. Self-Organized Criticality. *Phys. Rev. Lett.*, 38:364–374, 1988.

[9] Alessandro Battaglia, Elke Rustemeier, Ali Tokay, Ulrich Blahak, and Clemens Simmer. PARSIVEL Snow Observations: A Critical Assessment. *Journal of Atmospheric and Oceanic Technology*, 27(2):333–344, 2010. URL http://dx.doi.org/10.1175/2009JTECHA1332.1.

[10] K. V. Beard. Terminal velocity adjustment for cloud and precipitation aloft. *J. Atmos. Sci*, 34:1293–1298, 1977.

[11] H. Bendjoudi, P. Hubert, D. Schertzer, and S. Lovejoy. Interprétation multifractale des courbes intensité-durée-fréquence des précipitations, Multifractal point of view on rainfall intensity-duration-frequency curves. *Comptes Rendus de l'Académie des Sciences - Series IIA - Earth and Planetary Science*, 325: 323–326, 1997.

[12] Ildegardis Bertol, Jefferson Schick, Douglas H. Bandeira, Jorge Paz-Ferreiro, and Eva Vidal Vázquez. Multifractal and joint multifractal analysis of water and soil losses from erosion plots: A case study under subtropical conditions in santa catarina highlands, brazil. *Geoderma*, 287: 116 – 125, 2017. ISSN 0016-7061. doi: https://doi.org/10.1016/j.geoderma.2016.08.008. URL http://www.sciencedirect.com/science/article/pii/S0016706116303470. STRUCTURE AND FUNCTION OF SOIL AND SOIL COVER IN A CHANGING WORLD: CHARACTERIZATION AND SCALING.

[13] A. Biaou, F. Chauvin, J.-F. Royer, and D. Schertzer. Analyse multifractale des précipitations dans un scénario GIEC du CNRM. *Note de centre GMGEC, CNRM*, 101:45, 2005.

[14] Bert Blocken, Ted Stathopoulos, Jan Carmeliet, and Jan L.M. Hensen. Application of computational fluid dynamics in building performance simulation for the outdoor environment: an overview. *Journal of Building Performance Simulation*, 4(2):157–184, 2011. doi: 10.1080/19401493.2010.513740. URL https://doi.org/10.1080/19401493.2010.513740.

[15] Neill E. Bowler, Clive E. Pierce, and Alan W. Seed. STEPS: A probabilistic precipitation forecasting scheme which merges an extrapolation nowcast with downscaled NWP. *Quarterly Journal of the Royal Meteorological Society*, 132(620):2127–2155, 2006. URL http://dx.doi.org/10.1256/qj.04.100.

[16] Edward A. Brandes, Guifu Zhang, and J. Vivekanandan. Drop size distribution retrieval with polarimetric radar: Model and application. *Journal of Applied Meteorology*, 43(3):461–475, 2004. doi: 10.1175/1520-0450(2004)043¡0461:DSDRWP¿2.0.CO;2. URL https://doi.org/10.1175/1520-0450(2004)043<0461:DSDRWP>2.0.CO;2.

[17] V. Bringi, M. Thurai, and D. Baumgardner. Raindrop fall velocities from an optical array probe and 2-d video disdrometer. *Atmospheric Measurement Techniques*, 11(3):1377–1384, 2018. doi: 10.5194/amt-11-1377-2018. URL https://www.atmos-meas-tech.net/11/1377/2018/.

[18] V.N. Bringi and V Chandrasekar. *Polarimetric Doppler weather radar: principles and applications*. Cambridge university press, 2001.

[19] András Bárdossy and Geoffrey Pegram. Infilling missing precipitation records – a comparison of a new copula-based method with other techniques. *Journal of Hydrology*, 519:1162 – 1170, 2014. ISSN 0022-1694. doi: https://doi.org/10.1016/j.jhydrol.2014.08.025. URL http://www.sciencedirect.com/science/article/pii/S0022169414006350.

[20] Ming Cai, Emadoddin Abbasi, and Hamid Arastoopour. Analysis of the Performance of a Wind-Turbine Airfoil under Heavy-Rain Conditions Using a Multiphase Computational Fluid Dynamics Approach. *Industrial & Engineering Chemistry Research*, 52(9):3266–3275, March 2013. ISSN 0888-5885. doi: 10.1021/ie300877t. URL http://dx.doi.org/10.1021/ie300877t.

[21] R. Calif and F. G. Schmitt. Multiscaling and joint multiscaling description of the atmospheric wind speed and the aggregate power output from a wind farm. *Nonlinear Processes in Geophysics*, 21(2):379–392, 2014. doi: 10.5194/npg-21-379-2014. URL http://www.nonlin-processes-geophys.net/21/379/2014/.

[22] Campbell-Scientific-Ltd. PWS100 Present Weather Sensor, User Guide. 2012.

[23] Edwin Campos and Isztar Zawadzki. Instrumental Uncertainties in Z-R Relations. *Journal of Applied Meteorology*, 39(7):1088–1102, 2000. URL http://dx.doi.org/10.1175/1520-0450(2000)039<1088:IUIZRR>2.0.CO;2.

[24] Vincenzo Capozzi, Clizia Annella, Mario Montopoli, Elisa Adirosi, Giannetta Fusco, and Giorgio Budillon. Influence of wind-induced effects on laser disdrometer measurements: Analysis and compensation strategies. *Remote Sensing*, 13(15), 2021. ISSN 2072-4292. doi: 10.3390/rs13153028. URL https://www.mdpi.com/2072-4292/13/15/3028.

[25] Carlo Capsoni and Michele D'Amico. A Physically Based Radar Simulator. *Journal of Atmospheric and Oceanic Technology*, 15(2):593–598, April 1998. ISSN 0739-0572. doi: 10.1175/1520-0426(1998)015¡0593:APBRS¿2.0.CO;2. URL http://dx.doi.org/10.1175/1520-0426(1998)015<0593:APBRS>2.0.CO;2.

[26] Carlo Capsoni, Michele D'Amico, and Roberto Nebuloni. A Multiparameter Polarimetric Radar Simulator. *Journal of Atmospheric and Oceanic Technology*, 18(11):1799–1809, November 2001. ISSN 0739-0572. doi: 10.1175/1520-0426(2001)018¡1799:AMPRS¿2.0.CO;2. URL http://dx.doi.org/10.1175/1520-0426(2001)018<1799:AMPRS>2.0.CO;2.

[27] Olivier Caumont, VÃ©ronique Ducrocq, Guy Delrieu, Marielle Gosset, Jean-Pierre Pinty, Jacques Parent du ChÃ¢telet, Yvon LemaÃ®tre, and Georges Scialom. A Radar Simulator for High-Resolution Nonhydrostatic Models. *Journal of Atmospheric and Oceanic Technology*, 23(8):1049–1067, 2006. URL http://dx.doi.org/10.1175/JTECH1905.1.

[28] J. M. Chambers, C. L. Mallows, and B. W. Stuck. Method for simulating stable random-variables. *Journal of the American Statistical Association*, 71(354):340–344, 1976. URL <Go to ISI>://A1976BT96100013.

[29] B. L. Cheong, R. D. Palmer, and M. Xue. A Time Series Weather Radar Simulator Based on High-Resolution Atmospheric Models. *Journal of Atmospheric and Oceanic Technology*, 25(2):230–243, February 2008. ISSN 0739-0572. doi: 10.1175/2007JTECHA923.1. URL http://dx.doi.org/10.1175/2007JTECHA923.1.

[30] G. J. Ciach and W. F. Krajewski. On the estimation of radar rainfall error variance. *Advances in Water Resources*, 22(6):585–595, February 1999. URL <Go to ISI>://WOS:000079211500004.

[31] Aiden C. Cohan and Hamid Arastoopour. Numerical simulation and analysis of the effect of rain and surface property on wind-turbine airfoil performance. *International Journal of Multiphase Flow*, 81:46–53, May 2016. ISSN 0301-9322. doi: 10.1016/j.ijmultiphaseflow.2016.01.006. URL http://www.sciencedirect.com/science/article/pii/S0301932216000069.

[32] Matteo Colli, Luca G. Lanza, Roy Rasmussen, and Julie M. Thériault. The collection efficiency of shielded and unshielded precipitation gauges. part i: Cfd airflow modeling. *Journal of Hydrometeorology*, 17(1): 231 – 243, 2016. doi: 10.1175/JHM-D-15-0010.1.

[33] Matteo Colli, Luca G. Lanza, Roy Rasmussen, and Julie M. Thériault. The collection efficiency of shielded and unshielded precipitation gauges. part ii: Modeling particle trajectories. *Journal of Hydrometeorology*, 17(1):245 – 255, 2016. doi: 10.1175/JHM-D-15-0011.1.

[34] Matteo Colli, Michael Pollock, Mattia Stagnaro, Luca G. Lanza, Mark Dutton, and Enda O'Connell. A computational fluid-dynamics assessment of the improved performance of aerodynamic rain gauges. *Water Resources Research*, 54(2):779–796, 2018. doi: https://doi.org/10.1002/2017WR020549. URL https://agupubs.onlinelibrary.wiley.com/doi/abs/10.1002/2017WR020549.

[35] C. G. Collier. *Application of weather radar systems.* 1996.

[36] C.G. Collier. The impact of wind drift on the utility of very high spatial resolution radar data over urban areas. *Physics and Chemistry of the Earth, Part B: Hydrology, Oceans and Atmosphere*, 24(8):889–893, 1999. ISSN 1464-1909. doi: https://doi.org/10.1016/S1464-1909(99)00099-4. URL https://www.sciencedirect.com/science/article/pii/S1464190999000994.

[37] R. Corrigan and R. Demiglio. Effect of precipitation on wind turbine performance. nasa tm-86986. 1985.

[38] Qiang Dai, Dawei Han, Miguel A. Rico-Ramirez, and Tanvir Islam. The impact of raindrop drift in a three-dimensional wind field on a radar–gauge rainfall comparison. *International Journal of Remote Sensing*, 34(21):7739–7760, 2013. doi: 10.1080/01431161.2013.826838. URL https://doi.org/10.1080/01431161.2013.826838.

[39] Qiang Dai, Qiqi Yang, Dawei Han, Miguel A. Rico-Ramirez, and Shuliang Zhang. Adjustment of radar-gauge rainfall discrepancy due to raindrop drift and evaporation using the weather research and forecasting model and dual-polarization radar. *Water Resources Research*, 55(11):9211–9233, 2019. doi: https://doi.org/10.1029/2019WR025517. URL https://agupubs.onlinelibrary.wiley.com/doi/abs/10.1029/2019WR025517.

[40] B. De Coensel, D. Botteldooren, and T. De Muer. 1/f noise in rural and urban soundscapes. *Acta Acustica united with Acustica*, 89(2):287–295, 2003. ISSN 1610-1928. URL https://www.ingentaconnect.com/content/dav/aaua/2003/00000089/00000002/art00012.

[41] M. I. P. de Lima and Jlmp de Lima. Investigating the multifractality of point precipitation in the Madeira archipelago. *Nonlinear Processes in Geophysics*, 16(2):299–311, 2009. URL <Go to ISI>://000265743500013.

[42] M. I. P. de Lima and J. Grasman. Multifractal analysis of 15-min and daily rainfall from a semi-arid region in Portugal. *Journal of Hydrology*, 220(1-2):1–11, July 1999. URL <Go to ISI>://WOS:000081464500001.

[43] R. Deidda. Rainfall downscaling in a space-time multifractal framework. *Water Resour. Res.*, 36:1779–1794, 2000.

[44] Guy Delrieu, Isabelle Braud, Alexis Berne, Marco Borga, Brice Boudevillain, Frederic Fabry, Jim Freer, Eric Gaume, Eiichi Nakakita, Alan Seed, Pierre Tabary, and Remko Uijlenhoet. Weather radar and hydrology Preface. *Advances in Water Resources*, 32(7):969–974, July 2009. URL <Go to ISI>://WOS:000267676700001.

[45] J. Despotovic, J. Plavsic, N. Stefanovic, and D. Pavlovic. Inefficiency of storm water inlets as a source of urban floods. *Water Science and Technology*, 51(2):139–145, 01 2005. ISSN 0273-1223. doi: 10.2166/wst.2005.0041. URL https://doi.org/10.2166/wst.2005.0041.

[46] S. Diss, J. Testud, J. Lavabre, P. Ribstein, E. Moreau, and J. P. du Chatelet. Ability of a dual polarized X-band radar to estimate rainfall. *Advances in Water Resources*, 32(7):975–985, July 2009. URL <Go to ISI>://WOS:000267676700002.

[47] S. Djordjevic, D. Prodanovic, and C. Maksimovic. An approach to simulation of dual drainage. *Water Science and Technology*, 39(9):95–103, 1999.

[48] S. Djordjević, D. Prodanović, Č Maksimović, M. Ivetić, and D. Savić. SIPSON – Simulation of Interaction between Pipe flow and Surface Overland flow in Networks. *Water Science and Technology*, 52(5):275–283, September 2005. ISSN 0273-1223, 1996-9732. URL http://wst.iwaponline.com/content/52/5/275.

[49] Monssef Drissi-Habti, Venkadesh Raman, Aghiad Khadour, and Safiullah Timorian. Fiber optic sensor embedment study for multi-parameter strain sensing. *Sensors*, 17(4), 2017. ISSN 1424-8220. doi: 10.3390/s17040667. URL https://www.mdpi.com/1424-8220/17/4/667.

[50] Véronique Ducrocq, Isabelle Braud, Silvio Davolio, Rossella Ferretti, Cyrille Flamant, Agustin Jansa, Norbert Kalthoff, Evelyne Richard, Isabelle Taupier-Letage, Pierre-Alain Ayral, Sophie Belamari, Alexis Berne, Marco Borga, Brice Boudevillain, Olivier Bock, Jean-Luc Boichard, Marie-Noelle Bouin, Olivier Bousquet, Christophe Bouvier, Jacopo Chiggiato, Domenico Cimini, Ulrich Corsmeier, Laurent Coppola, Philippe Cocquerez, Eric Defer, Julien Delanoé, Paolo Di Girolamo, Alexis Doerenbecher, Philippe Drobinski, Yann Dufournet, Nadia Fourrié, Jonathan J. Gourley, Laurent Labatut, Dominique Lambert, José me Le Coz, Frank S. Marzano, Gilles Molinia, Andrea Montani, Guillaume Nord, Mathieu Nuret, Karim Ramage, Bill Rison, Odile Roussot, Frédérique Said, Alfons Schwarzenboeck, Pierre Testor, Joel Van Baelen, BÃ©atrice Vincendon, Montserrat Aran, and Jorge Tamayo. HyMeX-SOP1, the field campaign dedicated to heavy precipitation and flash flooding in the northwestern Mediterranean. *Bulletin of the American Meteorological Society*, 2014. URL http://dx.doi.org/10.1175/BAMS-D-12-00244.1.

[51] T. Einfalt, K. Arnbjerg-Nielsen, C. Golz, N. E. Jensen, M. Quirmbach, G. Vaes, and B. Vieux. Towards a roadmap for use of radar rainfall data in urban drainage. *Journal of Hydrology*, 299(3-4):186–202, December 2004. URL <Go to ISI>://000224934700004.

[52] E. El Tabach, I. Tchiguirinskaia, O. Mahmood, and D. Schertzer. Multi-Hydro: a spatially distributed numerical model to assess and manage runoff processes in peri-urban watersheds. In *Final conference of the COST Action C22 Urban Flood Management*, Paris 26/27.11.2009, France, 2009.

[53] R. A. Ellis, A. P. Sandford, G. E. Jones, J. Richards, J. Petzing, and J. M. Coupland. New laser technology to determine present weather parameters. *Measurement Science & Technology*, 17(7):1715–1722, July 2006. URL <Go to ISI>://WOS:000238645900011.

[54] I. Emmanuel, H. Andrieu, and P. Tabary. Evaluation of the new French operational weather radar product for the field of urban hydrology. *Atmospheric Research*, 103:20–32, January 2012. URL <Go to ISI>://WOS:000298776600003. Atmos. Res.

[55] J. S. Erkelens, V. K. C. Venema, H. W. J. Russchenberg, and L. P. Ligthart. Coherent Scattering of Microwaves by Particles: Evidence from Clouds and Smoke. *Journal of the Atmospheric Sciences*, 58(9): 1091–1102, May 2001. ISSN 0022-4928. doi: 10.1175/1520-0469(2001)058¡1091:CSOMBP¿2.0.CO;2. URL http://dx.doi.org/10.1175/1520-0469(2001)058<1091:CSOMBP>2.0.CO;2.

[56] Jordi Figueras i Ventura, Abdel-Amin Boumahmoud, Béatrice Fradon, Pascale Dupuy, and Pierre Tabary. Long-term monitoring of French polarimetric radar data quality and evaluation of several polarimetric quantitative precipitation estimators in ideal conditions for operational implementation at C-band. *Quarterly Journal of the Royal Meteorological Society*, pages n/a–n/a, 2012. URL http://dx.doi.org/10.1002/qj.1934.

[57] G Fitton, I Tchiguirinskaia, D Schertzer, and S Lovejoy. Torque fluctuations in the framework of a multifractal 23/9-dimensional turbulence model. *Journal of Physics: Conference Series*, 555:012038, dec 2014. doi: 10.1088/1742-6596/555/1/012038. URL https://doi.org/10.1088/1742-6596/555/1/012038.

[58] T. D. Fletcher, H. Andrieu, and P. Hamel. Understanding, management and modelling of urban hydrology and its consequences for receiving waters: A state of the art. *Advances in Water Resources*, 51(0):261–279, 2013. URL http://www.sciencedirect.com/science/article/pii/S0309170812002412.

[59] Renato Prata de Moraes Frasson, Luciana Kindl da Cunha, and Witold F. Krajewski. Assessment of the Thies optical disdrometer performance. *Atmospheric Research*, 101(1â€“2):237–255, 2011. URL http://www.sciencedirect.com/science/article/pii/S0169809511000639.

[60] Uriel Frisch, Pierre-Louis Sulem, and Mark Nelkin. A simple dynamical model of intermittent fully developed turbulence. *Journal of Fluid Mechanics*, 87(4):719–736, 1978. doi: 10.1017/S0022112078001846.

[61] Unai Garciarena and Roberto Santana. An extensive analysis of the interaction between missing data types, imputation methods, and supervised classifiers. *Expert Systems with Applications*, 89:52 – 65, 2017. ISSN 0957-4174. doi: https://doi.org/10.1016/j.eswa.2017.07.026. URL http://www.sciencedirect.com/science/article/pii/S095741741730502X.

[62] E. Gaume, N. Mouhous, and H. Andrieu. Rainfall stochastic disaggregation models: Calibration and validation of a multiplicative cascade model. *Advances in Water Resources*, 30 (5):1301–1319, May 2007. ISSN 0309-1708. doi: 10.1016/j.advwatres.2006.11.007. URL http://www.sciencedirect.com/science/article/pii/S0309170806002144.

[63] A. Giangola-Murzyn. *Modélisation et paramétrisation hydrologique de la ville, résilience aux inondations*. PhD thesis, Université Paris-Est, Champs-sur-Marne, France, 2013.

[64] A. Giangola-Murzyn, A. Gires, T. Hoang, I. Tchiguirinskaia, and D. Schertzer. Multi-Component Physically Based Model to Assess Systemic Resilience in Paris Region. *Proceedings Hydro-Informatics Conference, Hamburg, 14-18 July 2012, Germany*, 2012.

[65] A. Gires, D. Schertzer, I. Tchiguirinskaia, S. Lovejoy, C. Maksimovic, C. Onof, and N. Simoes. Impact of unmeasured rainfall variability on urban discharge: a case study in a multifractal framework. *Houille Blanche-Revue Internationale De L Eau*, (4):37–42, June 2011. URL <Go to ISI>://WOS:000295863800007. Houille Blanche-Rev. Int.

[66] A. Gires, I. Tchiguirinskaia, D. Schertzer, and S. Lovejoy. Analyses multifractales et spatio-temporelles des precipitations du modele Meso-NH et des donnees radar. *Hydrological Sciences Journal-Journal Des Sciences Hydrologiques*, 56(3):380–396, 2011. URL <Go to ISI>://WOS:000291263600003.

[67] A. Gires, C. Onof, C. Maksimovic, D. Schertzer, I. Tchiguirinskaia, and N. Simoes. Quantifying the impact of small scale unmeasured rainfall variability on urban runoff through multifractal downscaling: A case study. *Journal of Hydrology*, 442-443:117–128, 2012. URL http://www.sciencedirect.com/science/article/pii/S0022169412002685.

[68] A. Gires, D. Schertzer, I. Tchiguirinskaia, S. Lovejoy, C. Onof, C. Maksimovic, and N. Simoes. Impact of small scale rainfall uncertainty on urban discharge forecasts. In R. Moore, Cole J., and Anthony J. Illingworth, editors, *Weather Radar and Hydrology, IAHS Publ. 351*, pages 400–406. IAHS Publ., 2012.

[69] A. Gires, I. Tchiguirinskaia, D. Schertzer, and S. Lovejoy. Influence of the zero-rainfall on the assessment of the multifractal parameters. *Advances in Water Resources*, 45:13–25, 2012. URL http://www.sciencedirect.com/science/article/pii/S0309170812000814.

[70] A. Gires, I. Tchiguirinskaia, D. Schertzer, and S. Lovejoy. Development and analysis of a simple model to represent the zero rainfall in a universal multifractal framework. *Nonlinear Processes in Geophysics*, 20(3):343–356, 2013. doi: 10.5194/npg-20-343-2013. URL http://www.nonlin-processes-geophys.net/20/343/2013/.

[71] A. Gires, I. Tchiguirinskaia, D. Schertzer, and S. Lovejoy. Multifractal analysis of a semi-distributed urban hydrological model. *Urban Water Journal*, 10(3):195–208, 2013. URL http://dx.doi.org/10.1080/1573062X.2012.716447.

[72] A. Gires, I. Tchiguirinskaia, and D. Schertzer. Multifractal comparison of the outputs of two optical disdrometers. *Hydrological Sciences Journal*, 61(9):1641–1651, 2016. doi: 10.1080/02626667.2015.1055270. URL https://doi.org/10.1080/02626667.2015.1055270.

[73] A. Gires, I. Tchiguirinskaia, and D. Schertzer. Drop by drop backscattered signal of a 50×50×50m3 volume: A numerical experiment. *Atmospheric Research*, 178-179:164 – 174, 2016. ISSN 0169-8095. doi: https://doi.org/10.1016/j.atmosres.2016.03.024. URL http://www.sciencedirect.com/science/article/pii/S0169809516300874.

[74] A. Gires, I. Tchiguirinskaia, D. Schertzer, S. Ochoa-Rodriguez, P. Willems, A. Ichiba, L.-P. Wang, R. Pina, J. Van Assel, G. Bruni, D. Murla Tuyls, and M.-C. ten Veldhuis. Fractal analysis of urban catchments and their representation in semi-distributed models: imperviousness and sewer system. *Hydrology and Earth System Sciences*, 21(5):2361–2375, 2017. doi: 10.5194/hess-21-2361-2017. URL https://www.hydrol-earth-syst-sci.net/21/2361/2017/.

[75] A. Gires, I. Tchiguirinskaia, and D. Schertzer. Two months of disdrometer data in the paris area. *Earth System Science Data*, 10(2):941–950, 2018. doi: 10.5194/essd-10-941-2018. URL https://www.earth-syst-sci-data.net/10/941/2018/.

[76] A. Gires, I. Tchiguirinskaia, and D. Schertzer. Pseudo-radar algorithms with two extremely wet months of disdrometer data in the paris area. *Atmospheric Research*, 203:216 – 230, 2018. ISSN 0169-8095. doi: https://doi.org/10.1016/j.atmosres.2017.12.011. URL http://www.sciencedirect.com/science/article/pii/S0169809517307111.

[77] A. Gires, P. Bruley, A. Ruas, D. Schertzer, and I. Tchiguirinskaia. Disdrometer measurements under sensecity rainfall simulator. *Earth System Science Data*, 12(2):835–845, 2020. doi: 10.5194/essd-12-835-2020. URL https://www.earth-syst-sci-data.net/12/835/2020/.

[78] A. Gires, I. Tchiguirinskaia, and D. Schertzer. Approximate multifractal correlation and products of universal multifractal fields, with application to rainfall data. *Nonlinear Processes in Geophysics*, 27(1):133–145, 2020. doi: 10.5194/npg-27-133-2020. URL https://www.nonlin-processes-geophys.net/27/133/2020/.

[79] Auguste Gires, Agathe Giangola-Murzyn, Jean-Baptiste Abbes, Ioulia Tchiguirinskaia, Daniel Schertzer, and Shaun Lovejoy. Impacts of small scale rainfall variability in urban areas: a case study with 1d and 1d/2d hydrological models in a multifractal framework. *Urban Water Journal*, pages 1–11, 2014. URL http://dx.doi.org/10.1080/1573062X.2014.923917.

[80] Auguste Gires, Ioulia Tchiguirinskaia, Daniel Schertzer, Alma Schellart, Alexis Berne, and Shaun Lovejoy. Influence of small scale rainfall variability on standard comparison tools between radar and rain gauge data. *Atmospheric Research*, 138(0):125–138, 2014. URL http://www.sciencedirect.com/science/article/pii/S0169809513003293.

[81] Auguste Gires, Ioulia Tchiguirinskaia, Daniel Schertzer, and Alexis Berne. 2dvd Data Revisited: Multifractal Insights into Cuts of the Spatiotemporal Rainfall Process. *Journal of Hydrometeorology*, 16(2):548–562, April 2015. ISSN 1525-755X. doi: 10.1175/JHM-D-14-0127.1. URL http://dx.doi.org/10.1175/JHM-D-14-0127.1.

[82] Auguste Gires, Jean-Baptiste Abbes, Igor da Silva Rocha Paz, Ioulia Tchiguirinskaia, and Daniel Schertzer. Multifractal characterisation of a simulated surface flow: A case study with multi-hydro in jouy-en-josas, france. *Journal of Hydrology*, 558:482 – 495, 2018. ISSN 0022-1694. doi: https://doi.org/10.1016/j.jhydrol.2018.01.062. URL https://www.sciencedirect.com/science/article/pii/S0022169418300714.

[83] Auguste Gires, Ioulia Tchiguirinskaia, and Daniel Schertzer. Blunt extension of discrete universal multifractal cascades: development and application to downscaling. *Hydrological Sciences Journal*, 0(0):1–17, 2020. doi: 10.1080/02626667.2020.1736297. URL https://doi.org/10.1080/02626667.2020.1736297.

[84] Auguste Gires, Ioulia Tchiguirinskaia, and Daniel Schertzer. Infilling missing data of binary geophysical fields using scale invariant properties through an application to imperviousness in urban areas. *Hydrological Sciences Journal*, 66(7):1197–1210, 2021. doi: 10.1080/02626667.2021.1925121. URL https://doi.org/10.1080/02626667.2021.1925121.

[85] Tom Grylls and Maarten van Reeuwijk. Tree model with drag, transpiration, shading and deposition: Identification of cooling regimes and large-eddy simulation. *Agricultural and Forest Meteorology*, 298-299:108288, 2021. ISSN 0168-1923. doi: https://doi.org/10.1016/j.agrformet.2020.108288. URL https://www.sciencedirect.com/science/article/pii/S0168192320303907.

[86] Hoshin V. Gupta, Harald Kling, Koray K. Yilmaz, and Guillermo F. Martinez. Decomposition of the mean squared error and nse performance criteria: Implications for improving hydrological modelling. *Journal of Hydrology*, 377(1):80–91, 2009. ISSN 0022-1694. doi: https://doi.org/10.1016/j.jhydrol.2009.08.003. URL https://www.sciencedirect.com/science/article/pii/S0022169409004843.

[87] V. K. Gupta and E. Waymire. A Statistical Analysis of Mesoscale Rainfall as a Random Cascade. *J. Appl. Meteor*, 32:251–267, 1993.

[88] P. Hazenberg, H. Leijnse, and R. Uijlenhoet. Radar rainfall estimation of stratiform winter precipitation in the Belgian Ardennes. *Water Resources Research*, 47, February 2011. URL <Go to ISI>://WOS:000287037700001.

[89] R. W. Healy. Simulation of solute transport in variably saturated porous media with supplemental information on modifications to the us geological survey's computer program vs2d. *U.S. Geological Survey*, 1990.

[90] C. T. Hoang, I. Tchiguirinskaia, D. Schertzer, P. Arnaud, J. Lavabre, and S. Lovejoy. Assessing the high frequency quality of long rainfall series. *Journal of Hydrology*, 438-439(0):39–51, 2012. URL http://www.sciencedirect.com/science/article/pii/S002216941200087X.

[91] M. H. Hsu, S. H. Chen, and T. J. Chang. Inundation simulation for urban drainage basin with storm sewer system. *Journal of Hydrology*, 234(1â€“2):21–37, 2000. URL http://www.sciencedirect.com/science/article/pii/S0022169400002377.

[92] Qingfang Hu, Zhe Li, Leizhi Wang, Yong Huang, Yintang Wang, and Lingjie Li. Rainfall spatial estimations: A review from spatial interpolation to multi-source data merging. *Water*, 11(3), 2019. ISSN 2073-4441. doi: 10.3390/w11030579. URL https://www.mdpi.com/2073-4441/11/3/579.

[93] P. Hubert. Multifractals as a tool to overcome scale problems in hydrology. *Hydrological Sciences Journal-Journal Des Sciences Hydrologiques*, 46(6):897–905, December 2001. URL <Go to ISI>://WOS:000173295700006. Hydrol. Sci. J.-J. Sci. Hydrol.

[94] P. Hubert, Y. Tessier, P. Ladoy, S. Lovejoy, D. Schertzer, J. P. Carbonnel, S. Violette, I. Desurosne, and F. Schmitt. Multifractals and extreme rainfall events. *Geophys. Res. Lett.*, 20:931–934, 1993.

[95] P. Hubert, F. Friggit, and J. P. Carbonnel. Multifractal structure of rainfall occurrence in west Africa. In Z. W. Kundzewicz, editor, *New Uncertainty Concepts in Hydrology andWater Resources*, pages 109–113. Cambridge University Press, Cambridge, 1995.

[96] Andreas Hölzer and Martin Sommerfeld. New simple correlation formula for the drag coefficient of non-spherical particles. *Powder Technology*, 184(3):361–365, 2008. ISSN 0032-5910. doi: https://doi.org/10.1016/j.powtec.2007.08.021. URL https://www.sciencedirect.com/science/article/pii/S0032591007004792.

[97] A. Ichiba. *X-band radar data and predictive management in urban hydrology.* PhD thesis, Université Paris-Est, Champs-sur-Marne, France, 2016.

[98] A. Ichiba, A. Gires, I. Tchiguirinskaia, D. Schertzer, P. Bompard, and M.-C. Ten Veldhuis. Scale effect challenges in urban hydrology highlighted with a distributed hydrological model. *Hydrology and Earth System Sciences*, 22(1):331–350, 2018. doi: 10.5194/hess-22-331-2018. URL https://www.hydrol-earth-syst-sci.net/22/331/2018/.

[99] S Insa-Valor. *Canoe: logiciel d'hydrologie urbaine, conception et evaluation de reseaux d'assainissement, simulation des pluies, des ecoulements et de la qualite des eaux, Manuel de l'utilisateur*, 1999.

[100] IPCC. Working Group 1 contribution to the IPCC fifth report climate change 2013: the physical science basis, summary of policy makers. Technical report. 2013.

[101] J. Jaffrain, A. Studzinski, and A. Berne. A network of disdrometers to quantify the small-scale variability of the raindrop size distribution. *Wat. Resour. Res.*, 47(W00H06), 2011.

[102] Joel Jaffrain and Alexis Berne. Influence of the Subgrid Variability of the Raindrop Size Distribution on Radar Rainfall Estimators. *Journal of Applied Meteorology and Climatology*, 51(4):780–785, 2012. URL http://dx.doi.org/10.1175/JAMC-D-11-0185.1.

[103] Joel Jaffrain and Alexis Berne. Quantification of the Small-Scale Spatial Structure of the Raindrop Size Distribution from a Network of Disdrometers. *Journal of Applied Meteorology and Climatology*, 51(5): 941–953, 2012. URL http://dx.doi.org/10.1175/JAMC-D-11-0136.1.

[104] A. R. Jameson and A. B. Kostinski. Direct Observations of Coherent Backscatter of Radar Waves in Precipitation. *Journal of the Atmospheric Sciences*, 67(9):3000–3005, June 2010. ISSN 0022-4928. doi: 10.1175/2010JAS3488.1. URL http://dx.doi.org/10.1175/2010JAS3488.1.

[105] A. R. Jameson and A. B. Kostinski. Partially Coherent Backscatter in Radar Observations of Precipitation. *Journal of the Atmospheric Sciences*, 67(6):1928–1946, January 2010. ISSN 0022-4928. doi: 10.1175/2010JAS3336.1. URL http://dx.doi.org/10.1175/2010JAS3336.1.

[106] S. Jankowfsky. *Understanding and modelling of hydrological processes in small peri-urban catchments using an object-oriented and modular distributed approach. Application to the Chaudanne and Mercier sub-catchments (Yzeron catchment, France). PhD Thesis.* PhD thesis, IRSTEA, Lyon, France, 2011.

[107] F.J. Jiménez-Hornero, P. Pavón-Domínguez, E. Gutiérrez de Ravé, and A.B. Ariza-Villaverde. Joint multifractal description of the relationship between wind patterns and land surface air temperature. *Atmospheric Research*, 99(3):366 – 376, 2011. ISSN 0169-8095. doi: https://doi.org/10.1016/j.atmosres.2010.11.009. URL http://www.sciencedirect.com/science/article/pii/S0169809510003121.

[108] M.L. Kawas and Z. Chen. A radar-based stochastic model for the time-space arrivals of the rain fields onto a geographical region. *Stochastic Hydrology and Hydraulics*, 3(4):261–280, December 1989. ISSN 0931-1955. doi: 10.1007/BF01543460. URL http://dx.doi.org/10.1007/BF01543460.

[109] Aghiad Khadour and Julien Waeytens. 5 - monitoring of concrete structures with optical fiber sensors. In F. Pacheco-Torgal, Robert E. Melchers, Xianming Shi, Nele De Belie, Kim Van Tittelboom, and Andrés Sáez, editors, *Eco-Efficient Repair and Rehabilitation of Concrete Infrastructures*, Woodhead Publishing Series in Civil and Structural Engineering, pages 97–121. Woodhead Publishing, 2018. ISBN 978-0-08-102181-1. doi: https://doi.org/10.1016/B978-0-08-102181-1.00005-8. URL https://www.sciencedirect.com/science/article/pii/B9780081021811000058.

[110] Bastian Kirsch, Marco Clemens, and Felix Ament. Stratiform and convective radar reflectivity–rain rate relationships and their potential to improve radar rainfall estimates. *Journal of Applied Meteorology and Climatology*, 58(10):2259 – 2271, 2019. doi: 10.1175/JAMC-D-19-0077.1. URL https://journals.ametsoc.org/view/journals/apme/58/10/jamc-d-19-0077.1.xml.

[111] Pierre-Emmanuel Kirstetter, Jonathan J. Gourley, Yang Hong, Jian Zhang, Saber Moazamigoodarzi, Carrie Langston, and Ami Arthur. Probabilistic precipitation rate estimates with ground-based radar networks. *Water Resources Research*, pages n/a–n/a, 2015. ISSN 1944-7973. doi: 10.1002/2014WR015672. URL http://dx.doi.org/10.1002/2014WR015672.

[112] M. Kleidorfer, A. Deletic, T. D. Fletcher, and W. Rauch. Impact of input data uncertainties on urban stormwater model parameters. *Water Science and Technology*, 60(6):1545–1554, 09 2009. ISSN 0273-1223. doi: 10.2166/wst.2009.493. URL https://doi.org/10.2166/wst.2009.493.

[113] Charles A. Knight and L. Jay Miller. Early Radar Echoes from Small, Warm Cumulus: Bragg and Hydrometeor Scattering. *Journal of the Atmospheric Sciences*, 55(18):2974–2992, September 1998. ISSN 0022-4928. doi: 10.1175/1520-0469(1998)055¡2974:EREFSW¿2.0.CO;2. URL http://dx.doi.org/10.1175/1520-0469(1998)055<2974:EREFSW>2.0.CO;2.

[114] A. N. Kolmogorov. Local structure of turbulence in an incompressible liquid for very large Reynolds numbers. *Dokl. Acad. Sci. USSR.*, 30:299, 1941.

[115] A. N. Kolmogorov. A refinement of previous hypotheses concerning the local structure of turbulence in viscous incompressible fluid at high Reynolds number. *J. Fluid. Mech.*, 13(1):82–85, 1962.

[116] M. Kotz, A. Levermann, and L. Wenz. The effect of rainfall changes on economic production. *Nature*, 601:223–227, 2022. doi: 10.1038/s41586-021-04283-8. URL https://doi.org/10.1038/s41586-021-04283-8.

[117] W. F. Krajewski and J. A. Smith. Radar hydrology: rainfall estimation. *Advances in Water Resources*, 25(8-12):1387–1394, December 2002. URL <Go to ISI>://WOS:000180073300027.

[118] W. F. Krajewski, G. Villarini, and J. A. Smith. Radar - Rainfall uncertainties : Where are We after Thirty Years of Effort? *Bulletin of the American Meteorological Society*, 91(1):87–94, January 2010. URL <Go to ISI>://WOS:000275420100006.

[119] Witold F. Krajewski, R. Raghavan, and V. Chandrasekar. Physically Based Simulation of Radar Rainfall Data Using a SpaceTime Rainfall Model. *Journal of Applied Meteorology*, 32(2):268–283, February 1993. ISSN 0894-8763. doi: 10.1175/1520-0450(1993)032¡0268:PBSORR¿2.0.CO;2. URL http://dx.doi.org/10.1175/1520-0450(1993)032<0268:PBSORR>2.0.CO;2.

[120] Anton Kruger and Witold F. Krajewski. Two-Dimensional Video Disdrometer: A Description. *Journal of Atmospheric and Oceanic Technology*, 19(5):602–617, 2002. URL http://dx.doi.org/10.1175/1520-0426(2002)019<0602:TDVDAD>2.0.CO;2.

[121] Steven A. Lack and Neil I. Fox. An examination of the effect of wind-drift on radar-derived surface rainfall estimations. *Atmospheric Research*, 85(2):217–229, 2007. ISSN 0169-8095. doi: https://doi.org/10.1016/j.atmosres.2006.09.010. URL https://www.sciencedirect.com/science/article/pii/S0169809507000154.

[122] P. Ladoy, F. Schmitt, D. Schertzer, and S. Lovejoy. The multifractal temporal variability of nimes rainfall data. *Comptes Rendus de l'Academie Des Sciences Serie Ii*, 317(6):775–782, September 1993. URL <Go to ISI>://WOS:A1993MB86600009.

[123] E. G. Lappala, R. W. Healy, and E. P. Weeks. Documentation of Computer Program VS2d to Solve the Equation of Fluid Flow in Variably Saturated Porous Media. *U.S. Geological Survey, Denver, 184p.*, 1987.

[124] Tuomo Lauri, Jarmo Koistinen, and Dmitri Moisseev. Advection-based adjustment of radar measurements. *Monthly Weather Review*, 140(3):1014 – 1022, 2012. doi: 10.1175/MWR-D-11-00045.1. URL https://journals.ametsoc.org/view/journals/mwre/140/3/mwr-d-11-00045.1.xml.

[125] Ladoy P. Lavallée D, Lovejoy S. *Fractals in geography*, chapter Nonlinear variability and landscape topography: analysis and simulation., page 171–205. Prentice-Hall, New-York, 1993.

[126] A. Lazarev, D. Schertzer, S. Lovejoy, and Y. Chigirinskaya. Unified multifractal atmospheric dynamics tested in the tropics: part II, vertical scaling and Generalized Scale Invariance. *Nonlinear Processes in Geophysics*, 1:115–123, 1994.

[127] H. Leijnse, R. Uijlenhoet, C. Z. van de Beek, A. Overeem, T. Otto, C. M. H. Unal, Y. Dufournet, H. W. J. Russchenberg, J. Figueras i Ventura, H. Klein Baltink, and I. Holleman. Precipitation measurement at cesar, the netherlands. *Journal of Hydrometeorology*, 11(6):1322 – 1329, 2010. doi: 10.1175/2010JHM1245.1.

[128] Jussi Leinonen. High-level interface to T-matrix scattering calculations: architecture, capabilities and limitations. *Optics Express*, 22(2):1655–1660, 2014. URL http://www.opticsexpress.org/abstract.cfm?URI=oe-22-2-1655.

[129] Jussi Leinonen, Dmitri Moisseev, Matti Leskinen, and Walter A. Petersen. A Climatology of Disdrometer Measurements of Rainfall in Finland over Five Years with Implications for Global Radar Observations. *Journal of Applied Meteorology and Climatology*, 51(2):392–404, 2012. URL http://dx.doi.org/10.1175/JAMC-D-11-056.1.

[130] K. Lengfeld, M. Clemens, H. Münster, and F. Ament. Performance of high-resolution X-band weather radar networks and the PATTERN example. *Atmospheric Measurement Techniques*, 7(12):4151–4166, 2014. doi: 10.5194/amt-7-4151-2014. URL http://www.atmos-meas-tech.net/7/4151/2014/.

[131] R. M. Lhermitte. Cloud and precipitation remote sensing at 94 GHz. *Geoscience and Remote Sensing, IEEE Transactions on*, 26(3):207–216, 1988.

[132] Xuewei Li and Pengjian Shang. Multifractal classification of road traffic flows. *Chaos, Solitons and Fractals*, 31(5):1089–1094, 2007. ISSN 0960-0779. doi: https://doi.org/10.1016/j.chaos.2005.10.109. URL https://www.sciencedirect.com/science/article/pii/S0960077905010313.

[133] PaweÅ Licznar, Janusz Lomotowski, and David E. Rupp. Random cascade driven rainfall disaggregation for urban hydrology: An evaluation of six models and a new generator. *Atmospheric Research*, 99(3-4): 563–578, 2011. URL http://www.sciencedirect.com/science/article/pii/S0169809510003510.

[134] M. Lilley, S. Lovejoy, N. Desaulniers-Soucy, and D. Schertzer. Multifractal large number of drops limit in rain. *Journal of Hydrology*, 328(1-2):20–37, 2006. URL http://www.sciencedirect.com/science/article/pii/S0022169405006335.

[135] Yuexiao Liu, Lu Zhuo, Maria Pregnolato, and Dawei Han. An assessment of statistical interpolation methods suited for gridded rainfall datasets. *International Journal of Climatology*, n/a(n/a). doi: https://doi.org/10.1002/joc.7389. URL https://rmets.onlinelibrary.wiley.com/doi/abs/10.1002/joc.7389.

[136] S. Lovejoy and B. Mandelbrot. Fractal properties of rain and a fractal model. *Tellus*, 37(A):209–232, 1995.

[137] S. Lovejoy and D. Schertzer. Generalized scale invariance in the atmosphere and fractal models of rain. *Water Resources Research*, 21(8):1233–1250, 1985. doi: https://doi.org/10.1029/WR021i008p01233. URL https://agupubs.onlinelibrary.wiley.com/doi/abs/10.1029/WR021i008p01233.

[138] S. Lovejoy and D. Schertzer. Comments on Are rain rate processes self-similar? *Wat. Resour. Res.*, 25: 577–579, 1989.

[139] S. Lovejoy and D. Schertzer. *Nonlinear Dynamics in Geosciences*, chapter Scale, scaling and multifractals in geophysics: twenty years on, pages 311–337. Springer, New York, NY, 2007. ISBN 978-0-387-34917-6. URL <Go to ISI>://000250749100018.

[140] S. Lovejoy and D. Schertzer. Scaling and multifractal fields in the solid earth and topography. *Nonlinear Processes in Geophysics*, 14(4):465–502, 2007. URL <Go to ISI>://000249816600013.

[141] S. Lovejoy and D. Schertzer. On the simulation of continuous in scale universal multifractals, Part II Space-time processes and finite size corrections. *Computers & Geosciences*, 36(11):1404–1413, November 2010. URL <Go to ISI>://000284923900002.

[142] S. Lovejoy, D. Schertzer, and A. A. Tsonis. Function box-counting and multiple elliptical dimension in rain. *Science*, 235(4792):1036–1038, February 1987. URL <Go to ISI>://A1987G168200034.

[143] S. Lovejoy, M. R. Duncan, and D. Schertzer. Scalar multifractal radar observer's problem. *J. Geophys. Res.*, 101:26479–26492, 1996.

[144] S. Lovejoy, D. Schertzer, M. Lilley, K. B. Strawbridge, and A. Radkevich. Scaling turbulent atmospheric stratification. I: Turbulence and waves. *Quarterly Journal of the Royal Meteorological Society*, 134(631): 277–300, January 2008. URL <Go to ISI>://000259292500001.

[145] Sarann Ly, Catherine Charles, and Aurore Degré. Different methods for spatial interpolation of rainfall data for operational hydrology and hydrological modeling at watershed scale. a revie. *Biotechnol. Agron. Soc. Environ.*, 17(2):392–406, 2013.

[146] J. Macor. *Développement de techniques de prévision de pluie basées sur les propriétés multi-échelles des données radar et satellites.* PhD thesis, Ecole Nationale des Ponts et Chaussées, Marne La vallée, 2007.

[147] J. Macor, D. Schertzer, and S. Lovejoy. Multifractal Methods Applied to Rain Forecast Using Radar Data. *La Houille Blanche*, 4:92–98, 2007.

[148] D. Marsan, D. Schertzer, and S. Lovejoy. Causal space-time multifractal processes: Predictability and forecasting of rain fields. *J. Geophys. Res.*, 101:26333–26346, 1996.

[149] J. S. Marshall and W. M. Palmer. The distribution of raindrops with size. *J. Meteor.*, 5:165–166, 1948.

[150] V. Masson-Delmotte, P. Zhai, A. Pirani, S.L. Connors, C. Péan, S. Bergerand N. Caud, Y. Chen, L. Goldfarb, M.I. Gomis, M. Huang, K. Leitzell, E. Lonnoy, J.B.R. Matthews, T.K. Maycock, T. Waterfield, O. Yelekçi, R. Yu, , and B. Zhou. Ipcc, 2021: Climate change 2021: The physical science basis. contribution of working group i to the sixth assessment report of the intergovernmental panel on climate change. 2021.

[151] G. Matheron. *The theory of regionalized variables and its applications.* Paris : École Nationale Supérieure des Mines de Paris, 1971.

[152] Sergey Y. Matrosov, Kurt A. Clark, Brooks E. Martner, and Ali Tokay. X-Band Polarimetric Radar Measurements of Rainfall. *Journal of Applied Meteorology*, 41(9):941–952, 2002.

[153] Naika Meili, Gabriele Manoli, Paolo Burlando, Jan Carmeliet, Winston T.L. Chow, Andrew M. Coutts, Matthias Roth, Erik Velasco, Enrique R. Vivoni, and Simone Fatichi. Tree effects on urban microclimate: Diurnal, seasonal, and climatic temperature differences explained by separating radiation, evapotranspiration, and roughness effects. *Urban Forestry Urban Greening*, 58:126970, 2021. ISSN 1618-8667. doi: https://doi.org/10.1016/j.ufug.2020.126970. URL https://www.sciencedirect.com/science/article/pii/S1618866720307871.

[154] P. Meischner. *Weather Radar : Principles and Advanced Applications.* Springer, Berlin, 2004.

[155] M. Menabde and M. Sivapalan. Modeling of rainfall time series and extremes using bounded random cascades and Levy-stable distributions. *Water Resources Research*, 36(11):3293–3300, November 2000. URL <Go to ISI>://WOS:000090146100014.

[156] Charles Meneveau, K. R. Sreenivasan, P. Kailasnath, and M. S. Fan. Joint multifractal measures: Theory and applications to turbulence. *Phys. Rev. A*, 41:894–913, Jan 1990. doi: 10.1103/PhysRevA.41.894. URL https://link.aps.org/doi/10.1103/PhysRevA.41.894.

[157] Carlos Iglesias Merchan and Luis Diaz-Balteiro. Noise pollution mapping approach and accuracy on landscape scales. *Science of The Total Environment*, 449:115 – 125, 2013. ISSN 0048-9697. doi: https://doi.org/10.1016/j.scitotenv.2013.01.063. URL http://www.sciencedirect.com/science/article/pii/S0048969713001186.

[158] C. Merker, G. Peters, M. Clemens, K. Lengfeld, and F. Ament. A novel approach for absolute radar calibration: formulation and theoretical validation. *Atmos. Meas. Tech.*, 8(6):2521–2530, June 2015. ISSN 1867-8548. doi: 10.5194/amt-8-2521-2015. URL http://www.atmos-meas-tech.net/8/2521/2015/.

[159] Michael I. Mishchenko, Larry D. Travis, and Daniel W. Mackowski. T-matrix computations of light scattering by nonspherical particles: A review. *Journal of Quantitative Spectroscopy and Radiative Transfer*, 55 (5):535–575, 1996. URL http://www.sciencedirect.com/science/article/pii/0022407396000027.

[160] Marion P. Mittermaier, Robin J. Hogan, and Anthony J. Illingworth. Using mesoscale model winds for correcting wind-drift errors in radar estimates of surface rainfall. *Quarterly Journal of the Royal Meteorological Society*, 130(601):2105–2123, 2004. doi: https://doi.org/10.1256/qj.03.156. URL https://rmets.onlinelibrary.wiley.com/doi/abs/10.1256/qj.03.156.

[161] Guillermo Montero-Martinez and Fernando Garcia-Garcia. On the behaviour of raindrop fall speed due to wind. *Quarterly Journal of the Royal Meteorological Society*, 142(698):2013–2020, 2016. doi: 10.1002/qj.2794. URL https://rmets.onlinelibrary.wiley.com/doi/abs/10.1002/qj.2794.

[162] E. Moreau, J. Testud, and E. Le Bouar. Rainfall spatial variability observed by X-band weather radar and its implication for the accuracy of rainfall estimates. *Advances in Water Resources*, 32(7):1011–1019, 2009. URL http://www.sciencedirect.com/science/article/pii/S0309170808002078.

[163] H. Müller and U. Haberlandt. Temporal rainfall disaggregation using a multiplicative cascade model for spatial application in urban hydrology. *Journal of Hydrology*, January 2016. ISSN 0022-1694. doi: 10.1016/j.jhydrol.2016.01.031. URL http://www.sciencedirect.com/science/article/pii/S0022169416000494.

[164] Tero J. Niemi, Teemu Kokkonen, and Alan W. Seed. A simple and effective method for quantifying spatial anisotropy of time series of precipitation fields. *Water Resources Research*, 50(7):5906–5925, 2014. ISSN 1944-7973. doi: 10.1002/2013WR015190. URL http://dx.doi.org/10.1002/2013WR015190.

[165] D. K. Nykanen. Linkages between Orographic Forcing and the Scaling Properties of Convective Rainfall in Mountainous Regions. *J. of hydrometeorology*, 9:327–347, 2008.

[166] D. K. Nykanen and D. Harris. Orographic influences on the multiscale statistical properties of precipitation. *Journal of Geophysical Research-Atmospheres*, 108(D8), March 2003. URL <Go to ISI>://000182223400004.

[167] Susana Ochoa-Rodriguez, Li-Pen Wang, Auguste Gires, Rui Daniel Pina, Ricardo Reinoso-Rondinel, Guendalina Bruni, Abdellah Ichiba, Santiago Gaitan, Elena Cristiano, Johan van Assel, Stefan Kroll, Damian Murlà-Tuyls, Bruno Tisserand, Daniel Schertzer, Ioulia Tchiguirinskaia, Christian Onof, Patrick Willems, and Marie-Claire ten Veldhuis. Impact of spatial and temporal resolution of rainfall inputs on urban hydrodynamic modelling outputs: A multi-catchment investigation. *Journal of Hydrology*, (0), 2015. ISSN 0022-1694. doi: 10.1016/j.jhydrol.2015.05.035. URL http://www.sciencedirect.com/science/article/pii/S0022169415003856.

[168] J. Olsson. Evaluation of a scaling cascade model for temporal rainfall disaggregation. *Hydrology and Earth System Sciences*, 2(1):19–30, March 1998. URL <Go to ISI>://000081369600003.

[169] J. Olsson, J. Niemczynowicz, and R. Berndtsson. Fractal analysis of high-resolution rainfall time series. *J. Geophys. Res.*, 98:23265–23274, 1993.

[170] OTT. Operating instructions, Present Weather Sensor OTT Parsivel2. 2014.

[171] T. M. Over and V. K. Gupta. A space-time theory of mesoscale rainfall using random cascades. *Journal of Geophysical Research-Atmospheres*, 101(D21):26319–26331, November 1996. URL <Go to ISI>://A1996VW42100015.

[172] Hans A Panofsky. Objective weather-map analysis. *J. Meteor*, 6(6):386–392, 1949.

[173] G. Parisi and U. Frish. A multifractal model of intermittency. In M. Ghill, R. Benzi, and G. Parisi, editors, *Turbulence and predictability in geophysical fluid dynamics*, pages 111–114. Elsevier North Holland, New-York, 1985.

[174] S.-G. Park, Hae-Lim Kim, Young-Woong Ham, and Sung-Hwa Jung. Comparative evaluation of the ott parsivel2 using a collocated two-dimensional video disdrometer. *Journal of Atmospheric and Oceanic Technology*, 34(9):2059–2082, 2017. doi: 10.1175/JTECH-D-16-0256.1. URL https://doi.org/10.1175/JTECH-D-16-0256.1.

[175] S.Y. Park, K.W. Lee, I.H. Park, and S.R. Ha. Effect of the aggregation level of surface runoff fields and sewer network for a swmm simulation. *Desalination*, 226(1): 328–337, 2008. ISSN 0011-9164. doi: https://doi.org/10.1016/j.desal.2007.02.115. URL https://www.sciencedirect.com/science/article/pii/S0011916408001653. 10th IWA International Specialized Conference on Diffuse Pollution and Sustainable Basin Management.

[176] I. Paz, B. Willinger, A. Gires, A. Ichiba, L. Monier, C. Zobrist, B. Tisserand, I. Tchiguirinskaia, and D. Schertzer. Multifractal comparison of reflectivity and polarimetric rainfall data from c- and x-band radars and respective hydrological responses of a complex catchment model. *Water (Switzerland)*, 10(3), 2018. doi: 10.3390/w10030269. cited By 0.

[177] Henning Schjørring Pedersen and Bent Hasholt. Influence of wind speed on rainsplash erosion. *CATENA*, 24(1):39 – 54, 1995. ISSN 0341-8162. doi: https://doi.org/10.1016/0341-8162(94)00024-9. URL http://www.sciencedirect.com/science/article/pii/0341816294000249.

[178] Shang Peng-Jian and Shen Jin-Sheng. Multi-fractal analysis of highway traffic data. *Chinese Physics*, 16(2):365–373, jan 2007. doi: 10.1088/1009-1963/16/2/016. URL https://doi.org/10.1088/1009-1963/16/2/016.

[179] Gerhard Peters, Bernd Fischer, Hans Münster, Marco Clemens, and Andreas Wagner. Profiles of raindrop size distributions as retrieved by microrain radars. *Journal of Applied Meteorology*, 44(12):1930 – 1949, 2005. doi: 10.1175/JAM2316.1. URL https://journals.ametsoc.org/view/journals/apme/44/12/jam2316.1.xml.

[180] V. Pitsikalis and P. Maragos. Filtered dynamics and fractal dimensions for noisy speech recognition. *IEEE Signal Processing Letters*, 13(11):711–714, Nov 2006. ISSN 1070-9908. doi: 10.1109/LSP.2006.879424.

[181] M. Pitt. The Pitt Review : Learning lessons from the 2007 floods, http://webarchive.nationalarchives.gov.uk/20100807034701/http:/archive.cabinetoffice.gov.uk/pittreview/thepittrevie (accessed 20-10-2014). 2008.

[182] Arezoo Rafieeinasab, Amir Norouzi, Sunghee Kim, Hamideh Habibi, Behzad Nazari, Dong-Jun Seo, Haksu Lee, Brian Cosgrove, and Zhengtao Cui. Toward high-resolution flash flood prediction in large urban areas – analysis of sensitivity to spatiotemporal resolution of rainfall input and hydrologic modeling. *Journal of Hydrology*, 531:370–388, 2015. ISSN 0022-1694. doi: https://doi.org/10.1016/j.jhydrol.2015.08.045. URL https://www.sciencedirect.com/science/article/pii/S0022169415006605. Hydrologic Applications of Weather Radar.

[183] T. H. Raupach and A. Berne. Retrieval of the raindrop size distribution from polarimetric radar data using double-moment normalisation. *Atmospheric Measurement Techniques*, 10(7):2573–2594, 2017. doi: 10.5194/amt-10-2573-2017. URL https://amt.copernicus.org/articles/10/2573/2017/.

[184] J. Richard, I. Tchiguirinskaia, and D. Schertzer. Gis data Assimilation interface for distributed hydrological models. *Proceedings Hydro-Informatics Conference, Hamburg, 14-18 July 2012, Germany*, 2012.

[185] F. Rodriguez, H. Andrieu, and F. Morena. A distributed hydrological model for urbanized areas - model development and application to case studies. *Journal of Hydrology*, 351:268–287, 2008.

[186] L. A. Rossman. Storm Water Management Model, User's Manual. Version 5.0. *U.S. Environmental Protection Agency, EPA/600/R-05/040.*, 2010.

[187] D. E. Rupp, P. Licznar, W. Adamowski, and M. LeÅniewski. Multiplicative cascade models for fine spatial downscaling of rainfall: parameterization with rain gauge data. *Hydrol. Earth Syst. Sci.*, 16(3):671–684, 2012. URL http://www.hydrol-earth-syst-sci.net/16/671/2012/ http://www.hydrol-earth-syst-sci.net/16/671/2012/hess-16-671-2012.pdf.

[188] S. Russ and B. Sapoval. Increased damping of irregular resonators. *Phys. Rev. E*, 65:036614, Feb 2002. doi: 10.1103/PhysRevE.65.036614. URL https://link.aps.org/doi/10.1103/PhysRevE.65.036614.

[189] Elga Salvadore, Jan Bronders, and Okke Batelaan. Hydrological modelling of urbanized catchments: A review and future directions. *Journal of Hydrology*, 529, Part 1:62–81, October 2015. ISSN 0022-1694. doi: 10.1016/j.jhydrol.2015.06.028. URL http://www.sciencedirect.com/science/article/pii/S0022169415004412.

[190] G. Salvadori, D. Schertzer, and S. Lovejoy. Multifractal objective analysis: conditioning and interpolation. *Stoch. Environ. Res. and Risk Anal.*, 15(4):261–283, 2000.

[191] Caroline Sandford. Correcting for wind drift in high resolution radar rainfall products: a feasibility study. *Journal of Hydrology*, 531:284–295, 2015. ISSN 0022-1694. doi: https://doi.org/10.1016/j.jhydrol.2015.03.023. URL https://www.sciencedirect.com/science/article/pii/S0022169415001948. Hydrologic Applications of Weather Radar.

[192] B. Sarkis. *Etude multi-échelle des réseaux d'assainissement*. PhD thesis, Ecole des Ponts ParisTech, Marne la Vallée, France, 2008.

[193] D. Schertzer and S. Lovejoy. Physical modelling and analysis of rain and clouds by anisotropic scaling and multiplicative processes. *J. Geophys. Res.*, 92(D8):9693–9714, 1987.

[194] D. Schertzer and S. Lovejoy. Hard and soft multifractal processes. *Physica A*, 185(1-4):187–194, 1992.

[195] D. Schertzer and S. Lovejoy. Universal multifractals do exist!: Comments. *Journal of Applied Meteorology*, 36(9):1296–1303, September 1997. URL <Go to ISI>://WOS:A1997XU62400016. J. Appl. Meteorol.

[196] D. Schertzer and S. Lovejoy. Multifractals, generalized scale invariance and complexity in geophysics. *International Journal of Bifurcation and Chaos*, 21(12):3417–3456, December 2011. URL <Go to ISI>://WOS:000300016000003.

[197] D. Schertzer and I. Tchiguirinskaia. Multifractal vector fields and stochastic Clifford algebra. *Chaos*, 25: 123127, 2015. doi: DOI:http://dx.doi.org/10.1063/1.4937364.

[198] D. Schertzer, I. Tchiguirinskaia, S. Lovejoy, and P. Hubert. No monsters, no miracles: in nonlinear sciences hydrology is not an outlier! *Hydrological Sciences Journal-Journal Des Sciences Hydrologiques*, 55(6):965–979, 2010. URL <Go to ISI>://000282231300010.

[199] D. Schertzer, I. Tchiguirinskaia, and S. Lovejoy. Getting higher resolution rainfall estimates: X-band radar technology and multifractal drop distribution. *Proceedings of the Weather Radar and Hydrology symposium held in Exeter, UK, April 2011, IAHS Publ. 351*, 2011.

[200] Daniel Schertzer and Ioulia Tchiguirinskaia. A century of turbulent cascades and the emergence of multifractal operators. *Earth and Space Science*, 7(3):e2019EA000608, 2020. doi: 10.1029/2019EA000608. URL https://agupubs.onlinelibrary.wiley.com/doi/abs/10.1029/2019EA000608. e2019EA000608 10.1029/2019EA000608.

[201] D. Schindler, J. Bauhus, and H. Mayer. Wind effects on trees. *Eur J Forest Res*, 131:159–163, 2012. doi: 10.1007/s10342-011-0582-5. URL https://doi.org/10.1007/s10342-011-0582-5.

[202] F. G. Schmitt. Continuous multifractal models with zero values: a continuous b-multifractal model. *Journal of Statistical Mechanics: Theory and Experiment*, 2014(2), 2014. URL http://stacks.iop.org/1742-5468/2014/i=2/a=P02008.

[203] A. W. Seed. A Dynamic and Spatial Scaling Approach to Advection Forecasting. *Journal of Applied Meteorology*, 42(3):381–388, 2003. URL http://dx.doi.org/10.1175/1520-0450(2003)042<0381:ADASSA>2.0.CO;2.

[204] Laurent Seuront and François G. Schmitt. Multiscaling statistical procedures for the exploration of biophysical couplings in intermittent turbulence. part i. theory. *Deep Sea Research Part II: Topical Studies in Oceanography*, 52(9):1308 – 1324, 2005. ISSN 0967-0645. doi: https://doi.org/10.1016/j.dsr2.2005.01.006. URL http://www.sciencedirect.com/science/article/pii/S0967064505000470. Observations and modelling of mixed layer turbulence: Do they represent the same statistical quantities?

[205] Laurent Seuront and François G. Schmitt. Multiscaling statistical procedures for the exploration of biophysical couplings in intermittent turbulence. part ii. applications. *Deep Sea Research Part II: Topical Studies in Oceanography*, 52(9):1325 – 1343, 2005. ISSN 0967-0645. doi: https://doi.org/10.1016/j.dsr2.2005.01.005. URL http://www.sciencedirect.com/science/article/pii/S0967064505000482. Observations and modelling of mixed layer turbulence: Do they represent the same statistical quantities?

[206] Lígia T. Silva, Marta Oliveira, and José F. Silva. Urban form indicators as proxy on the noise exposure of buildings. *Applied Acoustics*, 76:366 – 376, 2014. ISSN 0003-682X. doi: https://doi.org/10.1016/j.apacoust.2013.07.027. URL http://www.sciencedirect.com/science/article/pii/S0003682X13001990.

[207] Glécio M. Siqueira, Ênio F.F. Silva, Eva Vidal-Vázquez, and Antonio Paz-González. Multifractal and joint multifractal analysis of general soil properties and altitude along a transect. *Biosystems Engineering*, 168:105 – 120, 2018. ISSN 1537-5110. doi: https://doi.org/10.1016/j.biosystemseng.2017.08.024. URL http://www.sciencedirect.com/science/article/pii/S1537511016305943. Computational Tools to Support Soil Management Decisions.

[208] Wallingford Software. *InfoWorks CS Help Documentation*. HR Wallingford Group, Wallingford, UK, 2009.

[209] M. Steiner. Estimation of Precipitation Using Ground-based, Active Microwave Sensors. In M. G. Anderson, editor, *Encyclopedia of hydrological sciences*. Wiley, 2005.

[210] David J. Stephenson. Selection of stormwater model parameters. *Journal of Environmental Engineering*, 115:210–220, 1989.

[211] J. E. Stout, S. P. Arya, and E. L. Genikhovich. The effect of nonlinear drag on the motion and settling velocity of heavy particles. *Journal of the Atmospheric Sciences*, 52(22):3836–3848, 1995. doi: 10.1175/1520-0469(1995)052¡3836:TEONDO¿2.0.CO;2. URL https://doi.org/10.1175/1520-0469(1995)052<3836:TEONDO>2.0.CO;2.

[212] H. Takayasu. *Fractals in the physical sciences*. Manchester University Press, Manchester, 1990.

[213] F. J. Tapiador, R. Checa, and M. de Castro. An experiment to measure the spatial variability of rain drop size distribution using sixteen laser disdrometers. *Geophysical Research Letters*, 37(16):L16803, 2010. ISSN 1944-8007. doi: 10.1029/2010GL044120. URL http://dx.doi.org/10.1029/2010GL044120.

[214] E. Le Tavernier, P. Simard, M. Bulo, and D. Boichu. Fractal study of the boiling of water. *IFAC Proceedings Volumes*, 30(18):1213 – 1217, 1997. ISSN 1474-6670. doi: https://doi.org/10.1016/S1474-6670(17)42562-6. URL http://www.sciencedirect.com/science/article/pii/S1474667017425626. IFAC Symposium on Fault Detection, Supervision and Safety for Technical Processes (SAFEPROCESS 97), Kingston upon Hull, UK, 26-28 August 1997.

[215] I. TCHIGUIRINSKAIA. Scale invariance and stratification: The unified multifractal model of hydraulic conductivity. *Fractals*, 10(03):329–334, 2002. doi: 10.1142/S0218348X02001373. URL https://doi.org/10.1142/S0218348X02001373.

[216] I. Tchiguirinskaia, D. Schertzer, H. Bendjoudi, P. Hubert, and S. Lovejoy. Multiscaling geophysics and sustainable development. *Scales in Hydrology and Water Management, IAHS Publ. 287*, pages 113–136, 2004.

[217] RALF TESCH, MARK D. NORMAND, and MICHA PELEG. On the apparent fractal dimension of sound bursts in acoustic signatures of two crunchy foods1. *Journal of Texture Studies*, 26(6):685–694, 1995. doi: 10.1111/j.1745-4603.1996.tb00991.x. URL https://onlinelibrary.wiley.com/doi/abs/10.1111/j.1745-4603.1996.tb00991.x.

[218] Y. Tessier, S. Lovejoy, and D. Schertzer. Universal Multifractals: theory and observations for rain and clouds. *Journal of Applied Meteorology*, 32(2):223–250, February 1993. URL <Go to ISI>://A1993KL90900009.

[219] Jacques Testud, Stéphane Oury, Robert A. Black, Paul Amayenc, and Xiankang Dou. The Concept of "Normalized" Distribution to Describe Raindrop Spectra: A Tool for Cloud Physics and Cloud Remote Sensing. *Journal of Applied Meteorology*, 40(6):1118–1140, June 2001. ISSN 0894-8763. doi: 10.1175/1520-0450(2001)040¡1118:TCONDT¿2.0.CO;2. URL http://dx.doi.org/10.1175/1520-0450(2001)040<1118:TCONDT>2.0.CO;2.

[220] ThiesCLIMA. 3d ultrasonic anemometer, instructions for use. 2013.

[221] ThiesCLIMA. Clima sensor us, instructions for use. 2013.

[222] ALFRED H. THIESSEN. Precipitation averages for large areas. *Monthly Weather Review*, 39(7):1082 – 1089, 1911. doi: 10.1175/1520-0493(1911)39¡1082b:PAFLA¿2.0.CO;2. URL https://journals.ametsoc.org/view/journals/mwre/39/7/1520-0493$_1$911$_3$9$_1$082$b_p afla_{20c} o_2 .xml$.

[223] S. Thorndahl, T. Einfalt, P. Willems, J. E. Nielsen, M.-C. ten Veldhuis, K. Arnbjerg-Nielsen, M. R. Rasmussen, and P. Molnar. Weather radar rainfall data in urban hydrology. *Hydrology and Earth System Sciences*, 21(3):1359–1380, 2017. doi: 10.5194/hess-21-1359-2017. URL http://www.hydrol-earth-syst-sci.net/21/1359/2017/.

[224] M. Thurai, G. J. Huang, V. N. Bringi, W. L. Randeu, and M. SchÃ¶nhuber. Drop Shapes, Model Comparisons, and Calculations of Polarimetric Radar Parameters in Rain. *Journal of Atmospheric and Oceanic Technology*, 24(6):1019–1032, 2007. URL http://dx.doi.org/10.1175/JTECH2051.1.

[225] M. Thurai, M. Schönhuber, G. Lammer, and V. Bringi. Raindrop shapes and fall velocities in "turbulent times". *Advances in Science and Research*, 16:95–101, 2019. doi: 10.5194/asr-16-95-2019. URL https://www.adv-sci-res.net/16/95/2019/.

[226] Merhala Thurai and V. N. Bringi. Drop Axis Ratios from a 2d Video Disdrometer. *Journal of Atmospheric and Oceanic Technology*, 22(7):966–978, 2005. URL http://dx.doi.org/10.1175/JTECH1767.1.

[227] Li Tian, Yu-Jie Zeng, and Xing Fu. Velocity ratio of wind-driven rain and its application on a transmission tower subjected to wind and rain loads. *Journal of Performance of Constructed Facilities*, 32(5):04018065, 2018. doi: 10.1061/(ASCE)CF.1943-5509.0001210.

[228] F. Tridon, J. Van Baelen, and Y. Pointin. Aliasing in micro rain radar data due to strong vertical winds. *Geophysical Research Letters*, 38(2), 2011. doi: https://doi.org/10.1029/2010GL046018.

[229] G. A. M. van Kuik, J. Peinke, R. Nijssen, D. Lekou, J. Mann, J. N. Sørensen, C. Ferreira, J. W. van Wingerden, D. Schlipf, P. Gebraad, H. Polinder, A. Abrahamsen, G. J. W. van Bussel, J. D. Sørensen, P. Tavner, C. L. Bottasso, M. Muskulus, D. Matha, H. J. Lindeboom, S. Degraer, O. Kramer, S. Lehnhoff, M. Sonnenschein, P. E. Sørensen, R. W. Künneke, P. E. Morthorst, and K. Skytte. Long-term research challenges in wind energy – a research agenda by the European Academy of Wind Energy. *Wind Energ. Sci.*, 1(1):1–39, February 2016. ISSN 2366-7451. doi: 10.5194/wes-1-1-2016. URL http://www.wind-energ-sci.net/1/1/2016/.

[230] M. L. Velleux, J. F. England, and P. Y. Julien. TREX Watershed Modelling Framework User's Manual: Model Theory and Description. *Department of civil engineering, Colorado State University, Fort Collins*, page 106p, 2011.

[231] D. Veneziano and P. Furcolo. Multifractality of rainfall and scaling of intensity-duration-frequency curves. *Water Resources Research*, 38(12), December 2002. URL <Go to ISI>://WOS:000181245600001.

[232] S. Verrier, L. de Montera, L. Barthes, and C. Mallet. Multifractal analysis of African monsoon rain fields, taking into account the zero rain-rate problem. *Journal of Hydrology*, 389(1-2):111–120, July 2010. URL <Go to ISI>://000280452500010.

[233] Sebastien Verrier, Laurent Barthes, and Cecile Mallet. Theoretical and empirical scale dependency of z-r relationships: evidence, impacts, and correction. *Journal of Geophysical Research: Atmospheres*, 118(14): 7435–7449, 2013. URL http://dx.doi.org/10.1002/jgrd.50557.

[234] P.-A. Versini, A. Gires, I. Tchiguirinskaia, and D. Schertzer. Fractal analysis of green roof spatial implementation in european cities. *Urban Forestry & Urban Greening*, 49: 126629, 2020. ISSN 1618-8667. doi: https://doi.org/10.1016/j.ufug.2020.126629. URL http://www.sciencedirect.com/science/article/pii/S1618866719306090.

[235] Pierre-Antoine Versini, Auguste Gires, Ioulia Tchinguirinskaia, and Daniel Schertzer. Toward an operational tool to simulate green roof hydrological impact at the basin scale: a new version of the distributed rainfall–runoff model Multi-Hydro. *Water Science and Technology*, 2016.

[236] Versini, Pierre-Antoine, Gires, Auguste, Fitton, George, Tchiguirinskaia, Ioulia, and Schertzer, Daniel. Toward an assessment of the hydrological components variability in green infrastructures: Pilot site of the green wave (champs-sur-marne). *La Houille Blanche*, (4):34–42, 2018. doi: 10.1051/lhb/2018040. URL https://doi.org/10.1051/lhb/2018040.

[237] R. Vojak and J. Levy Vehel. Multifractal description of road traffic structure. In *Proceedings of IFAC'94,Tanjin, China, August 1994*, pages 24–6, 1994.

[238] S.N. Walker and J.E. Wade. Effect of precipitation on wind turbine performance, doe de1ioo1144. 1986.

[239] Zheng-Ying WANG, Qiao-Sheng SHU, Li-Ya XIE, Zuo-Xin LIU, and B.C. SI. Joint multifractal analysis of scaling relationships between soil water-retention parameters and soil texture. *Pedosphere*, 21 (3):373 – 379, 2011. ISSN 1002-0160. doi: https://doi.org/10.1016/S1002-0160(11)60138-0. URL http://www.sciencedirect.com/science/article/pii/S1002016011601380.

[240] James W. Wilson and Edward A. Brandes. Radar measurement of rainfall: A summary. *Bulletin of the American Meteorological Society*, 60(9):1048–1058, 1979. URL http://dx.doi.org/10.1175/1520-0477(1979)060<1048:RMORS>2.0.CO;2.

[241] W. Wolff, A. Overeem, H. Leijnse, and R. Uijlenhoet. Rainfall retrieval algorithm for commercial microwave links: stochastic calibration. *Atmospheric Measurement Techniques*, 15(2):485–502, 2022. doi: 10.5194/amt-15-485-2022. URL https://amt.copernicus.org/articles/15/485/2022/.

[242] Wen-Jie Xie, Zhi-Qiang Jiang, Gao-Feng Gu, Xiong Xiong, and Wei-Xing Zhou. Joint multifractal analysis based on the partition function approach: analytical analysis, numerical simulation and empirical application. *New Journal of Physics*, 17(10):103020, 2015. URL http://stacks.iop.org/1367-2630/17/i=10/a=103020.

[243] A. M. Yaglom. The influence on the fluctuation in energy dissipation on the shape of turbulent characteristics in the inertial interval. *Sov. Phys. Dokl.*, 2:26–30, 1966.

[244] Yu Zhang, Thomas Adams, and James V. Bonta. Subpixel-scale rainfall variability and the effects on separation of radar and gauge rainfall errors. *Journal of Hydrometeorology*, 8(6):1348–1363, 2007. URL http://dx.doi.org/10.1175/2007JHM835.1.

[245] J. Zwiebel, J. Van Baelen, S. Anquetin, Y. Pointin, and B. Boudevillain. Impacts of orography and rain intensity on rainfall structure. the case of the hymex iop7a event. *Quarterly Journal of the Royal Meteorological Society*, 142(S1):310–319, 2016. doi: https://doi.org/10.1002/qj.2679.